

NMR Spectroscopic Investigations of Brønsted Acid Catalyzed Transfer Hydrogenations

Dissertation

zur Erlangung des Doktorgrades der Naturwissenschaften

(Dr. rer. nat.)

der Fakultät für Chemie und Pharmazie

der Universität Regensburg



vorgelegt von

Kerstin Rothermel

aus Olching

im Jahr 2019

Die vorliegende Dissertation beruht auf Arbeiten, die zwischen Dezember 2015 und Juni 2019 am Arbeitskreis von Frau Professor Dr. Ruth M. Gschwind am Institut für Organische Chemie der Universität Regensburg durchgeführt wurden.

Promotionsgesuch eingereicht am: 13. Juni 2019

Die Arbeit wurde angeleitet von: Prof. Dr. Ruth M. Gschwind

Promotionsausschuss:

Vorsitzender: Apl. Prof. Dr. Rainer Müller

1. Gutachter: Prof. Dr. Ruth M. Gschwind

2. Gutachter: Prof. Dr. Werner Kremer

3. Prüfer: Prof. Dr. Julia Rehbein

Danksagung

An dieser Stelle möchte ich mich bei allen bedanken, die zum Gelingen dieser Arbeit beigetragen haben. Dabei geht mein besonderer Dank an meine Doktormutter Frau Prof. Dr. Ruth Gschwind, die mit der überaus interessanten Themenstellung und zahlreichen Diskussionen, diese Arbeit entscheidend geprägt hat.

Des Weiteren danke ich Prof. Dr. Werner Kremer für die Übernahme des Zweitgutachtens. Bei Prof. Dr. Julia Rehbein und Apl. Prof. Dr. Reiner Müller möchte ich mich für die Ausübung des Amtes als Dritprüferin bzw. als Vorsitzenden sehr herzlich bedanken.

Einen besonderen Dank möchte ich auch meinen aktuellen und ehemaligen Kollegen aussprechen, die meine Zeit um Ak Gschwind enorm bereichert haben. Hier gilt mein Dank besonders Dr. Julian Greindl. Merce dir für die vielen Anregungen und Diskussionen, mit denen du mir den Einstieg in die Welt der Wasserstoffbrücken erleichtert hast. Und merce dir dafür, dass du mit deinem Humor immer für gute Stimmung im Büro gesorgt hast. Ein großes Danke geht auch an den harten Kern des Bierdienstags Dr. Andreas Seegerer, Philipp Nitschke und Willi Stockerl für die vielen lustigen und unvergesslichen Stunden. Nicht zu vergessen sind Nele Berg und Verena Streitferdt: Bei euch möchte ich mich für die unglaublich schöne Zeit in Berlin, Mainz, Philadelphia und natürlich Regensburg bedanken! Außerdem danke ich Florian Hastreiter, Johannes Gramüller, Daniel Schneider, Dr. Hanna Bartling, Dr. Michael Haindl, Dr. Johnny Hioe, Dr. Maxime Melikian, Dr. Lokesh Nanjundappa, Dr. Nils Sorgenfrei und Dr. Matej Zabka für das angenehme Arbeitsklima und die schöne gemeinsame Zeit an der Uni!

Natürlich gilt mein Dank auch Nikola Kastner-Pustet und Ulrike Weck sowie allen Mitarbeitern der NMR-Abteilung Dr. Ilya Shenderovich, Fritz Kastner, Veronica Scheidler, Georgine Stühler und Annette Schramm für ihre immer freundliche Hilfe und Unterstützung

Ganz besonders möchte ich mich bei dir Vera für die unzähligen und wunderschönen gemeinsamen Stunden und dein offenes Ohr bedanken! Danke – du bist die Beste! Außerdem danke ich meinen ehemaligen Kommilitonen Julia Bamberger, Resi Fischer, Jana Schiller und Basti Stockerl für eine unvergessliche Studienzeit!

Ein besonderes großes Dankeschön geht an meine Brüder und vor allem an meine Eltern, die mir mit ihrer bedingungslosen Unterstützung dieses Studium ermöglicht haben!

Am allermeisten danke ich aber meinem Freund Uli, der immer für mich da ist und mich mit seinem Rückhalt und Zuspruch immer wieder bestärkt hat! Danke auch für dein Verständnis in den letzten Monaten!

Vielen Dank!

NMR Spectroscopic Investigations of Brønsted Acid Catalyzed Transfer Hydrogenations

Kerstin Rothermel

Table of Contents

1	Introduction and Outline	1
1.1.	Brønsted acid catalysis	1
1.2.	Substrate activation <i>via</i> hydrogen bonds	4
1.3.	Hydrogen bond analysis	6
1.4.	Outline	7
1.5.	References	9
2	NMR Spectroscopic Characterization of Charge Assisted Strong Hydrogen Bonds in Brønsted Acid Catalysis	11
2.1.	Abstract	13
2.2.	Introduction	13
2.3.	Results and Discussion	15
2.3.1.	Model Systems	15
2.3.2.	Computational Details	17
2.3.3.	Detection and Characterization of Hydrogen Bonds by NMR	17
2.3.4.	Hydrogen Bond Analysis Based on $\delta^1\text{H}$, $\delta^{15}\text{N}$ and $^1J_{\text{NH}}$	19
2.3.5.	Comparison of NMR Data and Theoretical Calculations	23
2.4.	Conclusions	32
2.5.	References	33
3	Internal Acidity Scale and Reactivity Evaluation of Chiral Phosphoric Acids with different 3,3'-Substituents in Brønsted Acid Catalysis	37
3.1.	Abstract	39
3.2.	Introduction	39
3.3.	Results and Discussion	43
3.3.1.	Investigated systems/complexes	43
3.3.2.	Determination of the Internal Acidity	44
3.3.3.	Reactivity Analysis	49
3.4.	Conclusion	56
3.5.	Supporting information	57
3.5.1.	Synthesis of Imine Substrates	58
3.5.2.	Sample preparation of binary complexes in CD_2Cl_2	64
3.5.3.	Spectrometer data	65
3.5.4.	Steiner-Limbach correlation	66
3.5.5.	Comparison of the calculated and experimental $^1J_{\text{NH}}$	73
3.5.6.	Calculation of the external pKa values	74
3.5.7.	Reaction kinetics of the transfer hydrogenation	75

3.5.8.	Amount of free imine in the ^1H spectra	79
3.5.9.	Formation of the binary complex	82
3.5.10.	Reactivity at 180 K and 220 K of TRIM/imine complex with Hantzsch Ester	83
3.5.11.	Determination of the <i>E</i> -to- <i>Z</i> -isomerization rates	84
3.5.12.	Decay curves	86
3.5.13.	Investigations of the ternary complex with TRIP, imine 5 and Hantzsch ester.....	88
3.5.14.	Investigations on the ternary complex of TRIM, imine 5 and Hantzsch ester	91
3.5.15.	Barrier of the hydride transfer	93
3.5.16.	Solubility of Hantzsch ester in toluene	93
3.5.17.	Computational details	93
3.6.	References.....	93
4	Disulfonimides Versus Phosphoric Acids in Brønsted Acid Catalysis: The Effect of Weak Hydrogen Bonds and Multiple Acceptors on Complex Structures and Reactivity.....	97
4.1.	Abstract.....	99
4.2.	Introduction	99
4.3.	Results and Discussion	102
4.3.1.	Model system.....	102
4.3.2.	Hydrogen bond analysis of the <i>N</i> -aryl-imine-complexes	103
4.3.3.	Structural investigations of the <i>N</i> -aryl-imine-complexes	107
4.3.4.	Reactivity analysis of CPAs, DSIs and BINSAs in transfer hydrogenations	111
4.3.5.	Analysis of the binary <i>N</i> -alkyl-imine-complexes	111
4.4.	Conclusion	114
4.5.	Supporting information	116
4.5.1.	Synthesis of Imine Substrates	116
4.5.2.	Sample preparation of binary complexes in CD_2Cl_2	122
4.5.3.	Spectrometer data	122
4.5.4.	NMR Parameters and Spectra of the binary DSI/imine Complexes.....	123
4.5.5.	Complete set of spectra.....	124
4.5.6.	Steiner-Limbach correlation.....	133
4.5.7.	^{15}N -labeling of the DSI 1e.....	135
4.5.8.	Comparison of the spectra of ^{15}N -labeled and not labeled $(\text{CF}_3)_2$ -DSI 1e/2a (CD_2Cl_2 , 180K).....	140

4.5.9. Calculated $^2hJ_{NN}$, $^1J_{NH}$ and $^1hJ_{NH}$ coupling constants	141
4.5.10. Assignments of the 1H and ^{13}C chemical shifts	142
4.5.11. Predicted structures of the DSI-complexes by calculations	144
4.5.12. Structure identification of all binary complexes	145
4.5.13. In-situ NMR-kinetics of the transfer hydrogenation	155
4.5.14. Reaction kinetics of the transfer hydrogenation	156
4.5.15. HPLC conditions	156
4.5.16. Enantiomeric excess by using different catalysts	159
4.5.17. Reactivity analysis	160
4.6. References	165
5 A Quantitative Analysis of the E,Z-Isomerization of Hydrogen Bonded N-Aryl-Imines	167
5.1. Abstract	169
5.2. Introduction	169
5.3. Results and Discussion	175
5.3.1. Model system	175
5.3.2. Z-to-E-isomerization	176
5.3.3. E-to-Z-Isomerization	180
5.3.4. Thermal Isomerization Barriers of the Imines at low temperature	184
5.3.5. Extrapolation of the Thermal Isomerization Barriers to 298 K	188
5.3.6. Isomerization mechanism	192
5.3.7. Photosensitized isomerization of imine 2a at 455 nm	193
5.4. Conclusion	196
5.5. Supporting information	198
5.5.1. E/Z-ratios after reaching the photostationary state	198
5.5.2. Temperature calibration	198
5.5.3. Additional decay curves	200
5.5.4. Determination of the activation energy E_a	204
5.5.5. Eyring Polanyi plot for Z-to-E-isomerization	207
5.5.6. Cyclic voltammetry of imine 2a	209
5.5.7. Fluorescence emission quenching of RFTA	210
5.5.8. Synthesis of the imines	211
5.5.9. Sample Preparation	215

5.6. References.....	218
6 Conclusion.....	221
7 Abbreviation Register	227

1 Introduction and Outline

1.1. Brønsted acid catalysis

In the past two decades, using small organic molecules as catalysts in organic reactions became more and more important. The advantages of the so called organocatalysts compared to common metal catalysts are that they are resource-friendly and easily available, non-toxic and not sensitive to water and oxygen.^[1] Chiral Brønsted acids, which enable the access to enantiomeric products, are extremely successful in the enormous field of organocatalysts.^[2] In 2004 Akiyama and Terada published some highly enantioselective Mannich type reactions with chiral phosphoric acids as catalysts.^[3,4] They consist of an axially chiral 1,1'-bi-2-naphthol (BINOL) backbone with various substituents in 3,3'-position, which provide due to their spatial demanding structure the chiral environment for enantioselective transformations (Figure 1). The enormous potential of these catalysts is for example demonstrated in more than 100 publications in 2013, which utilized them as catalysts for synthetic applications.^[5] One main reason for the wide applicability of phosphoric acid catalysts is their bi-functionality: On the one hand the phosphoryl oxygen atom acts as Brønsted base and on the other hand the proton of the hydroxyl group acts as Brønsted acid.^[6] Thus, this prominent class of catalysts can be used in versatile reactions, mostly under simple and mild reaction conditions. Beside the Mannich type reaction mentioned above, these powerful catalysts are used in several asymmetric transformations, like Friedel-Crafts reactions, 1,3-dipolar cycloadditions, Diels-Alder reactions, aldol reactions, Nazarov cyclizations, transfer hydrogenations or Strecker reactions.^[5]

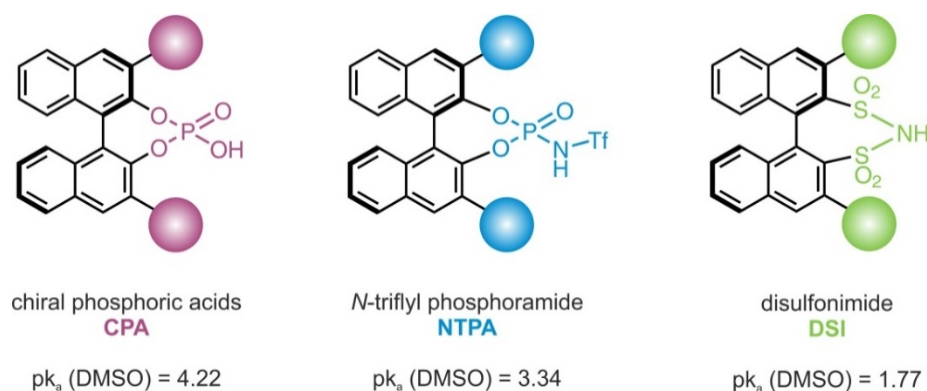


Figure 1: A selection of different BINOL-derived Brønsted acid catalysts. Beside the acidic motif also the 3,3'-substituents (= Ar) can be varied to change the properties of the catalysts. The shown $\text{p}K_a$ values were experimentally measured with potentiometric, spectrometric and conductometric methods (for CPA and NTPA: Ar = 2,4,6-(t -Pr)₃-C₆H₂ and for DSI: Ar = H).^[7]

1 Introduction and Outline

However, the limited acidity of chiral phosphoric acids is insufficient to effectively activate less basic substrates. Hence, different acidic motives of the BINOL-derived catalysts were developed to modify the acidity of this outstanding class of catalysts (Figure 1).^[5] For example the reduction of *N*-alkyl-imines with Hantzsch ester was possible with highly acidic^[7] disulfonimide catalysts (DSI), whereas chiral phosphoric acids typically fail (Figure 2a).^[8] Furthermore, disulfonimide catalyst can be used to activate aldehydes.^[4] Thus, for the disulfonimide catalyzed Mukaiyama aldol reaction of naphthaldehyde with ketene acetal high yields and *ee* were obtained, while with phosphoric acid catalysts almost no product could be detected (Figure 2b).^[9]

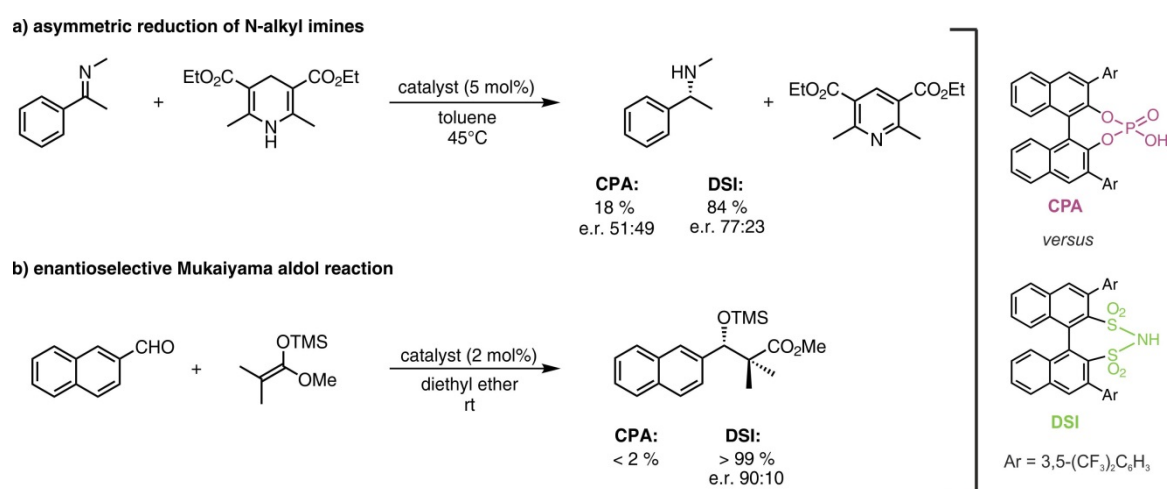


Figure 2: In some Brønsted acid catalyzed reactions the acidity of chiral phosphoric acids (CPAs) is not sufficient. By using more acidic but structural similar disulfonimide catalysts (DSIs) the yields and *ee*-values could be increased. Exemplarily the a) asymmetric reduction of *N*-alkyl imines^[8] and the b) enantioselective Mukaiyama aldol reaction^[9] are shown.

Also the activation of unfunctionalized carbonyls with common phosphoric acid catalysts is still demanding.^[10] By introducing a strong electron-withdrawing *N*-trifluoromethanesulfonyl (*N*-Triflyl = NTf) group the acidity of the phosphoric acid catalyst is increased significantly (Figure 1).^[2,5,7] The obtained *N*-triflyl phosphoramidate (NTPA) could be successfully used as catalyst in an asymmetric Diels-Alder reaction of ethyl vinyl ketones with siloxy dienens (Figure 3a).^[11] By using the *N*-triflyl phosphoramidate catalyst the product was provided in excellent yield and selectivity, whereas the phosphoric acid catalyst gave no product.^[11] Also in an asymmetric protonation reaction of silyl enol ethers of 2-substituted cyclic ketones no product was found with phosphoric acid catalysts, whereas by catalyzing the reaction with the more acidic *N*-triflyl phosphoramidate the product was afforded in almost quantitative yield (Figure 3b).^[12]

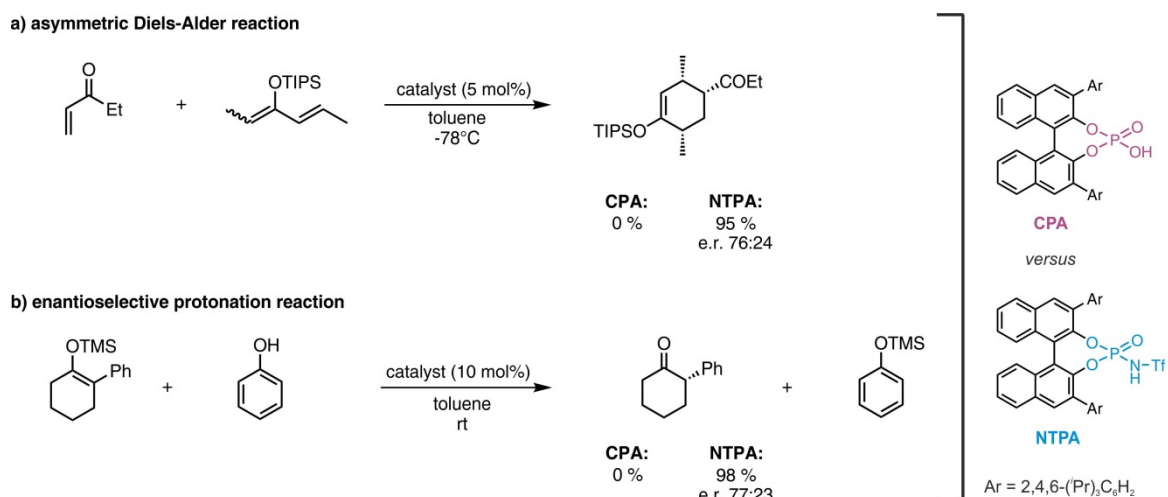


Figure 3: The acidity of chiral phosphoric acids (CPAs) is not sufficient enough for some Brønsted acid catalyzed reactions. By using more acidic but structural similar *N*-triflyl phosphoramides (NTPAs) yields and *ee* could be increased. Amongst others this is the case for a) an asymmetric Diels-Alder reaction^[11] and b) an enantioselective protonation reaction.^[12]

Even if this class of catalysts can be used in several reactions and provide excellent yields and *ee*, the occurring reaction mechanisms are so far scarcely explored and therefore in many cases only proposed. Equally, investigations regarding the occurring intermediates and interactions are very rare. Indeed in recent years, several theoretical models have been developed to describe the interactions between catalyst and substrate and their influence on the reaction outcome.^[13] Nevertheless, due to the relatively large molecular size of these catalysts often simplified catalyst structures had to be assumed for the calculations. However, the experimental access to occurring structures, interactions and mechanisms is extremely difficult due to countless interactions between substrate and catalyst as well as the high flexibility within the catalyst/substrate-complex, which enable the existence of several conformations. Despite these difficulties, the groups of Schneider and MacMillan found two crystal structures for different phosphoric acid/imine complexes.^[14,15] In both cases a hydrogen bond is formed between the *E*-imine and the phosphoric acid catalyst. However, the imine is differently orientated to the catalyst.^[14,15] In solution our group could show that not only two but four different core structures of the phosphoric acid catalyst/imine-complex are present.^[16,17] Thus, for both *E*- and *Z*-imine two different orientations of the imine were found. Partially also dimers of the catalyst/imine-complex could be identified.^[17] Nevertheless, also in solution a strong, ionic hydrogen bond between catalyst and imine exists, which acts as a structural anchor.

1 Introduction and Outline

1.2. Substrate activation *via* hydrogen bonds

In general, a hydrogen bond can be described as a beginning proton transfer reaction: $X-H \cdots Y$ to $X^- \cdots H-Y^+$.^[18] That means that depending on the acidity of the proton donor X and the proton acceptor Y the position of the proton inside the hydrogen bond varies. Therefore, the X-H bond is weakened, while a partial H-Y bond is already formed.^[18,19] In case, that the proton is located directly in the middle between proton donor and acceptor the hydrogen bond is referred as symmetric or strong.^[18]

The formation of a hydrogen bond plays a crucial role in several reaction mechanisms. Thus, in the whole field of organocatalysis several examples are known where the substrate-activation *via* hydrogen bond formation is assumed.^[20,21] For some examples, even a bidentate binding of the catalyst to the substrate reduces the conformational freedom and therefore increases the catalytic efficiency.^[20] This dual hydrogen bond interaction^[22] is also responsible for the success of thiourea derived catalysts (Figure 4a).^[21,23–25] By adding an additional primary, secondary or tertiary amine functionality to a chiral thiourea derivative, it is possible to activate two substrates simultaneously before the reaction takes place. Meanwhile, also for these bifunctional catalysts several examples are known.^[23,24,26] One of them is the enantioselective addition of ketones to nitroolefins. Here the ketone forms an enamine intermediate with the amine group while the nitroolefin is activated through dual hydrogen bonding between the thiourea moiety and the nitro-group of the substrate (Figure 4b).^[27]

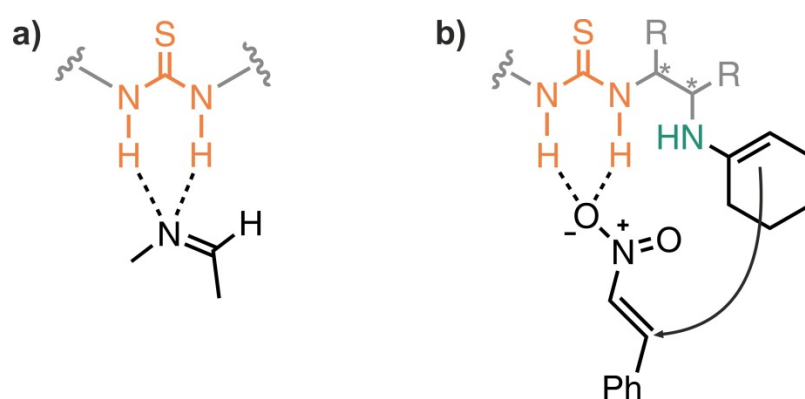


Figure 4: a) Proposed transition state of a thiourea catalyzed Strecker reaction.^[28] Between catalyst and imine two hydrogen bonds are formed.^[28] b) The proposed transition state for a highly enantioselective addition of ketones to nitroolefins is shown. The bifunctional catalyst consists of a thiourea moiety (orange) and an amine functionality (green). Both groups are connected with a chiral linker (grey). In this way ketone and nitroolefin are activated simultaneously.^[27]

Also in photocatalytic reactions hydrogen bonded intermediates are proposed. For example for a ketyl-olefin cyclisation a hydrogen-bonded pre-catalytic species between Brønsted acid catalyst and the ketyl moiety is assumed (Figure 5).^[29] Therefore the single-electron transfer (SET) from the reduced photocatalyst is facilitated. Simultaneously, the proton of the Brønsted acid is transferred along the hydrogen bond to obtain a neutral ketyl radical, which reacts with the electron-poor olefin moiety. Finally, the hydrogen atom transfer (HAT) from the Hantzsch ester affords the product.^[29] Equally, for the conversion of amides, alcohols or ketones a hydrogen bonded intermediate is proposed prior to the proton-coupled electron transfer (PCET).^[30–32]

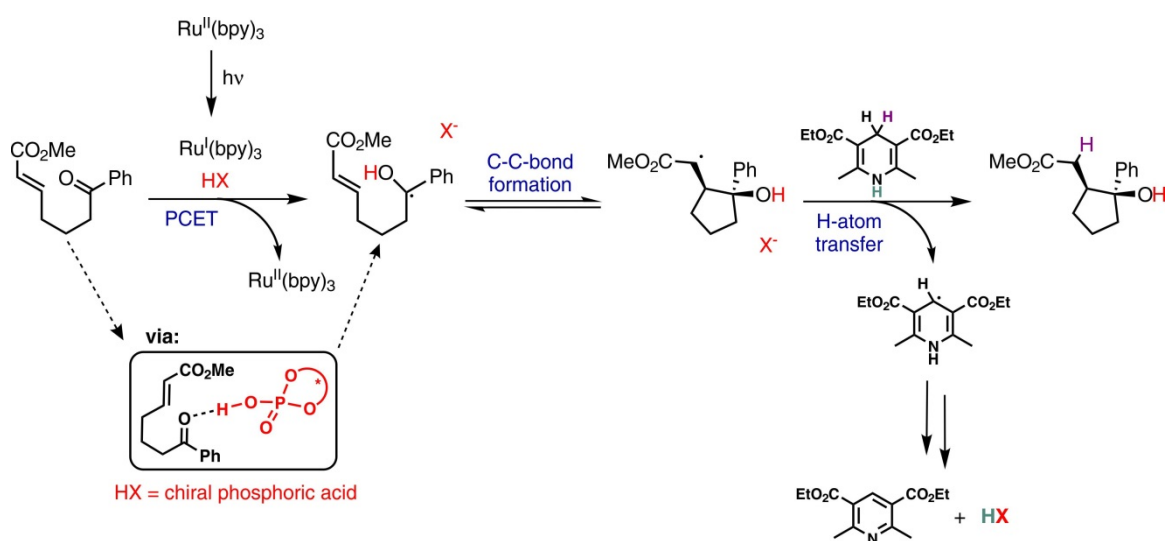


Figure 5: The proposed mechanism for an intramolecular ketyl-olefin coupling is shown. The activation of the substrate takes place *via* a hydrogen bond formation. Subsequently, a proton-coupled electron transfer (PCET), the C-C-bond formation and the hydrogen atom transfer (HAT) takes place.^[29]

Despite the generic assumption of hydrogen bonding, the experimental detection of hydrogen bonds is often very challenging. This is particularly the case for short living intermediates, which are additionally in fast exchange with each other. Hence, in many cases the existence of hydrogen bonds within a reaction mechanism has to be assumed, but could not be proven experimentally.

1 Introduction and Outline

1.3. Hydrogen bond analysis

Beside IR-spectroscopy, one method of choice for investigating hydrogen bonds is NMR-spectroscopy.^[18] However, due to fast chemical exchange of different hydrogen bonded species often the obtained signals are averaged. In order to slow down the fast exchange, the formation of extended hydrogen bond networks, as they appear in proteins, can be useful.^[33] The interplay of many different intramolecular interactions results in a rigid and less dynamic system. Thus, in 1998 the first trans-hydrogen bond ${}^2hJ_{\text{NN}}$ scalar couplings, in the order of magnitude of 7 Hz, could be measured in Watson-Crick base pairs of ${}^{15}\text{N}$ -labeled RNA.^[34] Two years later, it was possible to detect the significant weaker trans-hydrogen bond ${}^3hJ_{\text{PN}}$ und ${}^2hJ_{\text{PH}}$ coupling constants between a protein and a nucleotide^[35] as well as in a flavoprotein.^[36]

Another possibility to prevent the fast exchange of the hydrogen bonded species is the use of low-temperature measurement, in many cases at 180 K or below. The advantage is that in this way also small molecules can be investigated. For example Limbach *et al.* analyzed in several studies the occurring OHN hydrogen bond between different Schiff bases and carboxylic acids (Figure 6).^[37,38] Due to the fact that with increasing hydrogen bond strengths also the shielding of the hydrogen bonded proton is increased, a correlation between the ${}^1\text{H}$ chemical shift and the position of the proton inside the hydrogen bond can be obtained.^[18] In a similar way the ${}^{15}\text{N}$ chemical shift is continuously high field shifted with increasing degree of protonation. Thus, the valence bond orders as well as the atomic distances can be calculated from the ${}^1\text{H}$ and ${}^{15}\text{N}$ chemical shifts.^[38,39] Furthermore, the trans-hydrogen bond scalar coupling constants enable an experimental access to the hydrogen bond angles and can therefore be used as a highly sensitive indicator for small changes in the hydrogen bond geometry.^[37,38,40]

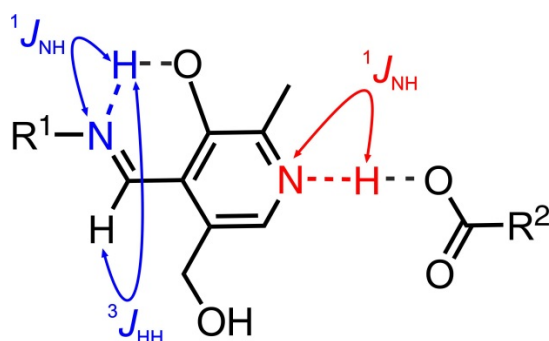


Figure 6: Limbach *et al.* investigated several Schiff bases/carboxylic acid-complexes by means of NMR-spectroscopy. These complexes exhibit an intra- (blue) and an intermolecular (red) hydrogen bond. Beside the ${}^1\text{H}$ and ${}^{15}\text{N}$ chemical shifts also ${}^1J_{\text{NH}}$ and ${}^3J_{\text{HH}}$ coupling constants are experimentally accessible.^[37]

1.4. Outline

In all chapters of this thesis the focus was on the NMR-spectroscopic investigation of the occurring intermediates in Brønsted acid catalysis. Even through the broad applicability of BINOL derived Brønsted acids in asymmetric synthesis, the experimental insight into the involved structures and intermediates is still rare. Furthermore, the substrate binding and activation is often assumed to take place *via* hydrogen bonding. But, due to the fast exchange of various hydrogen bonded species it is most of the time not possible to verify these hydrogen bonds experimentally. Thus, these studies should contribute to get more insights into the activation modes in a Brønsted acid catalysed asymmetric transfer hydrogenation of imines and maybe extended on other reactions.

In chapter 2 the POHN-hydrogen bonds between a phosphoric acid catalyst (TRIP) and several imines were investigated in detail by low-temperature NMR-spectroscopy and quantum chemical calculations. Since, the frequently proposed full protonation of the substrate is an oversimplification and an extreme point of view, the hydrogen bond situation in the intermediates of the transfer hydrogenation was investigated. To this point, the binding situation in a real catalyst/substrate-complex was experimentally not analysed, even though the properties of an external quantified hydrogen bond are not comparable to the situation in an effective intermediate during the reaction. By means of a Steiner-Limbach curve, which correlates the ^1H and ^{15}N chemical shifts empirically, the analysis of the hydrogen bond strengths in the real catalyst/imine-complexes and the associated determination of the atomic distances was conducted. Furthermore, the $^1J_{\text{NH}}$ coupling constant as well as the $^2hJ_{\text{PH}}$ and $^3hJ_{\text{PN}}$ trans-hydrogen bond couplings constants were measured and related to the hydrogen bond geometry. The variation of the steric and electronic properties of the imines does not influence the geometry of the hydrogen bonds. Thus, the strong hydrogen bonds can be seen as a structural anchor between catalyst and substrate.

The 3rd chapter of the thesis expands the hydrogen bond analysis of Brønsted acid catalyst/imine complexes by varying the 3,3'-substituents of BINOL derived phosphoric acid catalysts. For catalysts with different 3,3'-substituents major differences in reactivity and stereoselectivity for the same reaction were observed. However, the most suitable catalyst differs from reaction to reaction and the most effective BINOL-derived catalyst is in many cases identified by trial and error. Up to now, the structural features, which are dependent on the 3,3'-substituents and decisive for the reactivity and stereoselectivity, have been scarcely explored by experiments. In contrast, *in silico* the occurring

1 Introduction and Outline

interactions and structures are much more investigated. In order to drive the experimental access to these key issues forward, the pre-catalytic binary complexes with different phosphoric acids were investigated by NMR-spectroscopy. For this propose an internal acidity scale was implemented as a tool to correlate the acidity of the different phosphoric acid catalysts with their reactivity in the asymmetric reduction of imines.

In chapter 4 the influence of the functional acidic group of the BINOL-derived Brønsted acid catalyst was studied. Because the limited acidity of chiral phosphoric acids complicates the activation of less basic substrates, the by far more acidic disulfonimide catalysts are used in many reactions. It has not yet been clarified whether the increase in reactivity with disulfonimide catalysts is only traced back to the higher acidity or whether also other factors play a crucial role. In general, to our knowledge there are neither theoretical nor experimental studies, which investigate the properties of the disulfonimides. To gain new insights into this class of Brønsted acid catalysts a hydrogen bond as well as structural analysis of the pre-catalytic disulfonimide/imine-complexes was performed. Additionally, it was investigated whether the more acidic catalysts still form charge-assisted hydrogen bonds or whether pure ion pairs without hydrogen bond contribution are present. This issue is of great importance because it was previously assumed that the hydrogen bond acts as a structural anchor and is responsible for a high stereoselectivity. In addition, due to the presence of five hydrogen bond acceptors of disulfonimide catalyst an enormous mobility of the imine in the binary disulfonimide complexes is expected. Thus, structural investigations should contribute to identify the existing pre-catalytic species.

The focus of chapter 5 was a detailed study of the imine-isomerization. Recently, our group developed method to decrypt the transition states of the asymmetric transfer hydrogenation of imines by light (DTS-hv method). However, for the successful use of this technique it is required that the isomerization is the rate-determining step. Up to now, there are only indirect hints for a slow isomerization. Thus, in case of the transfer hydrogenation the slow isomerization was assumed due to the separated signals of both imine-isomers in a ^1H -spectra even at 300 K. Nevertheless, the experimental quantification of the isomerization rates is still missing and thus, no direct comparison between the isomerization rate and other possible rate-determining is possible. Therefore, by means of in-situ NMR photoisomerization a detailed quantification of the imine-isomerization was conducted. Due to the different reactivities of the previously investigated Brønsted acid catalysts with varying acidities, the influence of the degree of

imine-protonation on the isomerization rate was of particular interest. The obtained *E*-to-*Z*- and *Z*-to-*E*-isomerization rates revealed that, an interplay of the sterical imine environment and the degree of protonation is responsible for the isomerization rates.

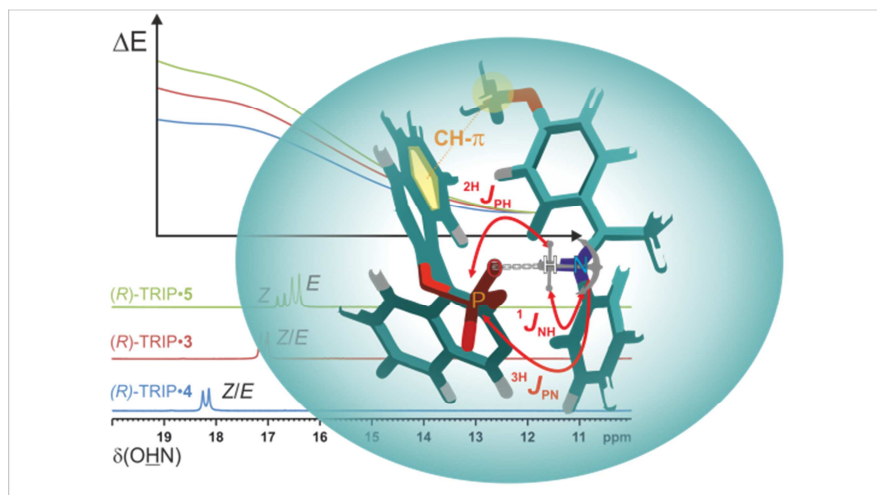
1.5. References

- [1] P. Dalko, L. Moisan, *Angew. Chemie* **2001**, *113*, 3840–3864.
- [2] K. Kaupmees, N. Tolstoluzhsky, S. Raja, M. Rueping, I. Leito, *Angew. Chemie Int. Ed.* **2013**, *52*, 11569–72.
- [3] T. Akiyama, J. Itoh, K. Yokota, K. Fuchibe, *Angew. Chemie Int. Ed.* **2004**, *43*, 1566–1568.
- [4] D. Uraguchi, M. Terada, *J. Am. Chem. Soc.* **2004**, *126*, 5356–5357.
- [5] D. Parmar, E. Sugiono, S. Raja, M. Rueping, *Chem. Rev.* **2014**, *114*, 9047–9153.
- [6] M. Terada, *Synthesis (Stuttg.)* **2010**, 1929–1982.
- [7] P. Christ, A. G. Lindsay, S. S. Vormittag, J.-M. Neudörfl, A. Berkessel, A. C. O'Donoghue, *Chem. - A Eur. J.* **2011**, *17*, 8524–8528.
- [8] V. N. Wakchaure, P. S. J. Kaib, M. Leutzsch, B. List, *Angew. Chemie - Int. Ed.* **2015**, *54*, 11852–11856.
- [9] P. García-García, F. Lay, P. García-García, C. Rabalakos, B. List, *Angew. Chemie Int. Ed.* **2009**, *48*, 4363–4366.
- [10] C. H. Cheon, H. Yamamoto, *Chem. Commun.* **2011**, *47*, 3043–3056.
- [11] D. Nakashima, H. Yamamoto, *J. Am. Chem. Soc.* **2006**, *128*, 9626–9627.
- [12] C. H. Cheon, H. Yamamoto, *J. Am. Chem. Soc.* **2008**, *39*, 9246–9247.
- [13] R. Maji, S. C. Mallojjala, S. E. Wheeler, *Chem. Soc. Rev.* **2018**, *47*, 1142–1158.
- [14] R. I. Storer, D. E. Carrera, Y. Ni, D. W. C. Macmillan, *J. Am. Chem. Soc.* **2006**, *128*, 84–86.
- [15] M. Sickert, F. Abels, M. Lang, J. Sieler, C. Birkemeyer, C. Schneider, *Chem. - A Eur. J.* **2010**, *16*, 2806–2818.
- [16] J. Greindl, J. Hioe, N. Sorgenfrei, F. Morana, R. M. Gschwind, *J. Am. Chem. Soc.* **2016**, *138*, 15965–15971.
- [17] M. Melikian, J. Gramüller, J. Hioe, J. Greindl, R. M. Gschwind, *Chem. Sci.* **2019**, *10*, 5226–5234.
- [18] T. Steiner, *Angew. Chem.* **2002**, *114*, 50–80.
- [19] H. B. Bürgi, J. D. Dunitz, *Acc. Chem. Res.* **1983**, *16*, 153–161.
- [20] P. R. Schreiner, *Chem. Soc. Rev.* **2003**, *32*, 289–296.
- [21] A. G. Doyle, E. N. Jacobsen, *Chem. Rev.* **2007**, *107*, 5713–5743.
- [22] P. Vachal, E. N. Jacobsen, *J. Am. Chem. Soc.* **2002**, *124*, 10012–10014.
- [23] Y. Takemoto, *Org. Biomol. Chem.* **2005**, *3*, 4299–4306.
- [24] S. J. Connon, *Chem. - A Eur. J.* **2006**, *12*, 5418–5427.
- [25] P. R. Schreiner, A. Wittkopp, *Org. Lett.* **2002**, *4*, 217–220.
- [26] O. V. Serdyuk, C. M. Heckel, S. B. Tsogoeva, *Org. Biomol. Chem.* **2013**, *11*, 7051–7071.

1 Introduction and Outline

- [27] S. B. Tsogoeva, S. Wei, *Chem. Commun.* **2006**, 1451–1453.
- [28] P. Vachal, E. N. Jacobsen, *J. Am. Chem. Soc.* **2002**, *124*, 10012–10014.
- [29] K. T. Tarantino, P. Liu, R. R. Knowles, *J. Am. Chem. Soc.* **2013**, *135*, 10022–10025.
- [30] Q. Zhu, D. E. Graff, R. R. Knowles, *J. Am. Chem. Soc.* **2018**, *140*, 741–747.
- [31] H. G. Yayla, H. Wang, K. T. Tarantino, H. S. Orbe, R. R. Knowles, *J. Am. Chem. Soc.* **2016**, *138*, 10794–10797.
- [32] G. Qiu, R. R. Knowles, *J. Am. Chem. Soc.* **2019**, *141*, 2721–2730.
- [33] S. Sharif, E. Fogle, M. D. Toney, G. S. Denisov, I. G. Shenderovich, G. Buntkowsky, P. M. Tolstoy, M. C. Huot, H. H. Limbach, *J. Am. Chem. Soc.* **2007**, *129*, 9558–9559.
- [34] A. J. Dingley, S. Grzesiek, *J. Am. Chem. Soc.* **1998**, *120*, 8293–8297.
- [35] M. Mishima, M. Hatanaka, **2000**, *122*, 5883–5884.
- [36] F. Löhr, S. Mayhew, H. Rüterjans, *J. Am. Chem. Soc.* **2000**, *122*, 9289–9295.
- [37] S. Sharif, D. Schagen, M. D. Toney, H.-H. Limbach, *J. Am. Chem. Soc.* **2007**, *129*, 4440–4455.
- [38] S. Sharif, G. S. Denisov, M. D. Toney, H. H. Limbach, *J. Am. Chem. Soc.* **2007**, *129*, 6313–6327.
- [39] I. G. Shenderovich, A. P. Burtsev, G. S. Denisov, N. S. Golubev, H. H. Limbach, *Magn Reson Chem* **2001**, *39*, 91–99.
- [40] H. Benedict, I. G. Shenderovich, O. L. Malkina, V. G. Malkin, G. S. Denisov, N. S. Golubev, H. Limbach, *J. Am. Chem. Soc.* **2000**, *122*, 1979–1988.
- [41] P. Renzi, J. Hioe, R. M. Gschwind, *J. Am. Chem. Soc.* **2017**, *139*, 6752–6760.

2 NMR Spectroscopic Characterization of Charge Assisted Strong Hydrogen Bonds in Brønsted Acid Catalysis



Nils Sorgenfrei, Johnny Hioe, Julian Greindl, **Kerstin Rothermel**, Fabio Morana, N. Lokesh and Ruth M. Gschwind

J. Am. Chem. Soc., **2016**, *138*, 16345–16354

DOI: 10.1021/jacs.6b09243

The majority of the NMR measurements and of the hydrogen bond analysis were performed by Dr. Nils Sorgenfrei. Dr. Johnny Hioe performed all theoretical calculations and he contributed to the evaluation of the Steiner-Limbach correlation. Dr. Julian Greindl contributed to the measurements of the (*R*)-TRIP-3-5 complexes and HBF₄-imine complexes. **Kerstin Rothermel** conducted the necessary preparations and measurements of the isotope effects and investigated a major part of the phenol/carboxylic acid complexes. Furthermore she contributed to sample preparations. Dr. Fabio Morana contributed in the optimization of the sample preparation and by synthesis of the catalyst (*R*)-TRIP. Dr. N. Lokesh assisted in the measurement of the isotope effects. Substrates were synthesized from all authors (as well as Thomas Hausler and Dr. Polysena Renzi), except Dr. N. Lokesh and Dr. Johnny Hioe.

Source of this chapter: <https://pubs.acs.org/doi/abs/10.1021%2Fjacs.6b09243>

Reproduced with permission. All further permissions related to the material excerpted should be directed to the ACS. Text and figures may differ from the published version. The corresponding Supporting Information is provided free of charge at <http://pubs.acs.org>

2 Characterization of Charge Assisted Strong Hydrogen Bonds

2.1. Abstract

Hydrogen bonding plays a crucial role in Brønsted acid catalysis. However, the hydrogen bond properties responsible for the activation of the substrate are still under debate. Here, we report an in depth study of the properties and geometries of the hydrogen bonds in (*R*)-TRIP imine complexes (TRIP: 3,3'-Bis(2,4,6-triisopropylphenyl)-1,1'-binaphthyl-2,2'-diylhydrogen phosphate). From NMR spectroscopic investigations ^1H and ^{15}N chemical shifts, a „Steiner-Limbach correlation”, a deuterium isotope effect as well as quantitative values of $^1J_{\text{NH}}$, $^{2\text{h}}J_{\text{PH}}$ and $^{3\text{h}}J_{\text{PN}}$ were used to determine atomic distances (r_{OH} , r_{NH} , r_{NO}) and geometry information. Calculations at SCS-MP2/CBS//TPSS-D3/def2-SVP-level of theory provided potential surfaces, atomic distances and angles. In addition, scalar coupling constants were computed at TPSS-D3/IGLO-III. The combined experimental and theoretical data reveal mainly ion pair complexes providing strong hydrogen bonds with an asymmetric single well potential. The geometries of the hydrogen bonds are not affected by varying the steric or electronic properties of the aromatic imines. Hence, the strong hydrogen bond reduces the degree of freedom of the substrate and acts as a structural anchor in the (*R*)-TRIP imine complex.

2.2. Introduction

Hydrogen bonding impacts the energetics and structures of molecules as well as the reactivity and stereoselectivity of their reactions and is therefore of utmost significance in nature.¹ Nowadays, hydrogen bonding is more and more recognized by chemists as potential activation mode for electrophilic substrates such as carbonyl compounds or imines in the field of asymmetric catalysis.^[2-4] A „privileged class” of asymmetric Brønsted acid catalysts constitute BINOL (1,1'-binaphthol) derived phosphoric acids, which were introduced by Akiyama and Terada^[2,5-7] and found applications in a wide pool of reactions with imines as substrates, including Mannich reactions, cycloadditions, aza-ene-type reactions, hydrocyanations and transfer-hydrogenations.^[7,8] Especially, for the asymmetric reductions of imines with Hantzsch 1,4-dihydropyridine ester **1** this class of chiral phosphoric acids provides high stereoselectivities and yields as, e.g. ,published by the groups of Rueping,^[9,10] List^[11] and MacMillan.^[12] The proposed catalytic cycle for this asymmetric reduction is shown in Figure 2.1a.^[3,9,11] The phosphoric acid protonates the imine and forms a chiral hydrogen bond assisted ion pair, which reacts subsequently with the Hantzsch ester **1** to form the chiral amine.

2 Characterization of Charge Assisted Strong Hydrogen Bonds

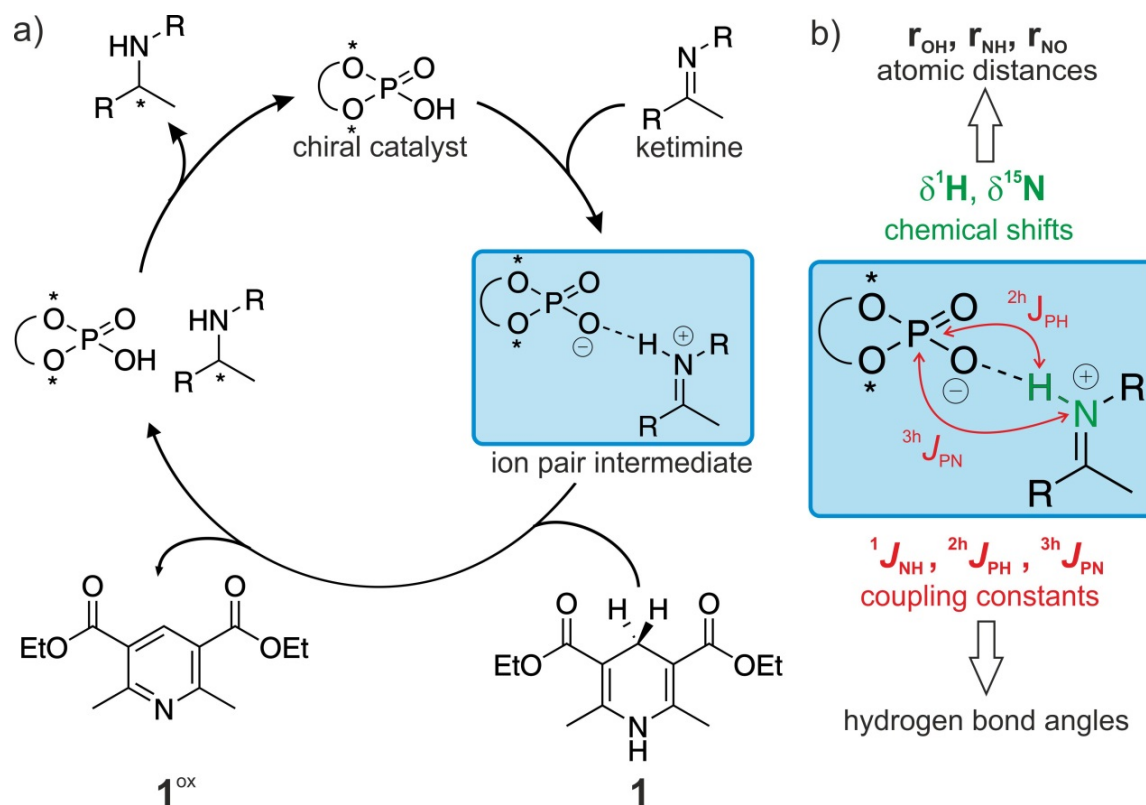


Figure 2.1. a) Catalytic cycle proposed for the Brønsted acid catalyzed enantioselective reduction of imines with Hantzsch-1,4-dihydropyridine ester **1**;^[9,11] b) experimental observables used in this study to characterize the hydrogen bond interaction in (*R*)-TRIP imine complexes.

Several DFT studies of the groups of Himo and Goodman addressed the issue of enantioselectivity in this catalytic reaction.^[13-16] They proposed a fast acid-base equilibrium between imine and catalyst followed by an *E/Z* isomerization of the iminium ion. Next a ternary complex is formed between the ion pair and the Hantzsch ester, which is stabilized by an additional hydrogen bond between the NH of the Hantzsch ester and the phosphoric acid. The absolute stereochemistry of the product and the enantiomeric excess (*ee*) is then determined by the relative energy of the ternary transition states of the *E* and *Z* iminium ion, respectively.^[13-17]

Furthermore, a detailed experimental study was published by Tang *et al.*, regarding the basis of enantioselectivity in the Brønsted acid catalyzed reduction of imines with gaseous H₂ as reduction agent and an achiral iridium complex as cocatalyst.^[8] Again, a ternary complex and the corresponding transition states were proposed to be responsible for the stereodiscrimination.

2 Characterization of Charge Assisted Strong Hydrogen Bonds

However, in the whole field of Brønsted acid catalysis detailed experimental data providing structural insights are extremely rare. Thus, so far not even the hydrogen bond situation in the binary ion pair intermediate has been clarified. The concept of full protonation of basic substrates such as imines by acidic catalyts - often proposed by synthetic chemists and theoreticians - is an oversimplification and an extreme point of view as noted by Toste *et al.*^[4] For example, purely hydrogen bonded complexes were proposed in a computational and NMR spectroscopic study of the activation of N-Boc protected imines by a chiral phosphoric acid.^[18] Furthermore, in a preceding NMR study of our group investigating achiral diphenylphosphoric acid (DPP) imine complexes, both hydrogen bonded complexes and ion pairs were proposed to coexist in solution.^[19] There, a typical temperature dependent ratio was observed, high temperatures favor hydrogen bonding, whereas at low temperatures ion pairs are more stabilized.^[19] Contrary results were obtained studying complexes of DPP with 2-methylquinoline at elevated temperatures.^[20] There, ion-pairing was found to be the dominant interaction motif.^[20] However, to our knowledge detailed experimental studies about the hydrogen bond properties in ketimine complexes with the chiral phosphoric acids have not been reported so far.

Therefore, in this work we present the first detailed, NMR based experimental investigations on the hydrogen bond activation of imines by chiral phosphoric acids. The hydrogen bonds in these binary catalyst substrate complexes were experimentally characterized by ^1H , ^{15}N chemical shifts and trans-hydrogen bond scalar couplings. From the chemical shifts the individual atomic distances (r_{OH} , r_{NH} , r_{NO}) within the hydrogen bonds were derived and the $^{2\text{h}}J_{\text{PH}}$ and $^{3\text{h}}J_{\text{PN}}$ scalar couplings give information about the angles (Figure 2.1b). These detailed experimental data are compared with high level theoretical calculations about the atomic distances, scalar couplings of the hydrogen bonds and structures of the binary complexes. This reveals not only unprecedented insights into the hydrogen bond activation of Brønsted acid catalysis but also the limitations of both experimental and theoretical models.

2.3. Results and Discussion

2.3.1. Model Systems

(*R*)-TRIP was chosen as catalyst, because structural information based on NOE data was available for some (*R*)-TRIP imine complexes (see below).^[21] In addition, imines with different steric and electronic properties were selected (Figure 2.2) to rationalize the

2 Characterization of Charge Assisted Strong Hydrogen Bonds

influence of the substrate on the hydrogen bonding properties of the ion pairs. Furthermore, tetrafluoroboric acid, was selected to mimic purely ionic complexes. Acetic acid (AcOH), trimethyl acetic acid (TMA), as well as phenols (4-chlorophenol, 4-nitrophenol, 3,5-dichlorophenol, 3-(trifluoromethyl)phenol) were chosen to form strictly neutral hydrogen bonded complexes. The preparation of ^{15}N -labeled imines and representative methods for sample preparation are described in the Supporting Information. All acid imine and phenol imine complexes were investigated in CD_2Cl_2 and/or freonic mixtures by NMR spectroscopy, because in these solvents the best NMR properties were detected in terms of chemical shift dispersion and line widths (for spectra in toluene see Supporting Information). Extremely low temperatures between 180 and 130 K were used to reach the slow hydrogen bond exchange regime. These low temperatures in combination with the selection of phosphoric acids and up to 98% ^{15}N enriched imines allowed for the detection of $^2\text{h}J_{\text{PH}}$ and $^3\text{h}J_{\text{PN}}$ as sensors for hydrogen bond angles and atomic distances.^[22]

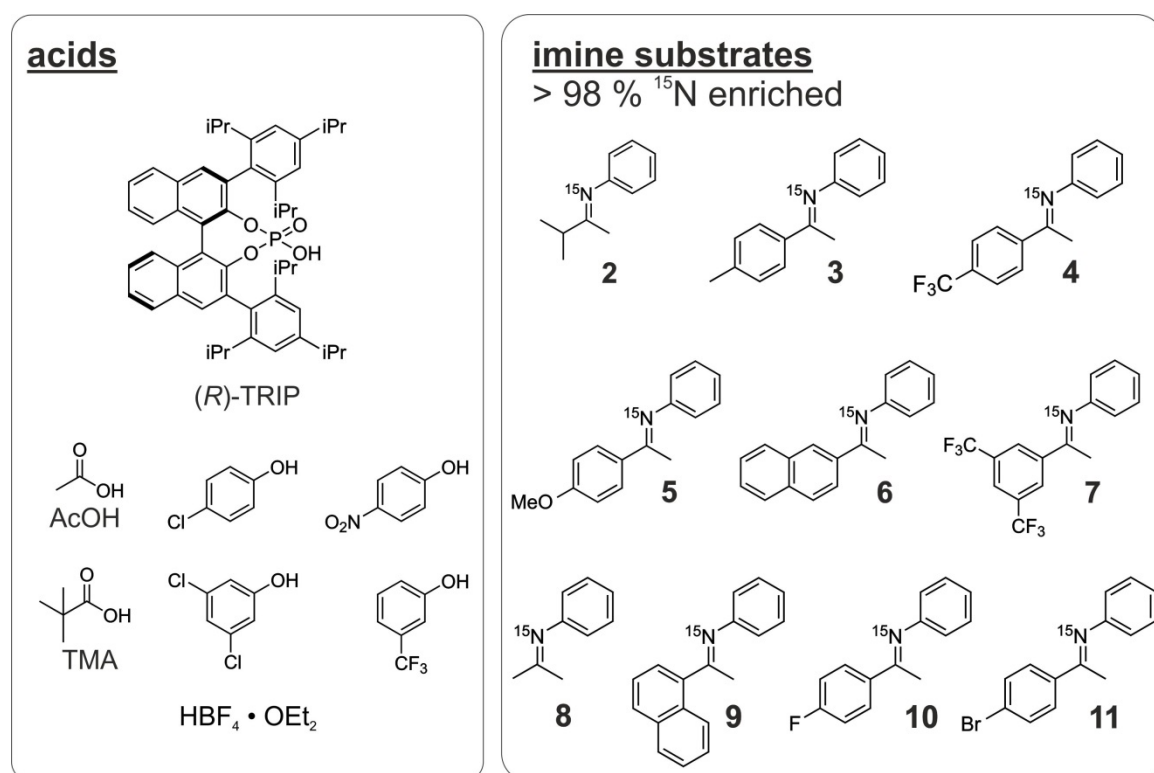


Figure 2.2. Model systems for hydrogen bond studies; Brønsted acid catalyst *(R)*-TRIP and other acidic compounds were used as donors; all imines **2–11**, tested as acceptors were 98% ^{15}N enriched to enable the detection of $\Delta\delta^{15}\text{N}$ and $^3\text{h}J_{\text{PN}}$.

2 Characterization of Charge Assisted Strong Hydrogen Bonds

2.3.2. Computational Details

The binary complexes consisting of (*R*)-TRIP and imines **3-5** and **8** were chosen as models in the theoretical calculations. The structures are optimized at RI-DFT level of theory using meta-GGA functional TPSS-D3 with def2-SVP basis set in the gas phase and in the continuum of dichloromethane (SMD model).^[23-25] A dielectric constant of 16.2 was used to simulate the low temperature measurement at 180 K. Bond parameters (distances and angles) were averaged over large conformational space (due to isopropyl rotation) according Boltzmann distributions at 180 K. The final free energies of the conformations were evaluated at SCS-RI-MP2/CBS level of theory (for extrapolation procedure see Supporting Information).^[26] Solvation energies were added subsequently to the Gibbs free energy using SMD solvation model at 180 K in dichloromethane. The ¹H and ¹⁵N chemical shifts, respectively the scalar coupling constants (¹J_{NH}, ^{2h}J_{PH} and ^{3h}J_{PN}), were computed at TPSS with IGLO-III basis set using the complete model, respectively the reduced model.^[27] The 2,4,6-triisopropylphenyl groups were replaced with hydrogens, and subsequently subjected to frozen optimization. For the geometry optimization, free energy of solvation and scalar coupling constant calculation Gaussian09 version D.01 was used. For single point calculation ORCA3.0.3 was used.^[28,29]

2.3.3. Detection and Characterization of Hydrogen Bonds by NMR

For most of the chiral phosphoric acid imine complexes ((*R*)-TRIP-**2–11**), two main ion pair species were detected representing hydrogen bridged ion pairs with *E* and *Z* configured imines. Therefore, in the following this general pattern and its assignment is described exemplarily on the hydrogen bonded complex of (*R*)-TRIP and **5** in CD₂Cl₂ at 180 K (Figure 2.3). For (*R*)-TRIP-**5E** and (*R*)-TRIP-**5Z** the proton in the hydrogen bond is detected at 16.47 and 16.75 ppm, respectively (Figure 2.3a). Such chemical shifts larger than 16 ppm are usually observed for hydrogen atoms in „strong” or „low-barrier hydrogen bonds”.^[1,30,31] Both signals are doublets with ¹J_{NH} coupling constants of 79.7 and 81.2 Hz showing the covalent connectivity to ¹⁵N and the existence of an ion pair structure (for further support see ¹H, ¹⁵N-HMQC spectra in the Supporting Information).^[19] The *E* and *Z* configurations of the imines were assigned based on ³J_{NH} couplings constants between ¹⁵N of imine and methyl protons and as well as by NOESY measurements (for details see Supporting Information). The ionic character of both isomers is further corroborated by the significant high-field shift of the ¹⁵N resonances to 206.7 and 209.2 ppm for *E* and *Z*, respectively (Figure 2.3b and d), compared to the free base **5** at 321.0 ppm (Figure 2.3e); Δδ¹⁵N > 110 ppm), which is a clear indicator for the

2 Characterization of Charge Assisted Strong Hydrogen Bonds

proton transfer to the lone pair of the nitrogen.^[32] Also the ^{13}C low field shifts of the imino groups ($\Delta\delta \sim 13.7$ and $\Delta\delta \sim 16.0$ ppm for *E* and *Z*, respectively; see Figure 2.3d and e) corroborate this analysis.^[33,34]

For (*R*)-TRIP imine complexes the large $^1J_{\text{NH}}$ coupling constants, the significant high field shift of the ^{15}N resonances upon complex formation and the refined spectroscopic and theoretical analysis of the data (see below) indicate a strong preference for the ionic hydrogen bond^[1,35] (Figure 2.3d) except for imine **7**, in which the two CF_3 -groups significantly reduce the basicity. The hydrogen bonded complex can be involved in association/dissociation equilibria with the isolated molecules or the separated ion pairs.^[36-38] In case of imines with low basicity (e.g., **4** or **7**) or in the presence of an excess of imine a separated ^{15}N signal of the free non protonated imine is observed at 180 K, which is in slow exchange with the imine in the complex.

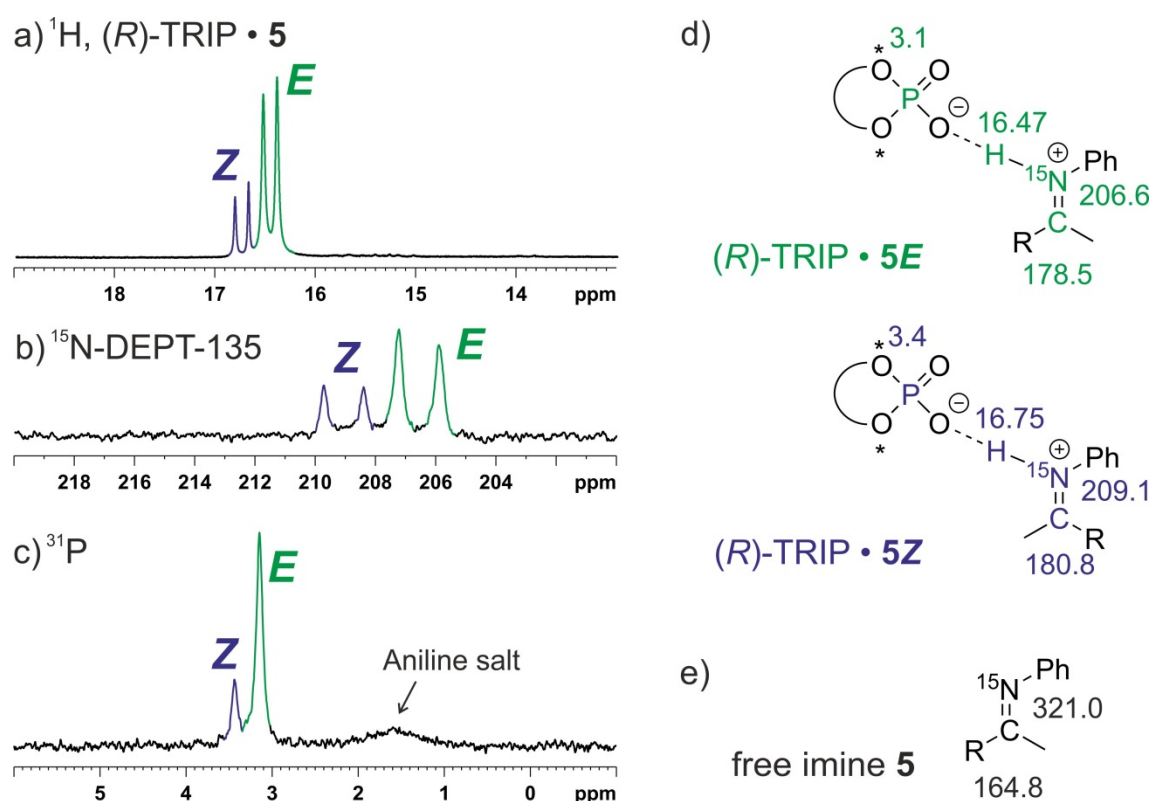


Figure 2.3. a-c) Sections of the ^1H , ^{15}N -DEPT-135 and ^{31}P spectra of a 1:1 complex of (*R*)-TRIP and **5** (CD_2Cl_2 , 180 K, 600 MHz), clearly showing the coexistence of both *E* and *Z* complexes; d) chemical shifts of (*R*)-TRIP • **5E/Z**; e) chemical shifts of unbound **5**.

2 Characterization of Charge Assisted Strong Hydrogen Bonds

Considering our experimental conditions (e.g., low temperatures and the noncoordinative CD_2Cl_2 as solvent) and the estimated strength of the formed hydrogen bonds (>70 kJ/mol),^[1] the formation of solvent separated ion pairs in (*R*)-TRIP complexes is negligible.^[39] This is substantiated by detection of large ${}^2\text{h}J_{\text{PH}}$ and ${}^3\text{h}J_{\text{PN}}$ coupling constants (see below).^[40] Thus, the ${}^1\text{H}$ and ${}^{15}\text{N}$ chemical shifts observed for the binary substrate complexes of (*R*)-TRIP with the imines at 180 K are the „intrinsic” chemical shifts of the individual hydrogen bonded species and can be used for the analysis of the hydrogen bond situation of these complexes.^[35,41]

2.3.4. Hydrogen Bond Analysis Based on $\delta^1\text{H}$, $\delta^{15}\text{N}$ and ${}^1J_{\text{NH}}$

In ${}^1\text{H}$ -NMR spectra, chemical shifts above 16 ppm are usually observed for hydrogen atoms in „strong” or „low-barrier hydrogen bonds”.^[1,30,31] According to literature the formation of strong hydrogen bonds is associated with a „proton-transfer reaction”^[1,38] between hydrogen bond donor and hydrogen bond acceptor. The progress of the proton transfer is dependent on the acidity of the hydrogen bond donor and the basicity of the acceptor, and as well as the polarity of the solvent.^[1,36,38,39,42] Therefore, empirical correlations of ${}^1\text{H}$ „ $\{\delta(\text{O}\underline{\text{H}}\text{N})\}$ ” and ${}^{15}\text{N}$ „ $\{\delta(\text{O}\underline{\text{H}}\underline{\text{N}})\}$ ” chemical shifts, as well as ${}^1J_{\text{NH}}$ „ $\{{}^1J(\text{O}\underline{\text{H}}\underline{\text{N}})\}$ ” coupling constants with the atomic distances can be used to determine the position of the proton inside the hydrogen bond, as previously developed by Limbach and Denisov in their studies of OHN hydrogen bonds in pyridine acid complexes (Equation 1-5).^[35,41,43,44] Using an extended set of complexes with varying acidic and basic properties of their hydrogen bond donors and acceptors, the proton position within the hydrogen bond can be varied stepwise. There, the parabolic dependence of $\delta(\text{O}\underline{\text{H}}\text{N})$ on $\delta(\text{O}\underline{\text{H}}\underline{\text{N}})$ was used to determine the valence bond orders $\rho_{\text{OH}}^{\text{H}}$ and $\rho_{\text{NH}}^{\text{H}}$ by employing the empirical correlations presented in Equation 1-2.

$$\delta(\text{O}\underline{\text{H}}\text{N}) = \delta(\text{O}\underline{\text{H}})^0 \rho_{\text{OH}}^{\text{H}} + \delta(\underline{\text{H}}\text{N})^0 \rho_{\text{HN}}^{\text{H}} + 4\delta(\text{O}\underline{\text{H}}\underline{\text{N}})^0 \rho_{\text{OH}}^{\text{H}} \rho_{\text{HN}}^{\text{H}} \quad (1)$$

$$\delta(\text{O}\underline{\text{H}}\underline{\text{N}})^{\text{ref}} = \delta(\underline{\text{N}})^0 \rho_{\text{OH}}^{\text{H}} + \delta(\underline{\text{H}}\text{N})^0 \rho_{\text{HN}}^{\text{H}} + 4\delta(\text{O}\underline{\text{H}}\underline{\text{N}})^0 \rho_{\text{OH}}^{\text{H}} \rho_{\text{HN}}^{\text{H}} \quad (2)$$

Furthermore, they proposed a correlation between ${}^1J(\text{O}\underline{\text{H}}\underline{\text{N}})$ and the valence bond orders as well.^[35,41,43,44]

$${}^1J(\text{O}\underline{\text{H}}\underline{\text{N}}) = {}^1J(\underline{\text{H}}\text{N})^0 \rho_{\text{HN}}^{\text{H}} - 8{}^1J(\text{O}\underline{\text{H}}\underline{\text{N}})(\rho_{\text{OH}}^{\text{H}})^2 \rho_{\text{HN}}^{\text{H}} \quad (3)$$

2 Characterization of Charge Assisted Strong Hydrogen Bonds

The determined ρ_{OH}^H and ρ_{NH}^H for a hydrogen bond are then consulted to derive the corresponding atomic distances (r_{OH} , r_{NH} , r_{NO}) according to Equations 4-5.

$$p_{NH} = \exp \left\{ \frac{-(r_{NH} - r_{NH}^0)}{b_{NH}} \right\} \quad (4)$$

$$p_{OH} = \exp \left\{ \frac{-(r_{OH} - r_{OH}^0)}{b_{OH}} \right\} \quad (5)$$

For a detailed explanation of the empirical equations and constants applied in this study for the acid imine complexes see Supporting Information. To enable a reliable parametrization of the constants $\{\delta(\underline{OHN})^\circ; \delta(\underline{HN})^\circ; \delta(\underline{HN})^\circ; \delta(\underline{N})^\circ; {}^1J(\underline{HN})^\circ; \delta(\underline{OHN})^*; \delta(\underline{OHN})^*, {}^1J(\underline{OHN})^*\}$ used in Equations 1-3, it was necessary to cover a wide range of the valence bond orders ρ_{OH}^H and ρ_{NH}^H . Hence, the database was extended from (*R*)-TRIP imine complexes with „strong” hydrogen bonds to ionic and neutral acid imine complexes with „moderate” hydrogen bond strength.^[1,35,41] As mentioned earlier, for the strictly ionic acid imine complexes, tetrafluoroboric acid was selected, which was already used in our previous study.^[19]

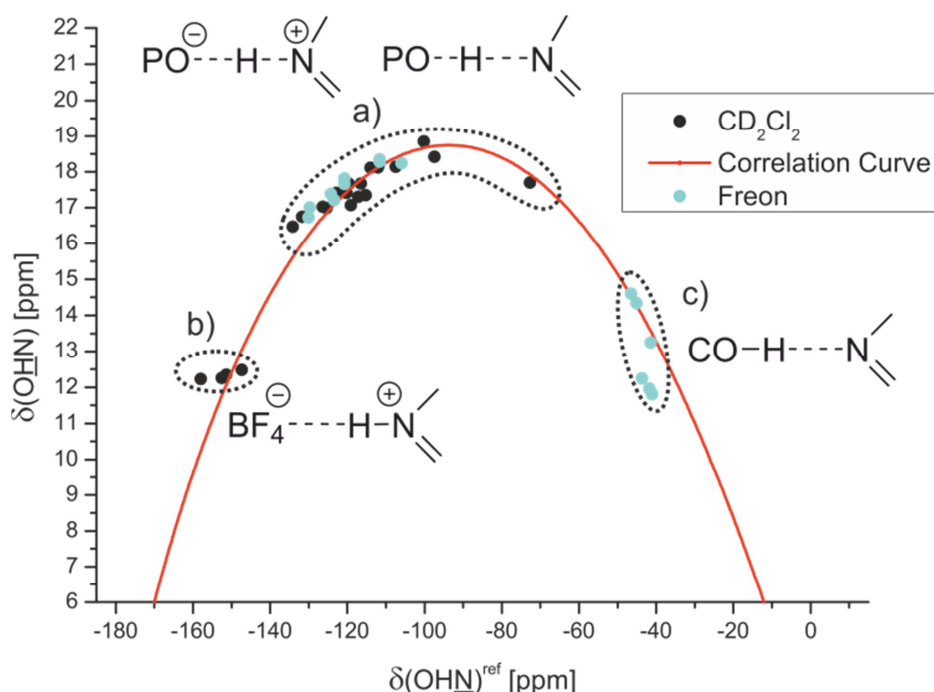


Figure 2.4. Plot of $\delta(\underline{OHN})^{\text{ref}}$ against the $\delta(\underline{OHN})$ of the hydrogen bonded complexes; a) (*R*)-TRIP with **2–11**; b) HBF_4 with **3** and **5**; c) carboxylic acids and phenols with **3** and **5**; the ^{15}N chemical shifts of all complexes are referenced to **7** $\{\delta(\underline{OHN})^{\text{ref}} = \delta(\underline{OHN}) - 340.8 \text{ ppm}\}$; spectra

2 Characterization of Charge Assisted Strong Hydrogen Bonds

corresponding to the different hydrogen bond types are shown in Figure 2.5; for details see Supporting Information.

Acetic acid (AcOH) and trimethylacetic acid (TMA) as well as several substituted phenols were selected for the strictly neutral acid imine complexes. The plot of $\delta(\text{OHN})^{\text{ref}}$ against $\delta(\text{OHN})$ of all acid imine complexes is shown in Figure 2.4. Representative ^1H and ^{15}N spectra related to the different hydrogen bond types are shown in Figure 2.5.

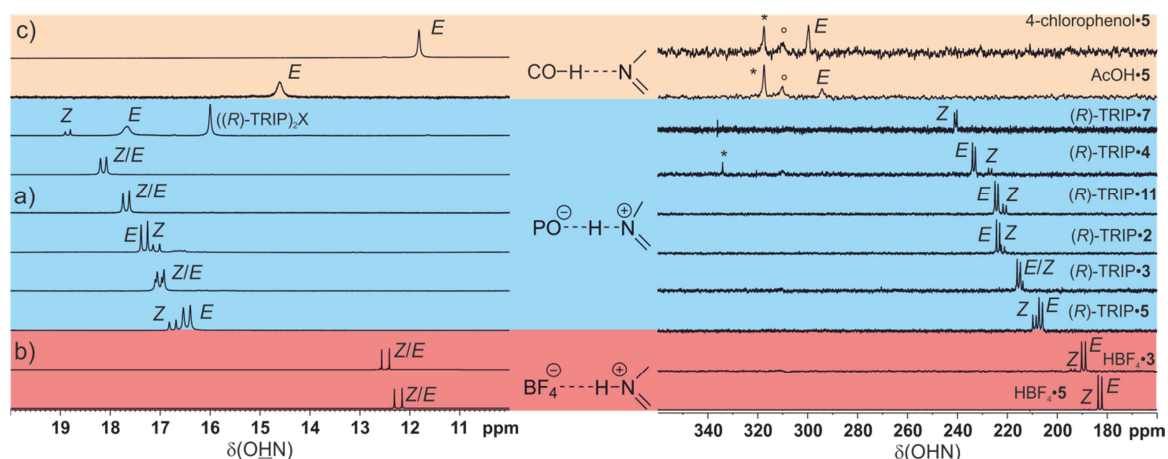


Figure 2.5. Dependence of $\delta(\text{OHN})$ and $\delta(\text{OHN})^{\text{ref}}$ on the hydrogen bond strength in the *E* and *Z* acid imine complexes shown by selected of ^1H (low field sections) and ^{15}N spectra in CD_2Cl_2 and freonic mixtures between 180 to 130 K; the shown spectra correspond to the hydrogen bond types in Figure 2.4; a) (*R*)-TRIP imine complexes; b) $\text{HBF}_4\cdot\mathbf{3}$ and $\text{HBF}_4\cdot\mathbf{5}$; c) $\text{AcOH}\cdot\mathbf{5}$ and 4-chlorophenol $\cdot\mathbf{5}$; for the ^{15}N spectra of (*R*)-TRIP $\cdot\mathbf{7}$, (*R*)-TRIP $\cdot\mathbf{5}$ and $\text{HBF}_4\cdot\mathbf{5}$ polarization transfer experiments were used (INEPT and DEPT); (*) signals of free imine; (deg) impurity or artifact; in case of (*R*)-TRIP $\cdot\mathbf{7}$ signals of $((R)\text{-TRIP})_2\text{X}$ complexes are observed^[35,55]; a list of $\delta(\text{OHN})$ and $\delta(\text{OHN})^{\text{ref}}$ of the individual complexes is provided in the Supporting Information Table S9-12.

In strictly ionic complexes with „moderate” hydrogen bonds ($\text{HBF}_4\cdot\mathbf{3}$, $\text{HBF}_4\cdot\mathbf{5}$) $\delta(\text{OHN})$ values between 12 and 13 ppm and high values of $^1J_{\text{NH}}$ about 92.6 Hz are observed, indicating a complete proton transfer reaction and therefore short r_{NH} (Figure 2.4b, Figure 2.5b).^[1] With decreasing acidity of the hydrogen bond donor (*R*)-TRIP and decreasing basicity of the acceptor ($\mathbf{5} > \mathbf{3} > \mathbf{2} > \mathbf{11} > \mathbf{4} > \mathbf{7}$) the proton is shifted toward the center of the hydrogen bond, which is interpreted as an increase of strength of the hydrogen bond (Figure 2.4a; Figure 2.5a).^[1,35,41] In the case of (*R*)-TRIP $\cdot\mathbf{7E}$, the proton is even shifted beyond the maximum indicating a decrease of the hydrogen bond strength and a considerable population of the neutral hydrogen bonded complex. In the predominant ionic complexes high proton chemical shifts are observed from 16.47 ((*R*)-TRIP $\cdot\mathbf{5E}$) to 18.85 ppm ((*R*)-TRIP $\cdot\mathbf{7Z}$) in combination with reduced absolute $^1J_{\text{NH}}$

2 Characterization of Charge Assisted Strong Hydrogen Bonds

coupling constants from 82.2 Hz ((*R*)-TRIP·**5E**) to 60.6 Hz ((*R*)-TRIP·**7Z**). In contrast, for the neutral hydrogen bonded complex (*R*)-TRIP·**7E** a reduced $^1J_{\text{NH}}$ coupling constant (42 Hz at 170 K) was observed, which is in full agreement with the trend in the Steiner-Limbach correlation curve. Continuing to the less acidic donors AcOH and 4-chlorophenol the proton is now shifted further on, toward the oxygen atom (Figure 2.4c, Figure 2.5c). This leads again to a weakening of the hydrogen bonds, visible by the high field shift of the proton signal at 11.81 ppm for 4-chlorophenol·**5**. Now with the proton close to the oxygen, the splitting due to the $^1J_{\text{NH}}$ coupling vanishes. In contrast, the ^{15}N resonance of the hydrogen bonded complexes is shifted continuously from 182.2 ppm for HBF_4 ·**5E** over 230.2 ppm for (*R*)-TRIP·**4Z** to 299.7 ppm for 4-chlorophenol·**5** (Figure 2.5a-c).

A satisfying curve fit of the data points was achieved, employing Equation 1 and Equation 2 (Figure 2.4, red curve; for details and fitting parameters see Supporting Information). The observed parabolic dependence of $\delta(\text{OHN})$ on $\delta(\text{OHN})$ is in good agreement with the previous investigations on pyridine-acid complexes by Limbach and co-workers.^[35,41] For (*R*)-TRIP imine complexes the continuous progression of the data points on the correlation curve is indicative for a strong hydrogen bond and excludes a tautomeric equilibrium between two proton positions in a classical double well potential (data points on two intersecting straight lines).^[35] Regarding the $^1J_{\text{NH}}$ coupling constants of the investigated Brønsted acid imine complexes, a good characterization by the valence bond model is achieved as well, shown by the plots of $^1J(\text{OHN})$ against $\delta(\text{OHN})$ and $\delta(\text{OHN})$ (see Supporting Information). The magnitude of the measured coupling constants (60.6 – 82.2 Hz) reflects again the above-described predominant ionic character of the (*R*)-TRIP imine complexes and the significantly reduced value of (*R*)-TRIP·**7E** (42 – 46 Hz) corroborates the shift toward neutral hydrogen bonds.

On the basis of the $\delta(\text{OHN})$ of the Brønsted acid imine complexes (see Table S9-12 in the Supporting Information) and the fitted correlation curve (Figure 2.4), the bond orders $\rho_{\text{OH}}^{\text{H}}$ and $\rho_{\text{NH}}^{\text{H}}$ of the individual (*R*)-TRIP imine complexes were obtained (see Supporting Information Table S13). Next equations 4-5 are used to determine the atomic distances r_{OH} , r_{NH} and r_{NO} . These experimentally derived values for r_{NH} and r_{OH} , are depicted in Figure 2.8 and discussed below together with the results from the theoretical calculations. For all values including r_{NO} see Table S13 in the Supporting Information. All hydrogen bond distances are in the range of strong OHN hydrogen bonds¹ and vary

2 Characterization of Charge Assisted Strong Hydrogen Bonds

between 111 and 136 pm for r_{NH} , 114–146 pm for r_{OH} , and 249–257 pm for r_{NO} . In addition, the obtained average proton donor distances - in the case of (*R*)-TRIP complexes r_{OH} - below 160 pm indicate the partial covalent character of the formed hydrogen bonds.^[45,46]

2.3.5. Comparison of NMR Data and Theoretical Calculations.

2.3.5.1. Ion Pair Structures

Next the results of this study were correlated with our recent NMR spectroscopic and computational study regarding the general structures of (*R*)-TRIP complexes with the aromatic imines (**3-5**) to gain further insight into the hydrogen bond interaction.^[21] In general two binding modes of *E/Z*-imines and catalyst (*R*)-TRIP are theoretically possible, which are stabilized by dispersive interactions.

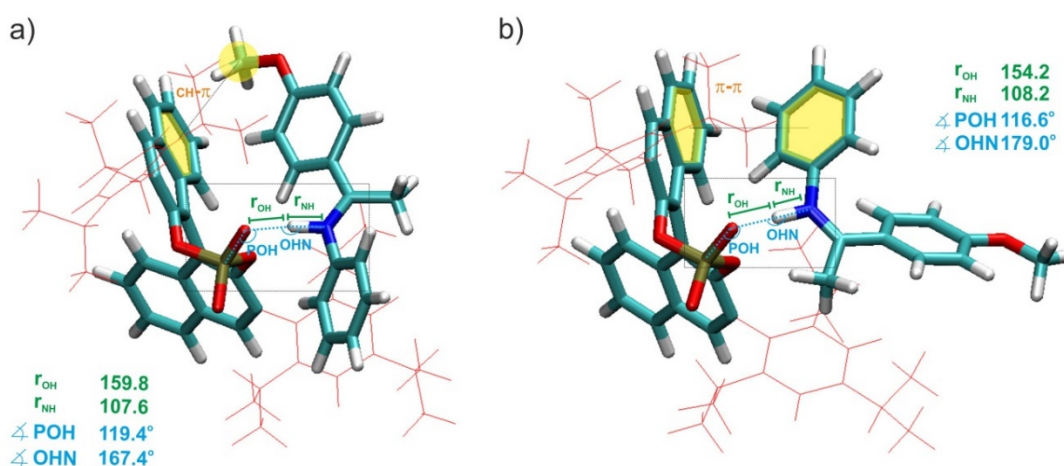


Figure 2.6. Global minima of (*R*)-TRIP·**5** in CD_2Cl_2 at 180 K ($\epsilon = 16.20$), optimized at DFT level of theory (for computational details see Supporting Information); a) (*R*)-TRIP·**5E**; b) (*R*)-TRIP·**5Z**.

For *E*-imines (**3-5**) theoretical calculations showed that the orientation, in which the *para*-substituted ketone moiety reclines on the chiral BINOL aromatic surface is majorly populated for all aromatic imines investigated (Figure 2.6a). However, initial experimental and theoretical structural studies with short aliphatic imines (**2** and **8**) and doubly substituted imines^[21] indicate the second orientation with a 180° rotated imine (structure not shown) to be also populated. In case of *Z*-imine complexes ((*R*)-TRIP·**3-5**) also, NOESY spectra predict that the two binding modes in the complex to be populated. The most stable one is depicted in Figure 2.6b.^[21] Furthermore, ^1H spectra, which showed only one averaged signal set for the protons at the BINOL moiety, suggested

2 Characterization of Charge Assisted Strong Hydrogen Bonds

that the *Z* isomers of the (*R*)-TRIP imine complexes are extremely dynamic even at very low temperatures. The theoretical calculations predicted that both orientations differ only by 4.5–6 kJ/mol. It is very likely that the compact structure of *Z*-imines allows the rotation and translation of the imines in the binary complex.^[21] Fortunately, the actual interpretation of the hydrogen bonds is not affected by this structural diversity, because the geometries of the hydrogen bonds are extremely similar in both conformations. For further discussion of hydrogen bond geometry (atomic distances and angles) and the interpretation of scalar coupling constants ($^1J_{\text{NH}}$, $^{2h}J_{\text{PH}}$, $^{3h}J_{\text{PN}}$), only Boltzmann averaged values over two orientations and the isopropyl rotation were considered.

2.3.5.2. Potential Surface of the Hydrogen Bond Complexes

The theoretical calculations showed that the alteration of hydrogen bond situation strongly depends on the dielectric medium, in which the complex is simulated (Figure 2.7a-c). In the gas phase, ion pair- and neutral hydrogen bond-complexes are true minima (Figure 2.7a). Without any solvent correction, the latter is thermally more stable (ca. 8 – 13 kJ/mol) and therefore almost exclusively populated. However, the solvent correction at 180 K ($\epsilon = 16.20$) to the gas phase structure (nonrelaxed) leads to a significant stabilization of the charge separated contact ion pair minima and inverts the population (Figure 2.7b).

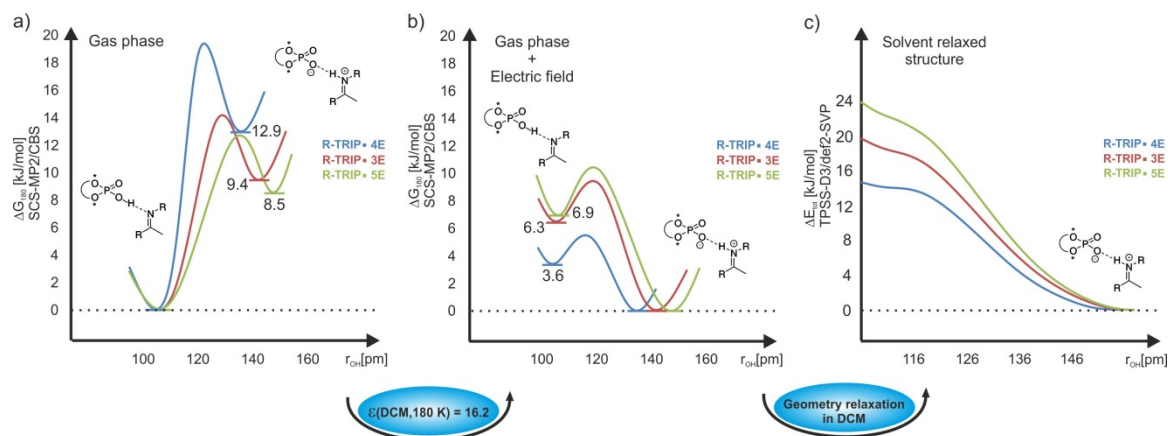


Figure 2.7. a) Schematic gas phase potential energy profiles of (*R*)-TRIP/imine complexes; b) schematic solvent corrected (in DCM: 180 K, nonrelaxed) potential energy profiles of (*R*)-TRIP/imine complexes; c) relaxed scan over r_{OH} of the complexes in DCM continuum at 180 K ($\epsilon = 16.20$).

After the relaxation in the continuum, the minimum of the neutral hydrogen bonded complex even disappeared and the potential surface becomes an asymmetric single well

2 Characterization of Charge Assisted Strong Hydrogen Bonds

potential (Figure 2.7c).^[47] Furthermore, weaker hydrogen bonds are calculated indicated by longer r_{OH} and r_{NO} as well as shorter r_{NH} values (for r_{OH} and r_{NH} see Figure 2.8). However, the calculated atomic distances of the solvent relaxed structures are still in the range of strong OHN hydrogen bonds ($r_{\text{NO}} \leq 265$ pm, for details see Supporting Information).^[31]

From the experimental data available, it is difficult to assess whether the second minimum of the neutral hydrogen bond really disappears in solution at 180 K. The most indicative parameter for a single well or double well potential is the deuterium isotope effect.^{31,48} For (*R*)-TRIP-**3,5E** a small positive isotope effect was measured ((*R*)-TRIP-**3E** $\Delta\delta(^1\text{H}-^2\text{H}, 180 \text{ K}, \text{CH}_2\text{Cl}_2) = 0.15$ ppm, (*R*)-TRIP-**5E** $\Delta\delta(^1\text{H}-^2\text{H}, 180 \text{ K}, \text{CH}_2\text{Cl}_2) = 0.27$ ppm, for spectra see Supporting Information), while a slightly larger isotopic effect was obtained for (*R*)-TRIP-**4E** ($\Delta\delta(^1\text{H}-^2\text{H}, 180 \text{ K}, \text{CH}_2\text{Cl}_2) \sim 0.36$ ppm). The slightly larger value for (*R*)-TRIP-**4E** could be caused by a flattened shape of the potential surface along the proton transfer coordinates and a vibrational motion of the proton near to the flattened surface,^[30] and is in agreement with its potential energy profile (see Figure 2.7c). The effects of the flattened surface and the dynamic motion of the proton near to the surface are further supported by the considerable deviation between experimental and theoretical values of $^1J_{\text{NH}}$ in (*R*)-TRIP-**4E** (see discussion below). Furthermore, complexes with less basic imines and considerable contributions of neutral hydrogen bonds such as (*R*)-TRIP-**7E** let expect the existence of double well potentials. Nevertheless, all accessible experimental isotope effects so far are in agreement with an asymmetric single well potential as shown in Figure 2.7c.^[48]

2 Characterization of Charge Assisted Strong Hydrogen Bonds

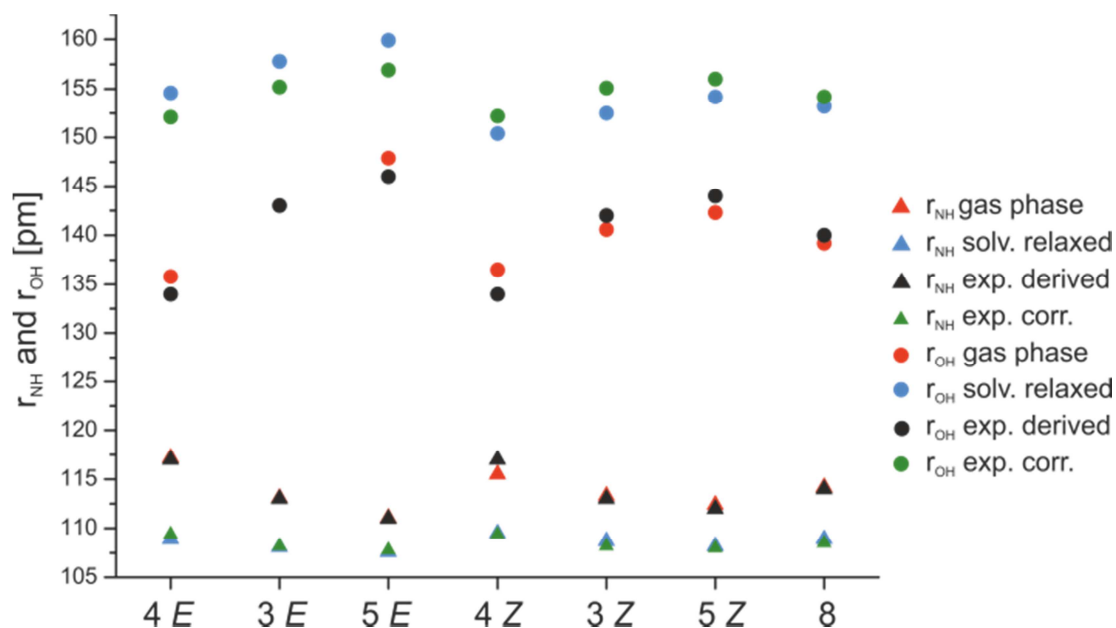


Figure 2.8. Comparison of the experimentally derived and calculated r_{NH} and r_{OH} distances of (*R*)-TRIP-3-5 and (*R*)-TRIP-8.

2.3.5.3. Validation of Theoretical Models Based on Atomic Distances, $^1J_{\text{NH}}$, and Chemical shifts

To further validate the applicability of the different theoretical models for the interpretation of the experimental data, next the theoretically calculated atomic distances were compared with those derived from the „Steiner-Limbach correlation” (Figure 2.8) for the normal case, the predominantly ionic complexes. The calculated distances of the contact ion pairs in the gas phase are very close to the values derived from the „Steiner-Limbach correlation”, which was at first glance very surprising. However, it is known that in the previous work of Limbach and co-workers^[35,41] the parameters and constants (r_{OH}° , r_{NH}° , b_{OH} , b_{NH}) were fitted with a solid state data set^[49] and compared to gas phase data.

To circumvent potential systematic offsets connected with indirectly derived NMR parameters, next $^1J_{\text{NH}}$ coupling constants as directly measurable values were selected. Experimental $^1J_{\text{NH}}$ values between 68.6 Hz – 82.2 Hz indicate the predominant occupation of the ion pair minimum. Therefore, in the following discussion of the theoretical values the limiting case of exclusive population of ion pairs was assumed, i.e., exclusively the values of the contact ion pair minima are considered even in the gas phase. Our results show that using the gas phase structures even for the exclusive interpretation of the ion pairs, the calculated $^1J_{\text{NH}}$ values are significant smaller than the directly measured coupling constants (red bars in Figure 2.9, for details see Supporting

2 Characterization of Charge Assisted Strong Hydrogen Bonds

Information). By the application of solvent relaxed structures a significant improvement was achieved in the prediction of the $^1J_{\text{NH}}$ coupling constants for *E* and *Z* complexes of (*R*)-TRIP-**3**, **5**, **8** (blue bars in Figure 2.9).

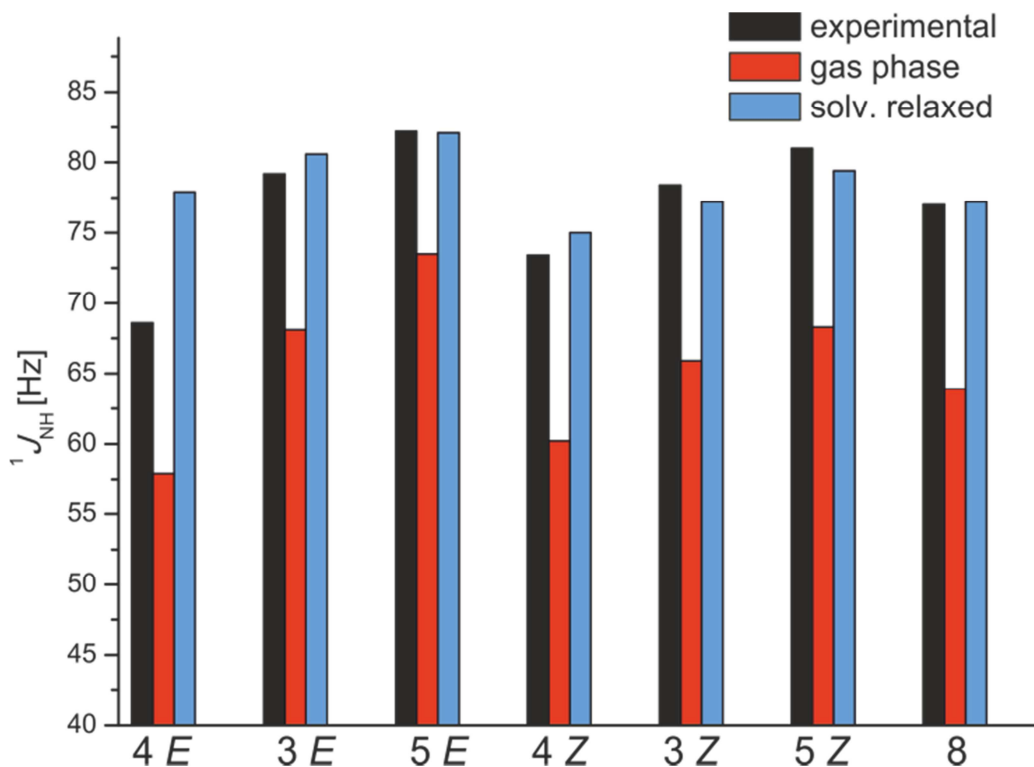


Figure 2.9. Comparison of experimental (black bars) and calculated (blue and red bars) $^1J_{\text{NH}}$ values of (*R*)-TRIP-**3**, **4**, **5**, **8** show an excellent agreement between experimental values and calculated values using solvent relaxed structures, with the exception of (*R*)-TRIP-**4 E**; only ion pair structures are considered in the calculations; values of the *E/Z* isomers were Boltzmann averaged over the two experimentally observed conformations, see text.

In these cases the absolute deviation between experiment and calculation is mostly marginal and amounts to ~ 2 Hz (Figure 2.9). Therefore, the relaxed structures in the solvent model are considered to represent the experimental condition/observation more realistically and are used for the further discussion. The only significant deviation (8.8 Hz for *E*) is obtained for (*R*)-TRIP-**4E**, which provides the strongest/shortest hydrogen bond due to the electron withdrawing CF_3 -substituent in the imine **4** (Figure 2.9). A partial decoupling of the $^1J_{\text{NH}}$ due to chemical exchange with the unbound imine would be a potential explanation for the reduced $^1J_{\text{NH}}$ values. However, an experiment with 2-fold excess of **4** revealed, that neither the chemical shift nor the observed $^1J_{\text{NH}}$ are affected significantly (see Supporting Information). This excludes a significant influence of chemical exchange on the $^1J_{\text{NH}}$ under our experimental conditions. (*R*)-TRIP-**4** is the

2 Characterization of Charge Assisted Strong Hydrogen Bonds

complex with the highest probability of a population of the neutral hydrogen bonded complex (see discussion about the potential above and Figure 2.7c). Now this reduced $^1J_{\text{NH}}$ scalar coupling constant can be an indication for the existence of a second minimum for the neutral hydrogen bonded complexes in solution. The next probable explanation is that the low basicity of **4** leads to a significant delocalization of the proton within the asymmetric single well potential. These dynamic motions of the proton can only be reproduced by dynamic calculation, which would be extremely costly for a system of this size. Both scenarios are in principle possible; however our current interpretation of isotopic effect favors the asymmetric potential picture as depicted in Figure 2.7c. In summary the application of the „Steiner-Limbach correlation” based on the chemical shifts and $^1J_{\text{NH}}$ coupling constants confirm the formation of strong hydrogen bonds in the (*R*)-TRIP imine complexes and the predominance of the contact ion pair structure. For (*R*)-TRIP complexes with highly basic imines theoretical and experimental data indicate an asymmetric single well potential. The comparison of the atomic distances reveals that the classical „Steiner-Limbach correlation” reproduces the distances of the gas phase structures. However, the comparison of the “direct” observables $^1J_{\text{NH}}$ with the different theoretical models demonstrates that the solvent relaxed structures resemble the experimental data the most, which was also corroborated by the analysis of the $^1\text{H}, ^{15}\text{N}$ chemical shifts and NBO^[50] (for details see Supporting Information). Despite of this substantial improvement, the large deviation between the calculated and experimental values for (*R*)-TRIP-**4E** demonstrated somewhat the limit of the applied theoretical treatment, which failed to describe either the correct shape of the potential surface or the dynamic motion of the proton in extreme cases.

The described offset in combination with our theoretical data about the solvent relaxed structures can now be used to introduce a solvent correction term (see Equation 6) in the empirical correlation between chemical shifts and atomic distances for phosphoric acid imine complexes.^[51]

$$r_{XH} = r_{XH}^{\text{Steiner-Limbach}} + f_{\text{solv}}(\Delta p) \quad (6)$$

The solvent correction term depends implicitly on the experimental condition (e.g., solvent, temperature) and explicitly on the bond order difference ($\Delta p = \rho_{\text{OH}^{\text{H}}} - \rho_{\text{OH}^{\text{H}}}$) from the Steiner-Limbach model. This difference in bond order indicates the strengths of the

2 Characterization of Charge Assisted Strong Hydrogen Bonds

hydrogen bond, the position in the Steiner-Limbach curve and the sign of the correction term to be applied. By considering the parabolic form of the Steiner-Limbach curve, the correction term should be larger with stronger hydrogen bond character and approaches a maximum with the strongest hydrogen bond. Therefore, Gauss-functions were applied for the correction term (see Equation 7 and for fitting procedures Supporting Information).

$$f_{solv}(\Delta p) = A * \text{sign}(p_{OH} - p_{NH}) \exp(-B * (p_{OH} - p_{NH})^2) + C \quad (7)$$

The constants A , B and C were obtained via fitting to the available theoretical data (for data see Supporting Information). Accordingly, the corrected empirical values are now very close to the predicted values in the solution phase (see Figure 8.2). A first cross validation of this solvent correction term derived from the TRIP complexes on a binary complex using another catalyst ((*R*)-3,3'-Bis(3,5-bis(trifluoromethyl)phenyl)-1,1'-binaphthyl-2,2'-diyl hydrogen phosphate)^[9] and **3E** provided only marginal offsets (deviation without correction: 2.1 pm for NH bond distance, respectively 6.1 pm for OH bond distance; with correction: 0.7 pm for NH bond distance, respectively 2.1 pm for OH bond distance) between the empirical value and the solvent relaxed structure. This suggests a general applicability to phosphoric acid imine complexes, however the full potential will be subject to further studies.

2.3.5.4. Analysis of Hydrogen Bond Geometry Based on $^{2h}J_{PH}$ and $^{3h}J_{PN}$

Trans-hydrogen bond scalar couplings can serve as valuable sensors for changes in hydrogen bond geometry.^[22] Therefore, next calculated and measured $^{2h}J_{PH}$ and $^{3h}J_{PN}$ scalar couplings^[52] (Figure 2.1b) were interpreted to get insight into the geometrical properties of the hydrogen bonds in (*R*)-TRIP imine complexes. In all calculated (*R*)-TRIP imine structures nearly linear hydrogen bonds were found (see Figure 2.6 for (*R*)-TRIP-**5**), which is expected for strong hydrogen bonds.^[1] The calculated angles (POH, OHN) and dihedral angles (α) vary only insignificantly between gas phase and solvent relaxed structures. Furthermore, there are only minor deviations between the imines **3-5** and **8**, regarding the POH and OHN hydrogen bond angles (for data, see Supporting Information). The $^{2h}J_{PH}$ couplings between the NH protons and ^{31}P were measured qualitatively by 1D/2D ^1H , ^{31}P -HMBC spectra and 3D HNPO spectra and quantitatively by spin echo difference experiments as reported previously^[53] (for spectra and pulse sequences, see Supporting Information). The sign of the $^{2h}J_{PH}$ and $^{3h}J_{PN}$ scalar couplings was not determined and therefore only absolute values are stated. Figure 2.10 shows a

2 Characterization of Charge Assisted Strong Hydrogen Bonds

plot of the ^1H chemical shift of the hydrogen bonded proton $\delta(\text{OHN})$ against the experimental $^{2\text{h}}J_{\text{PH}}$ coupling constants.

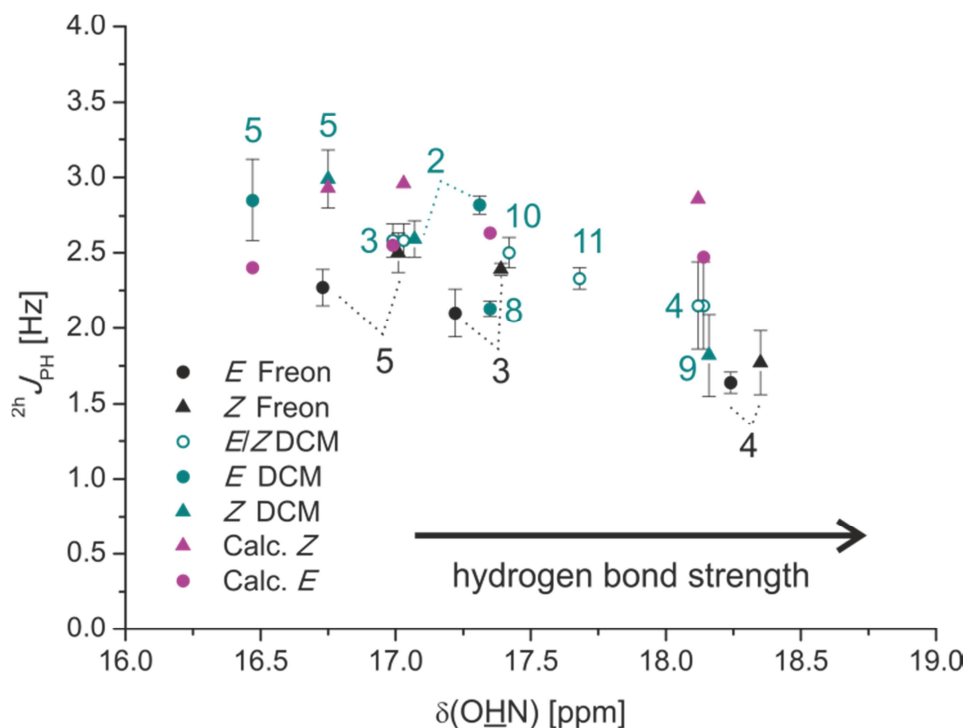


Figure 2.10. Plot of $^{2\text{h}}J_{\text{PH}}$ values versus $\delta(\text{OHN})$; experimental values black and cyan (180 K, except (*R*)-TRIP-**8** 200 K and (*R*)-TRIP-**4** 170 K); calculated, Boltzmann averaged values of (*R*)-TRIP-**3**, **4**, **5**, **8**: magenta.

With increasing $\delta(\text{OHN})$ a continuous decrease of the $^{2\text{h}}J_{\text{PH}}$ is observed (from 2.99 ± 0.19 Hz for (*R*)-TRIP-**5Z**, CD_2Cl_2 , 180 K to 1.64 ± 0.07 Hz for (*R*)-TRIP-**4E**, 170 K, Freon). In general, slightly smaller values were measured for the complexes in Freon mixtures, which is in agreement with the higher ^1H chemical shifts indicating a stronger hydrogen bond. From protein nucleotide complexes^[54] and their model systems^[22] the $^{2\text{h}}J_{\text{PH}}$ angle coupling constant is known to depend on r_{NO} and the POH angle. Considering the small variance of the POH-angles in our system ((*R*)-TRIP-**3-5**, **8E** 117° - 118° and (*R*)-TRIP-**3-5**, **8Z** 115° - 117°), the observed decrease of the $^{2\text{h}}J_{\text{PH}}$ should be connected with the increasing hydrogen bond strength and therefore decreasing r_{OH} (see above) and r_{NO} (see Supporting Information). In the study of Brüsweiler *et al.* increasing $^{2\text{h}}J_{\text{PH}}$ values are predicted for decreasing r_{NO} . In our (*R*)-TRIP imine systems the opposite trend is observed. Therefore, the $^{2\text{h}}J_{\text{PH}}$ coupling constants of (*R*)-TRIP-**3-5**, **8** in CD_2Cl_2 were calculated for the ion pair minima. First of all, the calculated $^{2\text{h}}J_{\text{PH}}$ values successfully reproduce the order of the magnitude of the experimental data (Figure 2.10). However,

2 Characterization of Charge Assisted Strong Hydrogen Bonds

the trend in the experimental data, i.e., decreasing ${}^2\text{h}J_{\text{PH}}$ with increasing hydrogen bond strength could not be found. Considering the discussion about the ${}^1J_{\text{NH}}$ scalar coupling constants of (*R*)-TRIP-4, any effect of a population of the neutral hydrogen bond or vibrational effects should also affect the corresponding ${}^2\text{h}J_{\text{PH}}$ data. The calculations reveal a negative sign for ${}^2\text{h}J_{\text{PH}}$ coupling constants similar to previous studies of protein nucleotide complexes^{22,54} and a positive sign for ${}^2\text{h}J_{\text{PH}}$ for the neutral hydrogen bonded complex. Thus, both a small population of the neutral hydrogen bonded complex as well as vibrations of the proton toward oxygen should result in reduced scalar coupling values as detected for (*R*)-TRIP-4. Next the ${}^3\text{h}J_{\text{PN}}$ coupling constants were investigated to get insight into the geometric properties regarding the dihedral angles POHN. The experimental ${}^3\text{h}J_{\text{PN}}$ coupling constants are in the range of $\sim 3.25 - 2.50$ Hz (see Figure 2.11).

The absolute magnitude of the ${}^2\text{h}J_{\text{PH}}$ and ${}^3\text{h}J_{\text{PN}}$ coupling constants is significantly larger than that reported by Mishima *et al.* for weak hydrogen bonds providing similar POH angles of around 107° to 120° .^[53] This can be rationalized by the different electron density distribution due to the strong and partially covalent hydrogen bond character in (*R*)-TRIP imine systems.^[1,45,46] Also for ${}^3\text{h}J_{\text{PN}}$ the calculations were able to reproduce the order of the magnitude and revealed a negative sign for ${}^3\text{h}J_{\text{PN}}$. However, both experimental and calculated ${}^3\text{h}J_{\text{PN}}$ values lack a clear dependence on the ${}^1\text{H}$ chemical shifts (Figure 2.11). Similar independence of the hydrogen bond strength was observed previously for ${}^2\text{h}J_{\text{FN}}$ in HF collidine complexes.^[36] From the calculated structures dihedral angles POHN around $90^\circ \pm 15^\circ$ are predicted (see Supporting Information). Exactly for this range of dihedral angles the smallest absolute values and smallest variations of ${}^3\text{h}J_{\text{PN}}$ are expected. Additionally, the OHN-angles are very linear (165° - 175° for (*R*)-TRIP *E*-imine and 170° - 180° for (*R*)-TRIP *Z*-imine; see Supporting Information for the complete data). Thus, the slight decrease of the ${}^2\text{h}J_{\text{PH}}$ and the stability of ${}^3\text{h}J_{\text{PN}}$ confirm the marginal variance of the hydrogen bond geometry found in the calculations.

2 Characterization of Charge Assisted Strong Hydrogen Bonds

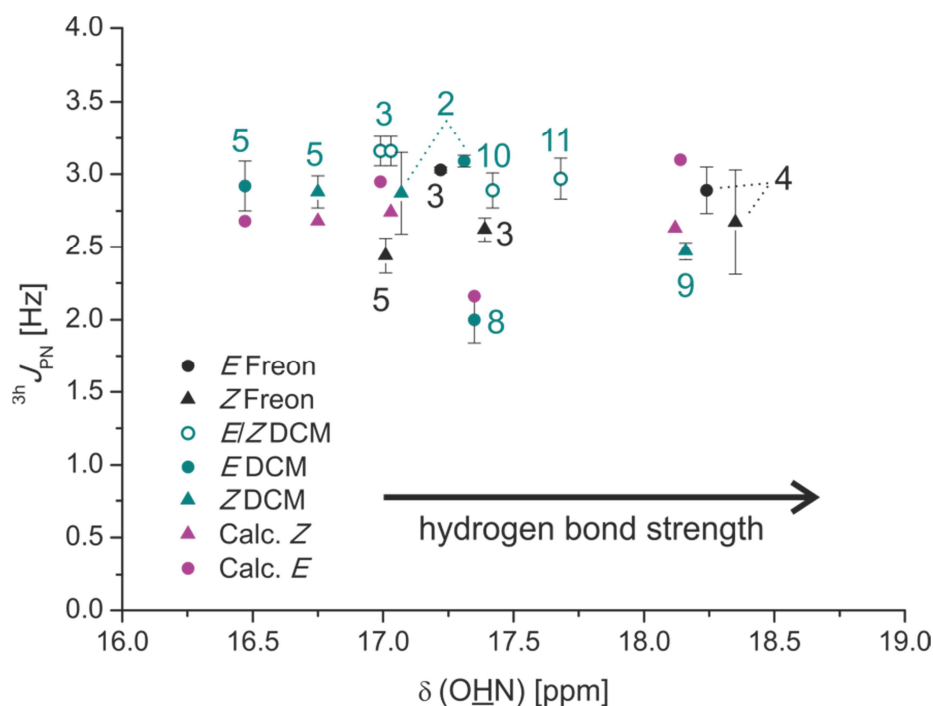


Figure 2.11. Plot of $^3h J_{\text{PN}}$ values versus $\delta(\text{OHN})$; experimental values black and cyan (180 K, except (*R*)-TRIP-8 200 K and (*R*)-TRIP-4 170 K); calculated, Boltzmann averaged values of (*R*)-TRIP-3, 4, 5, 8: magenta.

2.4. Conclusions

Thorough NMR and computational investigations of the activation of imine substrates via hydrogen bonding by (*R*)-TRIP, a catalyst with broad applicability in Brønsted acid catalysis, were conducted for the first time. A strong hydrogen bond constitutes the dominant interaction between (*R*)-TRIP and imine. The analysis of its ^1H , ^{15}N chemical shifts as well as its $^1J_{\text{NH}}$ values reveals mostly a predominantly ionic character of the hydrogen bonded complexes. For (*R*)-TRIP-7E, including the imine with the lowest basicity, also contributions of neutral hydrogen bonds were found. Individual atomic distances of the hydrogen bonds were elucidated by applying a „Steiner-Limbach correlation” based on ^1H , ^{15}N chemical shifts, which are in good agreement with the gas phase structures from the DFT based calculations, therefore a solvent correction term was introduced. Indeed, a comparison with $^1J_{\text{NH}}$ values as direct experimental data demonstrates the solvent relaxed structures to describe the system more realistic. The continuous shift of the proton by variation of the imine basicity is indicative for a strong hydrogen bond character. Theoretical calculations of the potential surface reveal a major population of the neutral hydrogen bond complex in the gas phase and an inverted population in solution phase. Moreover, in (*R*)-TRIP-4E/Z, the complex with the strongest

2 Characterization of Charge Assisted Strong Hydrogen Bonds

hydrogen bond calculated, the comparison between theoretical and experimental coupling constants suggests a potential participation of neutral hydrogen bond complexes or a strongly delocalized hydrogen atom due to vibrational motion, which cannot be described by our theoretical treatment. For the weaker but more neutral (*R*)-TRIP·**7E** complex even a double well potential is expected. The magnitude of deuterium isotope effect corroborates an asymmetric single well potential for (*R*)-TRIP·**3-5E** complexes. Furthermore, the trans-hydrogen scalar couplings ${}^{3h}J_{PN}$ and ${}^{2h}J_{PH}$ were detected via ${}^1\text{H}$, ${}^{31}\text{P}$ -HMBC and 3D-HNPO experiments and quantified via spin echo experiments. These experimental values in combination with structure and coupling constant calculations give a detailed insight into the spatial arrangement of the hydrogen bond atoms. Nearly linear hydrogen bonds are formed with minimal variations within one structural type independent of the imine investigated. That means, the variation of the steric and electronic properties of aromatic imines does not affect the structure as well as the hydrogen bond geometry. Thus, in the (*R*)-TRIP imine complexes investigated, the hydrogen bond acts as structural anchor in the precatalytic complex.

Preliminary results showed that the product formation is faster with stronger hydrogen bonds in the precatalytic (*R*)-TRIP imine complex. Further investigations about the formation, stability and the hydrogen bond interaction of ternary complexes are currently conducted.

2.5. References

- [1] Steiner, T. *Angew. Chem. Int. Ed.* **2002**, *41*, 48.
- [2] Taylor, M. S.; Jacobsen, E. N. *Angew. Chem. Int. Ed.* **2006**, *45*, 1520.
- [3] Mahlau, M.; List, B. *Angew. Chem. Int. Ed.* **2013**, *52*, 518.
- [4] Phipps, R. J.; Hamilton, G. L.; Toste, F. D. *Nat. Chem.* **2012**, *4*, 603.
- [5] Uraguchi, D.; Terada, M. *J. Am. Chem. Soc.* **2004**, *126*, 5356.
- [6] Akiyama, T.; Itoh, J.; Yokota, K.; Fuchibe, K. *Angew. Chem. Int. Ed.* **2004**, *43*, 1566.
- [7] Zamfir, A.; Schenker, S.; Freund, M.; Tsogoeva, S. B. *Org. Biomol. Chem.* **2010**, *8*, 5262.
- [8] Tang, W.; Johnston, S.; Iggo, J. a.; Berry, N. G.; Phelan, M.; Lian, L.; Bacsa, J.; Xiao, J. *Angew. Chem. Int. Ed.* **2013**, *52*, 1668.
- [9] Rueping, M.; Sugiono, E.; Azap, C.; Theissmann, T.; Bolte, M. *Org. Lett.* **2005**, *7*, 3781.
- [10] Rueping, M.; Azap, C.; Sugiono, E.; Theissmann, T. *Synlett* **2005**, 2367.
- [11] Hoffmann, S.; Seayad, A. M.; List, B. *Angew. Chem.* **2005**, *117*, 7590.
- [12] Storer, R. I.; Carrera, D. E.; Ni, Y.; MacMillan, D. W. C. *J. Am. Chem. Soc.* **2006**, *128*, 84.
- [13] Simón, L.; Goodman, J. M. *J. Am. Chem. Soc.* **2008**, *130*, 8741.

2 Characterization of Charge Assisted Strong Hydrogen Bonds

- [14] Marcelli, T.; Hammar, P.; Himo, F. *Chem. - Eur. J.* **2008**, *14*, 8562.
- [15] Marcelli, T.; Hammar, P.; Himo, F. *Adv. Synth. Catal.* **2009**, *351*, 525.
- [16] Simón, L.; Goodman, J. M. *J. Org. Chem.* **2011**, *76*, 1775.
- [17] Reid, J. P.; Simón, L.; Goodman, J. M. *Acc. Chem. Res.* **2016**, *49*, 1029.
- [18] Gridnev, I. D.; Kouchi, M.; Sorimachi, K.; Terada, M. *Tetrahedron Lett.* **2007**, *48*, 497.
- [19] Fleischmann, M.; Drettwan, D.; Sugiono, E.; Rueping, M.; Gschwind, R. M. *Angew. Chem. Int. Ed.* **2011**, *50*, 6364.
- [20] Kim, H.; Sugiono, E.; Nagata, Y.; Wagner, M.; Bonn, M.; Rueping, M.; Hunger, J. *ACS Catal.* **2015**, *5*, 6630.
- [21] Greindl, J.; Hioe, J.; Sorgenfrei, N.; Morana, F.; Gschwind, R. M. *J. Am. Chem. Soc.*, **2016**, *138*, 15965.
- [22] Czernek, J.; Brüscheiler, R. *J. Am. Chem. Soc.* **2001**, *123*, 11079.
- [23] Tao, J.; Perdew, J. P.; Staroverov, V. N.; Scuseria, G. E. *Phys. Rev. Lett.* **2003**, *91*, 146401.
- [24] Grimme, S.; Antony, J.; Ehrlich, S.; Krieg, H. *J. Chem. Phys.* **2010**, *132*, 154104.
- [25] Marenich, A. V.; Cramer, C. J.; Truhlar, D. G. *J. Phys. Chem. B* **2009**, *113*, 6378.
- [26] Grimme, S. *J. Chem. Phys.* **2003**, *118*, 9095.
- [27] Kutzelnigg W., Fleischer U., Schindler M., *Interpretation of NMR Chemical Shifts and Magnetic Susceptibilities, Springer-Verlag, Heidelberg, 1990*, vol. 23.
- [28] Frisch, M. J.; Trucks, G. W.; Schlegel, H. B.; Scuseria, G. E.; Robb, M. A.; Cheeseman, J. R.; Scalmani, G.; Barone, V.; Mennucci, B.; Petersson, G. A.; Nakatsuji, H.; Caricato, M.; Li, X.; Hratchian, H. P.; Izmaylov, A. F.; Bloino, J.; Zheng, G.; Sonnenberg, J. L.; Hada, M.; Ehara, M.; Toyota, K.; Fukuda, R.; Hasegawa, J.; Ishida, M.; Nakajima, T.; Honda, Y.; Kitao, O.; Nakai, H.; Vreven, T.; Montgomery, J. A., Jr.; Peralta, J. E.; Ogliaro, F.; Bearpark, M.; Heyd, J. J.; Brothers, E.; Kudin, K. N.; Staroverov, V. N.; Kobayashi, R.; Normand, J.; Raghavachari, K.; Rendell, A.; Burant, J. C.; Iyengar, S. S.; Tomasi, J.; Cossi, M.; Rega, N.; Millam, J. M.; Klene, M.; Knox, J. E.; Cross, J. B.; Bakken, V.; Adamo, C.; Jaramillo, J.; Gomperts, R.; Stratmann, R. E.; Yazyev, O.; Austin, A. J.; Cammi, R.; Pomelli, C.; Ochterski, J. W.; Martin, R. L.; Morokuma, K.; Zakrzewski, V. G.; Voth, G. A.; Salvador, P.; Dannenberg, J. J.; Dapprich, S.; Daniels, A. D.; Farkas, Ö.; Foresman, J. B.; Ortiz, J. V.; Cioslowski, J.; Fox, D. J. *Gaussian 09*, Revision D.01, Gaussian, Inc., Wallingford CT, 2009.
- [29] Neese, F. *Wiley Interdiscip. Rev. Comput. Mol. Sci.* **2012**, *2*, 73.
- [30] Frey, P. a. *Magn. Reson. Chem.* **2001**, *39*, 190.
- [31] Frey, P. a; Whitt, S. a; Tobin, J. B. *Science* **1994**, *264*, 1927.
- [32] Günther, H. *NMR Spectroscopy Basic Principles, Concepts, and Applications in Chemistry*, 3rd ed.; Wiley-VCH Verlag GmbH & Co. KGaA: Weinheim, **2013**.
- [33] Olah, G. A.; Kreienbuh, P. *J. Am. Chem. Soc.* **1967**, *15*, 4756.
- [34] Olah, G. A.; Donovan, D. J. *J. Org. Chem.* **1978**, *43*, 860.
- [35] Sharif, S.; Denisov, G. S.; Toney, M. D.; Limbach, H. *J. Am. Chem. Soc.* **2007**, *129*, 6313.

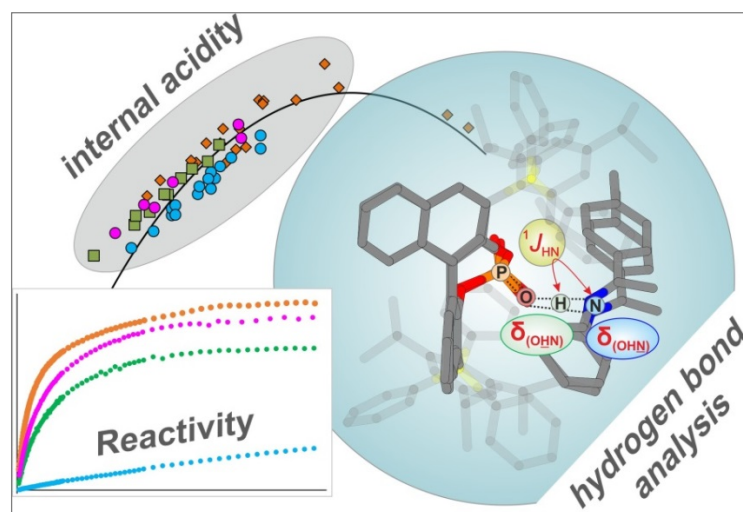
2 Characterization of Charge Assisted Strong Hydrogen Bonds

- [36] Golubev, N. S.; Shenderovich, I. G.; Smirnov, S. N.; Denisov, G. S.; Limbach, H.-H. *Chem. - Eur. J.* **1999**, *5*, 492.
- [37] Shenderovich, I. G.; Burtsev, A. P.; Denisov, G. S.; Golubev, N. S.; Limbach, H.-H. *Magn. Reson. Chem.* **2001**, *39*, 91.
- [38] Ishikita, H.; Saito, K. *J. R. Soc. Interface* **2014**, *11*, 20130518.
- [39] Reichhardt, C.; Welton, T. In *Solvents and Solvent Effects in Organic Chemistry*; Wiley-VCH Verlag GmbH & Co. KGaA: Weinheim, **2011**; pp 136–138.
- [40] Anderson, K. M.; Esadze, A.; Manoharan, M.; Brüscheiler, R.; Gorenstein, D. G.; Iwahara, J. *J. Am. Chem. Soc.* **2013**, *135*, 3613.
- [41] Limbach, H.-H.; Pietrzak, M.; Sharif, S.; Tolstoy, P. M.; Shenderovich, I. G.; Smirnov, S. N.; Golubev, N. S.; Denisov, G. S. *Chem. - Eur. J.* **2004**, *10*, 5195.
- [42] Reichhardt, C.; Welton, T. In *Solvents and Solvent Effects in Organic Chemistry*; Wiley-VCH Verlag GmbH & Co. KGaA: Weinheim, **2011**; pp 417–422.
- [43] Benedict, H.; Shenderovich, I. G.; Malkina, O. L.; Malkin, V. G.; Denisov, G. S.; Golubev, N. S.; Limbach, H. *J. Am. Chem. Soc.* **2000**, *122*, 1979.
- [44] Limbach, H.-H.; Pietrzak, M.; Benedict, H.; Tolstoy, P. M.; Golubev, N. S.; Denisov, G. S. *J. Mol. Struct.* **2004**, *706*, 115.
- [45] Grabowski, S. J. *Chem. Rev.* **2011**, *111*, 2597.
- [46] Grabowski, S. J.; Sokalski, W. A.; Dyguda, E.; Leszczyn, J. *J. Phys. Chem. B* **2006**, *110*, 6444.
- [47] The y-axis in Figure 2.7c has a scale in total energy due to the vanishing neutral hydrogen bond minima (no stationary point can be found; hence, no vibrational analysis can be performed)
- [48] Smirnov, S. N.; Golubev, N. S.; Denisov, G. S.; Benedict, H.; Schah-Mohammedi, P.; Limbach, H.-H. *J. Am. Chem. Soc.* **1996**, *118*, 4094.
- [49] Steiner, T. *J. Phys. Chem. A* **1998**, *102*, 7041.
- [50] E. D. Glendening, J. K. Badenhop, A. E. Reed, J. E. Carpenter, J. A. Bohmann, C. M. Morales, C. R. Landis, and F. Weinhold, NBO 6.0., Theoretical Chemistry Institute, University of Wisconsin: Madison, WI, **2013**.
- [51] The adjustment of the constants employed in equations 4 and 5 (b_{XH}^0 and r_{XH}^0) to our theoretical data (see Supporting Information) is not suitable, because it impairs the weak neutral hydrogen bonded systems.
- [52] For the description of the trans-hydrogen bond scalar couplings the definition of Dingley *et al.* is used. The abbreviation ${}^3\text{h}J_{\text{PN}}$ stands for scalar coupling between ${}^{15}\text{N}$ and ${}^{31}\text{P}$ over three bonds including a hydrogen bond and ${}^2\text{h}J_{\text{PH}}$ for scalar coupling between a ${}^1\text{H}$ and ${}^{31}\text{P}$ over two bonds. For reference see A. J. Dingley, F. Cordier, S. Grzesiek, *Concepts Magn. Reson.*, **2001**, *13*, 103-127.
- [53] Federwisch, G.; Kleinmaier, R.; Drettwan, D.; Gschwind, R. M. *J. Am. Chem. Soc.* **2008**, *130*, 16846.
- [54] Mishima, M.; Hatanaka, M.; Shigeyuki, Y.; Takahisa, I.; Wälchli, M.; Ito, Y.; Shirakawa, M. *J. Am. Chem. Soc.* **2000**, *122*, 5883.

2 Characterization of Charge Assisted Strong Hydrogen Bonds

- [55] Detering, C.; Tolstoy, P. M.; Golubev, N. S.; Denisov, G. S.; Limbach, H. *Dokl. Phys. Chem.* **2001**, *379*, 191

3 Internal Acidity Scale and Reactivity Evaluation of Chiral Phosphoric Acids with different 3,3'-Substituents in Brønsted Acid Catalysis



Kerstin Rothermel, Maxime Melikian, Johnny Hioe, Julian Greindl, Johannes Gramüller, Matej Žabka, Nils Sorgenfrei, Thomas Hausler, Fabio Morana and Ruth M. Gschwind

Chem. Sci., 2019, accepted

DOI: 10.1039/C9SC02342A

Most of the in-situ NMR reaction kinetics as well as the whole analysis of the isomerization rates were performed by **Kerstin Rothermel**. The NMR measurements for the hydrogen bond analysis were done by Dr. Nils Sorgenfrei, Thomas Hausler, Dr. Maxime Melikian, Dr. Julian Greindl and Johannes Gramüller. Dr. Matej Žabka supported the ex-situ reaction kinetics. The data of the ternary complex were obtained from Dr. Julian Greindl and Johannes Gramüller. Dr. Fabio Morana contributed in the optimization of the sample preparation and by synthesis of the catalyst (*R*)-TRIP. The imine substrates were synthesized by all authors except Dr. Johnny Hioe. All computational studies were performed by Dr. Johnny Hioe. The major part of the manuscript was written by **Kerstin Rothermel**.

Source of this chapter:

<https://pubs.rsc.org/en/content/articlelanding/2019/sc/c9sc02342a#!divAbstract>

Reproduced with permission. All further permissions related to the material excerpted should be directed to the RSC. Text and figures may differ from the published version.

3 Internal Acidity Scale and Reactivity Evaluation

3.1. Abstract

The concept of hydrogen bonding for enhancing substrate binding and controlling selectivity and reactivity is central in catalysis. However, the properties of these key hydrogen bonds and their catalyst dependent variations are extremely difficult to determine directly by experiments. Here, for the first time the hydrogen bond properties of a whole series of BINOL-derived chiral phosphoric acid (CPA) catalysts in their substrate complexes with various imines were investigated to derive the influence of different 3,3'-substituents on the acidity and reactivity. NMR ^1H and ^{15}N chemical shifts and $^1J_{\text{NH}}$ coupling constants of these hydrogen bonds were used to establish an internal acidity scale corroborated by calculations. Deviations from calculated external acidities reveal the importance of intermolecular interactions for this key feature of CPAs. For CPAs with similarly sized binding pockets a correlation of reactivity and hydrogen bond strengths of the catalyst was found. A catalyst with a very small binding pocket showed significantly reduced reactivities. Therefore, NMR isomerization kinetics, population and chemical shift analyses of binary and ternary complexes as well as reaction kinetics were performed to address the rate determining zone of the transfer hydrogenation. The results of CPAs with different 3,3'-substituents show a delicate balance between the isomerization and the ternary complex formation as rate-determining zone. For CPAs with an identical acidic motif and similar sterics, reactivity and internal acidity correlated inversely. In case higher sterical demand within the binary complex hinders the binding of the second substrate the correlation between acidity and reactivity breaks down

3.2. Introduction

Over the past decade, a large number of reactions were developed, where enantioenriched products are formed using a chiral organic molecule with acidic functionality as catalyst.^[1-3] A prominent example of the so-called chiral Brønsted acid catalysis was a Strecker reaction catalyzed by peptide-based thiourea derivatives.^[1,4-6] One success factor of Brønsted acid catalysts in enantioselective transformations is the formation of a central hydrogen bond between catalyst and substrate, thus anchoring the structures, which favor one enantiotopic face over the other.^[1] Another milestone was the development of chiral phosphoric acid (CPAs) catalysts with BINOL (1,1'-bi-2-naphthol) backbones by Akiyama and Terada.^[7,8] These catalysts are applicable in several highly enantioselective reactions with imines such as transfer hydrogenations,^[9-11] reductive aminations,^[12,13] Mannich type reactions^[14-16] and Strecker reactions.^[17] Particularly, in the asymmetric reduction of imines with Hantzsch 1,4-dihydropyridine ester these BINOL

3 Internal Acidity Scale and Reactivity Evaluation

derived CPAs can achieve high yields as well as high enantioselectivities.^[12,18–20] Rueping et al. proposed a catalytic cycle (Figure 1a), where the imine is protonated by the phosphoric acid and forms a hydrogen bond assisted ion pair.^[3,7] In the last step, the hydride transfer from the Hantzsch ester leads to the chiral amine, while the pyridinium salt regenerates the Brønsted acid.^[18]

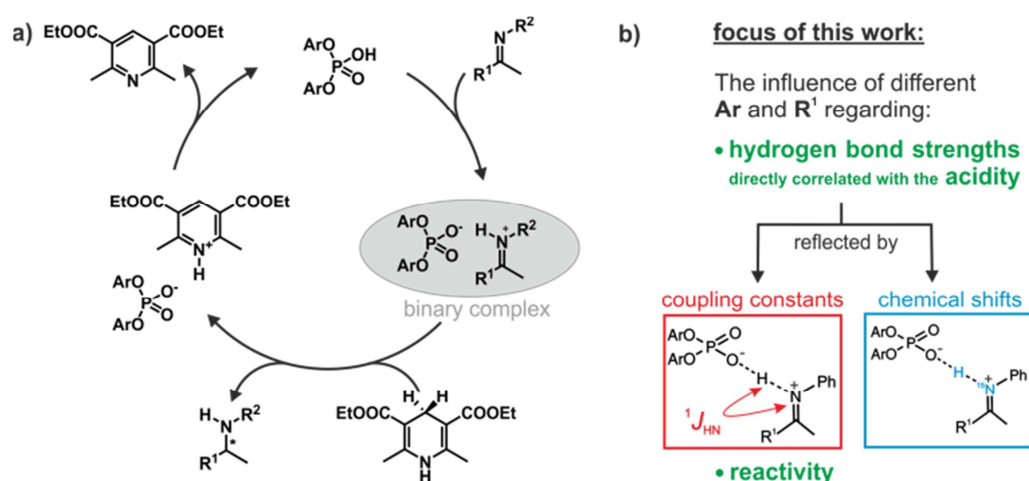


Figure 1. a) Proposed catalytic cycle for the asymmetric transfer hydrogenation. CPAs are used and Hantzsch ester acts as a reducing agent;^[18] b) the influence of different Ar and R¹ substituents on the hydrogen bond of the ion pair highlighted in grey is the focus of this work as well as their effect on the reactivity in the shown hydrogenation.

This asymmetric reduction of imines works with many different CPAs, which differ only in the 3,3'-substituents. Prominent examples are amongst others **TRIP** (3,3'-Bis(2,4,6-triisopropyl-phenyl)-1,1'-binaphthyl-2,2'-diyl-hydrogen phosphate), **TRIFP** (3,3'-Bis(3,5-bis(trifluoro-methyl)-phenyl)-1,1'-binaphthyl-2,2'-diyl-hydrogen phosphate) and **TIPSY** (3,3'-Bis(triphenyl-silyl)-1,1'-binaphthyl-2,2'-diylhydrogen phosphate) (Figure 2a).^[19,21,22] Thus, the 3,3'-substituents are the key to *ee* values and yields and sometimes even reverse stereoselectivity.^[23–26] The way that structures of the catalysts influence the outcome varies from reaction to reaction and, up to now, there have been few direct experimental measurements of relevant structural features.^[27] Thus, the screening of the catalysts to find the most effective BINOL derived CPA is still the predominantly employed method in synthesis. On the contrary, in silico, the understanding of the occurring interactions and structures is by far more developed.^[28] One approach follows a multivariate regression model analysis, utilizing various parameters to develop a mathematical model that explains the relationship between structure and reactivity or

3 Internal Acidity Scale and Reactivity Evaluation

selectivity. This model is capable of distinguishing certain crucial non-covalent interactions present between the catalyst and the substrate.^[29,30]

In 2016, Goodman *et al.* introduced some parameters to describe the steric bulk of the 3,3'-substituents of the catalysts. Thus, they could show that the stereoselectivity of the asymmetric transfer hydrogenation of imines (Figure 1a) is widely dependent on two parameters: the rotation barrier describing the proximal bulk and the AREA (θ) taking the distal bulk into account.^[31] Also, other groups investigated the influence of different 3,3'-substituents of CPAs in several reactions regarding the occurring transition states, the structural differences and/or the enantioselectivity by theoretical methods.^[32–40] Nevertheless, our recent NMR study about the influence of 3,3' substituents on the structures and populations of binary CPA/imine complexes revealed a significant deviation of experimental populations compared to those calculated with the standard theoretical methods applied to these systems.^[41] In general, experimental insight into the structures involved in Brønsted acid catalysis is very rare.^[42,43] In earlier studies we revealed the hydrogen bond strengths and geometries of TRIP/imine complexes in detail.^[42] In addition, we could experimentally show that for TRIP, TRIFP, TiPSY and TRIM (3,3'-Bis(2,4,6-trimethyl-phenyl)-1,1'-binaphthyl-2,2'-diyl-hydrogen phosphate) four different core structures of their binary CPA/imine complexes are omnipresent in solution (*Type I/II E* and *Type I/II Z*).^[41,43] The different 3,3'-substituents influence mainly the energetics/population of these binary complexes, however, much less their general sterically features and interaction patterns.^[41] Nevertheless, despite the crucial function of hydrogen bonds in Brønsted acid catalysis as structural anchor^[43] or regarding acidity/reactivity correlations^[44] detailed experimental insights about the effect of 3,3' substituents on this hydrogen bond are elusive so far.

In general, the formation of hydrogen bonds in catalyst/substrate complexes is often highly relevant and plays a key role in the activation of the substrate. For example, in the field of asymmetric catalysis, the activation of electrophilic substrates such as carbonyls or imines seems to take place *via* a hydrogen bond.^[3,9,45,46] Also in photochemistry several examples are known, where the proposed mechanisms is based on a hydrogen bonded species. Exemplary, Knowles *et al.* could show that ketones, amides or alcohols can be converted by a proton-coupled electron transfer (PCET) and assumed a hydrogen bond formation between the substrate and proton donor/acceptor prior to the electron transfer.^[47–49] Finally, there are various examples throughout organocatalysis, in which the substrate binding and activation *via* a hydrogen bonded species is

3 Internal Acidity Scale and Reactivity Evaluation

proposed.^[50-54] However the central hydrogen-bonded species are often in fast chemical exchange or have short lifetimes, therefore it is for most of the systems experimentally not possible to detect these hydrogen bonds.

In the literature hydrogen bonds are described as a beginning proton transfer reaction.^[55,56] This means that the position of the proton inside the hydrogen bond varies depending on the acidity of the hydrogen bond donor respectively basicity of the acceptor. Limbach *et al.* developed on model systems a NMR spectroscopic access to the position of these hydrogen atoms inside the hydrogen bonds using an empirical correlation of the ^1H and the ^{15}N chemical shifts.^[57,58] This in combination with our recently developed access to the hydrogen bonds in CPA/imine complexes^[42] allows for the first time to tackle the effect of the 3,3'-substituent on the hydrogen bonds and thus on the acidity with NMR. This acidity may play a crucial role regarding reactivity. However, up to now there are only few experimentally determined pK_a values of CPAs. In 2011, O'Donoghue *et al.* determined pK_a values for TRIP and TRIFP in DMSO by using a spectrophotometric titration method.^[59] Here, variations of the 3,3'-substituents resulted in modulation of the pK_a -values of the CPAs up to ~ 1.5 pK_a units ($\text{pK}_{a\text{TRIP}}(\text{DMSO}) = 4.22$ and $\text{pK}_{a\text{TRIFP}}(\text{DMSO}) = 2.63$).^[60] In acetonitrile, a similar variation range of experimental pK_a values for five phosphoric acids between 12.5 and 14.0 is found ($\text{pK}_{a\text{TRIP}}(\text{ACN}) = 13.3$).^[44] However BINOL derived N-triflyl-phosphoramides show significant smaller pK_a values between 6.3 and 6.9.^[44] Thus, at least in acetonitrile, the acidity of the catalysts is significantly influenced by the acidic motif, while the 3,3'-substituents have minor effects.^[44] Most interestingly, in a Nazarov cyclization higher rates were found for more acidic Brønsted acids and a direct correlation between acidity and reactivity was postulated.^[44] Given the large deviations of CPA acidities between the previous studies and our access to hydrogen bonds in CPA imine complexes for TRIP this opens up the possibility to measure an internal acidity scale, to investigate the influence of 3,3'-substituents and to check the correlation between the internal acidity and the reactivity of these complexes.

Therefore, in this study, we used four different CPAs and several imines to develop for the first time an internal acidity scale for binary CPA/imine complexes. Low temperature measurements and NMR-spectroscopic hydrogen bond analysis of the binary complexes allowed to determine the acidity of the CPAs *via* chemical shifts or $^1J_{\text{NH}}$ coupling constants. Finally, the resulting internal acidity scale was compared with the reactivity of the catalysts in the transfer hydrogenation.

3.3. Results and Discussion

3.3.1. Investigated systems/complexes

In order to investigate the influence of different 3,3'-substituents on the acidity of CPAs and to correlate this internal acidity with the reactivity in transfer hydrogenations, we selected four different CPAs and twelve imines with different electronic and steric properties (Figure 2). The binary complexes of the four CPAs **1a-1d** with the imines **2** and **6-13** were used to cover the whole range of the Steiner-Limbach curve, while imines **3**, **4** and **5** were chosen for a detailed hydrogen bond analysis within the binary complexes. Altogether, we screened 32 different binary complexes.¹⁵N labelling of the imines allowed the access to the ¹⁵N chemical shifts^[42] and CD₂Cl₂ was chosen as solvent, since CD₂Cl₂ provides the best chemical shift dispersion and smallest line widths of all solvents investigated. To reach the slow exchange regime of the hydrogen bonds all spectra were recorded at 180 K unless otherwise mentioned.

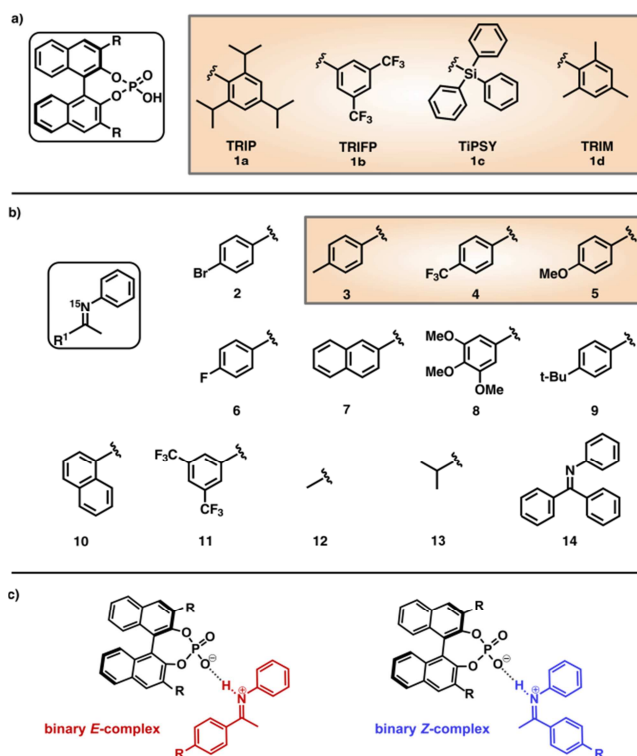


Figure 2. Structures of the investigated a) phosphoric acids with different 3,3'-substituents and b) imines. The hydrogen bonds of the binary complexes of TRIP **1a**, TRIFP **1b**, TiPSY **1c** and TRIM **1d** with the imines **3**, **4** and **5** were investigated in detail by means of NMR. The other imines **2** and **6-13** are necessary to cover the complete hydrogen bond range of the Steiner-Limbach curve. The non-isomerizable imine **14** was used to investigate the influence of the Hantzsch ester concentration on the reaction rate. c) The main focus of this work was the NMR-spectroscopic investigation of the binary CPA/imine-complexes. The imine exists either as *E*- or *Z*-isomer.

3 Internal Acidity Scale and Reactivity Evaluation

3.3.2. Determination of the Internal Acidity

Since external pKa measurements/calculations are performed versus protons whereas in the transfer hydrogenation a binding to an imine occurs, there is no reason why there necessarily should be a correlation between external acidity and reactivity. Therefore, an internal acidity scale was constructed within the binary CPA imine complexes to be later compared to the reactivity. The Steiner-Limbach correlation can be used to characterize hydrogen bonds in phosphoric acid catalyst/imine complexes as previously demonstrated for TRIP/imine complexes.^[42] By plotting the ^1H chemical shift $\delta(\text{OHN})$ of the acidic proton against the ^{15}N chemical shift $\delta(\text{OHN})$ of the basic nitrogen, a parabolic correlation curve can be fitted through the data points (see Figure 3 and SI). In order to achieve a sufficient fit, hydrogen bonds in a variety of different strengths are required. Thus, for the data points of weaker hydrogen bonds on the outer parts of the curve several phenol derivatives, carboxylic acids and tetrafluoroboric acid were added from our previous work (for details see SI).^[42] All CPA/imine complexes investigated in this work feature a strong hydrogen bond with ^1H chemical shifts ranging from 15 to 19 ppm (see highlighted points in Figure 3a). Their referenced ^{15}N chemical shifts (for details see SI) range from -90 to -150 ppm. Furthermore, for many of these binary complexes magnetisation transfers across the hydrogen bond via $^3\text{h}J_{\text{PN}}$ and $^2\text{h}J_{\text{PH}}$ are detectable. All of these parameters are typical for a strong hydrogen bond with a substantial covalent character providing high geometrical preferences for a linear arrangement. The position of these binary complexes on the left side of the curve highlighted in Figure 3a) shows that these binary complexes have a partial ion pair character.

3 Internal Acidity Scale and Reactivity Evaluation

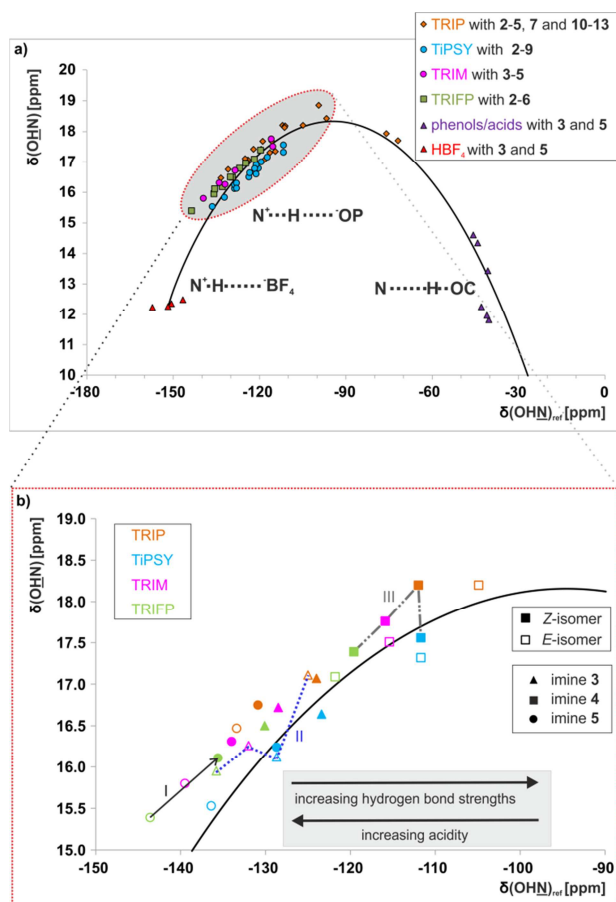


Figure 3. In the Steiner-Limbach curve the $\delta(\text{OHN})$ is plotted versus $\delta(\text{OHN})_{\text{ref}}$ of the hydrogen bonded complexes. All CPA/imine complexes are located on the left side of the curve (highlighted in grey) and form hydrogen-bond assisted ion pairs. The data for the complexes with TRIP, HBF_4 , phenols and carboxylic acids were taken from reference.^[42] All ^{15}N chemical shifts are referenced to $\{\delta(\text{OHN}) = \delta(\text{OHN})_{\text{exp}} - 340 \text{ ppm}\}$ (for details and exact values see SI); b) enlarged section of the Steiner-Limbach curve showing only the binary complexes of CPAs **1a-1d** and imine **3, 4** and **5** for the sake of clarity. The arrow I visualizes the observed increasing hydrogen bond strengths for the Z-complexes. The comparison of the hydrogen bond strengths of the different CPAs with one given imine is illustrated with the dotted lines II (E-complexes) and III (Z-complexes). These trends are exemplary shown with one imine but can be observed for imines **3-5**.

Since in the first step of the asymmetric transfer hydrogenation the imine-activation *via* a hydrogen bond formation is assumed (Figure 1a), this hydrogen bond of the binary complex can be used to monitor the binding between catalyst and substrate. In general, three parameters can be used to determine the hydrogen bond strength: the chemical shifts of ^1H and ^{15}N as well as the $^1J_{\text{NH}}$ coupling constants. In case that only the hydrogen bond character influences these parameters all of them should directly correlate, i.e. the stronger the hydrogen bond the larger the ^1H and ^{15}N chemical shifts (smaller negative values) and the smaller the $^1J_{\text{NH}}$ coupling constant. The ^1H chemical shift is known to be significantly influenced by anisotropic shielding effects e.g. from

3 Internal Acidity Scale and Reactivity Evaluation

aromatic moieties and other neighbourhood effects, while for TRIP/imine complexes the ^{15}N chemical shift was shown to reflect directly the hydrogen bond situation.^[42] Therefore, the ^{15}N chemical shift was used as a descriptor for the hydrogen bond strength and acidity, which also directly correlates with the $^1J_{\text{NH}}$ coupling constant (see discussion below).

The simplified excerpt of the Steiner-Limbach curve presenting only complexes with imines **3**, **4** and **5** in Figure 3b reveals different hydrogen bond strengths for the four catalysts and common trends for *E*- and *Z*-imines. In general, for all CPA/*Z*-imine complexes stronger hydrogen bonds are observed than for the complexes with *E*-imines, as indicated by the low field shift of the hydrogen atom as well as the nitrogen atom (Figure 3b, exemplarily illustrated for imine **5** with the black arrow I). Due to the reduced steric requirements of the imine in the *Z*-configuration the imine can approach closer to the catalyst. This is corroborated by the experimentally derived atomic distances of the hydrogen bonds of the TRIP complexes^[42] and further supported by the distances in the calculated structures of various binary complexes (for coordinates see SI). Furthermore, within the *E*- and *Z*-complexes different trends regarding the hydrogen bond strengths upon variation of the catalyst are observed: For the *E*-complexes TRIP forms the strongest hydrogen bonds (least negative ^{15}N chemical shift), followed by TiPSY, TRIM and TRIFP (Figure 3b, exemplarily illustrated for *E*-imine **3** with the blue, dotted line II). For *Z*-complexes TiPSY forms the strongest hydrogen bond directly followed by TRIP and then with a slight gap again followed by TRIM and TRIFP (Figure 3b, exemplarily illustrated for *Z*-imine **4** with the grey, dotted line III). These trends of the hydrogen bond strengths (TRIP > TiPSY > TRIM > TRIFP for *E*-complexes and TiPSY \geq TRIP > TRIM > TRIFP for *Z*-complexes) were observed for imines **3-5** and could be confirmed by the $^1J_{\text{NH}}$ coupling constants (see below). The hydrogen bond strengths can be directly correlated with the internal acidity,^[61] because with a given imine a variation of the acidity of the catalyst changes the position of the proton in the hydrogen bond. In case of the investigated hydrogen assisted ion pair complexes, which are located on the left side of the Steiner-Limbach curve, a higher acidity effects a weaker hydrogen bond. That means a higher acidity or lower pKa value relates to a reduced ^1H and ^{15}N chemical shift (larger negative value for the referenced ^{15}N) and an increased $^1J_{\text{NH}}$ coupling constant. For the catalysts in their binary complexes two different internal acidity scales for the *E*- and the *Z*-complexes were obtained. For the *E*-complexes the internal acidity gave the following trend: $\text{pKa}_{\text{TRIP}} > \text{pKa}_{\text{TiPSY}} > \text{pKa}_{\text{TRIM}} > \text{pKa}_{\text{TRIFP}}$ (Figure 3b, exemplary illustrated for *E*-imine **3** with the blue, dotted line II). Whereas, for the *Z*-complexes TiPSY is the

3 Internal Acidity Scale and Reactivity Evaluation

least acidic catalyst and an order of $\text{pK}_{\text{a}}^{\text{TiPSY}} \geq \text{pK}_{\text{a}}^{\text{TRIP}} > \text{pK}_{\text{a}}^{\text{TRIM}} > \text{pK}_{\text{a}}^{\text{TRIFP}}$ (Figure 3b, exemplary illustrated for *Z*-imine **4** with the grey, dotted line III) was obtained.

The analysis of the $^1J_{\text{NH}}$ coupling constants (Figure 4) confirms the internal acidity for both, *E*- and *Z*-complexes. Furthermore, the Hammett σ_{para} values of the aryl substituents of the imines correlate with the coupling constants for *E*- and *Z*-complexes of imine **3-6** (see SI). Given the fact, that the hydrogen bond of all investigated CPA/imine complexes tends towards ionic complexes, i.e. to a complete proton transfer, lower $^1J_{\text{NH}}$ coupling constants correspond to stronger hydrogen bonds. Within all investigated CPA/*E*-imine complexes TRIP shows the smallest $^1J_{\text{NH}}$ coupling constants, followed by TiPSY, TRIM and TRIFP. This is in accordance with the internal acidities ($\text{pK}_{\text{a}}^{\text{TRIP}} > \text{pK}_{\text{a}}^{\text{TiPSY}} > \text{pK}_{\text{a}}^{\text{TRIM}} > \text{pK}_{\text{a}}^{\text{TRIFP}}$) discussed before based on the ^{15}N chemical shifts. For the *Z*-complexes, in almost all cases slightly smaller $^1J_{\text{NH}}$ coupling constants were observed, corroborating the stronger hydrogen bonds derived from the chemical shift analysis (see above) i.e. the reduced internal acidity of the *Z*- compared to the *E*-complexes. For the CPA/*Z*-imine complexes $^1J_{\text{NH}}$ coupling constants for TiPSY are slightly smaller than for TRIP, suggesting stronger hydrogen bond and shorter distance from the catalyst, thus congesting the active catalyst pocket (Figure 4), which is also reflected in the acidity scale for the *Z*-complexes ($\text{pK}_{\text{a}}^{\text{TiPSY}} \geq \text{pK}_{\text{a}}^{\text{TRIP}} > \text{pK}_{\text{a}}^{\text{TRIM}} > \text{pK}_{\text{a}}^{\text{TRIFP}}$), obtained from the ^{15}N chemical shifts. For the *E*-complexes the order of $^1J_{\text{NH}}$ (TRIP < TiPSY < TRIM < TRIFP) agrees with the acidity trend $\text{pK}_{\text{a}}^{\text{TRIP}} > \text{pK}_{\text{a}}^{\text{TiPSY}} > \text{pK}_{\text{a}}^{\text{TRIM}} > \text{pK}_{\text{a}}^{\text{TRIFP}}$ as discussed above.

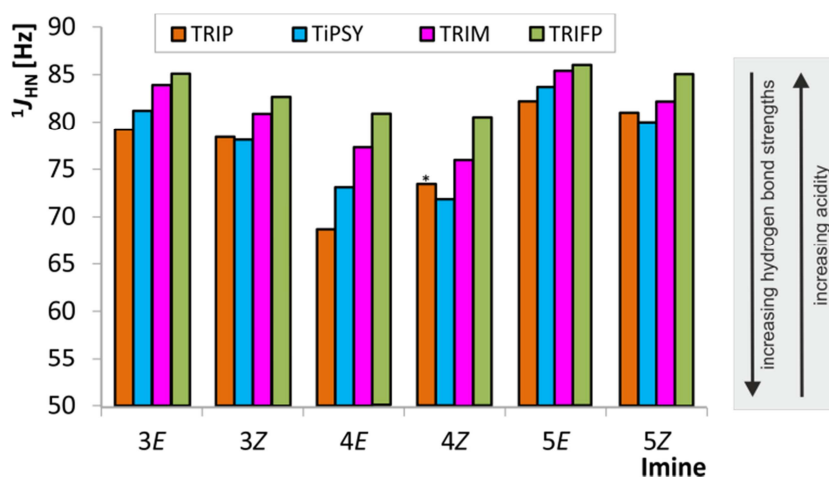


Figure 4. The experimental CPA/imine $^1J_{\text{NH}}$ coupling constants are shown for *E*- and *Z*-imines of **3**, **4** and **5**. The following trend is observed for the *E*-imines: $^1J_{\text{NH}}^{\text{TRIP}} < ^1J_{\text{NH}}^{\text{TiPSY}} < ^1J_{\text{NH}}^{\text{TRIM}} < ^1J_{\text{NH}}^{\text{TRIFP}}$. For *Z*-complexes slightly different trend was found: $^1J_{\text{NH}}^{\text{TiPSY}} < ^1J_{\text{NH}}^{\text{TRIP}} < ^1J_{\text{NH}}^{\text{TRIM}} < ^1J_{\text{NH}}^{\text{TRIFP}}$.

3 Internal Acidity Scale and Reactivity Evaluation

TRIM < $^1J_{\text{HN}}$ TRIFP. Due to overlap the $^1J_{\text{HN}}$ of TRIP/4Z was determined from HN-HMBC spectra (marked by an asterisk; for all values see SI).

In our theoretical calculations, the same qualitative trend for the scalar coupling constants ($^1J_{\text{NH}}$ TRIP < $^1J_{\text{NH}}$ TIPSY < $^1J_{\text{NH}}$ TRIM < $^1J_{\text{NH}}$ TRIFP, for details see SI) could be reproduced for the *E*-complexes. Indeed, for the *Z*-complexes, the switched order of TRIP and TIPSY is not reflected in the calculations. Next, this internal acidity was compared to experimental and theoretical external acidities. The experimental, external acidities of TRIFP and TRIP as described by O'Donoghue ($\text{pK}_{\text{aTRIFP}} < \text{pK}_{\text{aTRIP}}$) in DMSO,^[60] correlate at least in their trend with our internal acidities. Absolute pKa values of many CPAs in DMSO (SMD) at 298 K using various thermodynamic cycles have been also computed at DFT level of theory.^[62] Thus, to compare the internal acidities in DCM at 180 K with the external acidity, we calculated relative external acidity of TRIP, TRIM and TIPSY to TRIFP. In general, the relative external acidities of the investigated CPAs in DCM confirm the previous calculated relative pKa values in DMSO within ~0.5 pKa units. This indicates that the implicit solvent model may vary the absolute pKa values but not the order. Thus, regardless of the choice of dielectric medium, the relative external acidity scale deviates significantly from the internal acidity scale. Especially the almost identical internal acidities of TRIM and TIPSY are not reflected in the calculated external acidities. As a result, this internal acidity scale can be used as a direct experimental indicator for the importance of intermolecular interactions such as dispersion^[63,64] in Brønsted acid catalysis, which was already proposed for CPA's and other catalytic systems^[65,66] but so far only accessible via theoretical calculations/analyses or multicomponent experimental data such as reactivities.^[64,67,68]

Table 1: Calculated pKa-values relative to TRIFP in DMSO at 298 K and DCM at 180 K

	pK_{a,calc} in DCM at 180K (relative to TRIFP)	pK_{a,calc} in DMSO at 298K (relative to TRIFP)^[52]
TRIP	+0.85	+0.55
TRIM	+1.57	+2.26
TIPSY	+6.00	n.a.

3 Internal Acidity Scale and Reactivity Evaluation

The presented first internal acidity scale of CPA/imine complexes and to our knowledge the first systematic and broad experimental NMR-study about the trends in hydrogen bond strengths within catalyst/substrate complexes in enantioselective catalysis shows that the intermolecular interactions between catalyst and substrate and potentially also the modulated solvent interactions of the complex significantly affect even the relative acidities. Furthermore, the comparison of the internal with the external acidity may in the future represent a useful tool to evaluate the non-covalent interactions in these complexes and especially the interactions of the 3,3'-substituents, because at least for the imines **3–5** there are common internal acidity trends.

3.3.3. Reactivity Analysis

Previously, a correlation was postulated between the acidity of CPAs and their reactivity in a different system. In a Nazarov cyclisation, the highest reactivity was observed for the most acidic CPA catalyst.^[44] With the internal acidities at hand, we tested whether this relationship is transferable to the transfer hydrogenation of imines, and whether also there the relative reactivities of the four catalysts match the internal acidities obtained from our NMR investigations. To compare the internal acidities with reaction rates, the reactivities were determined in CD₂Cl₂.

In the transfer hydrogenation with imine **3** we identified TRIP as the most reactive catalyst. TRIM showed a slightly lower reactivity, followed by TRIFP, while for TiPSY a considerable drop in reactivity was observed (Figure 5). For the transfer hydrogenation of imine **5** under identical conditions, the order of reactivity is conserved, however we observed an overall significantly lower reaction rate in agreement with the Hammett σ_{para} values of the aryl substituents (for details see SI). Obviously, the order of reactivity for the investigated transfer hydrogenation (TRIP > TRIM > TRIFP >> TiPSY) does not match the internal acidity scale, which show that TRIP and TiPSY have similar acidities (weakest acids $\text{pK}_{\text{a-TRIP}} \geq \text{pK}_{\text{a-TiPSY}} > \text{pK}_{\text{a-TRIM}} > \text{pK}_{\text{a-TRIFP}}$) and should in case of an acidity/reactivity correlation exhibit similar reactivities. Excluding TiPSY as a potential exception, the comparison of reactivity and internal acidity for the remaining catalysts TRIP, TRIM and TRIFP interestingly shows an inverse correlation. In contrast to the previously reported direct correlation with acidity in a Nazarov cyclisation,^[44] our investigated transfer hydrogenation is not proportionally correlated with the internal acidity.

3 Internal Acidity Scale and Reactivity Evaluation

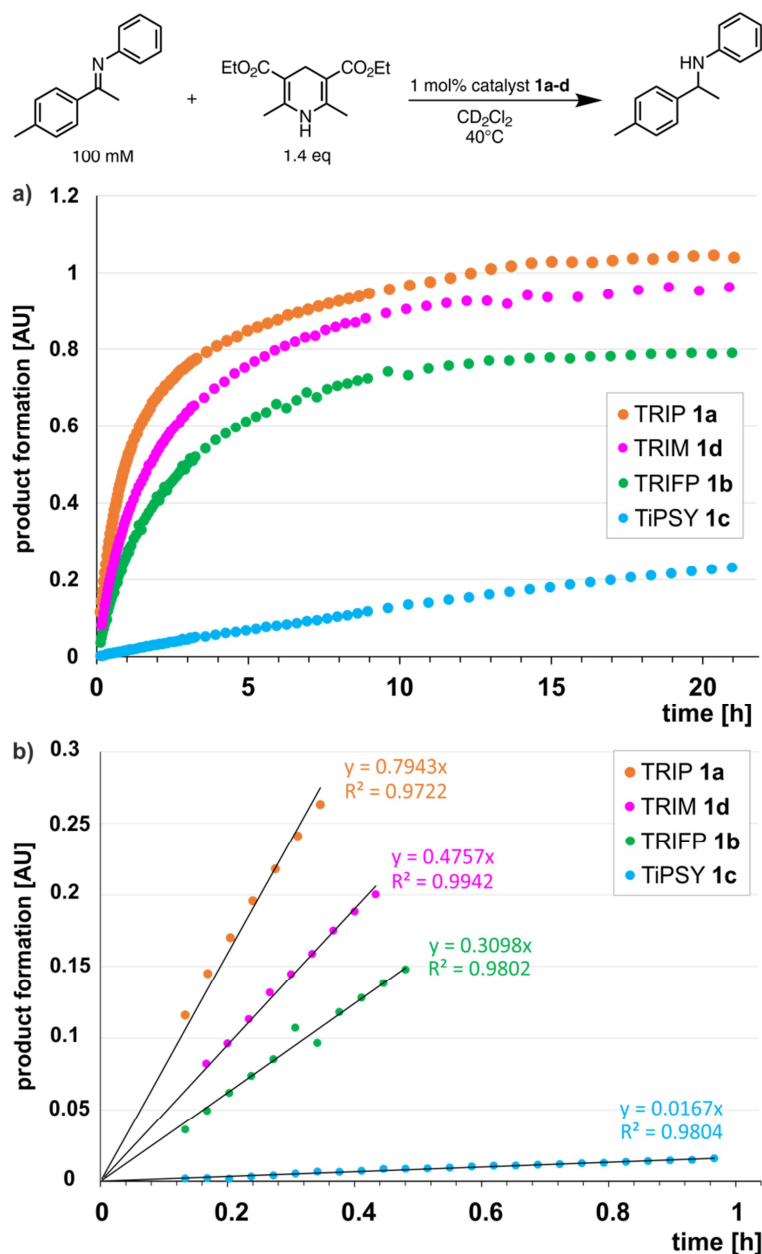


Figure 5. a) The reaction profiles for the symmetric transfer hydrogenation of imine **3** were done *in situ* in the NMR spectrometer with 1.4 equivalents of Hantzsch ester and 1 mol% catalyst (TRIP, TRIFP, TiPSY and TRIM) at 40°C in CD₂Cl₂. b) The slope of the linear ranges allows to access the rate constants.

Nevertheless, three catalysts (TRIP, TRIM and TRIFP) show an inverse correlation, while an extreme drop in reactivity of TiPSY is observed (94.6 % in the initial linear product build up compared to TRIFP). The low reactivity of TiPSY was already recognized in various reactions, e.g. a higher catalyst loading is often necessary. Hence, next the individual steps of the catalytic cycle were considered for a correlation with the reactivity.

3 Internal Acidity Scale and Reactivity Evaluation

In general, there are five possible rate-determining steps for the investigated transfer hydrogenation catalytic cycle: binary complex formation (Figure 6, step **A**), *E*-to-*Z*-imine isomerization (step **B**), formation of the ternary complex (step **C**), hydride transfer (step **D**) and product release/product inhibition (step **E**).

The binary complex formation (step **A**) can be readily observed by mixing the imine and CPA (1:1) and directly measuring its NMR spectra. The equilibrium between free imine and imine in the binary complex enables the experimental access to the association constant K_a^b of the binary complex. 1:1-samples of the catalysts **1a-1d** and imine **5** show for all catalysts approximately the same amount of free imine (TRIP: 26%, TRIFP: 16%, TRIM: 35% and TiPSY: 27% free imine; for K_a values see Table 2). The same outcome is observed even with sample preparation at 180 K. At this low temperature condition, no product formation takes place proving that the binary complex formation ($rate_a^B$) is faster than the observed overall rate ($rate_{obs}$). This indicates a sufficient association constant for this pre-equilibrium (especially at 1 mol % of catalyst, the imine is likely to saturate the catalyst) and suggests kinetics of the binary complex formation not contributing to the rate determining step.

The transition state of the hydride transfer originating from the minor-populated *Z*-imine complex has been postulated by calculations and confirmed by our previous studies to be energetically more favoured than that of the *E*-imine complex in this transformation.^[69] Hence, after the binary complex formation, the isomerization of the imine may contribute to the rate-determining step (step **B**). Therefore, we experimentally determined the rate constants of the *E*-to-*Z*-isomerization using a combination of low temperature, *in situ* illumination NMR device developed in our group,^[70] and photoisomerization. A temperature of 190 K was chosen to suppress thermal back isomerization and thus, upon irradiation with 365 nm, the photostationary states with highest possible *Z/E* binary complex ratios between 1:1 and 2:1 were reached. Next, the temperature was raised to 230 K, the light was switched off, and the decay curves of the thermal *Z*-to-*E*-back-isomerization were recorded (for details see SI). Fitting of these curves allowed us to obtain the activation barriers for the *Z*-to-*E*-isomerization of the binary complexes. From these data and the known Boltzmann distribution of the binary *E*- and *Z*-complexes in the thermodynamic equilibrium (¹H spectra), the *E*-to-*Z*-isomerization rates were calculated. This experimental access to the isomerization process is independent of the exact mechanism of isomerization (inversion, protonation-rotation and addition-rotation-elimination^[71-74]), which may be differently operative dependent on the catalyst.

3 Internal Acidity Scale and Reactivity Evaluation

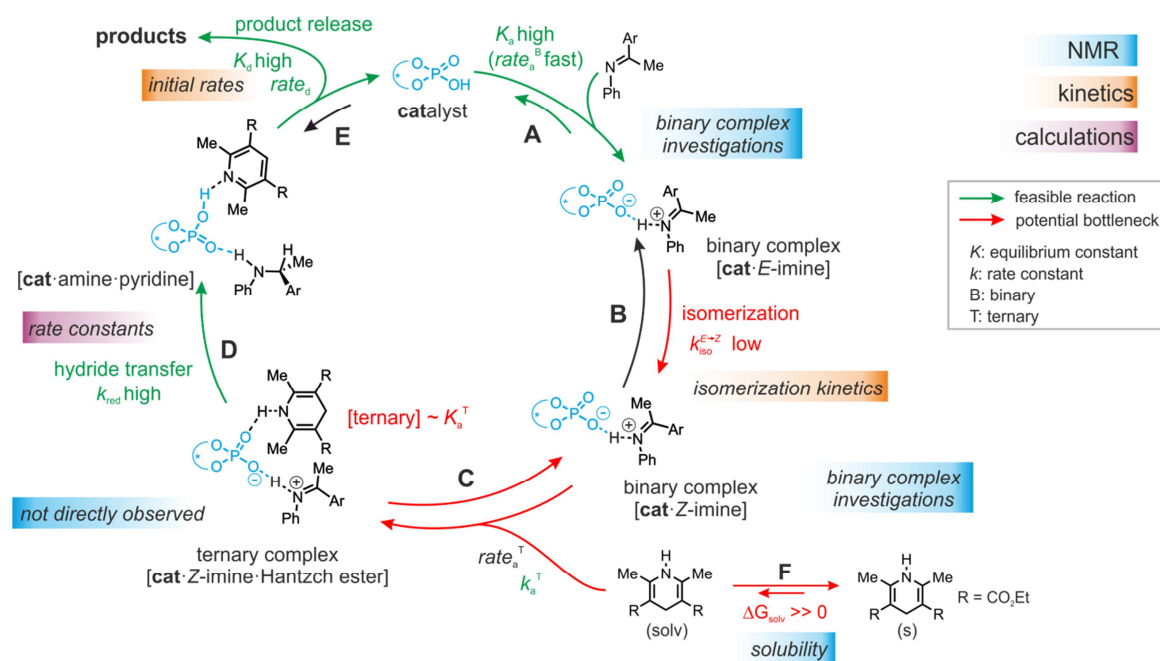


Figure 6. The catalytic cycle of the investigated transfer hydrogenation of imines is shown. Therefore, all possible rate determining steps are shown. These steps which could be neglected as rate-determining steps by experiments or calculations are shown in green, while the potential bottlenecks are shown in red. Finally, we assume the delicate equilibrium between the *E*-to-*Z*-isomerization and the ternary complex formation to be the rate-determining step.

At 230 K, the experimentally determined isomerization process is fastest for TRIP/5 ($k_{E \rightarrow Z} = 1.36 \cdot 10^{-3}$ 1/s) and similar for TiPSY/5 ($k_{E \rightarrow Z} = 5.71 \cdot 10^{-4}$ 1/s) and TRIFP/5 ($k_{E \rightarrow Z} = 4.45 \cdot 10^{-4}$ 1/s). While the similar offset in the isomerization rates, $k_{\text{iso}}(\text{TRIP}/5):k_{\text{iso}}(\text{TRIFP}/5) = 3.05$ and in the observed reaction rate, $r_{\text{obs}}(\text{TRIP}/5):r_{\text{obs}}(\text{TRIFP}/5) = 3.43$ fit for TRIP and TRIFP, those for TRIP and TiPSY show a large deviation: $k_{\text{iso}}(\text{TRIP}/5):k_{\text{iso}}(\text{TiPSY}/5) = 2.38$ and $r_{\text{obs}}(\text{TRIP}/5):r_{\text{obs}}(\text{TiPSY}/5) = 34.33$ (see SI for reaction kinetic of CPA/5). For TRIM such an analysis was not possible due to severe signal overlap. Thus, our results showed that the relative rate of transfer hydrogenation between TRIP and TRIFP is in the same qualitative trend with their relative isomerization rates. However, for the reaction with TiPSY, additional factors may contribute to the rate determining zone.

The next step in the catalytic cycle is the formation of a ternary complex between CPA, imine and Hantzsch ester (step C) as proposed by theoretical calculations.^[11,75–77] Despite extensive efforts in our working group to make the ternary complex accessible by NMR spectroscopy, we have not been able so far to detect any separated proton signals of the ternary complex upon Hantzsch ester addition. For mixtures of TRIP,

3 Internal Acidity Scale and Reactivity Evaluation

Hantzsch ester and imine **5** some small changes of chemical shifts were detected (see SI), which are most pronounced for the *ortho*-methyl protons of Hantzsch ester and also observable for the hydrogen bond signals of the binary complex. This potentially indicates a fast chemical exchange of the ternary complex formation on the NMR time scale (for spectra see SI). Structural analysis of the computed ternary complex revealed a spatial proximity of the *ortho*-methyl group to the CPA BINOL backbone, which explains the observed high-field shift due to shielding by the aromatic ring (see SI for model structure). For TRIM, under similar conditions no chemical shift changes of the hydrogen bond protons of the binary complex were observed. Thus, the NMR studies of the ternary complex suggests a low (TRIM) to moderate (TRIP) association constant K_a^T and a fast exchange between binary and ternary complex on the NMR time scale even at temperatures down to 180 K, where no reaction occurs.

Additionally, the low solubility of Hantzsch ester (endergonic ΔG_{solv} in step **F**) in the organic solvents used in this study reduces the concentration of the ternary complex even further and thus amplifies the problem of a low to moderate association constant (K_a^T). Given these experimental results the ternary complex formation/concentration can contribute to the reaction rate or even become the rate determining step and thus influence the relative reactivities of the catalysts. In addition, for a non-isomerizable imine **14**, a 1st order dependence of the dissolved Hantzsch ester concentration on the observed overall reaction rate was found (see SI). A similar shift of the rate determining step due to concentration modulations has been intentionally used in our previous mechanistic study of dienamines.^[78]

Assuming the ternary complex formation contributes significantly to the rate-determining zone and the solubility of Hantzsch ester is similar in all reactions, the origin of differences in reactivity with various catalysts lies in the alternation of association constant (K_a^T) and/or barrier for the ternary complex formation (k_a^T). Especially the bulkiness of the 3,3'-substituents and their effect on the size of the binding pocket is expected to affect the association constant (K_a^T) and barrier for formation (k_a^T).

Indeed, the AREA (θ) value, a sterical descriptor introduced by Goodman *et. al.*, which describes the cone angle of the substrate binding pocket of the CPA is for TiPSY significantly smaller than for the other CPAs.^[31] These values (TiPSY: 29°, TRIFP: 62°, TRIM: 61°, TRIP: 51°)^[31] demonstrate that the 3,3'-substituents of TiPSY are sterically by far more demanding and may therefore hinder the formation of the ternary complex.

3 Internal Acidity Scale and Reactivity Evaluation

Despite the largest sterical hindrance of TiPSY (smallest AREA (θ)), for the binary Z-complex the strongest hydrogen bond was found, i.e. the formation of the binary complex is not affected by the steric demands of the SiPh₃-groups. Thus, the flexibility of the substituents allows the structural adaptation of the catalyst to the imine. This is also corroborated by the experiments, which showed comparable association constants K_a for all catalysts (Table 2). After the binary complex is formed, the degree of freedom of the 3,3'-substituents is reduced in order to maximize the interaction with the imine enthalpically. The structural comparison between TRIP/**3** and TiPSY/**3** revealed a sterical shield for the Hantzsch ester binding for TiPSY/**3**, which indicates a large reorganization penalty (Figure 7). In contrast, for TRIP/**3** almost no reorganization is required. Thus, the steric of the 3,3'-substituents can explain the large difference in the reactivity of TiPSY compared to the other structurally analogous CPAs.

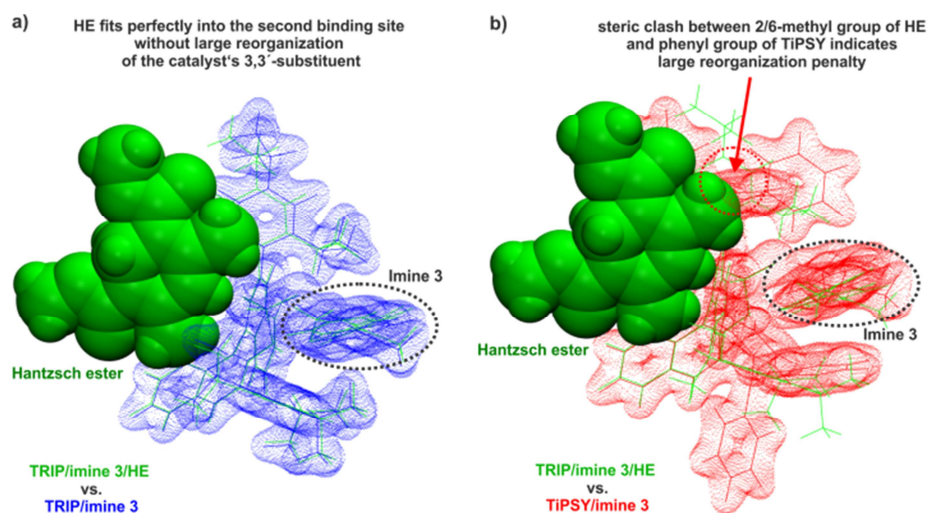


Figure 7. a) The comparison of the calculated structures of the binary (blue) and ternary (green) complex with TRIP and imine **3** shows that for the Hantzsch ester (HE) binding almost no reorganization is required. b) Whereas, the binary complex of TiPSY and imine **3** revealed a sterical shield for the Hantzsch ester. Thus, before the ternary complex formation a large reorganization is assumed.

The next step in the catalytic cycle, the hydride transfer (step **D**) is not accessible by NMR methods. Our calculations for TRIP indicated that the hydride transfer has a by far higher rate constant k_{red} than the isomerization k_{iso} (see SI) and can be neglected as the rate-determining step if the ternary complex is formed in a sufficient amount. However, as described above, the marginal ternary complex concentration decelerates the overall rate of the hydride transfer. Therefore, this step is coupled to the ternary complex

3 Internal Acidity Scale and Reactivity Evaluation

formation. This is in agreement with the experimentally observed 1st order dependence on the Hantzsch ester concentration for the non-isomerizable imine **14**.

To minimize the potential inhibition of the acidic catalyst by the product basic sites and its effect on the observed reaction rate (step **E**), we followed the initial rate kinetics approach during our investigations. In this way, product inhibition has a negligible contribution to the rate-determining step in the catalytic cycle. This is most probably valid throughout the course of the reaction. On the contrary, an increase in the reaction turnover with CPA has been reported for the transfer hydrogenation of *N*-methyl imines by protecting the formed highly basic amine. Thus, the *N*-methyl amine was proposed to inhibit the catalyst and leads therefore to a slowdown of the reaction.^[79] For our reaction using *N*-phenyl imines, the generated products are unlikely to significantly inhibit the catalytic cycle due to lower basicity of the aromatic amines as evidenced by the high yields. Nevertheless, the initial rate kinetics discussed here avoid the problem of potential product inhibition.

Table 2: All experimental data discussed above are summarized. Beside the relative, calculated external pKa values, all experimentally obtained parameters, like the internal acidity (obtained from ¹⁵N chemical shift and ¹J_{NH} coupling constant) for both *E*- and *Z*-complexes, the association constants *K*_a of the binary complexes as well as the isomerisation rate *k*_{iso} are given. For the sake of completeness also the AREA (Θ) values were added.^[31] The influence of all these parameters on the relative reaction rate was investigated. TiPSY does not follow this trends observed for the other catalysts TRIP, TRIM and TRIFP (visualized with grey bars).

	external acidity rel. pKa	internal acidity				<i>K</i> _a [M ⁻¹]	<i>k</i> _{iso} [10 ⁻³ s ⁻¹]	AREA(Θ)	relative reaction rate
		<i>E</i>		<i>Z</i>					
		¹ J _{NH} [Hz]	δ ¹⁵ N [ppm]	¹ J _{NH} [Hz]	δ ¹⁵ N [ppm]				
TRIP	0.85	82.2	206.6	81.0	209.1	219	1.36	51	47.6
TRIM	1.57	85.4	200.5	82.2	206.0	106	nd	61	28.5
TRIFP	0	86.0	196.4	85.1	204.4	656	0.45	62	18.6
TiPSY	6	83.7	203.6	80.0	211.3	200	0.57	29	1.0

direction of increasing H-bond → ← → ← → →

All of the experimental data discussed above are summarized in Table 2. Based on the results presented there, a previously established correlation of an increased acidity giving higher reactivity in chiral phosphoric acid-catalyzed reactions^[44] cannot be transferred to the asymmetric transfer hydrogenation of imines. However, a possible inverse relationship of the internal acidity for TRIP, TRIM and TRIFP with the reactivity could be observed, thus in our system, the less acidic catalysts give the fastest reactions (see Table 2). In contrast, TiPSY does not follow this trend. Despite having the strongest hydrogen bond, as well as a binary complex association constant *K*_a and an isomerization rate constant *k*_{iso}, comparable to the other catalysts, the observed

3 Internal Acidity Scale and Reactivity Evaluation

reactivity is by far the slowest. The only parameter deviating significantly from the other catalysts is the AREA (θ) value, which is extremely small. In addition, the blockage of the second binding site in TiPSY complexes may amplify the issue of the ternary complex formation inside the rate-determining zone (see discussion above and Figure 7). The experimental and theoretical studies on aromatic imines provided, show that the formation of the binary complex as well as product inhibition can be neglected as rate determining steps. Furthermore, the rate constant of hydride transfer (k_{red}) is by far higher than for the isomerization (k_{iso}). Finally, isomerization and ternary complex formation have to be decisive for the observed overall reaction rate. Thus, the comparison of isomerization rates, reaction rates and ternary complex formation of CPAs with different 3,3'-substituents shows that in a delicate equilibrium isomerization rates and ternary complex formation contribute to the rate-determining zone. Thus, the presented results suggest that within a similar acidic motif and similar sterics of the CPAs the reactivity is inverse correlated to the internal acidity. For CPAs with small AREA (θ) values the steric bulk seems to overrule the internal acidity and the reactivity is significantly decreased.

3.4. Conclusion

By means of NMR-spectroscopic studies, a hydrogen bond analysis of 32 CPA/imine complexes regarding ^1H and ^{15}N chemical shifts as well as $^1J_{\text{NH}}$ coupling constants was established. This allowed for the first time to implement an internal acidity scale of CPA/imine complexes as a direct experimental tool to probe a correlation between acidity and reactivity. All CPA/imine complexes form strong, charge-assisted hydrogen bonds. The analysis of the chemical shifts and the resulting hydrogen bond strengths of the four Brønsted acid catalysts TRIP, TiPSY, TRIM and TRIFP show two different acidity scales for *E*- and *Z*-imines complexes (*E*-imines: $\text{pK}_{\text{aTRIP}} > \text{pK}_{\text{aTiPSY}} > \text{pK}_{\text{aTRIM}} > \text{pK}_{\text{aTRIFP}}$; *Z*-imines: $\text{pK}_{\text{aTiPSY}} > \text{pK}_{\text{aTRIP}} > \text{pK}_{\text{aTRIM}} > \text{pK}_{\text{aTRIFP}}$). All the investigated imines showed the same trend. The internal acidity analysis by chemical shifts was corroborated by experimentally determined $^1J_{\text{NH}}$ coupling constants and theoretical calculations of the complexes. Our calculated external acidity scale in DCM ($\text{pK}_{\text{aTRIFP}} < \text{pK}_{\text{aTRIP}} < \text{pK}_{\text{aTRIM}} < \text{pK}_{\text{aTiPSY}}$) deviates from the experimental internal acidity scale. This shows that intermolecular interactions in CPA/imine complexes are essential to describe the acidic properties of these complexes correctly and either experimental data or calculations of the binary complexes have to be accounted for.

3 Internal Acidity Scale and Reactivity Evaluation

While the calculated external acidity scale does not exhibit any correlation with the reactivity of the transfer hydrogenation, the internal acidity at least of TRIP, TRIM and TRIFP shows an inverse correlation. Thus, the least acidic TRIP with the strongest hydrogen bond gives the highest reactivity. However, TiPSY does not follow this trend, demonstrating that for Brønsted acids with an identical acidic functional group, also other factors may contribute. Isomerization rates, reaction rates and ternary complex formation data of CPAs with different 3,3'-substituents show that a delicate balance between the isomerization and the ternary complex formation is potentially the rate-determining zone. The collected experimental data of TRIP, TRIM and TRIFP suggest that the lower the internal acidity, the higher the isomerization rates and the higher the reactivity in the transfer hydrogenation. This trend can be predicted by calculating internal acidities (*i.e.* $^1J_{\text{NH}}$ coupling constants), which match the experimental results best. However, for a small binding pocket the correlation with the internal acidities fails, *i.e.* for TiPSY, still a very strong hydrogen bond is formed, but the reactivity breaks down most probably due to sterical congestion at the active site for the second binding partner.

3 Internal Acidity Scale and Reactivity Evaluation

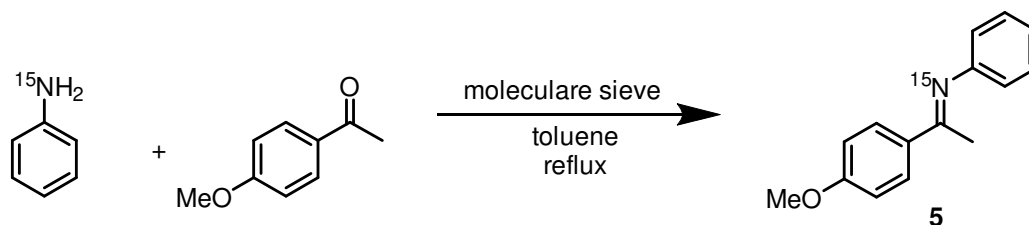
3.5. Supporting information

3.5.1. Synthesis of Imine Substrates

The imines were prepared according to a modified literature procedure.^[80–85] The toluene was used either in p.A. quality or was dried by refluxing over sodium. The ¹⁵N-enriched aniline for the presented syntheses below was purchased from Euriso-top GmbH and Sigma Aldrich. For the preparation of imines **10-13** see reference.^[80]

Exemplary procedure for (E)-1-(4-methoxyphenyl)-N-phenylethan-1-imine (98% ¹⁵N) 5

For the syntheses of the imines, the same procedure was used as in our previous publication.^[80]



Molecular sieves 4 Å (1.625 g) were weighed into a 25 ml Schlenk flask equipped with a reflux condenser and a stopper. The setup was connected to a vacuum line and was evacuated and dried with a heat gun. 4-Methoxyacetophenone (0.500 g, 3.33 mmol) and Aniline (98% ¹⁵N, 0.31 ml, 0.316 g, 3.35 mmol) were added to the Schlenk flask under argon atmosphere and were dissolved in 5 ml toluene. The stop cock was exchanged with a drying tube filled with CaCl₂ and the solution was heated to reflux overnight. The orange solution was filtered off from the molecular sieves and was concentrated under reduced pressure. The remaining solid was recrystallized from methanol. The product was obtained as yellow solid (0.303 g, 1.33 mmol, 40%) and predominantly as *E*-isomer (>99 % via ¹H-NMR analysis).

¹H-NMR (400.1 MHz, CD₂Cl₂) δ_H = 7.95 (m, 2H, Aryl-H), 7.35 (m, 2H, Aryl-H), 7.07 (m, 1H, Aryl-H), 6.96 (m, 2H, Aryl-H), 6.77 (m, 2H, Aryl-H), 3.86 (s, 3H, -OCH₃), 2.18 ppm (d, ³J_{HN} = 1.76 Hz, -CH₃)

3 Internal Acidity Scale and Reactivity Evaluation

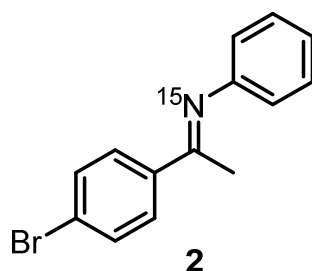
$^{13}\text{C-NMR}$ {1H} (100.6 MHz, CD_2Cl_2): $\delta_{\text{C}} = 164.5$ (d, $^1J_{\text{NC}} = 7.1$ Hz), 161.9, 152.5 (d, $^2J_{\text{NC}} = 1.7$ Hz), 132.5 (d, $^1J_{\text{NC}} = 8.4$ Hz), 129.3, 129.2 (d, $^3J_{\text{NC}} = 3.3$ Hz), 123.2, 119.9 (d, $^2J_{\text{NC}} = 2.3$ Hz), 113.9, 55.8, 17.2 ppm (d, $^2J_{\text{NC}} = 2.7$ Hz)

$^{15}\text{N-NMR}$ (40.5 MHz, CD_2Cl_2): $\delta_{\text{N}} = 325.5$ ppm

^1H - and ^{13}C -spectra were in accordance with the literature.^[86]

(E)-1-(4-bromophenyl)-N-phenylethan-1-imine (98 % ^{15}N) 2

For the syntheses of the imines, the same procedure was used as in our previous publication.^[80]



The reaction was carried out on 4.32 mmol scale.

The remaining yellow-orange residue was dissolved in 1 ml MeOH under gentle heating (water bath 60°C) and was stored in the fridge (~ 4°C). The crystallized product was sucked off over a Büchner funnel and was washed with ice-cold MeOH. Solvent residues were removed under reduced pressure. The product was obtained as almost yellow crystalline solid (0.438 g, 38 %) and predominantly as *E*-isomer (~ 99% via $^1\text{H-NMR}$ analysis).

$^1\text{H-NMR}$ (400.1 MHz, CD_2Cl_2) $\delta_{\text{H}} = 7.87$ (2H, m, Aryl-H), 7.59 (2H, m, Aryl-H), 7.36 (2H, m, Aryl-H), 7.09 (1H, m, Aryl-H), 6.77 (2H, m, Aryl-H), 2.20 ppm (3H, d, $^3J_{\text{NH}} = 1.8$ Hz, $-\text{CH}_3$)

$^{13}\text{C-NMR}$ {1H} (100.6 MHz, CD_2Cl_2): $\delta_{\text{C}} = 164.5$ (d, $^1J_{\text{CN}} = 7.2$ Hz), 151.9 ($^1J_{\text{CN}} = 1.5$ Hz), 138.9 (d, $^2J_{\text{CN}} = 8.6$ Hz), 131.8, 129.3, 129.2 (d, 3.3 Hz), 125.2, 123.6, 119.6 (2.3 Hz), 17.3 (d, $^2J_{\text{CN}} = 2.8$ Hz)

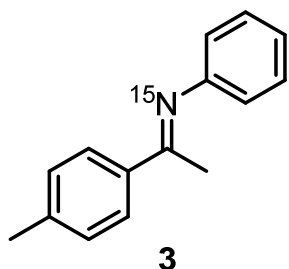
$^{15}\text{N-NMR}$ (40.5 MHz, CD_2Cl_2): $\delta_{\text{N}} = 333.4$ ppm

^1H - and ^{13}C -spectra were in accordance with the literature.^[87]

3 Internal Acidity Scale and Reactivity Evaluation

(*E*)-1-(4-methylphenyl)-*N*-phenylethan-1-imine (98% ¹⁵N) 3

For the syntheses of the imines, the same procedure was used as in our previous publication.^[80]



The reaction was carried out on 3.73 mmol scale.

The solidified residue was washed with cooled MeOH (~-35°C). After drying under reduced pressure over CaCl₂, the product was obtained as orange crystals (0.220 g, 1.05 mmol, 28 %) predominantly as *E*-isomer (>99 % via ¹H-NMR analysis). The product was used without further purification.

¹H-NMR (400.1 MHz, CD₂Cl₂) δ_H = 7.87 (m, 2H, Aryl-H), 7.34 (m, 2H, Aryl-H), 7.26 (m, 2H, Aryl-H), 7.07 (m, 1H, Aryl), 6.76 (m, 2H), 2.41 (s, 3H, -CH₃), 2.19 ppm (d, ³J_{NH} = 1.76 Hz, 3H, -CH₃)

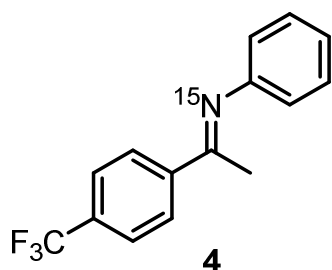
¹³C-NMR {1H} (100.6 MHz, CD₂Cl₂): δ_C = 165.3, 152.4, 141.2, 133.9, 129.5, 129.3, 127.5, 123.3, 119.7, 21.5, 17.4 ppm

¹⁵N-NMR (40.5 MHz, CD₂Cl₂): δ_N = 328.9 ppm

¹H- and ¹³C-spectra were in accordance with the literature.^[83]

(*E*)-*N*-phenyl-1-(4-(trifluoromethyl)phenyl)ethan-1-imine (98% ¹⁵N) 4

For the syntheses of the imines, the same procedure was used as in our previous publication.^[80]



The reaction was carried out on 1.59 mmol scale.

The obtained yellow solid was further dried in the desiccator over KOH. The product was obtained as yellow solid (0.306, 1.16 mmol, 72 %) predominantly as *E*-isomer (>99 % via ¹H-NMR analysis). The product was used without further purification.

¹H-NMR (400.1 MHz, CD₂Cl₂): δ_H = 8.11 (m, 2H, Aryl-H), 7.73 (m, 2H, Aryl-H), 7.38 (m, 2H, Aryl-H), 7.12 (m, 1H, Aryl-H), 6.80 (m, 2H, Aryl-H), 2.25 ppm (d, ³J_{NH} = 1.8 Hz, 3H, -CH₃)

3 Internal Acidity Scale and Reactivity Evaluation

¹³C-NMR {1H} (100.6 MHz, CD₂Cl₂): δ_C = 164.5, 152.0, 143.2, 132.1, 129.4, 128.0, 125.6, 124.6, 123.9, 119.5, 17.5 ppm

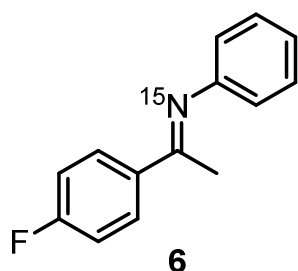
¹⁹F-NMR {1H} (376 MHz, CD₂Cl₂): δ_F = - 63.1 ppm

¹⁵N-NMR (60.8 MHz, CD₂Cl₂): δ_N = 338.2 ppm

¹H- and ¹³C-spectra were in accordance with the literature.^[83]

(E)-1-(4-fluorophenyl)-N-phenylethan-1-imine (98 % ¹⁵N) 6

For the syntheses of the imines, the same procedure was used as in our previous publication.^[80]



The reaction was carried out on 4.32 mmol scale.

The remaining yellow-orange residue was dissolved in 1 ml MeOH under gentle heating (water bath 60°C) and was stored in the fridge (~ 4°C). The crystallized product was washed with ice-cold MeOH.

Solvent residues were removed under reduced pressure. The product was obtained as almost colorless/slightly yellowish crystalline solid (0.248 g, 27 %) and predominantly as *E*-isomer (~ 99% via ¹H-NMR analysis).

¹H-NMR (400.1 MHz, CD₂Cl₂) δ_H = 8.00 (2H, m, Aryl-H), 7.35 (2H, m, Aryl-H), 7.14 (2H, m, Aryl-H), 7.09 (1H, m, Aryl-H), 6.77 (2H, m, Aryl-H), 2.20 ppm (3H, d, ³J_{NH} = 1.8 Hz, -CH₃)

¹³C-NMR {1H} (100.6 MHz, CD₂Cl₂): δ_C = 164.6, 164.3, 152.1, 136.2, 129.7, 129.3, 123.5, 119.6, 115.5, 17.4 ppm

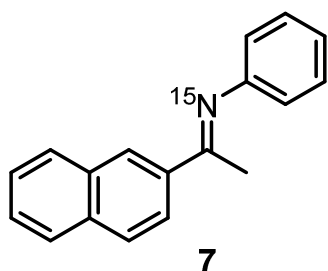
¹⁵N-NMR (40.54 MHz, CD₂Cl₂): δ_N = 330.9 ppm

¹H- and ¹³C-spectra were in accordance with the literature.^[86]

3 Internal Acidity Scale and Reactivity Evaluation

(E)-1-(naphthalen-2-yl)-N-phenylethan-1-imine (98% ¹⁵N) 7

For the syntheses of the imines, the same procedure was used as in our previous publication.^[80]



The reaction was carried out on 4.33 mmol scale.

The intensive orange solution was cooled down and was quickly filtered off from the molecular sieves. The product started crystallizing at r.t. Crystallization was completed in an ice bath for 2 h. The yellow crystals were sucked off with a Büchner funnel and were washed with ice-cold toluene. The liquid residue was concentrated under reduced pressure and the resulting solid was suspended in 2.5 ml methanol and was shortly heated at 60°C in a water bath. After cooling down, the yellow solid was sucked off with a Büchner funnel and washed with ice cold methanol. Solvent residues were removed under reduced pressure. The product was obtained as yellow solid (0.489 g, 1.99 mmol, 45 % yield) predominantly as *E*-isomer (>99 % via ¹H-NMR analysis).

¹H-NMR (400.1 MHz, CD₂Cl₂) δ_H = 8.37 (s, 1H, Aryl-H), 8.24 (dd, ³J_{HN} = 8,68 Hz, ⁴J = 1.64 Hz, 1H, Aryl-H) 7.99 – 7.94 (m, 1H, Aryl-H), 7.94 – 7.87 (m, 2H, Aryl-H), 7.60 – 7.52 (m, 2H, Aryl-H), 7.42 – 7.35 (m, 2H, Aryl-H), 7.11 (m, 1H, Aryl-H), 6.83 (m, 2H, Aryl-H), 2.34 ppm (d, ³J_{HN} = 1.76 Hz, 3H, -CH₃)

¹³C-NMR {1H} (100.6 MHz, CD₂Cl₂): δ_C = 165.3, 152.3, 137.3, 134.8, 133.3, 129.3, 129.2, 128.2, 128.1, 128.0, 127.6, 126.7, 124.6, 123.5, 119.7, 17.4 ppm

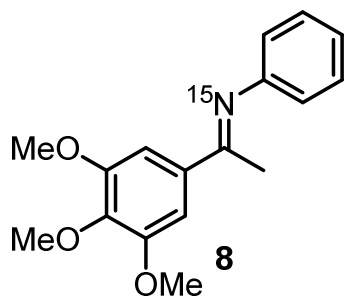
¹⁵N-NMR (40.5 MHz, CD₂Cl₂): δ_N = 333.5 ppm

¹H- and ¹³C-spectra were in accordance with the literature.^[86]

3 Internal Acidity Scale and Reactivity Evaluation

(E)-N-phenyl-1-(3',4',5'-(trimethoxy)phenyl)ethan-1-imine (98% ¹⁵N) 8

For the syntheses of the imines, the same procedure was used than in our previous publication.^[80]



To the mixture of 3,4,5-Trimethoxyacetophenone (0.486 g, 2.30 mmol) and Aniline (98% ¹⁵N, 0.22 ml, 2.30 mmol) additionally sodium bicarbonate (1g, 11.9 mmol) was added. The reaction was carried out in 2.30 mmol scale.

The solidified residue was washed with cooled MeOH (~-35°C). After drying under reduced pressure, the product was obtained as colourless solid (0.140 g, 0.49 mmol, 21 %) predominantly as *E*-isomer (>99 % via ¹H-NMR analysis). The product was used without further purification.

¹H-NMR (400.1 MHz, CD₂Cl₂) δ_H = 7.35 (m, 2H, Aryl-H), 7.24 (s, 2H, Aryl-H), 7.08 (m, 1H, Aryl-H), 6.76 (m, 2H, Aryl-H), 3.91 (s, 6H, OCH₃), 3.83 (s, 3H, -OCH₃), 2.19 ppm (d, ³J_{HN} = 1.75 Hz, 3H, -CH₃)

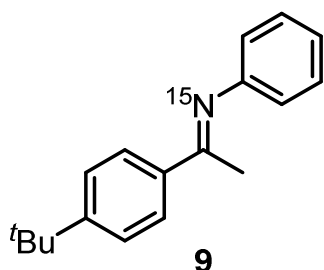
¹³C-NMR {1H} (100.6 MHz, CD₂Cl₂): δ_C = 164.9, 153.8, 152.3, 140.8, 135.5, 129.7, 123.8, 120.0, 105.4, 61.4, 56.9, 17.8

¹⁵N-NMR (40.5 MHz, CD₂Cl₂): δ_N = 329.7 ppm

3 Internal Acidity Scale and Reactivity Evaluation

(E)-N-phenyl-1-(4-(tert-butyl)phenyl)ethan-1-imine (98% ¹⁵N) 9

For the syntheses of the imines, the same procedure was used than in our previous publication.^[80]



The reaction was carried out in 2.84 mmol scale.

The solidified residue was recrystallized in 0,4 ml ethanol and washed with cooled MeOH (~-35°C). After drying under reduced pressure, the product was obtained as colorless crystals (0.160 g, 0.63 mmol, 22 %) predominantly as *E*-isomer (>99 % via ¹H-NMR analysis). The product was used without further purification.

¹H-NMR (400.1 MHz, CD₂Cl₂) δ_H = 7.91 (m, 2H, Aryl-H), 7.48 (m, 2H, Aryl-H), 7.35 (m, 2H, Aryl-H), 7.07 (m, 1H, Aryl-H), 6.76 (m, 2H, Aryl-H), 2.20 (d, ³J_{HN} = 1.83 Hz, 3H, -CH₃), 1.34 (s, 9H, *tert*-Butyl)

¹³C-NMR {1H} (100.6 MHz, CD₂Cl₂): δ_C = 165.9, 154.9, 153.1, 137.9, 129.6, 128.0, 126.3, 124.0, 120.4, 35.7, 32.0, 18.1 ppm

¹⁵N-NMR (40.5 MHz, CD₂Cl₂): δ_N = 329.4 ppm

¹H- and ¹³C-spectra were in accordance with the literature.^[83]

3.5.2. Sample preparation of binary complexes in CD₂Cl₂

Deuterated solvents were purchased from Deutero or Sigma Aldrich. When anhydrous solvents were required, CD₂Cl₂ was freshly distilled over CaH₂ under argon atmosphere. The catalysts were purchased from Sigma Aldrich or synthesized from the corresponding binaphthols according to the procedure of Klusmann et al.^[88]

The catalyst was dried for 30 min at 150°C under reduced pressure. Ketimine and phosphoric acid catalyst were directly weighed into a 5 mm NMR tube under an inert argon atmosphere. CD₂Cl₂ (0.6 ml) and 1.0 ml of tetramethylsilane atmosphere were added to the tube. The sample was stored in an -80°C freezer. For all samples a 1:1 ratio of catalyst/ketimine was used. Even after careful sample preparation, partial hydrolysis of the imine could not be completely prevented. Therefore the imine/CPA-ratios are slightly different from 1:1. A concentration of 25 mmol or 50 mmol/L was used for all samples, depending on solubility at low temperatures.

3 Internal Acidity Scale and Reactivity Evaluation

3.5.3. Spectrometer data

NMR experiments were performed on Bruker Avance III HD 400 MHz spectrometer, equipped with 5 mm BBO BB-1H/D probe head with Z-Gradients and a Bruker Avance III HD 600 MHz spectrometer, equipped with a 5 mm TBI $^1\text{H}/^{31}\text{P}$ and a 5 mm CPPBBO BB- $^1\text{H}/^{19}\text{F}$. Triple resonance experiments were performed on the TBI probe head. The temperature was controlled in the VT-experiments by BVT 3000 and BVTE 3900. For NMR measurements employing standard NMR solvents, 5 mm NMR tubes were used, if not otherwise noted. NMR data were processed, evaluated and plotted with TopSpin 3.2 software. Further plotting of the spectra was performed with Corel Draw X7, X8 or 2017 software. ^1H and ^{13}C chemical shifts were referenced to TMS or the respective solvent signals. The heteronuclear ^{15}N and ^{19}F spectra were referenced, employing $\nu(X) = \nu(\text{TMS}) \times \Xi_{\text{reference}} / 100 \%$ according to Harris *et al.*^[89] The following frequency ratios and reference compounds were used: $\Xi(^{15}\text{N}) = 10.132912$ (lq. NH_3) and $\Xi(^{19}\text{F}) = 94.094011$ (CCl_3F)

Pulse programs

All pulse programs used are standard Bruker NMR pulse programs.

Acquisition Parameters

^1H -NMR: Pulse program: zg; Relaxation delay = 2 – 3 s, Acquisition time = 2.48 s, SW = 22.0 ppm, TD = 64k, NS = 8 – 64; zg30; Relaxation delay = 2 s, Acquisition time = 2.48 s, SW = 22.0 ppm, TD = 64k, NS = 8 – 64;

^{15}N -NMR: Pulse program: zg; Relaxation delay = 10.00 s, Acquisition time = 0.54 s, SW = 502.8 ppm, TD = 32k, NS = 256 – 2048;

^{13}C -NMR: Pulse program: zgpg30; Relaxation delay = 2.00 s, Acquisition time = 0.80 s, SW = 270.0 ppm, TD = 64k, NS = 1k – 2k;

^{19}F -NMR: Pulse program: zg30; Relaxation delay = 2 – 3 s, Acquisition time = 11.60 s, SW = 10.0 ppm, TD = 128k, NS = 8 – 64;

3 Internal Acidity Scale and Reactivity Evaluation

3.5.4. Steiner-Limbach correlation

Theory

All investigations regarding the hydrogen bond analysis were done in accordance with our previous work on TRIP/imine complexes.^[80]

The ¹H and ¹⁵N chemical shifts of an OHN hydrogen bond can be correlated by multiplication of the constants $\delta(\underline{OH})^\circ$, $\delta(\underline{HN})^\circ$, $\delta(\underline{HN})^\circ$ and $\delta(\underline{N})^\circ$ with the defined valence bond orders p_{OH}^H (equation S1 and S2). $\delta(\underline{OH})^\circ$, $\delta(\underline{HN})^\circ$, $\delta(\underline{HN})^\circ$ and $\delta(\underline{N})^\circ$ reflect the ¹H respectively ¹⁵N chemical shifts of the isolated diatomic units.^[58,90]

$$\delta(OHN) = \delta(OH)^\circ p_{OH}^H + \delta(HN)^\circ p_{HN}^H + 4 \delta(OHN)^* p_{OH}^H p_{HN}^H \quad (S1)$$

$$\delta(OHN)_{ref} = \delta(N)^\circ p_{OH}^H + \delta(HN)^\circ p_{HN}^H + 4 \delta(OHN)^* p_{OH}^H p_{HN}^H \quad (S2)$$

$\delta(\underline{HN})^\circ$ and $\delta(\underline{HN})^\circ$ are the ¹⁵N, respectively ¹H chemical shift of the completely protonated imine and are experimentally accessible. $\delta(\underline{OH})^\circ$ is the chemical shift of the free phosphoric acid (CPA). Because of dimerization and remaining water, $\delta(\underline{OH})^\circ$ has to be fitted. $\delta(\underline{N})^\circ$ takes into account the referencing of the ¹⁵N chemical shift (see chapter 3.2). To consider the asymmetry of the OHN hydrogen bond compared to symmetric XHX hydrogen bond, the correction factors $\delta(OHN)^*$ and $\delta(OHN)^*$ are used (for values see table S1). These parameters were slightly modified compared to our previous publication.^[80]

Table S 1: NMR parameters used for the hydrogen-bond correlations.

systems	$\delta(\underline{N})^\circ$ [ppm]	$\delta(\underline{HN})^\circ$ [ppm]	$\delta(OHN)^*$ [ppm]	$\delta(\underline{OH})^\circ$ [ppm]	$\delta(\underline{HN})^\circ$ [ppm]	$\delta(OHN)^*$ [ppm]
pyridine–HA ^[90] in CDF ₃ /CDF ₂ Cl	0	126	-4	2	7	20
collidine–HA ^[90] in CDF ₃ /CDF ₂ Cl	0	126	-8	2	7	20
solid collidine–HA ^[61]	0	126	0	-3	7	20
imine/TRIP ^[80]	0	-170	-6	2	6	16
imine/TiPSY, imine/TRIFP and imine/TRIM	0	-151.6	-4.89	1.04	12.33	14.2

3 Internal Acidity Scale and Reactivity Evaluation

To consider the zero anharmonic vibrations of the hydrogen atom within the hydrogen bond Limbach and Denisov proposed the correction factors for the valence bond orders p_{OH}^H and p_{NH}^H (equation S3 and S4).^[58,90,91] For explanation and details of these terms see reference.^[91]

$$p_{OH}^H = p_{OH} - c^H (p_{OH} p_{HN})^f (p_{OH} - p_{HN}) - d^H (p_{OH} p_{HN})^g \quad (S3)$$

$$p_{HN}^H = p_{HN} + c^H (p_{OH} p_{HN})^f (p_{OH} - p_{HN}) - d^H (p_{OH} p_{HN})^g \quad (S4)$$

After a mathematical fitting the parameters d^H , c^H , f and g were slightly modified in comparison to our previous work (table S2).^[80,90]

Table S 2: Correction factors used for the hydrogen-bond correlations.

systems	f	g	c^H	d^H
weak and medium strong OHN bonds ^[90]	0	0	0	0
pyridine/HA and collidine/HA ^[90] in CDF ₃ /CDF ₂ Cl	5	2	360	0.7
pyridine/HA and collidine/HA solid ^[61]	5	2	360	0.7
imine/TRIP ^[80]	8	2	360	0.3
imine/TiPSY, imine/TRIFP and imine/TRIM	7.3	1.36	349.9	0.33

In accordance with Limbach and Denisov, the measured NMR data of the hydrogen bonds were correlated with their geometries by using the concept of valence bond orders of Pauling.^[57,58,90] The valence bond orders for the hydrogen bonds of the proton and the heavy atoms within an OHN hydrogen bond are given by p_{OH}^H (equation S5) and p_{NH}^H (equation S6). Both values are dependent on the atom distances (r_{OH} and r_{NH}).

$$p_{OH}^H = \exp\left\{\frac{-(r_{OH}-r_{OH}^{\circ})}{b_{OH}}\right\} \quad (S5)$$

3 Internal Acidity Scale and Reactivity Evaluation

$$p_{NH}^H = \exp\left\{\frac{-(r_{NH}-r_{NH}^{\circ})}{b_{NH}}\right\} \quad (S6)$$

$$p_{OH}^H + p_{NH}^H = 1 \quad (S7)$$

Referencing of the ^{15}N chemical shift

As proposed in the literature, the ^{15}N chemical shifts were referenced to the chemical shift of the non-hydrogen bonded imine **11** ($\delta^{15}\text{N} = 340.8$ ppm, 300 K, CD_2Cl_2).^[58] Thus, the ^{15}N chemical shifts reflect the deviation of the complexed imines from their neutral form ($\delta^{15}\text{N} = \sim 330$ ppm) and range from -90 to -150 ppm. Because of this correction $\delta(\underline{\text{N}})^{\circ}$ can be set to 0.

Steiner-Limbach correlation curve: experimental ^1H and ^{15}N chemical shifts

Table S 3: NMR parameters ($\delta^1\text{H}$ and $\delta^{15}\text{N}$ chemical shift as well as $^1J_{\text{NH}}$) of $\text{HBF}_4/\text{imine}$, TRIP/imine , carboxylic acids and phenol/imine complexes in CD_2Cl_2 . All values are obtained from literature.^[80]

Complex	$\delta^1\text{H}$ [ppm]	$\delta^{15}\text{N}$ [ppm]	$^1J_{\text{NH}}$ [Hz]	Solvent	T [K]	Ref.
$\text{HBF}_4/3E$	12.35	189.4	92.3	CD_2Cl_2	180	TMS
$\text{HBF}_4/3Z$	12.48	193.4	91.9	CD_2Cl_2	180	TMS
$\text{HBF}_4/5E$	12.23	182.8	92.5	CD_2Cl_2	180	TMS
$\text{HBF}_4/5Z$	12.26	188.2	92.6	CD_2Cl_2	180	TMS
R-TRIP/2E	17.68	224.3	75.4	CD_2Cl_2	180	TMS
R-TRIP/2Z	17.68	221.1	n.d.	CD_2Cl_2	180	TMS
R-TRIP/3E	17.07	216.0	79.2	CD_2Cl_2	180	CHDCl_2
R-TRIP/3Z	17.11	215.0	78.4	CD_2Cl_2	180	CHDCl_2
R-TRIP/4E	18.20	235.1	68.7	CD_2Cl_2	180	TMS
R-TRIP/4Z	18.20	228.0	74.8 ^[a]	CD_2Cl_2	180	TMS
R-TRIP/5E	16.47	206.6	82.2	CD_2Cl_2	180	TMS
R-TRIP/5Z	16.75	209.1	81.0	CD_2Cl_2	180	TMS
R-TRIP/6E	17.42	220.6	77.3	CD_2Cl_2	180	TMS
R-TRIP/6Z	17.42	217.9	n.d.	CD_2Cl_2	180	TMS
R-TRIP/10E	18.42	243.3	67.7	CD_2Cl_2	180	TMS
R-TRIP/10Z1	18.18	228.9	74.3	CD_2Cl_2	180	TMS
R-TRIP/10Z2	18.13	228.7	75.2	CD_2Cl_2	180	TMS
R-TRIP/11E	17.70	268.1	n.d.	CD_2Cl_2	180	TMS
R-TRIP/11E	17.93	264.1	41.7	CD_2Cl_2	170	TMS
R-TRIP/11Z	18.85	240.6	60.6	CD_2Cl_2	180	TMS

3 Internal Acidity Scale and Reactivity Evaluation

R-TRIP/ 12	17.35	225.5	77.0	CD ₂ Cl ₂	200	TMS
R-TRIP/ 13E	17.31	223.6	78.1	CD ₂ Cl ₂	180	TMS
R-TRIP/ 13Z	17.07	221.7	79.3	CD ₂ Cl ₂	180	TMS
4-NO ₂ -Phenol/ 3	13.43	299.3	n.d.	CDCl ₂ F ^[b]	130	TMS
4-Cl-Phenol / 5	11.81	299.7	n.d.	CDCl ₂ F ^[b]	130	TMS
3,5-Cl-Phenol/ 5	12.25	297.1	n.d.	CDCl ₂ F ^[b]	130	TMS
3-CF ₃ -Phenol/ 5	11.96	299.0	n.d.	CDCl ₂ F ^[b]	130	TMS
Acetic Acid/ 5	14.60	294.3	n.d.	CDCl ₂ F ^[b]	130	TMS
TMA/ 5	14.34	295.8	n.d.	CDCl ₂ F ^[b]	130	TMS

^[a]derived from HN-HMBC ^[b] Freonic mixture; CDCl₂F/CDClF₂ ratio slightly varies between samples. For sample preparation, see reference.^[80]

3 Internal Acidity Scale and Reactivity Evaluation

Table S 4: NMR parameters ($\delta^1\text{H}$ and $\delta^{15}\text{N}$ chemical shift as well as $^1J_{\text{NH}}$) of TRIFP/imine, TiPSY/imine and TRIM/imine complexes in CD_2Cl_2 .

Complex	$\delta^1\text{H}$ [ppm]	$\delta^{15}\text{N}$ [ppm]	$^1J_{\text{NH}}$ [Hz]	Solvent	T [K]	Ref.
R-TRIFP/2E	16.49	210.6	82.8	CD_2Cl_2	170	TMS
R-TRIFP/2Z	16.96	215.2	81.1	CD_2Cl_2	170	TMS
R-TRIFP/3E	15.95	204.2	85.1	CD_2Cl_2	170	TMS
R-TRIFP/3Z	16.50	209.9	82.7	CD_2Cl_2	170	TMS
R-TRIFP/4E	17.09	218.2	80.8	CD_2Cl_2	170	TMS
R-TRIFP/4Z	17.39	220.4	80.5	CD_2Cl_2	170	TMS
R-TRIFP/5E	15.39	196.4	86.0	CD_2Cl_2	170	TMS
R-TRIFP/5Z	16.11	204.4	85.1	CD_2Cl_2	170	TMS
R-TRIFP/6E	16.18	207.1	83.0	CD_2Cl_2	170	TMS
R-TRIFP/6Z	16.79	213.1	82.3	CD_2Cl_2	170	TMS
R-TIPSY/2E*	16.79	219.6	77.3	CD_2Cl_2	180	TMS
R-TIPSY/2Z*	17.16	222.7	73.9	CD_2Cl_2	180	TMS
R-TIPSY/3E	16.12	211.3	81.2	CD_2Cl_2	180	TMS
R-TIPSY/3Z	16.64	216.6	78.1	CD_2Cl_2	180	TMS
R-TIPSY/4E	17.32	228.3	73.1	CD_2Cl_2	180	TMS
R-TIPSY/4Z	17.56	228.3	71.8	CD_2Cl_2	180	TMS
R-TIPSY/5E	15.53	203.6	83.7	CD_2Cl_2	180	TMS
R-TIPSY/5Z	16.24	211.3	80.0	CD_2Cl_2	180	TMS
R-TIPSY/6E	16.50	216.3	79.2	CD_2Cl_2	180	TMS
R-TIPSY/6Z	17.00	220.6	76.0	CD_2Cl_2	180	TMS
R-TIPSY/7E	16.30	212.0	81.4	CD_2Cl_2	180	TMS
R-TIPSY/7Z	16.90	218.8	77.2	CD_2Cl_2	180	TMS
R-TIPSY/8E	15.78	207.8	83.5	CD_2Cl_2	180	TMS
R-TIPSY/8Z	16.74	218.3	77.0	CD_2Cl_2	180	TMS
R-TIPSY/9E	16.13	212.0	81.7	CD_2Cl_2	180	TMS
R-TIPSY/9Z	16.60	218.8	77.7	CD_2Cl_2	180	TMS
R-TRIM/3E	16.26	208.0	83.9	CD_2Cl_2	180	TMS
R-TRIM/3Z	16.72	211.5	80.9	CD_2Cl_2	180	TMS
R-TRIM/4E	17.51	224.6	77.3	CD_2Cl_2	180	TMS
R-TRIM/4Z	17.76	224.1	76.0	CD_2Cl_2	180	TMS
R-TRIM/5E	15.80	200.5	85.4	CD_2Cl_2	180	TMS
R-TRIM/5Z	16.31	206.0	82.2	CD_2Cl_2	180	TMS

*this complex showed precipitation inside the NMR tube

3 Internal Acidity Scale and Reactivity Evaluation

Plot of $^1J_{\text{HN}}$ against δ_{OHN}

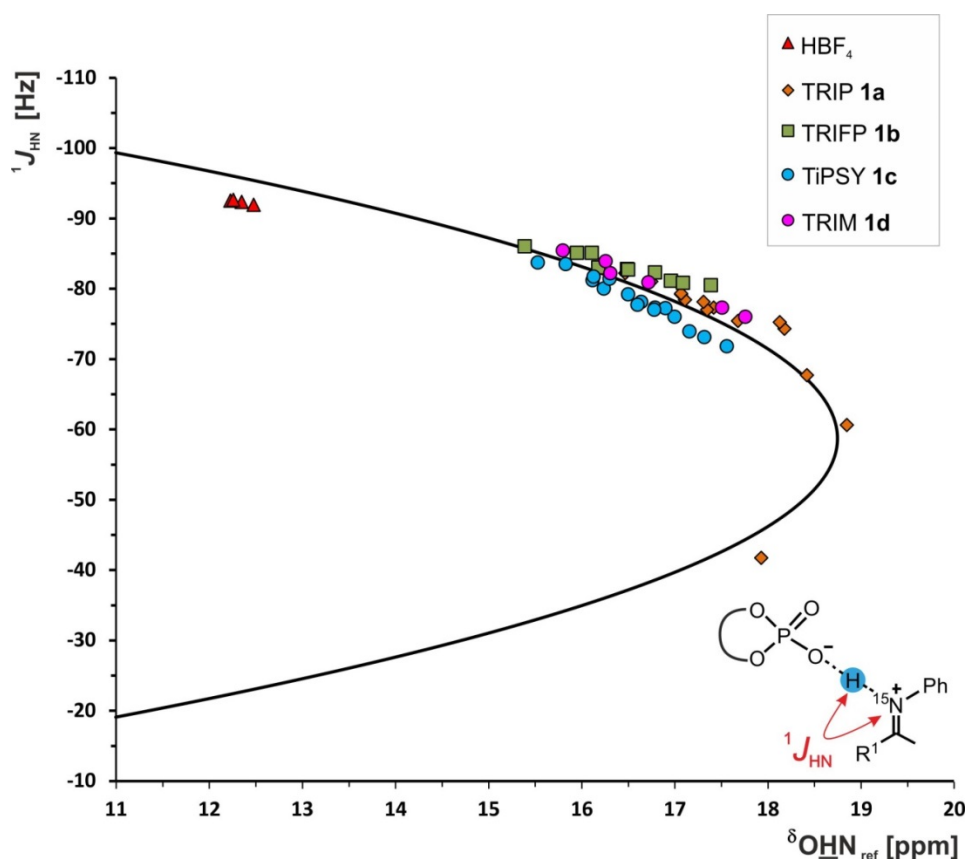


Figure S 1: Plot of $^1J_{\text{HN}}$ values against $\delta(\text{OHN})$. Experimental $\delta(\text{OHN})/^1J_{\text{HN}}$ pair values derived from TiPSY/imine complexes (blue), TRIFP/imine complexes (green), TRIM/imine (pink), TRIP/imine complexes^[80] (orange) and HBF_4 /imine^[80] (red).

Measurements of scalar couplings $^1J_{\text{NH}}$ in CPA/imine complexes were also performed. Also, the ^1H chemical shift and scalar coupling are related to one another according to the following equation S10:^[58,90]

$$^1J(\text{OHN}) = ^1J(\text{HN})^{\circ} p_{\text{HN}}^{\text{H}} - 8^1J(\text{OHN})^* (p_{\text{OH}}^{\text{H}})^2 p_{\text{HN}}^{\text{H}} \quad (\text{S10})$$

Three clusters appeared corresponding to each of the four investigated catalysts. The complexes formed with TRIP have overall higher ^1H chemical shift values (~16.5 ppm to ~18.5 ppm) compared to the complexes formed with TiPSY, TRIM, and TRIFP. This indicates the formation of a stronger hydrogen bond. Differences in ^1H chemical shifts between the other three catalysts are smaller. Still, higher ^1H shifts values were found for complexes involving TiPSY and TRIM compared to the TRIFP/imine-complexes.

3 Internal Acidity Scale and Reactivity Evaluation

On the other hand, the separation between TiPSY, TRIM and TRIFP clusters is mainly due to the $^1J_{\text{NH}}$ values (for values see table S3 and S4). Consistently higher $^1J_{\text{NH}}$ values (smaller in absolute values) were obtained with TiPSY complexes followed by TRIM and TRIFP. Since the focus of the curve (right side of the plot) corresponds to the shorter hydrogen bonds, complexes formed with TiPSY are overall slightly stronger than complexes formed with TRIM and TRIFP.

Plot of $^1J_{\text{HN}}$ against δ_{OHN}

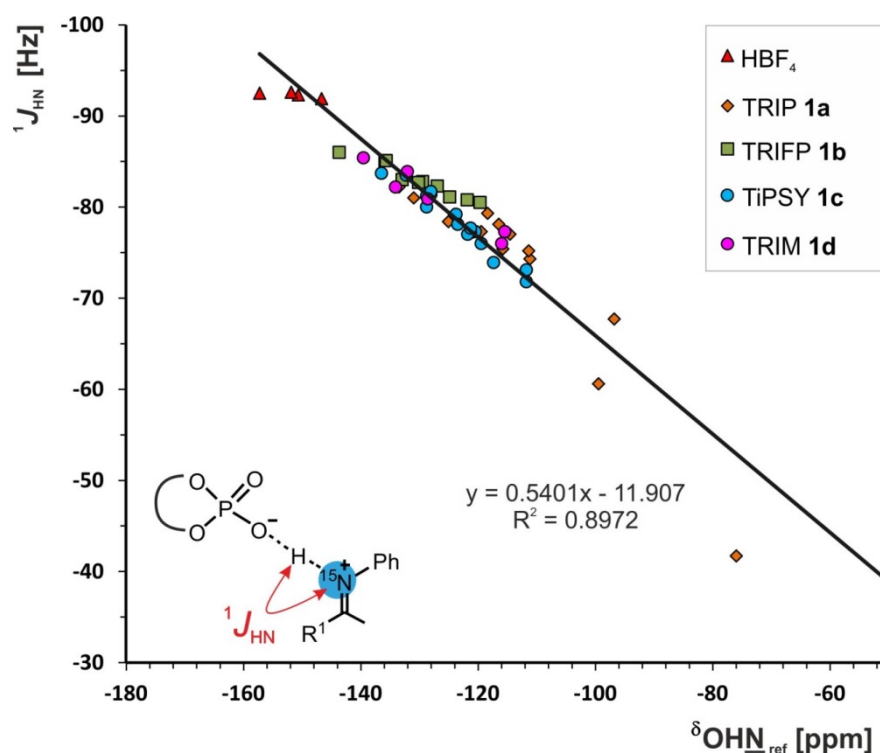


Figure S 2: Plot of $^1J_{\text{HN}}$ values against $\delta(\text{OHN})$. Experimental $\delta(\text{OHN})/{}^1J_{\text{HN}}$ pairs derived from TiPSY/imine complexes (blue), TRIFP/imine complexes (green), TRIM/imine (pink), TRIP/imine complexes^[80] (orange) and HBF₄/imine^[80] (red). $\delta(\text{OHN})$ was referenced to **11** (340 ppm, 300K).

3 Internal Acidity Scale and Reactivity Evaluation

3.5.5. Comparison of the calculated and experimental $^1\text{H} J_{\text{NH}}$

Table S 5: Experimental and calculated $^1\text{H} J_{\text{NH}}$ coupling constants for all catalysts with imines **3**, **4** and **5** are shown. The experimental values are obtained in CD_2Cl_2 at 180K.

catalyst	imine	$^1\text{H} J_{\text{NH}}$ [Hz]	$^1\text{H} J_{\text{NH}}$ [Hz]
		calc	exp
TRIP	3E	-79.87	79.2
	3Z	-77.24	78.4
	4E	-77.35	68.7
	4Z	-75.04	74.8
	5E	-82.03	82.2
	5Z	-79.42	81.0
TRIFP	3E	-81.76	85.1
	3Z	-82.08	82.7
	4E	-79.65	80.8
	4Z	-80.80	80.5
	5E	-82.86	86.0
	5Z	-83.56	85.1
TIPSY	3E	-80.42	81.2
	3Z	-78.59	78.1
	4E	-76.41	73.1
	4Z	-76.00	71.8
	5E	-81.84	83.7
	5Z	-80.49	80.0
TRIM	3E	-81.65	83.9
	3Z	-78.74	80.9
	4E	-78.82	77.3
	4Z	-76.13	76.0
	5E	-83.63	85.4
	5Z	-80.25	82.2

3 Internal Acidity Scale and Reactivity Evaluation

3.5.6. Calculation of the external pKa values

An experimental acidity scale with pK_a values of different Brønsted acid catalysts, including TRIP and TRIFP was published by O'Donoghue in 2011.^[60] To our knowledge, there is no such scale including the four catalysts TRIP, TRIFP, TRIM and TiPSY. Therefore, relative pK_a values in DCM of TRIP, TRIFP, TRIM and TiPSY for an external acidity scale were calculated at DG₁₈₀ SCS-MP2/CBS//TPSS-D3/def2-SVP level of theory using equation S11 and S12. For the computational data see appendix (DVD).

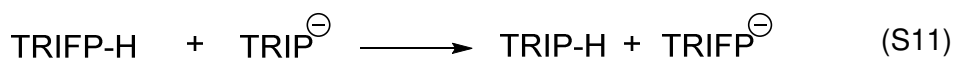


Table S 6: Calculated relative (in DCM at 180K) and experimental (in DMSO at 25°C)^[60] pK_a values of the CPAs.

	pK _a _{calc}	pK _a _{exp}
TRIFP	0	0
TRIP	+0.85	+1.59
TiPSY	+6.00	n.a.
TRIM	+1.57	n.a.

The calculations show the lowest pK_a value for TRIFP followed by TRIP, TRIM and TiPSY. The trend of the external acidity (pK_a_{TRIFP} < pK_a_{TRIP} < pK_a_{TRIM} < pK_a_{TiPSY}) predicted in the calculations does not correlate with the internal acidity scale obtained from the Steiner-Limbach analysis (*E*-imines: pK_a_{TRIFP} < pK_a_{TRIM} < pK_a_{TiPSY} < pK_a_{TRIP}; *Z*-imines: pK_a_{TRIFP} < pK_a_{TRIM} < pK_a_{TRIP} < pK_a_{TiPSY}). This demonstrates that other interactions (dispersion, steric, and electrostatic) significantly contribute in the internal scale.

3 Internal Acidity Scale and Reactivity Evaluation

3.5.7. Reaction kinetics of the transfer hydrogenation

Procedure for the in-situ kinetics

The reactions were performed with a 0.1 molar solution of imine **3** or **5** with 1.4 equivalents of diethyl 1,4-dihydro-2,6-dimethyl-3,5-pyridinedicarboxylate and 1 mol% of catalysts (TRIFP, TRIM and TiPSY) at 313.15 K in 0.5 ml deuterated dichloromethane. Due to solubility reasons, the reaction with TRIM was done in a 0.065 molar solution of **3** with 1.4 equivalents of diethyl 1,4-dihydro-2,6-dimethyl-3,5-pyridinedicarboxylate and 1 mol% of catalysts at 313.15 K in 0.5 ml deuterated dichloromethane. The imines were prepared as described in the experimental section 1.2. Both catalysts and Hantzsch ester were purchased from Sigma Aldrich. To compare the intensities of the spectra, the intensity of the alpha-methyl group of the imine in the first spectrum was used to calibrate the intensities of the alpha-methyl groups of the products. For this reaction in toluene higher yields and enantiomeric excesses are reported. Since structure determination^[41] and hydrogen bond analysis were done in dichloromethane, this solvent was also used for the reaction kinetics. Additionally, the signals in dichloromethane are better separated and enable therefore a more exact integration.

The fastest reaction is observed with TRIP, followed by TRIM and TRIFP. Catalyst TiPSY shows only a slow product formation.

Procedure for the ex-situ kinetics

A Schlenk tube with an attached septum was dried at 350 °C for 5 min under reduced pressure and then cooled down to room temperature. Imine **5** (73.7 mg, 327 µmol, 1.0 eq.) and Hantzsch Ester (116.0 mg, 457.8 µmol, 1.4 eq.) were weighed into the tube. The tube was evacuated and flushed with argon three times. A standard stock solution of 1,3,5-trimethoxybenzene (54 mM) in anhydrous toluene was prepared and 3 mL of the standard-stock solution were added to the tube under argon flow. The setup was placed into a metal-heating block and preheated to 35 °C. A catalyst stock solution was prepared by dissolving the catalyst (2.9 mM) in anhydrous toluene. To start the reaction, the catalyst stock solution (1.0 mL, 0.009 eq catalyst) was added to the reaction mixture. After 1, 5, 10, 15, 20, 25, 30, 45 and 60 min, samples of the reaction mixture (≈ 0.1 mL) were taken via a septum and quenched by adding to a solution of n-hexane (2.0 mL) and NEt₃ (10 µL, 7.3 µg, 0.072 mmol, 100 eq. based on the catalyst). The mixture was filtered through a syringe filter and analyzed

3 Internal Acidity Scale and Reactivity Evaluation

by CSP-HPLC. It was shown that the addition of NEt_3 quenches the reaction and that the standard does not interfere with the reaction.

HPLC conditions: CSP-HPLC, CHIRAPACK IC column (4.6mm x 250 mmL, particle size: 5 μm), eluent n-hexane/*i*-propanol 99/1, flowrate 0.9mL/min, column compartment temperature 20°C, $\lambda = 220$ nm. retention times: toluene/ NEt_3 : $\tau_1 = 3.73$ min; major (*R*)-amine: $\tau_2 = 10.1$ min; minor (*S*)-amine: $\tau_3 = 11.1$ min; 1,3,5-trimethoxybenzene: $\tau_4 = 15.4$ min; imine **5**: $\tau_5 = 24.9$ min; HE-pyridin: $\tau_6 = 42.8$ min;

3 Internal Acidity Scale and Reactivity Evaluation

Kinetics of the transfer hydrogenation with imine 5

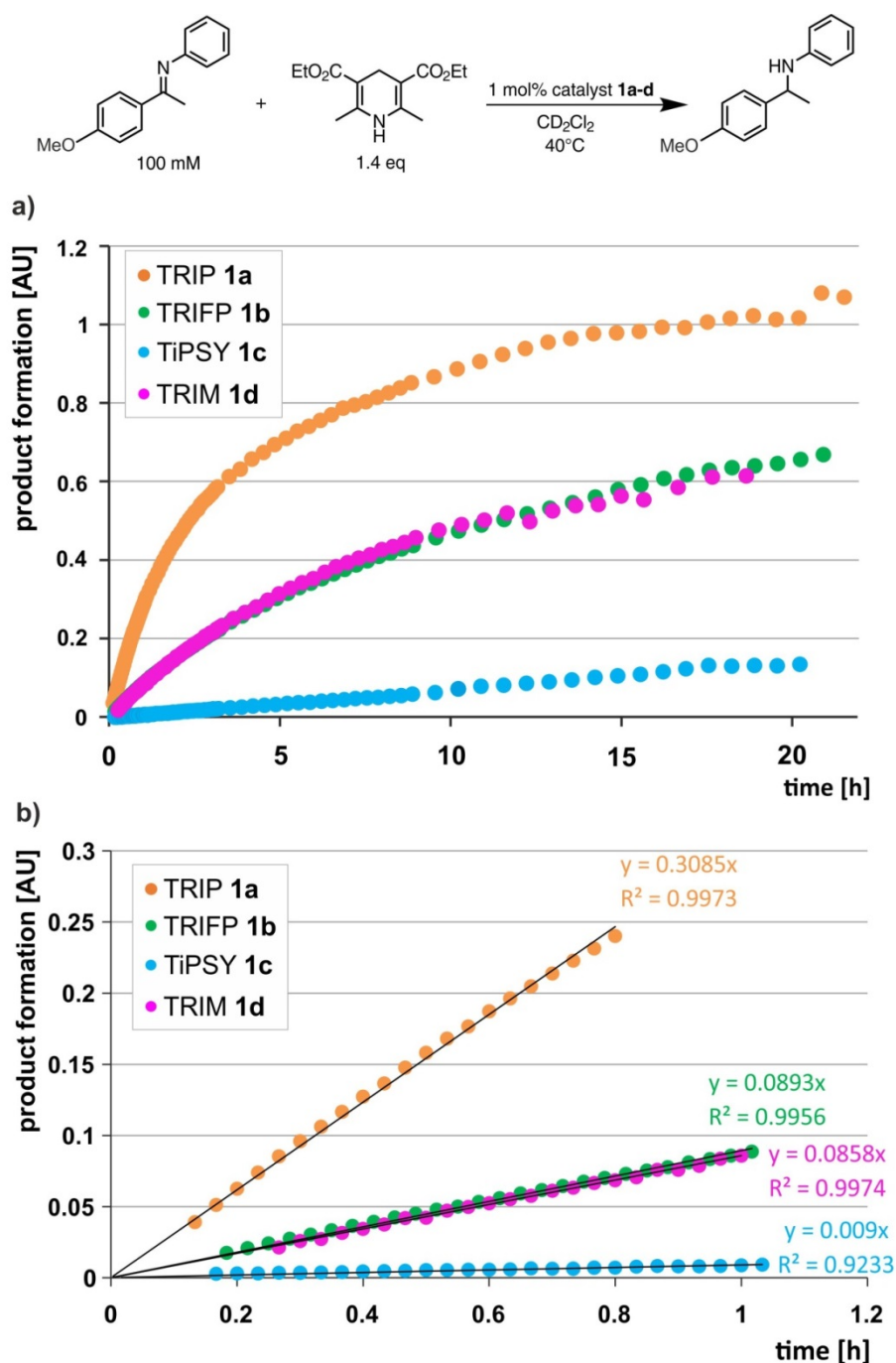


Figure S 3: a) The reaction profiles for the symmetric transfer hydrogenation of imine 5 are shown. The kinetics were done in-situ in the NMR spectrometer with 1.4 equivalents of Hantzsch ester and 1 mol% catalyst (TRIP, TRIFP, TiPSY and TRIM) at 40°C in CD₂Cl₂ b) the linear ranges enable the access to the rate constants.

3 Internal Acidity Scale and Reactivity Evaluation

In general, the reaction with imine **5** is significantly slower than with imine **3**. For all catalysts, the reaction rate of the transfer hydrogenation is reduced to more than half. This is also reflected in the isolated yields after five hours.^[69]

Also with imine **5** we identified TRIP as the most reactive catalyst and the reaction catalyzed by TiPSY is by far the slowest. However, the reactivity of TRIM and TRIFP is more or less the same (see Figure S3). These kinetic profiles were recorded in-situ in the NMR-spectrometer. The lower reactivity of TRIM with imine **5** compared to imine **3** may also be due to the low solubility of TRIM in CD_2Cl_2 . Thus, following the reaction kinetics without stirring has some potential drawbacks. Less amount of catalyst is dissolved in the reaction mixture and the reaction rate is slowed down compared to the other well-soluble catalysts. For this reason, ex-situ kinetics under the normal reaction conditions (in toluene at 35°C) were done. Here we observed the same result as with imine **3**: the reaction with TRIP is the fastest, followed by TRIM and TRIFP. The amount of product for the reaction catalyzed by TiPSY is small and could not be detected by HPLC.

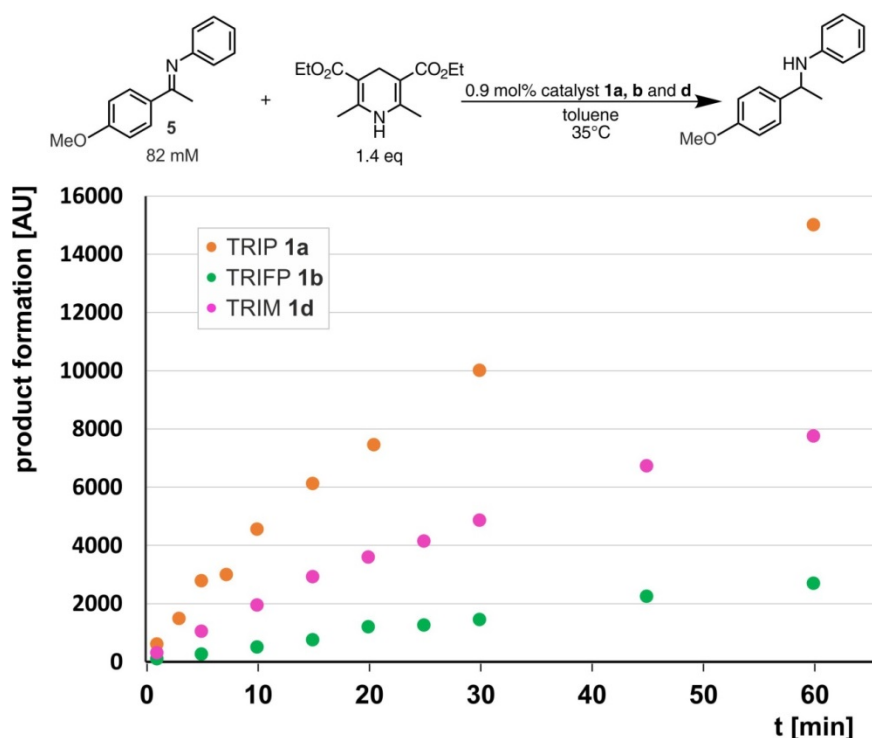


Figure S 4: The linear ranges of the reaction profiles for the symmetric transfer hydrogenation of imine **5** are shown. The kinetics were done ex-situ with 1.4 equivalents of Hantzsch ester and 0.9 mol% catalyst (TRIP, TRIFP, TiPSY and TRM) at 35°C in toluene. The amount of product was analyzed with chiral HPLC.

3.5.8. Amount of free imine in the ^1H spectra

The amount of free imine is experimentally accessible by the integration of the ^1H -signals obtaining from the OMe-groups of imine **5** in 1:1 sample of the catalyst and imine **5** in CD_2Cl_2 at 180K. In this region three different signals (free imine, hydrogen bonded *E*- and *Z*-imine) are visible. For referencing the signal of the hydrogen-bonded *E*-imine was set to 1 in all cases. The determination of the amount of free imine for other imines is unreliable because of signal overlapping.

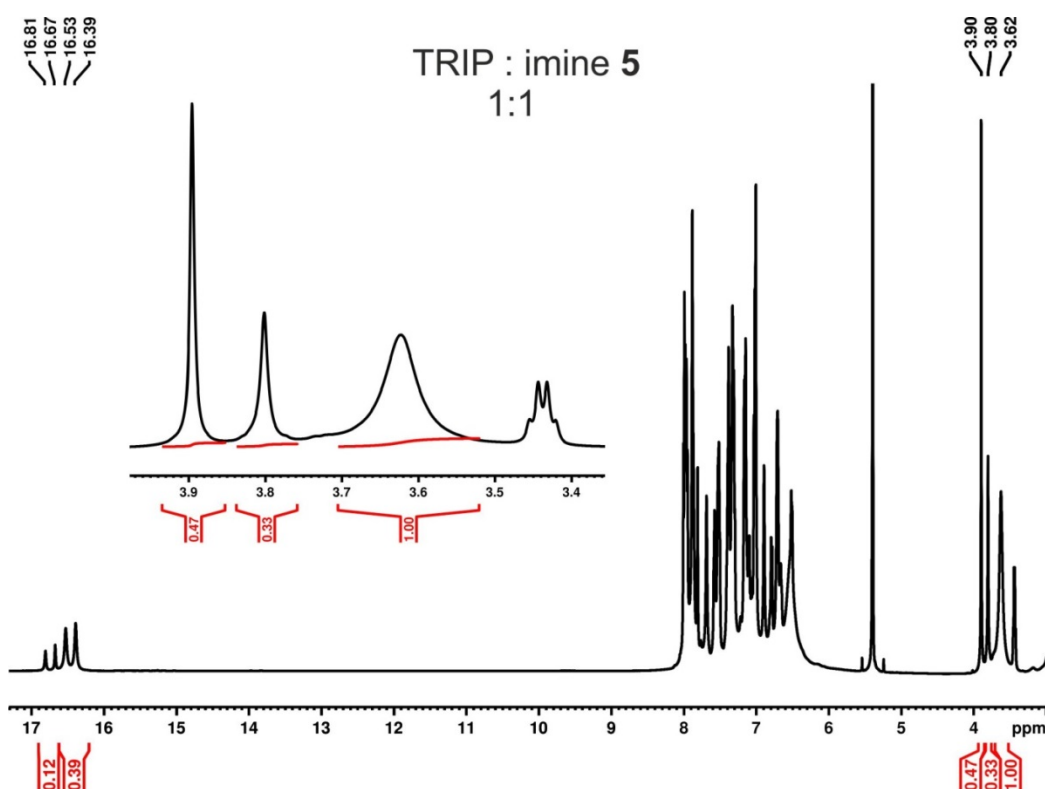


Figure S 5: ^1H -spectra of a 1:1 sample of TRIP and imine **5** in CD_2Cl_2 at 180K. For the determination of the amount of free imine the signals of the OMe-groups (free imine: 3.90 ppm, *Z*-imine: 3.80 ppm and *E*-imine: 3.62 ppm) were used. Furthermore, the signals of the hydrogen-bonded protons (*Z*-imine: 16.75 ppm and *E*-imine: 16.47 ppm) are shown.

3 Internal Acidity Scale and Reactivity Evaluation

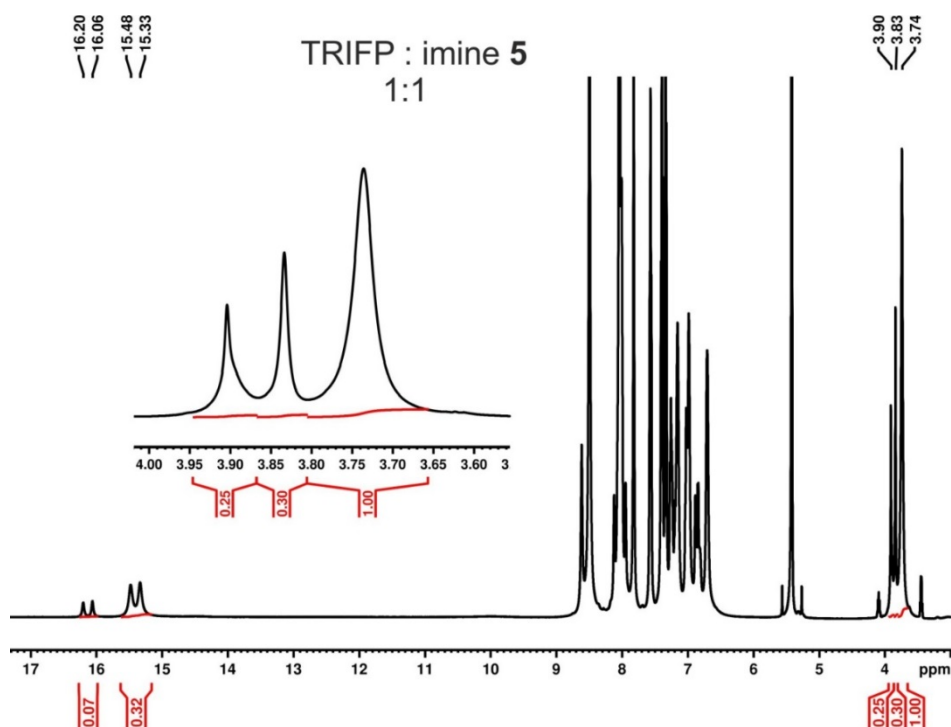


Figure S 6: ^1H -spectra of a 1:1 sample of TRIFP and imine 5 in CD_2Cl_2 at 180K. For the determination of the amount of free imine the signals of the OMe-groups (free imine: 3.90 ppm, *Z*-imine: 3.83 ppm and *E*-imine: 3.74 ppm) were used. Furthermore, the signals of the hydrogen-bbonded protons (*Z*-imine: 16.11 ppm and *E*-imine: 15.39 ppm) are shown.

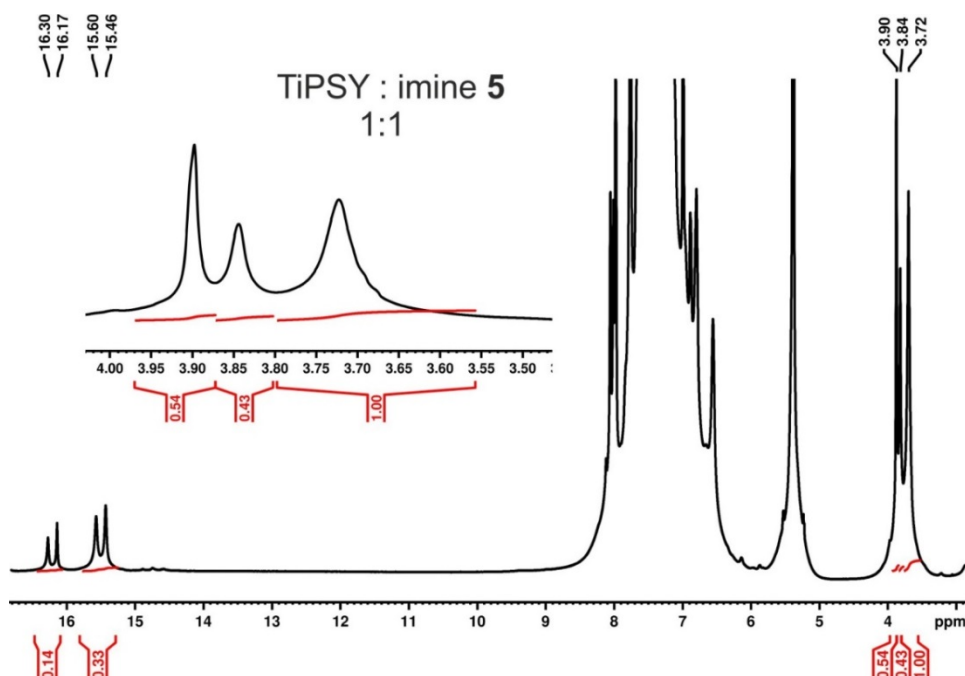


Figure S 7: ^1H -spectra of a 1:1 sample of TiPSY and imine 5 in CD_2Cl_2 at 180K. For the determination of the amount of free imine the signals of the OMe-groups (free imine: 3.90 ppm, *Z*-imine: 3.84 ppm and *E*-imine: 3.72 ppm) were used. Furthermore, the signals of the hydrogen-bbonded protons (*Z*-imine: 16.24 ppm and *E*-imine: 15.53 ppm) are shown.

3 Internal Acidity Scale and Reactivity Evaluation

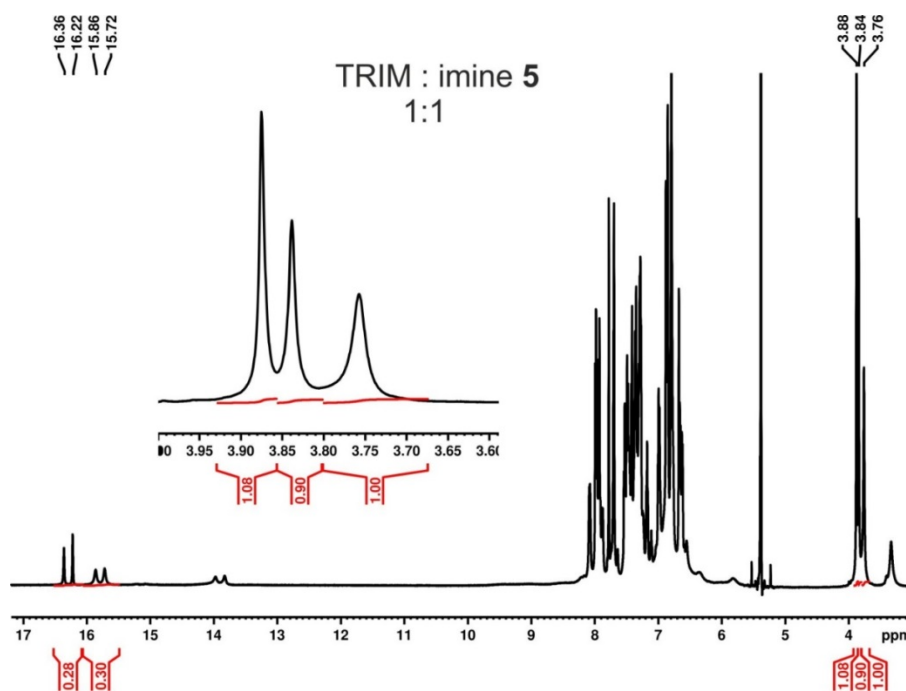


Figure S 8: ^1H -spectra of a 1:1 sample of TRIM and imine **5** in CD_2Cl_2 at 180K. For the determination of the amount of free imine the signals of the OMe-groups (free imine: 3.88 ppm, *Z*-imine: 3.84 ppm and *E*-imine: 3.76 ppm) were used. Furthermore, the signals of the hydrogen-bonded protons (*Z*-imine: 16.31 ppm and *E*-imine: 15.80 ppm) are shown.

For all cases, the obtained integrals (of free imine as well as hydrogen bonded *E*- and *Z*-imine) and the amount of free imine **5** are summarized in Table S9.

Table S 7: The integrals of the ^1H -signals in CD_2Cl_2 at 180 K are summarized. The OMe signals for the free imine as well as the hydrogen bonded *E*- and *Z*-imines were integrated and the the amount of free imine was calculated.

catalyst	imine	integral (E)	integral (Z)	integral (free)	free [%]
TRIP	5	1	0.31	0.47	26
TRIFP	5	1	0.30	0.25	16
TiPSY	5	1	0.43	0.54	27
TRIM	5	1	0.90	1.08	36

3 Internal Acidity Scale and Reactivity Evaluation

3.5.9. Formation of the binary complex

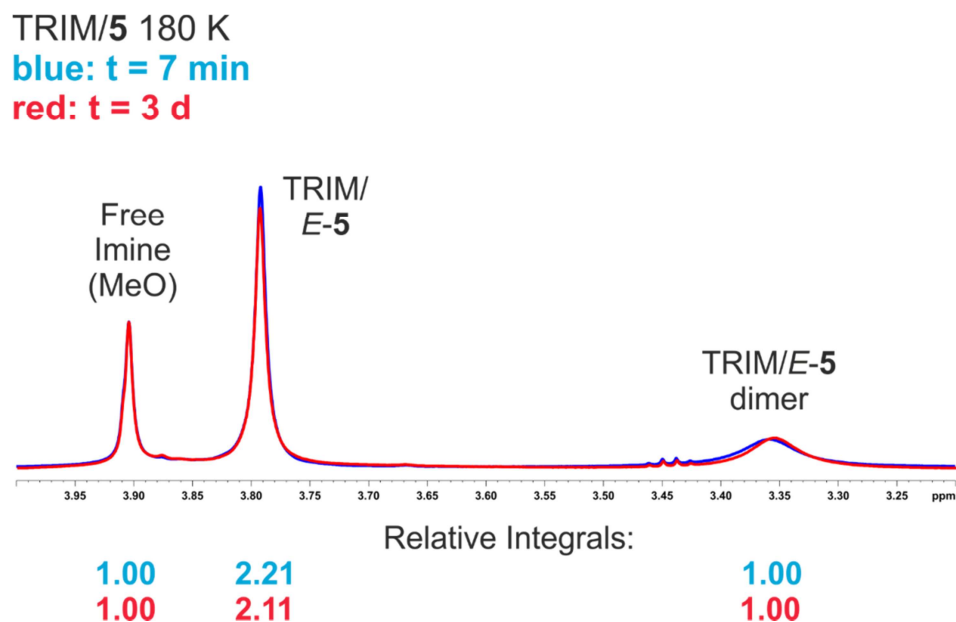


Figure S10: Fast formation of the binary complex. The blue spectrum was recorded 7 min after solvation of TRIM and imine **5** at -80°C , the red spectrum 3 days afterward (the sample was continuously kept at -80°C). The relative integrals show, that no further complexation occurs after 7 min.

3.5.10. Reactivity at 180 K and 220 K of TRIM/imine complex with Hantzsch Ester

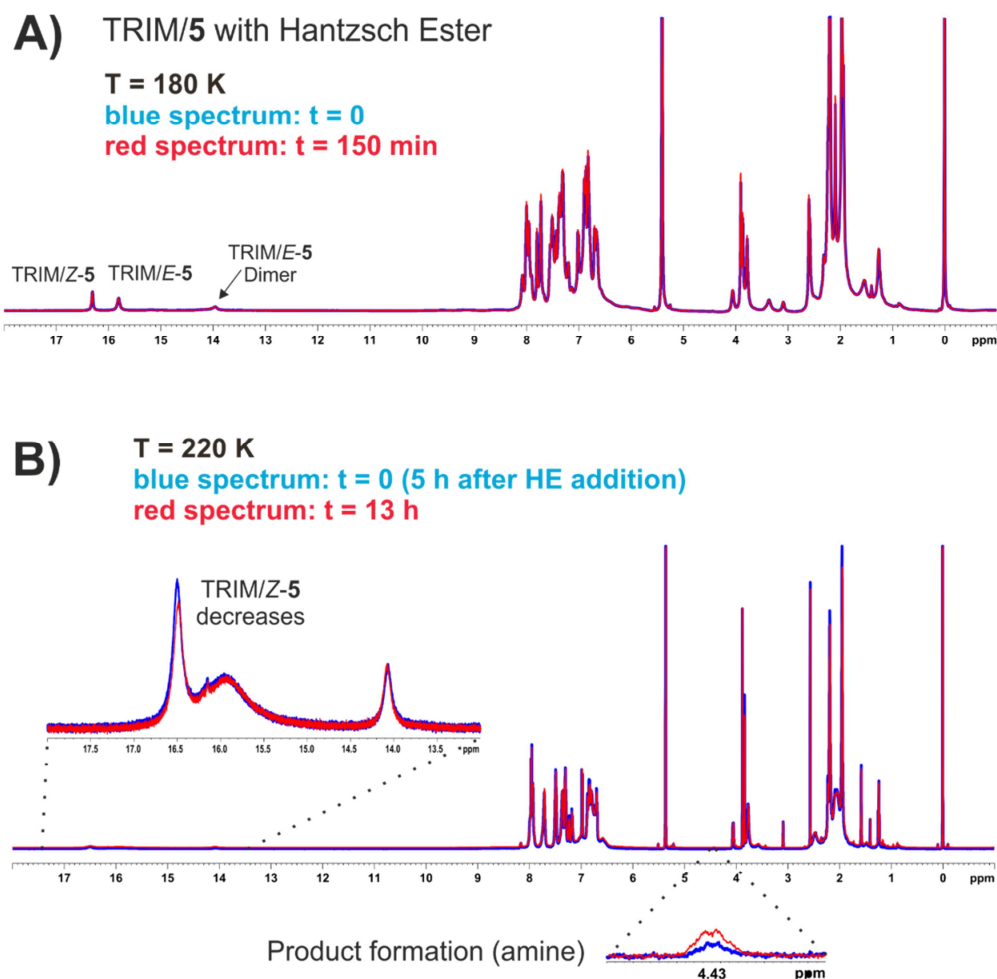


Figure S11: A 1:1 sample of TRIM and imine 5 was prepared (50 mM) at room temperature. The sample was cooled to 180 K and Hantzsch Ester (1.4 eq.) was added. A) Shows two overlapped spectra of the sample (blue: directly after HE addition, red: 150 min after the blue spectrum). Both spectra are identical despite the presence of dissolved Hantzsch Ester and binary E- and Z-complex, showing that no reaction occurs at 180 K. B) Overlap of two spectra of the sample ($\Delta t = 13$ h) at 220 K. The blue spectrum (t=0) was recorded 5 h after HE addition, the red spectrum 13 h afterwards. The product formation could be observed, as well as a signal decrease of TRIM/Z-5, showing that a slow reaction occurs at 220 K. In all recorded spectra, no additional signals appeared over time (despite the formed product), indicating that no build up of the ternary complex proceeds.

3 Internal Acidity Scale and Reactivity Evaluation

3.5.11. Determination of the *E*-to-*Z*-isomerization rates

For the determination of the *E*-to-*Z*-isomerization rates $k_{E \rightarrow Z}$, the ΔG_{ges} has to be determined first. ΔG_{ges} arises from equation S13. The definition of ΔG_1 and ΔG_2 , which are used in this work, is depicted in figure S6.

$$\Delta G_1 + \Delta G_2 = \Delta G_{ges} \quad (\text{S13})$$

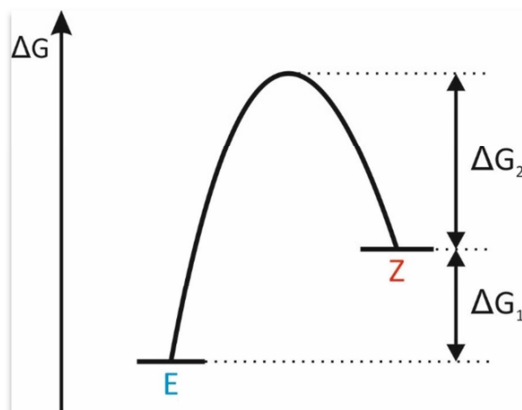


Figure S 9: The *E*-imine is thermodynamically more favored than the *Z*-imine. Additionally, the definition of the ΔG_1 and ΔG_2 used in this work is shown.

The only experimental way to determine the *Z*-to-*E*-isomerization rate is by increasing the amount of thermodynamically unfavored *Z*-imine by illumination with 365 nm (in-situ, for experimental set-up, see reference^[70]). Afterwards the back-isomerization to the more stable *E*-imine was observed with NMR. Finally, the decay-curves of the *Z*-imine can be fitted mathematically (with equation S14). The *Z*-to-*E*-isomerization rate is defined as $k_{Z \rightarrow E} = 1/t_1$. Then ΔG_2 can be calculated from equation S15. The obtained values are summarized in Table S7. The decay curves are shown in chapter 7.1.

$$y = A_1 * e^{\frac{-x}{t_1}} + y_0 \quad (\text{S14})$$

$$k_{Z \rightarrow E} = \frac{(k_B * T)}{h} * e^{-\frac{\Delta G_2}{RT}} \quad (\text{S15})$$

3 Internal Acidity Scale and Reactivity Evaluation

Table S 8: The experimentally observed Z-to-E-isomerization rates $k_{Z \rightarrow E}$, as well as the related ΔG_2 at different temperatures, are shown.

catalyst	imine	temperature [K]	$k_{Z \rightarrow E}$ [$\cdot 10^{-3}$ 1/s]	ΔG_2 [kJ]
TRIFP	5	230	2.52	67.28
TIPSY	5	230	1.19	68.71
TRIP	5	230	9.04	64.83

For the determination of the E-to-Z-isomerization rate constants, the amount of E- and Z-imine in the binary complex was determined. Here it is very important that the spectra were recorded in the thermodynamic equilibrium. After some mathematical transformations of the Boltzmann distribution (equation S16), ΔG_1 can be observed from equation S17. Here, N_0 represents the integral of the E-imine, which is set to 1 in all cases. N_i is the integral of the Z-imine.

$$\frac{N_i}{N_0} = e^{\frac{-\Delta G_1}{k_B T}} \quad (\text{S16})$$

$$\Delta G_1 = -RT * \ln\left(\frac{N_i}{N_0}\right) \quad (\text{S17})$$

After the calculation of ΔG_{ges} (equation S13) the E-to-Z-isomerization rate $k_{E \rightarrow Z}$ can be determined with equation S18. The obtained values for ΔG_1 , ΔG_{ges} and $k_{E \rightarrow Z}$ are summarized in table S8 for different catalysts at 230 K.

$$k_{E \rightarrow Z} = \frac{(k_B * T)}{h} * e^{\frac{-\Delta G_{\text{ges}}}{RT}} \quad (\text{S18})$$

Table S 9: The experimentally observed amounts of Z-imine (N_i) and E-imine (N_0) as well as the calculated ΔG_2 , ΔG_{ges} and the Z-to-E-isomerization rates $k_{Z \rightarrow E}$ at 230 K in CD_2Cl_2 are shown.

catalyst	imine	T [K]	N_i	N_0	ΔG_1 [kJ]	ΔG_{ges} [kJ]	$k_{E \rightarrow Z}$ [$\cdot 10^{-3}$ 1/s]
TRIFP	5	230	0.1768	1	3.31	70.59	0.45
TIPSY	5	230	0.4786	1	1.41	70.11	0.57
TRIP	5	230	0.1500	1	3.63	68.46	1.36

3 Internal Acidity Scale and Reactivity Evaluation

3.5.12. Decay curves

The amount of *Z*-imine is increased by illumination with 365 nm with a glass fiber inside the NMR.^[69,70] For the imine **5** the photostationary state in CD₂Cl₂ at 190 K was reached after 3 h (constant *E/Z*-ratio of 1/1.7). Then the thermal *Z*-to-*E*-back-isomerization is observed inside the NMR-spectrometer at 230K. 230K were chosen because here the *Z*-imine is thermally back converted to the *E*-isomer in a reasonable amount of time. Over 250 K the back-isomerization is so fast that it could not be detected. All the measured decay curves as well as the associated fit-equations (see also equation S14) are shown in figure S7 to S9.

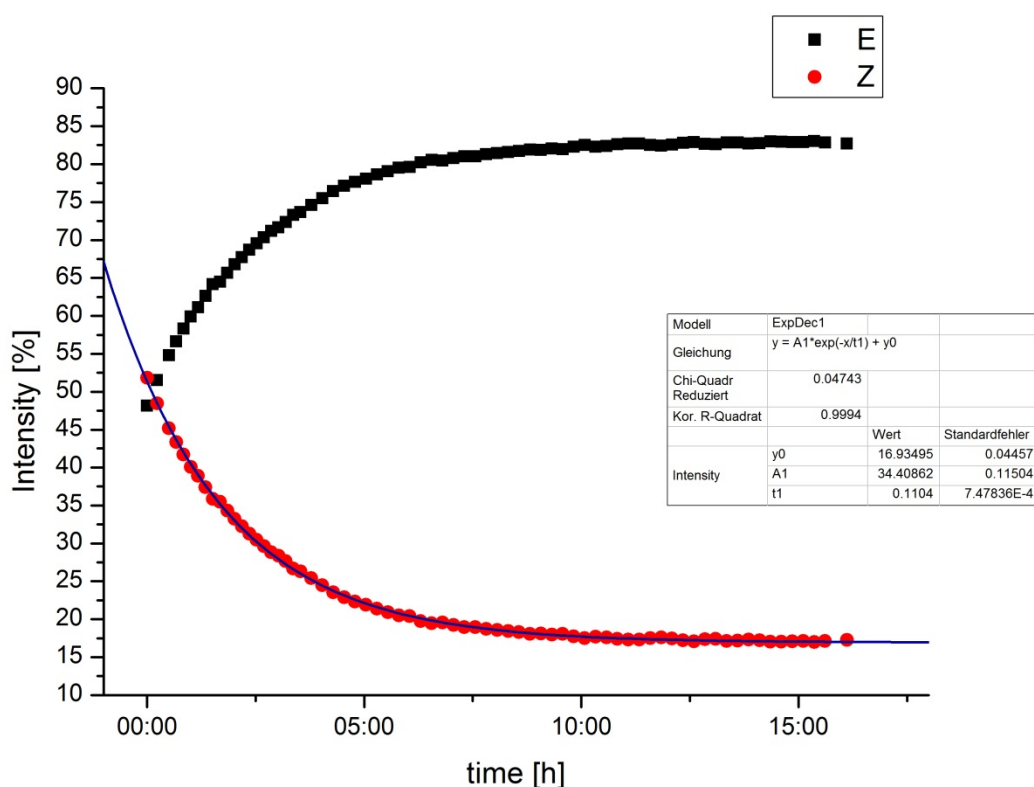


Figure S 10: The thermal back-isomerization of the *Z*-imine (red) in the binary TRIFP/**5**-complex at 230K in CD₂Cl₂ is shown. While the amount of *Z*-imine decreases, the amount of the thermodynamically more stable *E*-imine (black) is increased. The fit delivers the following values for the constants: $y_0 = 16.94 \pm 0.05$, $A_1 = 34.41 \pm 0.12$ and $t_1 = 0.1104 \pm 0.0008$.

3 Internal Acidity Scale and Reactivity Evaluation

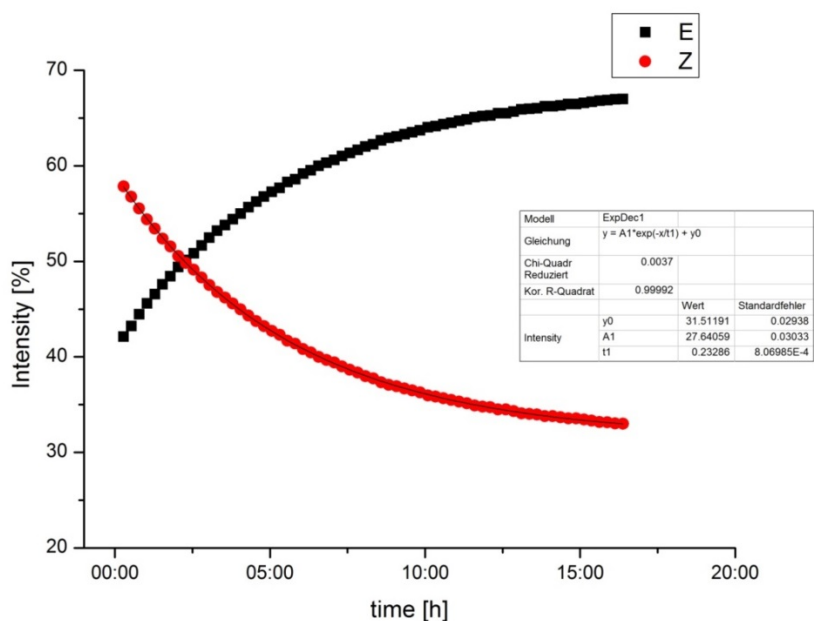


Figure S 11: The thermal back-isomerization of the Z-imine (red) in the binary TiPSY/5-complex at 230K in CD_2Cl_2 is shown. While the amount of Z-imine decreases, the amount of the thermodynamically more stable E-imine (black) is increased. The fit delivers the following values for the constants: $y_0 = 31.51 \pm 0.03$, $A_1 = 27.64 \pm 0.03$ and $t_1 = 0.2329 \pm 0.0008$.

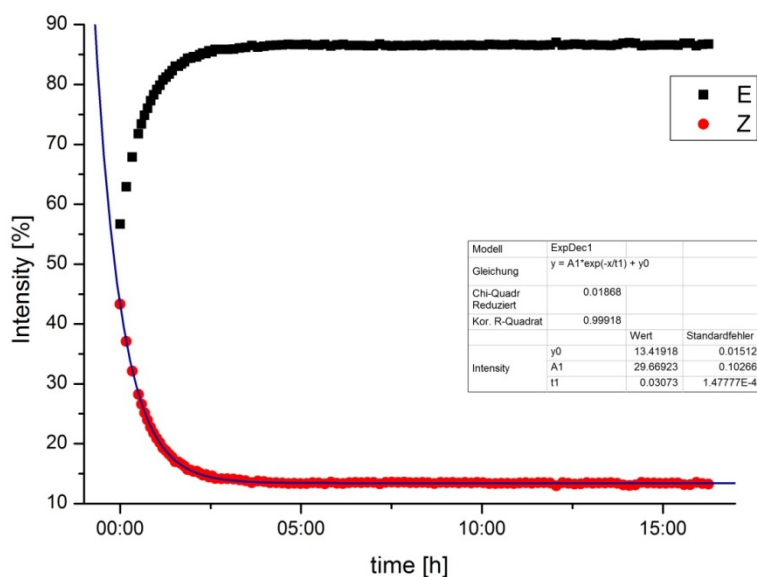


Figure S 12: The thermal back-isomerization of the Z-imine (red) in the binary TRIP/5-complex at 230K in CD_2Cl_2 is shown. While the amount of Z-imine decreases, the amount of the thermodynamically more stable E-imine (black) is increased. The fit delivers the following values for the constants: $y_0 = 13.41 \pm 0.02$, $A_1 = 29.67 \pm 0.10$ and $t_1 = 0.0307 \pm 0.0002$.

3 Internal Acidity Scale and Reactivity Evaluation

3.5.13. Investigations of the ternary complex with TRIP, imine **5** and Hantzsch ester

For the investigations of the ternary complex in this chapter, a TRIP/imine **5**/Hantzsch ester-ratio of 1:3:3 was used. This ratio was chosen to shift the equilibrium between the Hantzsch ester in its free form and the Hantzsch ester in the ternary complex to the side of the ternary complex.

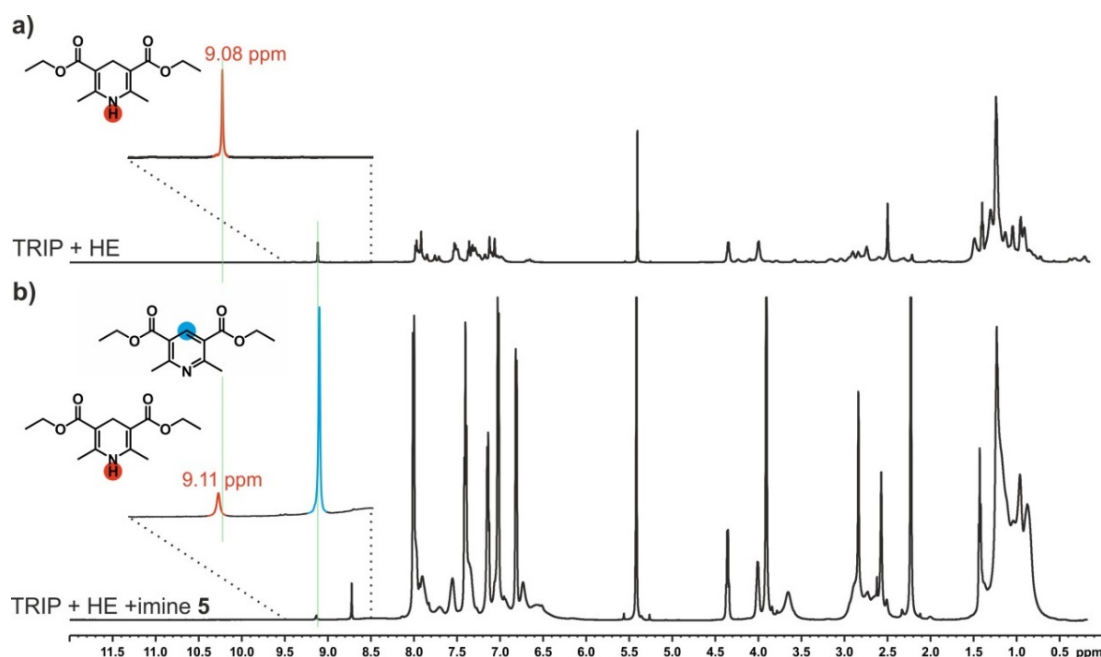


Figure S 13: The spectra of a) TRIP and Hantzsch ester (HE) and b) Hantzsch ester with TRIP and imine **5** in CD₂Cl₂ at 200K are shown. The very small shift ($\Delta\delta = 0.03$ ppm) of the NH-proton of the Hantzsch ester (red circle) in both spectra is a hint that only a small amount of ternary complex was formed. Both spectra are referenced to TMS.

3 Internal Acidity Scale and Reactivity Evaluation

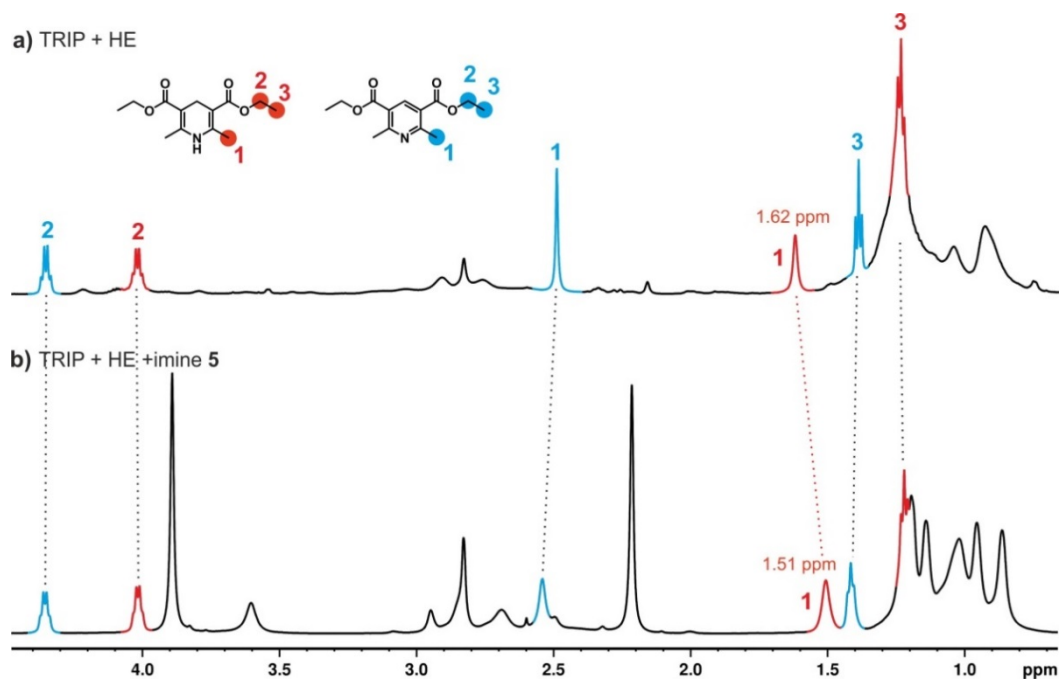


Figure S 14: The spectra of a) TRIP and Hantzsch ester (HE) and b) Hantzsch ester with TRIP and imine **5** in CD₂Cl₂ at 200K are shown. For the *ortho*-methyl group of the Hantzsch ester (red 1) a small highfield shift ($\Delta\delta = 0.51$ ppm) was observed. This may be due to the shielding by aromatic protons of the catalyst backbone. For the other aliphatic signals, almost no shift is observed. Both spectra are referenced to TMS.

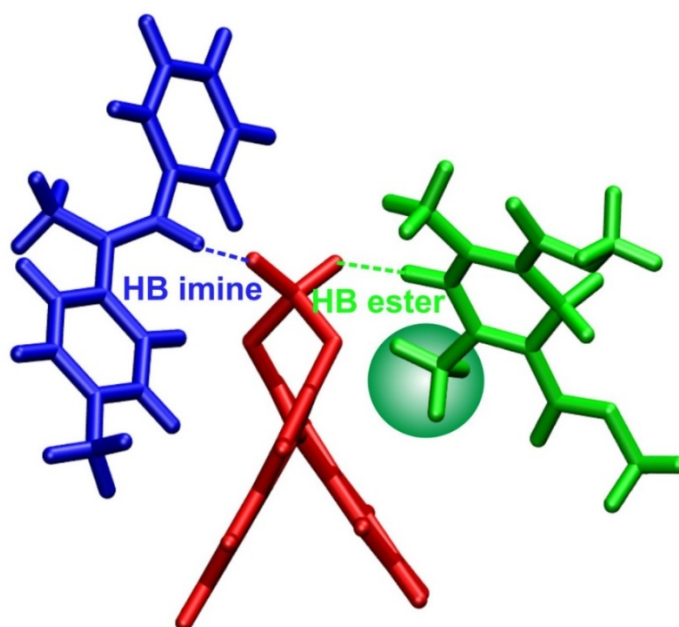
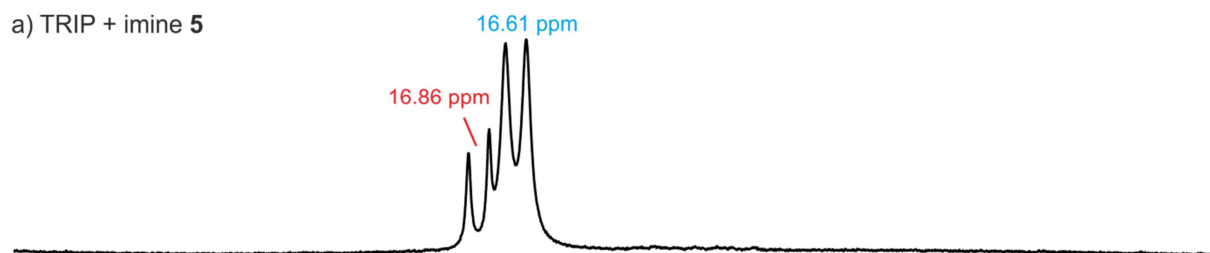


Figure S 15: Structural analysis of the computed ternary complex (imine **5**: blue, TRIP: red, Hantzsch ester: green) revealed spatial proximity of the *ortho*-methyl group (green circle) to the BINOL backbone of the TRIP which explains the high-field shift due to shielding by the aromatic ring. As an example, the *type I E*-imine **5** was chosen.

3 Internal Acidity Scale and Reactivity Evaluation

a) TRIP + imine **5**



b) TRIP + HE + imine **5**

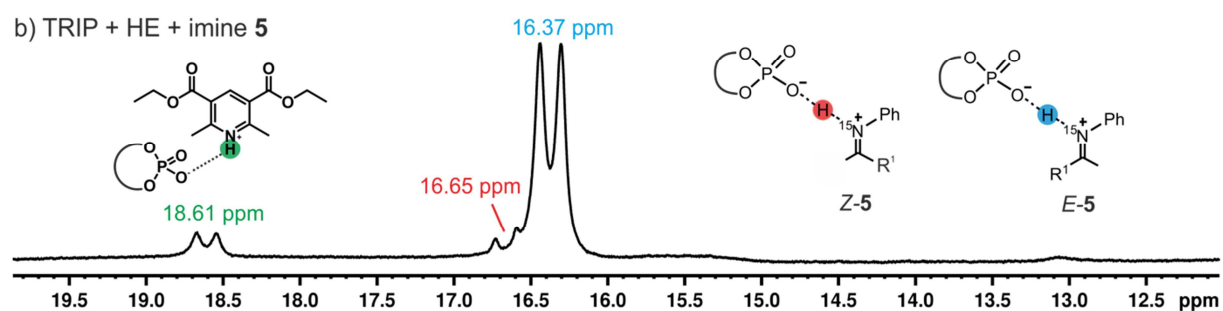


Figure S 16: a) In the spectra of imine **5** and TRIP the hydrogen-bonded protons of the E- and Z-complex (*E*-complex: 16.61 ppm and *Z*-complex: 16.86 ppm) are shown. b) By adding Hantzsch ester to imine **5** and TRIP both signals are slightly shifted (*E*-complex: 16.37 ppm and *Z*-complex: 16.65 ppm). Both spectra were recorded at 200 K in CD₂Cl₂.

3 Internal Acidity Scale and Reactivity Evaluation

3.5.14. Investigations on the ternary complex of TRIM, imine 5 and Hantzsch ester

In the investigations of the ternary complex in this chapter a TRIM/imine 5/Hantzsch ester-ratio of 1:1:1.4 was used.

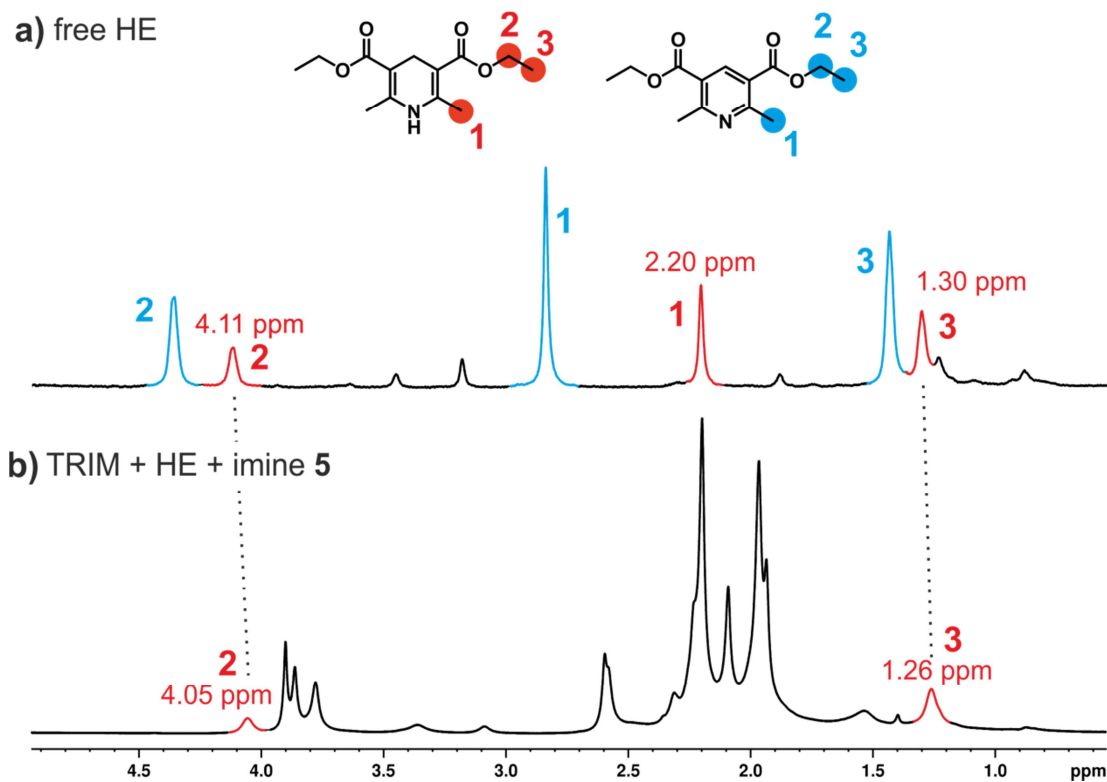


Figure S 17: The spectra of a) Hantzsch ester (HE) and b) Hantzsch ester with TRIP and imine 5 in CD_2Cl_2 at 180K are shown. For the signals 2 and 3 of the Hantzsch ester (red), small shift (for 2: $\Delta\delta = 0.06$ ppm and for 3: $\Delta\delta = 0.04$ ppm) could be observed. The assignment of proton 1 in spectrum b) is not unambiguous.

3 Internal Acidity Scale and Reactivity Evaluation

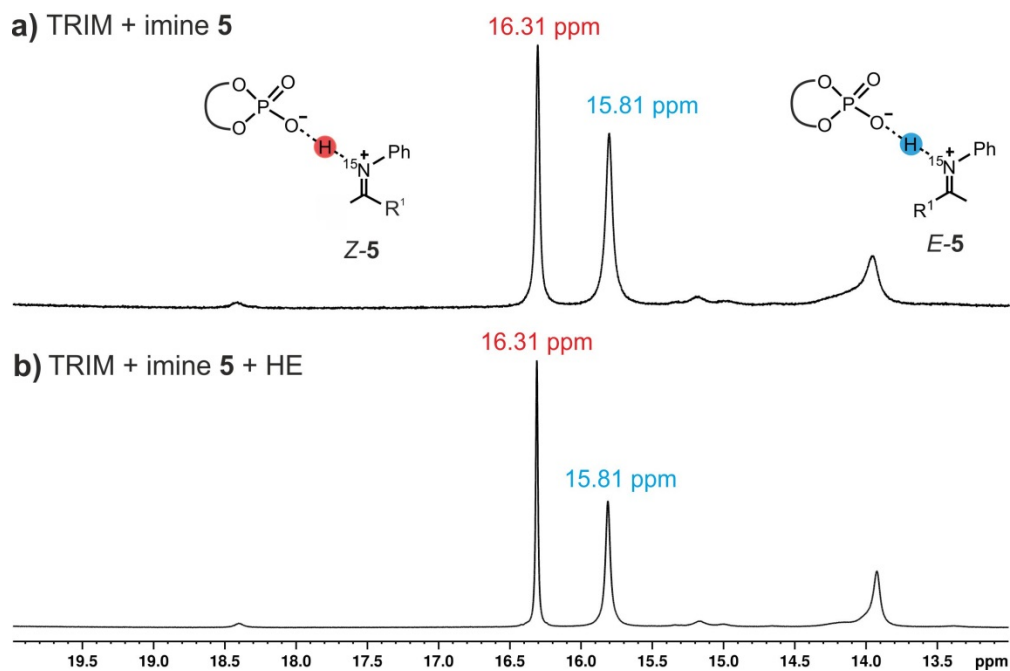


Figure S 18: a) In the spectra of imine **5** and TRIM the hydrogen-bonded protons of the E- and Z-complex (E-complex: 15.81 ppm and Z-complex: 16.31 ppm) are well separated. b) By adding Hantzsch ester to imine **5** and TRIM no shift of the signals is detectable (E-complex: 15.81 ppm and Z-complex: 16.31 ppm). Both spectra were recorded at 180 K in CD_2Cl_2 and referenced to TMS.

3 Internal Acidity Scale and Reactivity Evaluation

3.5.15. Barrier of the hydride transfer

According to the previous calculations, the barrier of hydride transfer equals 53 to 60 kJ/mol.^[69] Thus, under the assumption that the formation of the ternary complex is not rate limiting or thermodynamically unfavorable, the measured isomerization rate (barrier approx. 65 to 70 kJ/mol), is several order of magnitude slower than the hydride transfer step. The NMR spectra showed a fast exchange between the ternary complex and the binary complex. Hence, kinetically the formation of the ternary complex is not demanding; however, the minor shift of the Hantzsch ester acidic proton-signal suggests that the binding constant of Hantzsch ester is very low.

3.5.16. Solubility of Hantzsch ester in toluene

Hantzsch ester (14.50 mg, 0.057 mmol) was weighed into an NMR tube, and a solution of the standard (1,3,5-trimethoxybenzene, 2.88 mg, 0.017 mmol, 0.30 eq., 3.4 mM stock solution) in PhMe-*d*₈ (0.5 mL) was added. The sample was equilibrated at 308 K in the spectrometer for 15 min and ¹H NMR spectra (AQ: 10 s, pre-scan delay 2 s, 64 scans) of the dissolved Hantzsch ester were acquired on a 600 MHz instrument at 308 K (35 °C). The fast-relaxing methyl signals of the Hantzsch ester (δ 1.08 ppm) and the standard (δ 3.38 ppm) were integrated, and the concentration of the dissolved ester calculated.

Hantzsch ester from three different suppliers was used for this study for comparison. Some of the samples were stirred (600 rpm) in a Schlenk flask at 35 °C, treated with ultrasound (5 min) at 35 °C, or equilibrated for 1 h. In all cases, the concentration of the Hantzsch ester remained low and constant at 1.2 – 1.7 mg.mL⁻¹ (4.7 – 6.7 μ M).

3.5.17. Computational details

For details see Appendix (DVD).

3.6. References

- [1] M. Terada, *Synthesis (Stuttg)*. **2010**, 1929–1982.
- [2] D. Parmar, E. Sugiono, S. Raja, M. Rueping, *Chem. Rev.* **2014**, *114*, 9047–9153.
- [3] M. Mahlau, B. List, *Angew. Chemie - Int. Ed.* **2013**, *52*, 518–533.
- [4] M. S. Sigman, E. N. Jacobsen, *J. Am. Chem. Soc.* **1998**, *120*, 4901–4902.
- [5] M. S. Sigman, P. Vachal, E. N. Jacobsen, *Angew. Chemie - Int. Ed.* **2000**, *39*, 1279–1281.
- [6] P. Vachal, E. N. Jacobsen, *J. Am. Chem. Soc.* **2002**, *124*, 10012–10014.
- [7] T. Akiyama, J. Itoh, K. Yokota, K. Fuchibe, *Angew. Chemie Int. Ed.* **2004**, *43*, 1566–1568.
- [8] D. Uraguchi, M. Terada, *J. Am. Chem. Soc.* **2004**, *126*, 5356–5357.

3 Internal Acidity Scale and Reactivity Evaluation

- [9] M. Rueping, T. Theissmann, M. Stoeckel, A. P. Antonchick, *Org. Biomol. Chem.* **2011**, *9*, 6844–6850.
- [10] Q. Yin, S.-G. Wang, S.-L. You, *Org. Lett.* **2013**, *15*, 2688–2691.
- [11] T. Marcelli, P. Hammar, F. Himo, *Chem. - A Eur. J.* **2008**, *14*, 8562–8571.
- [12] R. I. Storer, D. E. Carrera, Y. Ni, D. W. C. Macmillan, *J. Am. Chem. Soc.* **2006**, *128*, 84–86.
- [13] K. Saito, T. Akiyama, *Chem. Commun.* **2012**, *48*, 4573–4575.
- [14] M. Yamanaka, J. Itoh, K. Fuchibe, T. Akiyama, *J. Am. Chem. Soc.* **2007**, *129*, 6756–64.
- [15] X. Xu, Y. Qian, L. Yang, W. Hu, *Chem. Commun.* **2010**, *47*, 797–799.
- [16] E. P. Ávila, R. M. S. Justo, V. P. Gonçalves, A. A. Pereira, R. Diniz, G. W. Amarante, *J. Org. Chem.* **2015**, *80*, 590–594.
- [17] K. Shen, X. Liu, Y. Cai, L. Lin, X. Feng, *Chem. – A Eur. J.* **2009**, *15*, 6008–6014.
- [18] M. Rueping, E. Sugiono, C. Azap, T. Theissmann, M. Bolte, *Org. Lett.* **2005**, *7*, 3781–3783.
- [19] S. Hoffmann, A. M. Seayad, B. List, *Angew. Chemie - Int. Ed.* **2005**, *44*, 7424–7427.
- [20] M. Rueping, C. Azap, E. Sugiono, T. Theissmann, *Synlett* **2005**, 2367–2369.
- [21] M. Rueping, E. Sugiono, C. Azap, T. Theissmann, *Org. Lett.* **2005**, *7*, 3781–3783.
- [22] S. G. Ouellet, A. M. Walji, D. W. C. Macmillan, *Acc. Chem. Res.* **2007**, *40*, 1327–1339.
- [23] S. Liao, I. Čorić, Q. Wang, B. List, *J. Am. Chem. Soc.* **2012**, *134*, 10765–10768.
- [24] X. Yu, Y. Wang, G. Wu, H. Song, Z. Zhou, C. Tang, *European J. Org. Chem.* **2011**, 3060–3066.
- [25] Q. Kang, Z.-A. Zhao, S.-L. You, *Org. Lett.* **2008**, *10*, 2031–2034.
- [26] Q. Gu, Z. Rong, C. Zheng, S. You, *J. Am. Chem. Soc.* **2010**, *132*, 4056–4057.
- [27] C. Min, D. Seidel, *Chem. Soc. Rev.* **2017**, *46*, 5889–5902.
- [28] R. Maji, S. C. Mallojjala, S. E. Wheeler, *Chem. Soc. Rev.* **2018**, *47*, 1142–1158.
- [29] A. J. Neel, A. Milo, M. S. Sigman, F. D. Toste, *J. Am. Chem. Soc.* **2016**, *138*, 3863–3875.
- [30] M. Orlandi, F. D. Toste, M. S. Sigman, *Angew. Chemie - Int. Ed.* **2017**, *56*, 14080–14084.
- [31] J. P. Reid, J. M. Goodman, *J. Am. Chem. Soc.* **2016**, *138*, 7910–7917.
- [32] S. E. Wheeler, T. J. Seguin, Y. Guan, A. C. Doney, *Acc. Chem. Res.* **2016**, *49*, 1061–1069.
- [33] T. J. Seguin, S. E. Wheeler, *Angew. Chemie - Int. Ed.* **2016**, *55*, 15889–15893.
- [34] T. J. Seguin, S. E. Wheeler, *ACS Catal.* **2016**, *6*, 7222–7228.
- [35] R. Maji, P. A. Champagne, K. N. Houk, S. E. Wheeler, *ACS Catal.* **2017**, *7*, 7332–7339.
- [36] M. Orlandi, M. J. Hilton, E. Yamamoto, F. D. Toste, M. S. Sigman, *J. Am. Chem. Soc.* **2017**, *139*, 12688–12695.
- [37] M. Orlandi, J. A. S. Coelho, M. J. Hilton, F. D. Toste, M. S. Sigman, *J. Am. Chem. Soc.* **2017**, *139*, 6803–6806.
- [38] R. B. Sunoj, *Acc. Chem. Res.* **2016**, *49*, 1019–1028.
- [39] J. P. Reid, J. M. Goodman, *Chem. - A Eur. J.* **2017**, *23*, 14248–14260.
- [40] F. Duarte, R. S. Paton, *J. Am. Chem. Soc.* **2017**, *139*, 8886–8896.
- [41] M. Melikian, J. Gramüller, J. Hioe, J. Greindl, R. M. Gschwind, *Chem. Sci.* **2019**, *10*, 5226–5234.

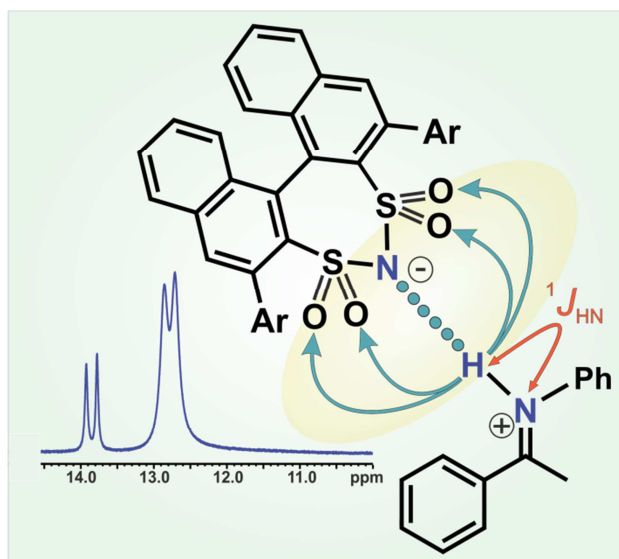
3 Internal Acidity Scale and Reactivity Evaluation

- [42] N. Sorgenfrei, J. Hioe, J. Greindl, K. Rothermel, F. Morana, N. Lokesh, R. M. Gschwind, *J. Am. Chem. Soc.* **2016**, *138*, 16345–16354.
- [43] J. Greindl, J. Hioe, N. Sorgenfrei, F. Morana, R. M. Gschwind, *J. Am. Chem. Soc.* **2016**, *138*, 15965–15971.
- [44] K. Kaupmees, N. Tolstoluzhsky, S. Raja, M. Rueping, I. Leito, *Angew. Chemie Int. Ed.* **2013**, *52*, 11569–72.
- [45] M. S. Taylor, E. N. Jacobsen, *Angew. Chemie - Int. Ed.* **2006**, *45*, 1520–1543.
- [46] R. J. Phipps, G. L. Hamilton, F. D. Toste, *Nat. Chem.* **2012**, *4*, 603–614.
- [47] Q. Zhu, D. E. Graff, R. R. Knowles, *J. Am. Chem. Soc.* **2018**, *140*, 741–747.
- [48] H. G. Yayla, H. Wang, K. T. Tarantino, H. S. Orbe, R. R. Knowles, *J. Am. Chem. Soc.* **2016**, *138*, 10794–10797.
- [49] G. Qiu, R. R. Knowles, *J. Am. Chem. Soc.* **2019**, *141*, 2721–2730.
- [50] K. Gratzer, V. Diemer, J. Clayden, *Org. Biomol. Chem.* **2017**, *15*, 3585–3589.
- [51] A. Eisenhofer, J. Hioe, R. M. Gschwind, B. König, *European J. Org. Chem.* **2017**, 2194–2204.
- [52] H. Rahaman, Ú. Madarász, I. Pápai, P. M. Pihko, *Angew. Chemie - Int. Ed.* **2011**, *50*, 6123–6127.
- [53] A. J. Neuvonen, T. Földes, Á. Madarász, I. Pápai, P. M. Pihko, *ACS Catal.* **2017**, *7*, 3284–3294.
- [54] T. Kano, K. Maruoka, *Chem. Commun.* **2008**, 5465–5473.
- [55] W. Tang, S. Johnston, J. A. Iggo, N. G. Berry, M. Phelan, L. Lian, J. Bacsá, J. Xiao, *Angew. Chemie - Int. Ed.* **2013**, *52*, 1668–1672.
- [56] L. Simón, J. M. Goodman, *J. Am. Chem. Soc.* **2008**, *130*, 8741–8747.
- [57] H. Benedict, I. G. Shenderovich, O. L. Malkina, V. G. Malkin, G. S. Denisov, N. S. Golubev, H. H. Limbach, *J. Am. Chem. Soc.* **2000**, *122*, 1979–1988.
- [58] S. Sharif, G. S. Denisov, M. D. Toney, H. H. Limbach, *J. Am. Chem. Soc.* **2007**, *129*, 6313–6327.
- [59] A. Kuett, I. Leito, I. Kaljurand, L. Soovaeli, V. M. Vlasov, L. M. Yagupolskii, I. A. Koppel, *J. Org. Chem.* **2006**, *71*, 5430–5439.
- [60] P. Christ, A. G. Lindsay, S. S. Vormittag, J.-M. Neudörfl, A. Berkessel, A. C. O'Donoghue, *Chem. - A Eur. J.* **2011**, *17*, 8524–8528.
- [61] S. Sharif, D. Schagen, M. D. Toney, H.-H. Limbach, *J. Am. Chem. Soc.* **2007**, *129*, 4440–4455.
- [62] C. Yang, X. S. Xue, J. L. Jin, X. Li, J. P. Cheng, *J. Org. Chem.* **2013**, *78*, 7076–7085.
- [63] S. Rösel, J. Becker, W. D. Allen, P. R. Schreiner, *J. Am. Chem. Soc.* **2018**, *140*, 14421–14432.
- [64] J. P. Wagner, P. R. Schreiner, *Angew. Chemie - Int. Ed.* **2015**, *54*, 12274–12296.
- [65] R. Y. Liu, S. L. Buchwald, P. Liu, Y. Yang, G. Lu, D. S. Lambrecht, C. Fang, *J. Am. Chem. Soc.* **2017**, *139*, 16548–16555.
- [66] X. Cai, A. Tohti, C. Ramirez, H. Harb, J. C. Fettingner, H. P. Hratchian, B. J. Stokes, *Org. Lett.* **2019**, *21*, 1574–1577.
- [67] D. Seebach, U. Groselj, W. B. Schweizer, *Helvetica Chimica Acta* **2010**, *93*, 1–16.
- [68] A. Armstrong, R. A. Boto, P. Dingwall, J. Contreras-García, M. J. Harvey, N. J. Mason, H. S. Rzepa, *Chem. Sci.* **2014**, *5*, 2057–2071.

3 Internal Acidity Scale and Reactivity Evaluation

- [69] P. Renzi, J. Hioe, R. M. Gschwind, *J. Am. Chem. Soc.* **2017**, *139*, 6752–6760.
- [70] C. Feldmeier, H. Bartling, E. Riedle, R. M. Gschwind, *J. Magn. Reson.* **2013**, *232*, 39–44.
- [71] C. H. Bushweller, J. W. O’Neil, H. S. Bilofsky, *Tetrahedron* **1971**, *27*, 5761–5766.
- [72] C. H. Bushweller, J. W. O’Neil, H. S. Bilofsky, *J. Am. Chem. Soc.* **1970**, *92*, 6349–6350.
- [73] M. I. Rodríguez-Franco, I. Dorronsoro, A. Castro, A. Martínez, *Tetrahedron* **2000**, *56*, 1739–1743.
- [74] M. Dewar, B. Jennings, *Tetrahedron Lett.* **1970**, *11*, 339–342.
- [75] L. Simón, J. M. Goodman, *J. Am. Chem. Soc.* **2008**, *130*, 8741–8747.
- [76] L. Simón, J. M. Goodman, *J. Org. Chem.* **2011**, *76*, 1775–1788.
- [77] J. P. Reid, L. Simón, J. M. Goodman, *Acc. Chem. Res.* **2016**, *49*, 1029–1041.
- [78] A. Seegerer, J. Hioe, M. M. Hammer, F. Morana, P. J. W. Fuchs, R. M. Gschwind, *J. Am. Chem. Soc.* **2016**, *138*, 9864–9873.
- [79] V. N. Wakchaure, P. S. J. Kaib, M. Leutzsch, B. List, *Angew. Chemie - Int. Ed.* **2015**, *54*, 11852–11856.
- [80] N. Sorgenfrei, J. Hioe, J. Greindl, K. Rothermel, F. Morana, N. Lokesh, R. M. Gschwind, *J. Am. Chem. Soc.* **2016**, *138*, 16345–16354.
- [81] J. Greindl, J. Hioe, N. Sorgenfrei, F. D. Morana, R. M. Gschwind, *J. Am. Chem. Soc.* **2016**, *49*, 15965–15971.
- [82] F. Aznar, C. Valde, *J. Am. Chem. Soc.* **2009**, *131*, 4031–4041.
- [83] Y. Schramm, F. Barrios-Landeros, A. Pfaltz, *Chem. Sci.* **2013**, *4*, 2760–2766.
- [84] F. H. Westheimer, K. Taguchi, *J. Org. Chem.* **1971**, *36*, 1570–1572.
- [85] M. C. Hansen, S. L. Buchwald, *Org. Lett.* **2000**, *2*, 713–715.
- [86] J. S. M. Samec, J. E. Bäckvall, *Chem. - A Eur. J.* **2002**, *8*, 2955–2961.
- [87] Z. Wang, X. Ye, S. Wei, P. Wu, A. Zhang, J. Sun, *Org. Lett.* **2006**, *8*, 999–1001.
- [88] M. Klusmann, L. Ratjen, S. Hoffmann, V. Wakchaure, R. Goddard, B. List, *Synlett* **2010**, *2010*, 2189–2192.
- [89] R. K. Harris, E. D. Becker, S. M. Cabral de Menezes, R. Goodfellow, P. Granger, *Magn. Reson. Chem.* **2002**, *40*, 489–505.
- [90] H.-H. Limbach, M. Pietrzak, S. Sharif, P. M. Tolstoy, I. G. Shenderovich, S. N. Smirnov, N. S. Golubev, G. S. Denisov, *Chem. - A Eur. J.* **2004**, *10*, 5195–5204.
- [91] H.-H. Limbach, M. Pietrzak, H. Benedict, P. M. Tolstoy, N. S. Golubev, G. S. Denisov, *J. Mol. Struct.* **2004**, *706*, 115–119.

4 Disulfonimides Versus Phosphoric Acids in Brønsted Acid Catalysis: The Effect of Weak Hydrogen Bonds and Multiple Acceptors on Complex Structures and Reactivity



Kerstin Rothermel, Matej Žabka, Johnny Hioe and Ruth M. Gschwind

J. Org. Chem., **2019**, accepted

DOI: 0.1021/acs.joc.9b01811

The NMR measurements for the hydrogen bond analysis and the structure determination were performed by **Kerstin Rothermel**. All chemical shift assignments were done by **Kerstin Rothermel**. **Kerstin Rothermel** and Dr. Matej Žabka contributed to the reactivity analysis. The ^{15}N -labeling of the DSI as well as the analysis of the binary *N*-alkyl-imine-complexes were done by Dr. Matej Žabka. The imine substrates were synthesized by all authors except Dr. Johnny Hioe. All computational studies were performed by Johnny Hioe.

Source of this chapter: <https://doi.org/10.1021/acs.joc.9b01811>

Reproduced with permission. All further permissions related to the material excerpted should be directed to the ACS. Text and figures may differ from the published version.

4.1. Abstract

In Brønsted acid catalysis, hydrogen bonds play a crucial role for reactivity and selectivity. However, the contribution of weak hydrogen bonds or multiple acceptors has been unclear so far, since it is extremely difficult to collect experimental evidence for weak hydrogen bonds. Here, our hydrogen bond and structural access to Brønsted acid/imine complexes was used to analyse BINOL-derived chiral disulfonimide (DSI)/imine-complexes. ^1H and ^{15}N chemical shifts as well as $^1J_{\text{NH}}$ coupling constants revealed for DSI/imine-complexes ion pairs with very weak hydrogen bonds. The high acidity of the DSIs leads to a significant weakening of the hydrogen bond as structural anchor. In addition, the five hydrogen bond acceptors of DSI allow an enormous mobility of the imine in the binary DSI-complexes. Theoretical calculations predict the hydrogen bonds to oxygen to be energetically less favored, however their considerable population is corroborated experimentally by NOE and exchange data. Furthermore, an *N*-alkyl-imine, which shows excellent reactivity and selectivity in reactions with DSI, reveals an enlarged structural space in complexes with the chiral phosphoric acid TRIP as potential explanation of its reduced reactivity and selectivity. Thus, considering factors such as flexibility and possible hydrogen bond sites is essential for catalyst development in Brønsted acid catalysis.

4.2. Introduction

In asymmetric synthesis, the substrate activation by a chiral catalyst has been established as a powerful strategy.^[1] Particularly, BINOL-derived Brønsted acids constitute a class of robust, highly enantioselective and extremely active catalysts available for many asymmetric transformations, including transfer hydrogenations, Strecker reactions, carbonyl additions and many others.^[1,2] One prominent example of these organocatalysts are chiral phosphoric acids (CPAs).^[1] Extensive NMR-studies of the binary complexes between different CPAs and aromatic *N*-aryl imines proved the formation of strong, charge-assisted hydrogen bonds in these catalysts/substrate-complexes, supported by a network of CH- π - and π - π -interactions.^[3-5] Thus, the induced stereoselectivity stems from the non-covalent interactions.^[6,7] However, for some transformations, even stronger Brønsted acids are required or at least show higher activities.^[8-12]

For this purpose, the groups of List and others reported the synthesis^[13-15] of disulfonimide catalysts (DSIs),^[16] which are more acidic than the CPAs and were successfully applied as catalysts for the transfer hydrogenation of *N*-alkyl imines.^[9]

4 Disulfonimides Versus Phosphoric Acids

Compared to *N*-aryl amines, the formed products are more basic and slow down the reaction by inhibiting the catalyst. In addition to the poor conversion, for the combination of CPA-catalysts and *N*-alkyl imines also disappointing stereoselectivities were observed. In contrast, the more acidic DSI-catalysts provided both high turnovers and astonishingly good enantioselectivities.^[9] In general, DSIs and other highly acidic catalysts have been applied in various reactions, in which the substrates are difficult to activate and the acidity of the CPAs is not sufficient.^[17–19]

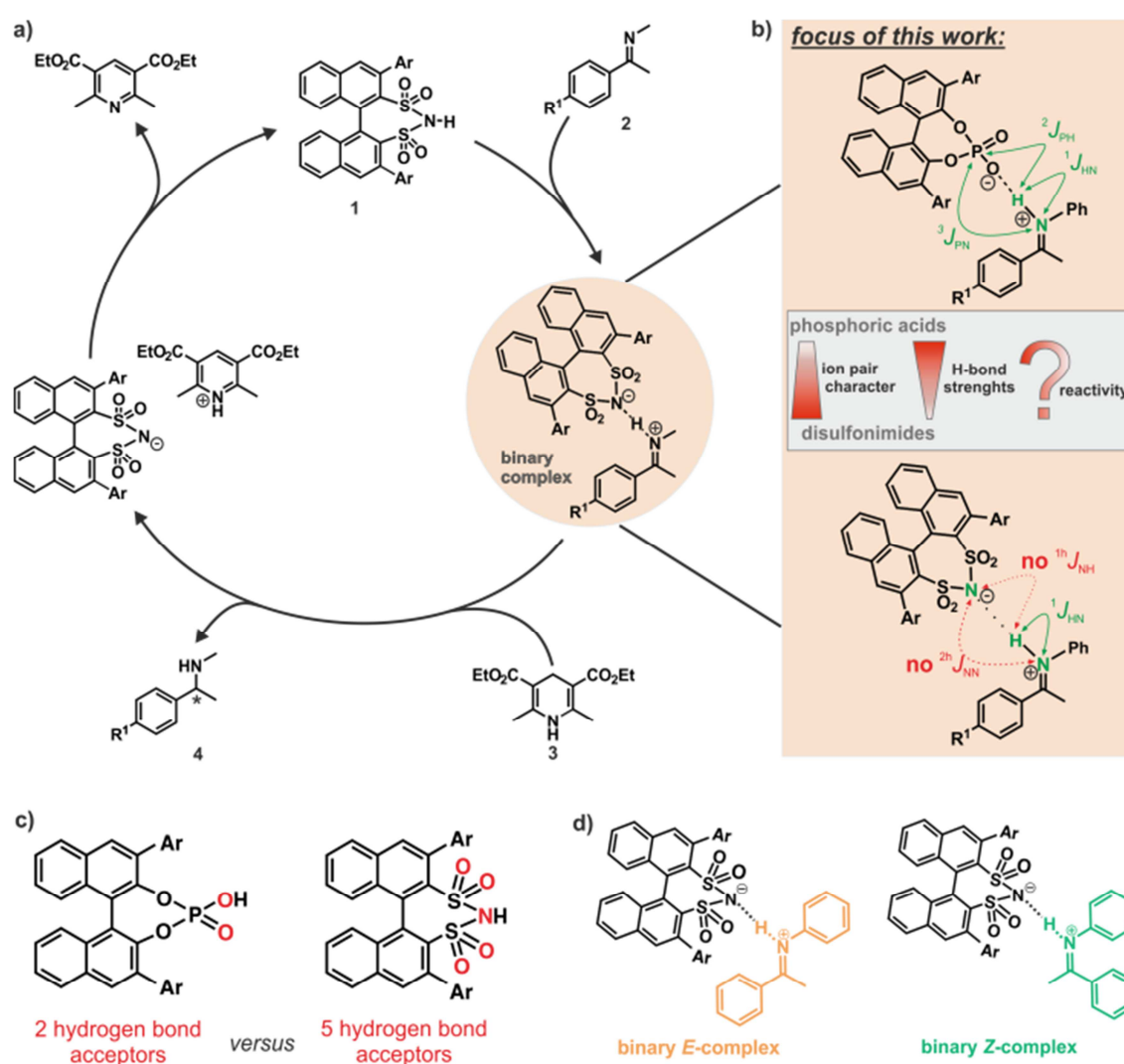


Figure 1. a) Assumed catalytic cycle for the DSI-catalyzed asymmetric transfer hydrogenation of *N*-alkyl imines **2** derived from that of CPAs. b) Focus of this study was a hydrogen bond as well as a structural analysis of DSI/imine-complexes regarding the influence of the weakened hydrogen bonds and the increased ion pair character. All results were compared to the previously investigated less acidic CPAs.^[3–5,20] Finally, the internal acidity of these different classes of catalysts was correlated to the reactivity in the transfer hydrogenation. c) In contrast to the CPAs, not only two but five possible hydrogen bond acceptors exist for the DSIs. d) The investigated binary *E*- and *Z*-complexes are shown.

4 Disulfonimides Versus Phosphoric Acids

The assumed catalytic cycle for the transfer hydrogenation with *N*-alkyl imines and DSI catalysts is similar to the proposed mechanism of the CPA-catalyst transfer hydrogenation^[21] and is shown in Figure 1. In the first step, the Brønsted acid catalyst **1** protonates the imine **2** and a pre-catalytic species, the binary complex, is formed. Subsequently, the Hantzsch ester **3** reduces the imine and the chiral amine **4** is formed as product. Finally, the catalyst **1** is regenerated by proton transfer.

In a Brønsted acid catalyzed Nazarov cyclization, a direct correlation between the pK_a -values of the catalysts and the observed reaction rate was found.^[22] For the cyclization, a faster reaction was observed for more acidic catalysts.^[22] In one of our previous studies, the internal acidity of different CPAs was compared with the reactivity in the transfer hydrogenation of *N*-aryl imines.^[5] There, it was shown that the reaction with the least acidic CPA was the fastest, while the slowest reaction was observed with the most acidic CPA.^[5] However, the most sterically hindered catalyst showed a drastic drop in reactivity. Since the formation of the binary complex (i.e. the binding of the imine) was similar to the other catalysts, most probably the binding of the Hantzsch ester is hindered.^[5] This suggested that the reaction rate of the transfer hydrogenation is not only dependent on the internal acidity of the catalyst but can be also modulated by other factors such as the steric demand of the 3,3'-substituents and the corresponding size of the binding pocket.^[5]

However, the use of stronger Brønsted acids rise the question, whether still binary complexes with charge-assisted hydrogen-bonds are present similar to the CPA/imine-complexes^[3,5] or whether pure ion pairs without hydrogen bond contribution are formed. As shown previously, the potential hydrogen bond is such a sensitive experimental indicator that the a hydrogen bond analysis can give information about the binding situation and even small structural changes within the binary complexes can be derived.^[3,5]

For CPA/imine-complexes, four highly conserved core structures were observed experimentally. Thus, in solution two different orientations (*type I* and *type II*) of each imine isomer (*E* and *Z*) inside the binary complex were detected.^[4] The structural investigations of various CPA complexes showed that the 3,3'-substituents affect the relative population of these core structures but not their existence.^[20] Despite the fact that low-temperature NMR spectroscopy was proven to be an excellent tool to investigate the occurring intermediates in Brønsted acid catalysis as well as the interactions between catalyst and substrates, up to now most of the NMR investigations are confined to CPAs or their derivatives.^[3-5,20,23,24] Similarly, the extensive computational studies within Brønsted acid catalysis focused mainly on CPAs.^[25-33] However, to our

4 Disulfonimides Versus Phosphoric Acids

knowledge, other acidic motifs and especially the promising DSI-catalysts have not been examined.

Therefore, in this study, we investigated the binary complexes of two DSIs with two *N*-aryl imines by low-temperature NMR-spectroscopy. A detailed hydrogen bond analysis, regarding ^1H and ^{15}N chemical shifts and coupling constants, as well as structural investigations were conducted. These results are compared with the corresponding CPA/imine complexes. Particularly, the effect of the increased number of hydrogen bond acceptors of the DSI compared to the CPA is addressed (Figure 1c). In addition, the differences of the more basic *N*-alkyl-imine in binary complexes with TRIP and DSI were compared. Finally, the expanded acidity range is correlated to the observed reaction rate in the transfer hydrogenation of imines.

4.3. Results and Discussion

4.3.1. Model system

In order to compare the NHN hydrogen bonds of binary DSI/imine-complexes with our previously investigated POHN hydrogen bonds of CPA/imine-complexes^[3,4,20] a detailed hydrogen bond and structural analysis was conducted. As catalysts we selected the commercially available DSIs **1e** and **1f** (Figure 2). To enable a comparison with our previous structural investigations on CPA/imine complexes^[3-5,20] and to reduce the severe chemical shift overlap the methoxy-substituted *N*-aryl imines **2a** and **2b** were chosen. ^{15}N labeling of the imine **2a** allowed to access $^1J_{\text{HN}}$ coupling constants. Furthermore, the imines **2a**, **2c** and **2d** were chosen for reactivity studies to consider the influence of electronic effects as well as isomerization. In addition, the highly acidic sulfonic acid (BINSa) **1g** was used in the reactivity comparison to expand the pK_a -range of the catalysts even more. Finally, the more basic *N*-alkyl imine **3a** was included into the structural investigations to address the special effects of *N*-alkyl versus *N*-aryl imines known from synthetic applications.^[9] To achieve the smallest possible signal linewidths, all NMR measurements were conducted in CD_2Cl_2 . All NMR spectra were recorded at 180 K to minimize exchange processes of the hydrogen-bonded protons.

4 Disulfonimides Versus Phosphoric Acids

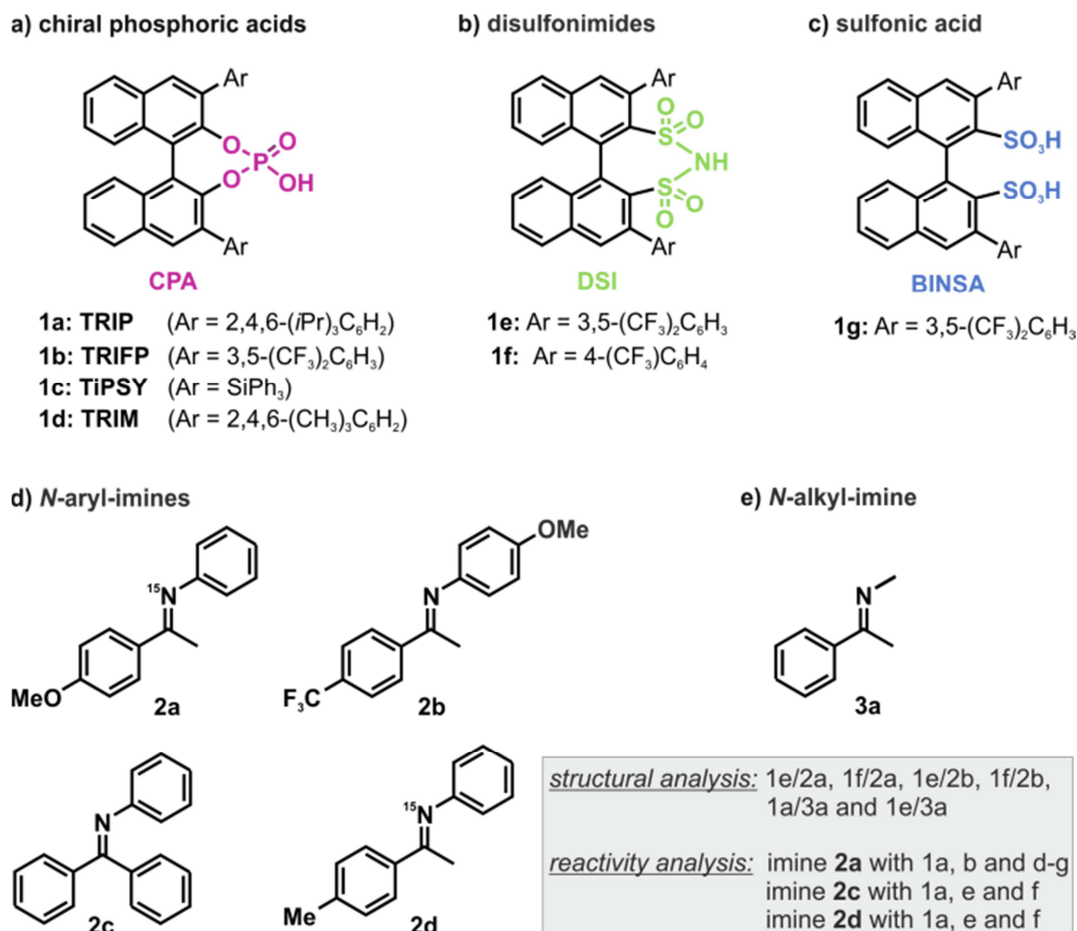


Figure 2. The binary complexes of different BINOL-derived Brønsted acids were analyzed. a) While the phosphoric acids (CPAs) 1a-1d were the main focus of our previous works.^[3-5,20] b) in this study the binary complexes between with the disulfonimides catalysts (DSIs) 1e and 1f were investigated. c) In addition, the sulfonic acid (BINSAs) 1g was used for the reactivity analysis. d) The hydrogen bond and structural analysis was done with imine 2a and 2b. Whereas, the reaction kinetics of imines 2a, 2c and 2d were investigated. e) Additionally, also the hydrogen bonds between the *N*-alkyl imine 3a and CPA 1a as well as DSI 1e were investigated.

4.3.2. Hydrogen bond analysis of the *N*-aryl-imine-complexes

In general, the position of the proton within a hydrogen bond is dependent on the acidity of the hydrogen bond donor and the basicity of the acceptor. Thus, with increasing acidity of the donor the proton is initially shifted towards the center of the hydrogen bond, where the strongest hydrogen bonds are formed, then further on to the hydrogen bond acceptor resulting in a hydrogen bond assisted ion pairs, and finally completely to the acceptor forming pure ion pairs (Figure 3a). To define the position of the proton within OHN hydrogen bonds in pyridine/acid-complexes Steiner and Denisov developed an empirical correlation of ¹H- and the ¹⁵N-chemical shifts.^[34,35] Recently, we showed that this correlation is also applicable to the POHN hydrogen bonds in CPA/imine-

4 Disulfonimides Versus Phosphoric Acids

complexes.^[3,5] For most of the binary CPA/imine-complexes, the ^1H chemical shifts of the hydrogen-bonded protons are above 16 ppm and follow a parabolic curve revealing very strong hydrogen bonds (Figure 3b).^[3,5] The position on the left upper half of the parabolic curve indicates hydrogen bond assisted ion pairs. In contrast to these CPA-complexes, those with DSIs exhibit high field shifts for both ^1H and ^{15}N . As a result, the DSI/imine-complexes are positioned far down on the left side of the Steiner-Limbach curve close to the almost pure ion pair with HBF_4 (Figure 3b). This position of the DSI-complexes on the curve shows that the proton within the hydrogen bond is significantly shifted towards the nitrogen as expected for the more acidic DSI-catalysts (Figure 3a). In general, ^1H and ^{15}N chemical shifts as well as the $^1J_{\text{NH}}$ coupling constants can be used to determine the hydrogen bond strengths. However, the ^1H chemical shift of the CPA/imine-complexes was significantly influenced by neighbourhood and shielding effects, whereas the ^{15}N chemical shift, which was directly correlated with the $^1J_{\text{HN}}$ coupling constant, is not so sensitive for these effects and could be used as an appropriate descriptor for the hydrogen bond strengths.^[3,5] For this reason the hydrogen bond analysis of the DSI-complexes was based on the ^{15}N chemical shifts. Especially, the *E*-configured DSI/**2a**-complexes show a ^{15}N chemical shift, which is similar to the HBF_4 -model system for purely ionic complexes, suggesting none or an extremely weak hydrogen bond. In contrast, for the investigated *Z*-complexes with DSI a position on the curve significantly closer to the CPA catalysts was found indicating a substantial contribution of a hydrogen bond within in these ion pairs (Figure 3b). However, from chemical shifts alone it is difficult to distinguish between hydrogen bond assisted ion pair and pure ion pair. Therefore, next the scalar couplings within and through the hydrogen bonds were investigated.

4 Disulfonimides Versus Phosphoric Acids

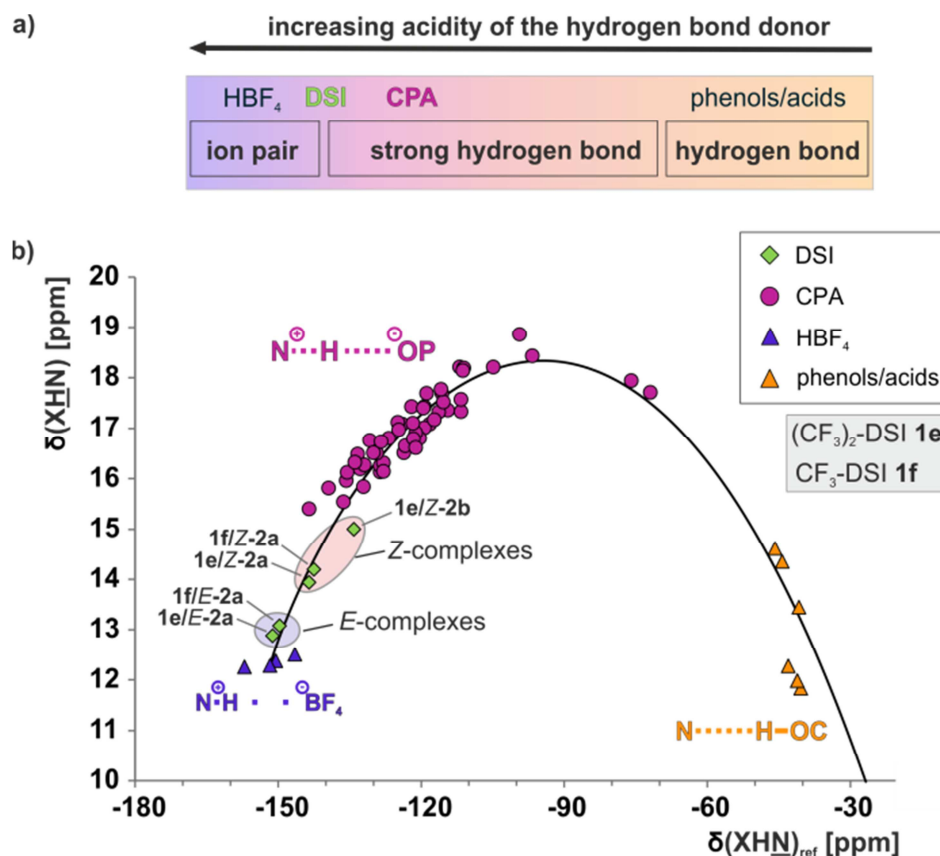


Figure 3. a) With increasing acidity of the hydrogen bond donor, the proton is shifted toward the nitrogen of the hydrogen bond acceptor until an ion pair is formed. b) Plot of $\delta_{(\text{OHN})}$ against $\delta_{(\text{OHN})_{\text{ref}}}$ of the hydrogen-bonded complexes. The binary complexes of DSIs **1e** and **1f** with the imines **2a** and **2b** (green diamonds) are complemented with the binary imine-complexes of HBF₄ (purple triangles), CPAs (pink cycles) and some carboxylic acids and phenols (orange triangles) from previous studies.^[3,5] All ¹⁵N chemical shifts are referenced [$\delta_{(\text{OHN})_{\text{ref}}} = \delta_{(\text{OHN})_{\text{exp}}} - 340\text{ppm}$] (for details and exact values see SI).

The observed $^1J_{\text{HN}}$ coupling constants are a measure for the binding strengths between proton and nitrogen of the imine, i.e. the larger the $^1J_{\text{HN}}$ the higher the ion pair character of the binary complex. The $^1J_{\text{HN}}$ coupling constants of the DSI/**2a**-complexes are larger than for all CPA-complexes ($^1J_{\text{HN}}$ between 82 and 86 Hz), but still slightly smaller than the $^1J_{\text{HN}}$ coupling constants of the completely protonated imine with HBF₄ (Figure 4). Due to signal broadening caused by exchange processes, for the *E*-imine **2a** only the $^1J_{\text{HN}}$ of the complex with (CF₃)₂-DSI **1e** was experimentally available ($^1J_{\text{HN}} = 90.6$ Hz). This coupling constant differs about 2 Hz from that observed for the completely protonated HBF₄/*E*-**2a**-complex ($^1J_{\text{HN}} = 92.5$ Hz) and thus reveals a very weak hydrogen bond for the (CF₃)₂-DSI **1e/2a**-complex. In all investigated CPA-complexes the $^1J_{\text{HN}}$ coupling constants for the *Z*-complexes are slightly smaller than for the *E*-complexes reflecting the reduced steric hindrance of the *Z*-imine allowing a closer approach to the catalyst

4 Disulfonimides Versus Phosphoric Acids

and thus stronger hydrogen bonds.^[3,5] This is also the case for the DSI-complexes. In accordance with this trend and the high acidity of DSI, the coupling constants for both *Z*-**2a**-complexes with DSIs **1e** and **1f** ($^1J_{\text{HN}} = 88.8$ Hz for both) are larger than those of the CPA-complexes ($^1J_{\text{HN}}$ between 80 and 85 Hz) and smaller than the respective *E*-complexes as well as the protonated imine with HBF_4 ($^1J_{\text{HN}} = 92.6$ Hz). These observations show unambiguously that for the *Z*-complexes a hydrogen bond assisted ion pair is present.

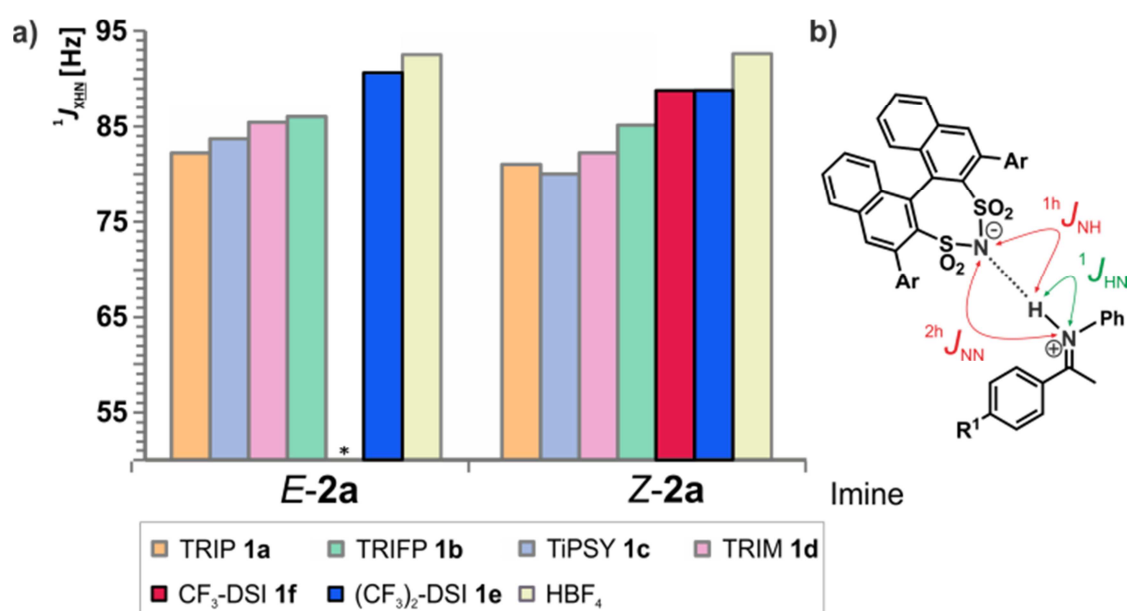


Figure 4. a) The experimental $^1J_{\text{HN}}$ coupling constants are shown for *E*- and *Z*-imine **2a** with the CPAs **1a**-**1d**^{[3] u Acidity}, HBF_4 ^[3] and the DSIs **1e** and **1f** (for values see SI). Due to fast chemical exchange the $^1J_{\text{HN}}$ of **1f**/*Z*-**2a** could not be determined (marked by an asterisk). b) Except the (green) $^1J_{\text{HN}}$ also trans-hydrogen bond scalar couplings (red $^1J_{\text{NH}}$ and $^2J_{\text{NN}}$) were addressed.

Next potential trans-hydrogen bond scalar couplings ($^1J_{\text{NH}}$ and $^2J_{\text{NN}}$) were addressed, since for magnetization transfers *via* $^2J_{\text{NN}}$ scalar couplings across NHN hydrogen bonds large coupling constants are expected. The first trans-hydrogen bond scalar coupling was measured across such hydrogen bonds between the nitrogen atoms of Watson-Crick base pairs in ^{15}N -labeled RNA and showed unexpectedly large through hydrogen bond scalar couplings of $^2J_{\text{NN}} \approx 7$ Hz.^[36] Later also $^3J_{\text{NC}}$ scalar couplings through COHN hydrogen bonds could be detected in proteins. Due to the additional bond the observed scalar coupling constants were one order of magnitude smaller (i.e. $^3J_{\text{CN}} = 0.2 - 0.9$ Hz)^[37] than the $^2J_{\text{NN}}$ coupling constants. Surprisingly, in our previous study of the CPA/imine-complexes for the POHN hydrogen bonds (similar to the protein situation) very large trans-hydrogen bond scalar couplings of $^3J_{\text{PN}} \approx 2$ -3 Hz were measured,

4 Disulfonimides Versus Phosphoric Acids

indicating the formation of strong, charge assisted hydrogen bonds.^[3] Comparable to the situation in RNA also in the DSI-complexes the additional oxygen atom within the hydrogen bond is missing. Therefore, compared to the $^3\text{h}J_{\text{PN}}$ coupling constants of the CPA-complexes, by far stronger trans-hydrogen bond $^2\text{h}J_{\text{NN}}$ scalar couplings were expected for hydrogen bonds with similar strengths. For more ionic DSI-complexes these through hydrogen bond scalar couplings should be the best sensor to probe the existence of weak hydrogen bonds. However, even with ^{15}N -labelled DSI **1e** neither the $^2\text{h}J_{\text{NN}}$ coupling nor the $^1\text{h}J_{\text{NH}}$ coupling between the acidic proton and DSI-nitrogen (see Figure 4b) were detectable in a 1D ^{15}N or 2D $^1\text{H},^{15}\text{N}$ -HSQC spectrum. Therefore, theoretical calculations were conducted and revealed for the **1e/E-2a**-complex a very small $^1\text{h}J_{\text{NH}}$ coupling constant of 0.5 Hz, and a $^2\text{h}J_{\text{NN}}$ coupling constant of 7 Hz. Considering the linewidths of the hydrogen bonded proton of the Z-complex in the ^1H -spectrum (half line widths ≈ 22.9 Hz), it is typical for conformational exchange and in none of the $^1\text{H},^{15}\text{N}$ -spectra through hydrogen bond cross peaks are detectable. Additionally, the ^{15}N -signal of the free labeled DSI is sharp (half line widths ≈ 3.5 Hz), while the ^{15}N -signal of the DSI in the binary complex is broadened significantly (for spectra see SI). Again, this line broadening suggests exchange processes, which would also explain the missing cross peaks *via* partial decoupling.

Overall the hydrogen bond analysis based on ^1H and ^{15}N chemical shift as well as $^1J_{\text{HN}}$ coupling constant revealed in all investigated DSI-complexes the formation of weak charge-assisted hydrogen bonds. Due to the higher acidity of the catalyst, the hydrogen bonds and the related effect as structural anchor is weakened compared to the CPAs. However, even with ^{15}N -labelled DSI it was not possible to detect any through hydrogen bond coupling (neither the $^2\text{h}J_{\text{NN}}$ coupling nor the $^1\text{h}J_{\text{NH}}$ coupling). This observation in combination with the line broadening of the ^{15}N -signal of the DSI in the binary complex suggests several exchange processes.

4.3.3. Structural investigations of the *N*-aryl-imine-complexes

To address the potential exchange processes suggested by the hydrogen bond analysis, next structural investigations of the DSI/imine-complexes were conducted. In this way the structural changes caused by the transition from strong to weak hydrogen bonds in the binary Brønsted acid/imine-complexes should be revealed. Furthermore, in this manner the differences of a single *versus* a multiple hydrogen bond acceptor catalyst within this system should become obvious.

4 Disulfonimides Versus Phosphoric Acids

In our previous studies of the CPA-complexes for each imine-isomer two different orientations of the imine (*type IE*, *type IIE*, *type IZ* and *type IIZ*) in the binary complex were found.^[4,20] These core structures are independent of the CPA and the substitution of the *N*-aryl-imine. In principle, two different exchange pathways between *type I* and *type II* are possible: Either the imine tilts inside the binary complex and switches the oxygen that constitutes the hydrogen bond, or the imine rotates around 180° under retention of the hydrogen bond. Although *type I* and *type II* are in fast exchange on the NMR time scale even at 180 K, it was possible to identify the effective exchange modes between the two orientations experimentally.^[4,20] For the *E*-imine in most of the investigated complexes exclusively the tilting-pathway was observed (with exception of TRIM), whereas for the *Z*-imines a combination of tilting and rotation was found.^[4,20] These tilting and rotation processes are fast on the NMR time scale. In contrast, the exchange of the free imine with the imine in the binary CPA-complex (dissociation/association of the imine) is slow on the NMR time scale.^[4,20]

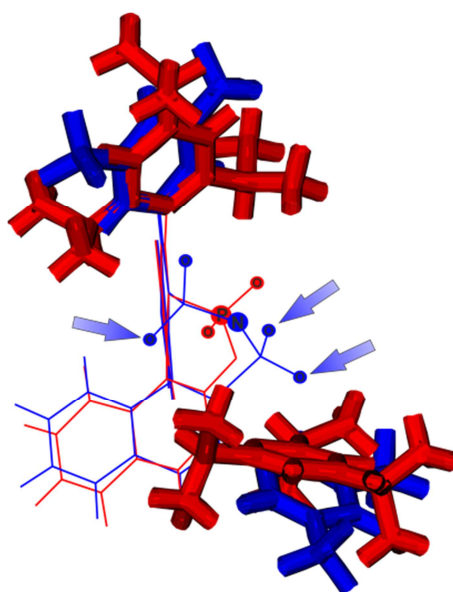


Figure 5. Overlay of TRIP 1a (red) and (CF₃)₂-DSI 1e (blue) showing the differences of the binding pockets (oxygen, phosphorus and nitrogen atoms are marked in respective colors). Indeed, the binding pocket of DSI is just slightly larger, but the hydrogen binding sites of the DSI (denoted with blue arrows) stick out of the binding pocket and are easier available for the substrate compared to TRIP. This in combination with the increased number of hydrogen bond acceptors may result in a higher mobility of the substrate.

Due to the significant weaker hydrogen bonds in the DSI/imine-complexes and the five readily accessible hydrogen binding sites of the DSI (Figure 5), additional exchange processes compared to CPAs were expected. Thus, for the first time a fast exchange

4 Disulfonimides Versus Phosphoric Acids

between the free imine and the *E*-imine in the binary complex was observed in the ^1H spectrum at 180 K (for spectra see SI), indicating a fast dissociation/association process of the *E*-imine. In addition, different sets of signals are observed for the *E*- and *Z*-imines within the complexes, but only one set of chemical shifts for the DSI-catalyst. This hints at a slow *E/Z*-isomerization in combination with various complex structures leading to an assimilation of the catalyst chemical shifts. Therefore, theoretical calculations were used to explore the structural space of the DSI/imine-complexes. These calculations predict for the *E*-imine one most stable complex structure, in which a hydrogen bond between the imine and the nitrogen of the DSI (*type E_N*) is formed (Figure 6a). The orientation of the imine in *type E_N* is equivalent to the *type IE*-structure of the CPA-complexes. In addition, various structures with a hydrogen bond to one of the oxygens (*type E_O*) were found, whereby two of these orientations are energetically preferred. One of them corresponds to *type IE* (here *type IE_O*) and the other to *type IIE* (here *type IIE_O*) of the CPA complexes (Figure 6b). In general, the calculations predict a stronger hydrogen bond to the nitrogen than to the different oxygens. Furthermore, initial movement calculations predict that for the exchanges between the different orientations of the imine not only the tilting-pathway (such as for most of the CPA-complexes) but also the rotation-mechanism is active.

To confirm the predicted structures experimentally, selective 1D ^1H , ^1H -NOESY as well as 2D NOESY spectra were recorded. The intense intermolecular NOEs between the *p*-methoxy group of the imine **2a** and the BINOL backbone of the DSI corroborate the existence of the energetically most favored structure (*type E_N*). Furthermore, the existence of the *type IIE_O* orientation was confirmed by a NOE between the *p*-methoxy group of the imine **2a** and the 3,3'-substituents of the DSI (green arrow in Figure 6b, for spectra see SI). Overall, the line broadening of the ^{15}N signal of the labeled $(\text{CF}_3)_2$ -DSI **1e** in the binary complex with imine **2a** (see the discussion about hydrogen bonds above), the detection of a single set of chemical shifts for the catalyst and the observed NOEs showed experimentally, that the hydrogen bond is not only formed to the strongest (here nitrogen), but also to the weaker hydrogen bond acceptors (here oxygen). Similar experimental data were found for the binary **1f/2a**- as well as the **1f/2b**-complex (for spectra and assignment see SI).

4 Disulfonimides Versus Phosphoric Acids

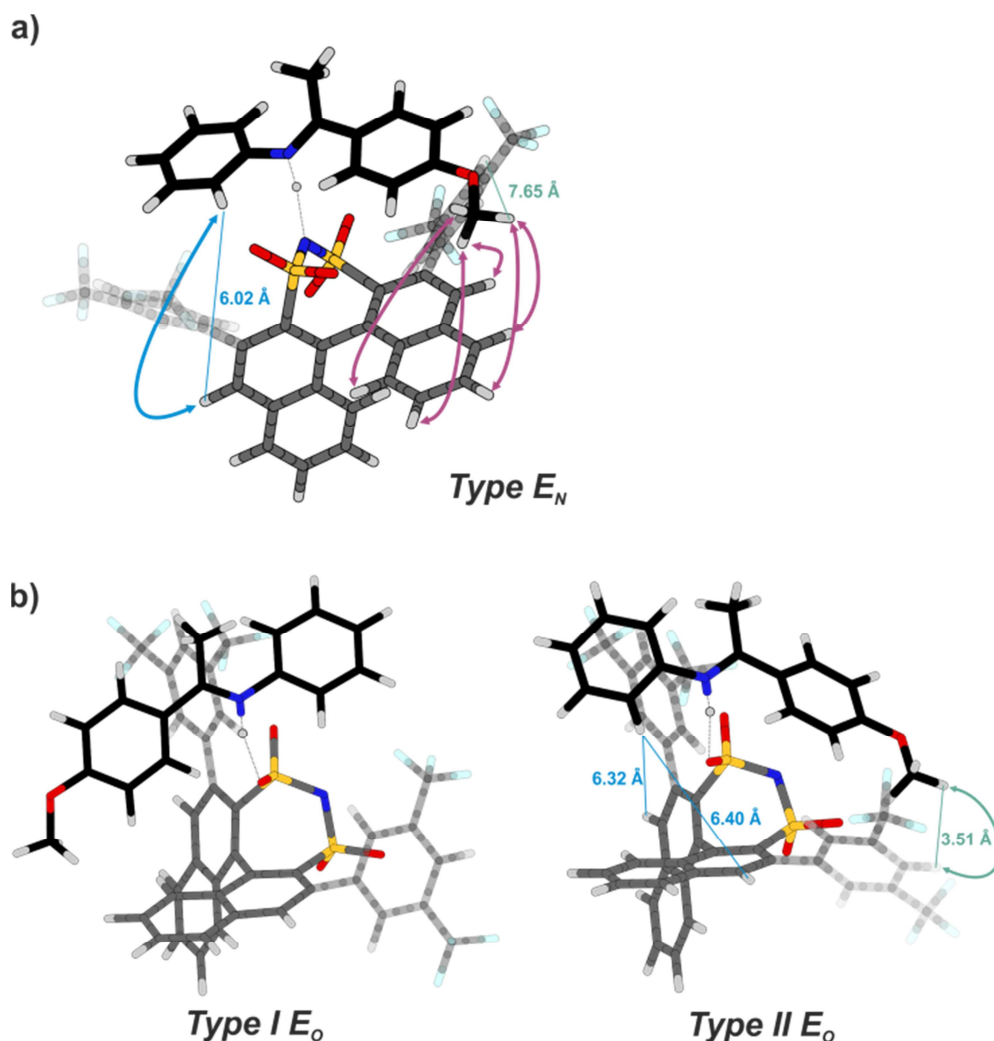


Figure 6. Calculations predict for the DSI/imine 2a-complexes the existence of a) one stable structure, where a hydrogen bond to the nitrogen of the DSI-catalyst (type EN), is formed and b) several orientations with a hydrogen bond to one of the oxygens. The two most stable structures are shown. type II E_o could be identified by the green NOE. All distances given in this figure were obtained from calculations.

Next, the structures of the DSI/Z-complexes were addressed. The theoretical calculations predict no structural preference for the Z-complexes despite the stronger hydrogen bonds compared to the E-complexes (see hydrogen bond analysis above). Thus, the sterically less demanding Z-imine seems to enable even more structural orientations within the binary complex than the corresponding E-complexes. This was confirmed by various sel. NOESY experiments, in which the NOE is transferred from the α -methyl-group to the whole catalyst-backbone as well as to the protons on the 3,3'-substituents (for spectra see SI). Even at smaller mixing times ($\tau_{\text{mix}} = 25$ ms) the same NOE pattern was observed, indicating a fast exchange between several hydrogen bonded species, which could not be identified unambiguously.

4 Disulfonimides Versus Phosphoric Acids

Overall the structural investigations of three different binary DSI-complexes showed a high mobility of the substrate inside the binding pocket of the DSI-catalyst due to the presence of five hydrogen bond acceptors. Despite theoretical calculations propose significantly weaker hydrogen bonds to the oxygens, these hydrogen bonds and the corresponding structures are considerably populated even at 180 K. Thus, the weaker and more diverse hydrogen within DSI/imine complexes do not longer act as tight structural anchor. Finally, in the *E*-complex the energetically most stable structure (*type E_N*) as well as another, where the hydrogen bond is formed to one of the oxygens (*type E_O*), was identified experimentally. On the other hand, for the complexes with the sterically less demanding *Z*-imines no structural preference was found. Despite this enormous flexibility of the binary complexes, the (*R*)-product is achieved in excess (imine **2a**: 70-78% *ee* with DSIs **1e** and **1f**, imine **2d**: 32-40% *ee* with DSIs **1e** and **1f**; see SI). Maybe also in DSI complexes the conformational and structural dynamics stabilize non-covalent interactions or minimize steric repulsion to achieve high selectivities, as proposed previously.^[38]

4.3.4. Reactivity analysis of CPAs, DSIs and BINSAs in transfer hydrogenations

Recently, for the CPA-catalyzed transfer hydrogenation of *N*-aryl-imines an inverse correlation between reactivity and internal acidity was obtained.^[5] This means that, the least acidic TRIP (i.e. forming the strongest hydrogen bond) shows the fastest overall reaction rate. Hence, it was investigated whether this correlation is also applicable for catalyst with different acidic functionalities. Therefore, the reactivities of imines **2a**, **2c** and **2d** were compared. However, no correlation was found between the different classes of catalysts (for data and discussion see SI). This may be due to the extremely weakening of the hydrogen bond in the DSI- and BINSAs-complexes. Thus, in DSI complexes not only the impact of the hydrogen bond as structural anchor in the pre-catalytic species is drastically decreased but also the influence of the hydrogen bond strengths on the reactivity gets lost.

4.3.5. Analysis of the binary *N*-alkyl-imine-complexes

Interestingly, the reaction outcome of the transfer hydrogenation of the more basic *N*-alkyl imines is extremely dependent on the used catalyst. While the highly acidic DSI catalysts were applied successfully and obtain the product in excellent yields and stereoselectivities, the less acidic CPA catalysts provided only disappointing enantioselectivities and low conversions.^[9] To figure out if exclusively the high differences in acidity of the catalysts are responsible for these observations, also the

4 Disulfonimides Versus Phosphoric Acids

pre-catalytic, binary complexes of imine **3a** with TRIP **1a** and (CF₃)₂-DSI **1e** at 180 K were analyzed.

Initially, the analysis of the binary TRIP/**3a**-complex revealed that apart the *E*- and *Z*-complexes, various other hydrogen bonded species are present (Figure 7, top spectrum). The additional species were not identified, but selective 1D ¹H,¹H-NOESY experiments showed that in two of these species the *Z*-imine and in the third the *E*-imine is involved (for spectra see SI). Most probably some of these complexes are dimeric species, which were observed previously in the TRIM/*N*-aryl-imine-complexes.^[20] The population of the additional *Z*-species is significantly higher compared to the complemented *E*-species, most likely due to the less sterical demand of the *Z*-imine. Furthermore, a dimeric species of the phosphoric acid was identified.^[3] Under the assumption that the transfer hydrogenation of the *N*-alkyl-imines also proceeds through the transition states of the *Z*-imine, as previously proposed for the *N*-aryl-imines,^[39] these off-cycle equilibria of the *Z*-imine reduce the amount of the reactive species and may result in a reduced reactivity. Furthermore, this is the first time that we observed an enlarged structural space (two additional *Z*-imine and one additional *E*-imine complex) in the core structures of TRIP/imine complexes in comparison to our previously reported *N*-aryl imine complexes,^[3-5,20] which may explain the low enantioselectivity with TRIP (26 % *ee*).

Furthermore, for the CPA-catalysts a correlation between their reactivity in the transfer hydrogenation of *N*-aryl-imines and the internal acidity was found: The least acidic TRIP (i.e. forming the strongest hydrogen bond) shows the fastest overall reaction rate.^[5] Thus, also the hydrogen bonds of the TRIP/**3a**-complex were analyzed. The position of the TRIP/**3a**-complexes on the Steiner-Limbach curve (see SI) and the ¹J_{HN} coupling constant of the binary *E*-complex (¹J_{HN} ≈ 85 Hz) revealed the formation of a charge-assisted hydrogen bond. However, the observed hydrogen bond is weakened compared to the CPA/*N*-aryl-imine-complexes. The weakening of the hydrogen bond is also indicated by the fact, that for the major *E*- and *Z*-complexes no magnetization is transferred from the hydrogen bonded proton to the phosphorus in a ¹H,³¹P-HMBC spectrum. In contrast, for the CPA/*N*-aryl-imine-complexes, which form stronger hydrogen bonds, this magnetization transfer was observed. Since, the weakening of a hydrogen bond comes along with an increased distance between the hydrogen bonded proton and proton-donor (TRIP), the through hydrogen bond magnetization transfer is complicated. Taking into account, that for weaker hydrogen bonds lower reactivities in

4 Disulfonimides Versus Phosphoric Acids

the CPA-catalysed transfer hydrogenation of *N*-aryl imines were observed,^[5] the even more weakened hydrogen bonds of the TRIP/*N*-alkyl-imine-complex may also be a reason for the disappointing reactivity.

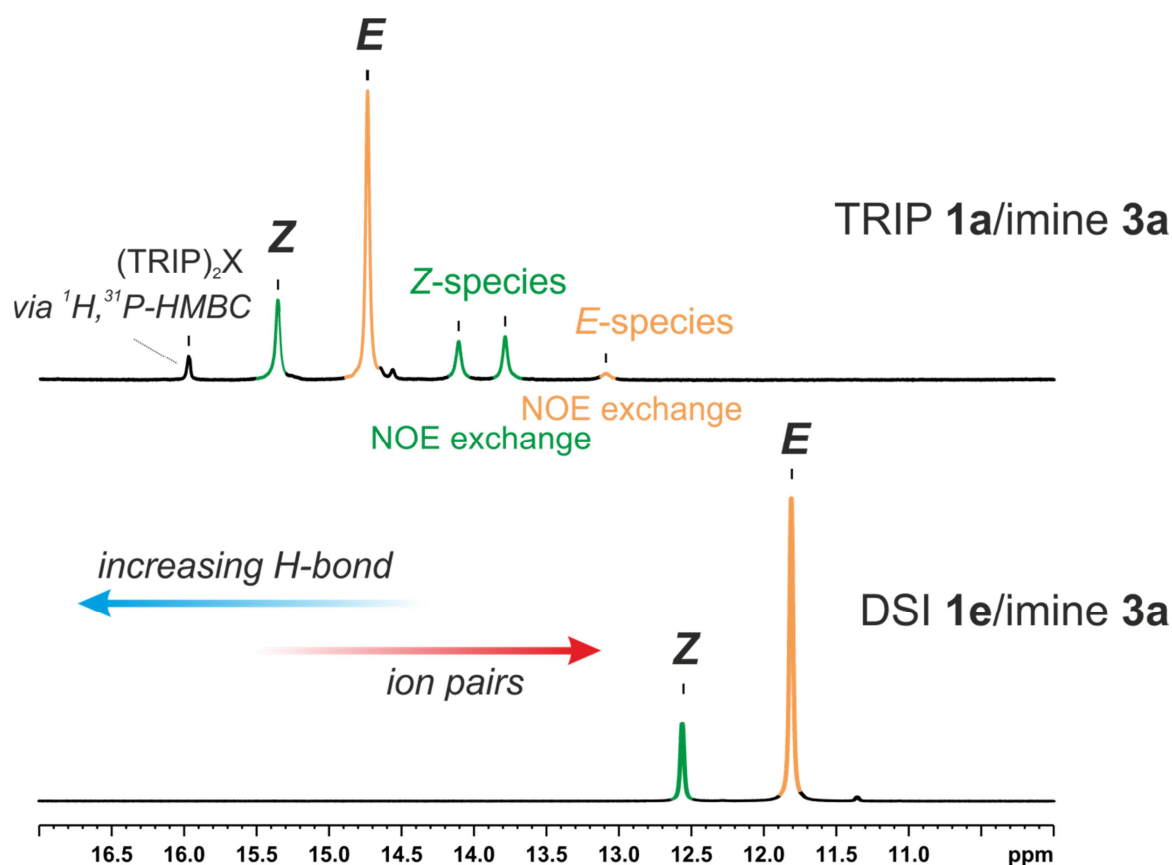


Figure 7. ^1H NMR spectra of the hydrogen bond region of the TRIP **1a/3a** and DSI **1e/3a** binary complexes in CD_2Cl_2 at 180 K, showing the presence of various hydrogen bonded species with TRIP. In contrast with the $(\text{CF}_3)_2$ -DSI only the major *E*- and *Z*-complexes were observed.

In contrast, in the ^1H -spectrum of the binary $(\text{CF}_3)_2$ -DSI **1e/3a**-complex only two hydrogen bonded species, which could be assigned as binary *E*- and *Z*-complex, were observed (Figure 7, bottom spectrum). The analysis of the Steiner-Limbach curve showed that these *E*- and *Z*-complexes are positioned in the region of the pure ion pairs (see SI). Nevertheless, the $^1J_{\text{HN}}$ coupling constant of the $(\text{CF}_3)_2$ -DSI **1e/E-3a**-complex (around 91 Hz) is still slightly lower than the coupling constant in the pure ion paired $\text{HBF}_4/\text{E-2a}$ -complex (92.5 Hz, see above), indicating a very minor contribution of the hydrogen bond. Thus, also for the DSI/*N*-alkyl-imine-complex the hydrogen bond is still present and can be decisive for the reactivity and selectivity. Again, weak hydrogen bond, possible switching between various DSI hydrogen bond donors and a large binding pocket allow the mobility of the imine. These properties, coupled to the smaller

4 Disulfonimides Versus Phosphoric Acids

size of the *N*-methyl substituent compared to *N*-phenyl, result in a fast exchange between all the possible complex structures and give only averaged NMR signals for each *E*- and *Z*-configurations even at 180 K.

Overall, the analysis of TRIP **1a**/*N*-methyl imine complex showed the presence of various hydrogen-bonded species, which might lower the reactivity and selectivity due to the competition and off-cycle equilibria. For highly acidic DSI **1e**/*N*-methyl imine complex, only two structures, specifically an *E*- and a *Z*-complex, were observed. In this case, off-cycle equilibria were not detectable. This may give a hint that the change in core structures could be decisive for the reaction outcome.

4.4. Conclusion

A hydrogen bond analysis of the binary complexes consisting of imines and disulfonimide (DSI) catalysts is performed and compared to chiral phosphoric acid (CPA) catalysts. With the highly acidic DSI catalysts, complexes with a high ion pair character were formed, but unexpectedly still weak hydrogen bonds were detected. By means of NMR spectroscopy, these hydrogen bonds were analyzed using the Steiner-Limbach curve and the chemical shifts as well as the observed $^1J_{\text{NH}}$ coupling constants suggest the formation of very weak hydrogen bonds. Exchange line broadening and the lack of magnetization transfers across hydrogen bonds indicate several exchange processes of the imine.

The weakening of the structural anchor allows a high mobility of the substrate inside the pocket. Additionally, the presence of multiple hydrogen bonding sites (four oxygens and one nitrogen) results in increased structural flexibility and reveals additional entropic contributions in the DSI-complexes. To identify the present species in the binary complex a structural analysis was conducted. Calculations predicted out of a multitude of structures three energetically most favored *E*-imine complexes (*type E_N*, *type IE_O* and *type IIE_O*) in a fast exchange *via* rotation and dissociation. Even though, these processes are fast on the NMR time scale, the existence of at least two structures with a hydrogen bond to the nitrogen or oxygen (*type E_N* and *type IIE_O*) were confirmed by various NOESY measurements. Thus, the experiments show that not only the strongest possible hydrogen acceptor (nitrogen) is engaged in hydrogen bonding, which should be considered in the future development of catalyst design.

4 Disulfonimides Versus Phosphoric Acids

In the transfer hydrogenation of *N*-alkyl imines, CPAs exhibit low activity and selectivity compared to DSIs. In comparison to the previously investigated *N*-aryl-imines, for an *N*-alkyl-imine several additional complex structures with TRIP were found. These additional structures and their equilibria may contribute to the poor performance of TRIP. In contrast, for the corresponding DSI-complexes only the typical binary *E*- and *Z*-complexes were observed.

Overall this study shows that a high structural flexibility is not in contrast to a good performance of a catalytic system.

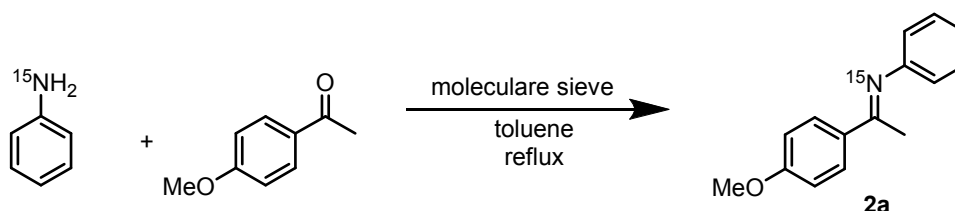
4 Disulfonimides Versus Phosphoric Acids

4.5. Supporting information

4.5.1. Synthesis of Imine Substrates

The imines were prepared according to a modified literature procedure.^[3,39] The toluene was used either in p.A. quality or was dried by refluxing over sodium. The used ¹⁵N-enriched aniline was purchased from Sigma Aldrich. All imines were synthesized in accordance to our previous publications.^[3,39]

(E)-1-(4-methoxyphenyl)-N-phenylethan-1-imine (98% ¹⁵N) 2a



Molecular sieves 4 Å (9.8 g) were activated by 450°C under reduced pressure. Under argon atmosphere 4-methoxyacetophenone (2.16 g, 14.3 mmol, 1.3 eq) and aniline (98% ¹⁵N, 1 ml, 1.02 g, 11.0 mmol) were added to the Schlenk flask and dissolved in 33 ml toluene. The solution was heated to reflux overnight with a drying tube filled with CaCl₂. The molecular sieves were removed, and the orange solution was concentrated under reduced pressure. The remaining solid was recrystallized from diethylether at -20°C. The product was obtained as yellow solid.

¹H-NMR (400.1 MHz, CD₂Cl₂) δ_H [ppm] = 7.95 (m, 2H, Aryl-H), 7.35 (m, 2H, Aryl-H), 7.07 (m, 1H, Aryl-H), 6.96 (m, 2H, Aryl-H), 6.77 (m, 2H, Aryl-H), 3.86 (s, 3H, -OCH₃), 2.18 (d, ³J_{HN} = 1.76 Hz, -CH₃)

¹³C-NMR [¹H] (100.6 MHz, CD₂Cl₂): δ_C [ppm] = 164.5, 161.9, 152.5, 132.5, 129.3, 129.2, 123.2, 119.9, 113.9, 55.8, 17.2

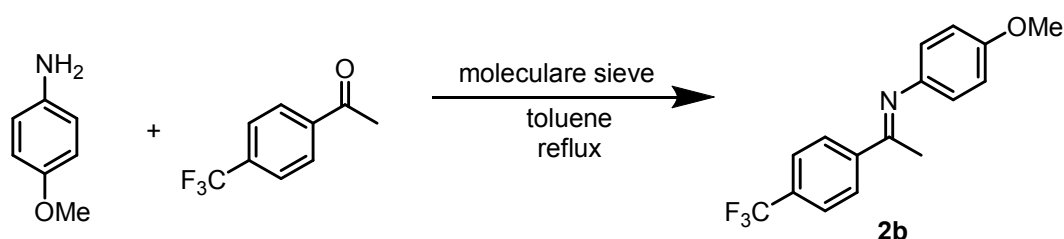
¹⁵N-NMR (40.5 MHz, CD₂Cl₂): δ_N [ppm] = 325.5

¹H- and ¹³C-spectra were in accordance with the literature.^[40]

For the reaction kinetics the imine **2a** was used in its unlabeled form. The synthesis was done according to this procedure only by using unlabeled aniline.

4 Disulfonimides Versus Phosphoric Acids

(E)-1-(4-trifluoromethyl)-N-phenylethan-1-anisidine **2b**



Molecular sieves 4 Å (9.7 g) were activated by 450°C under reduced pressure. Under argon atmosphere 4-trifluoromethylacetophenone (2.72 g, 14.3 mmol, 1.3 eq) and 4-anisidine (1.37 g, 11.0 mmol) were added to the Schlenk flask and dissolved in 33 ml toluene. The solution was heated to reflux overnight with a drying tube filled with CaCl₂. The molecular sieves were removed, and the reaction solution was concentrated under reduced pressure. The remaining solid was recrystallized from a diethylether/pentan-mixture (1:1) at -20°C. The product was obtained as yellow needles.

¹H-NMR (400.1 MHz, CD₂Cl₂) δ_H [ppm] = 8.10 (d, ³J_{HH} = 8.1 Hz, 2H), 7.71 (d, ³J_{HH} = 8.3 Hz, 2H), 6.93 (m, 2H), 6.76 (dm, 2H), 3.81 (s, 3H), 2.27 (s, 3H)

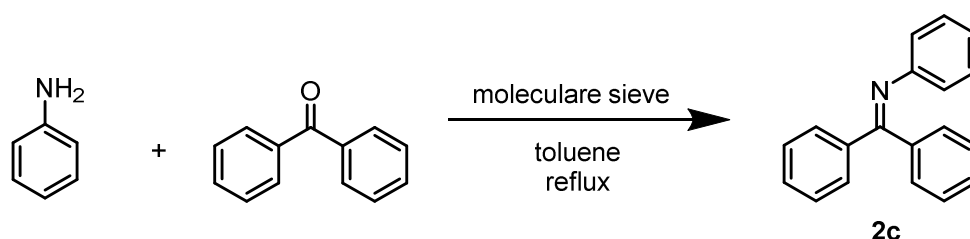
¹³C-NMR {¹H} (100.6 MHz, CD₂Cl₂): δ_C [ppm] = 164.5, 156.7, 144.6, 143.5, 127.9, 125.6, 121.0, 114.6, 55.8, 17.4

¹⁹F-NMR {¹H} (376 MHz, CD₂Cl₂): δ_F [ppm] = - 62.9

¹⁵N-NMR (40.5 MHz, CD₂Cl₂): δ_N [ppm] = 337.3

4 Disulfonimides Versus Phosphoric Acids

N,1,1-triphenylmethanimine **2c**



Molecular sieves 4 Å (10.0 g) were activated by 450°C under reduced pressure. Under argon atmosphere benzophenone (2.5 g, 14.0 mmol, 1.3 eq) and aniline (1 ml, 1.02 g, 11.0 mmol) were added to the Schlenk flask and dissolved in 33 ml toluene. The solution was heated to reflux overnight with a drying tube filled with CaCl₂. The molecular sieves were removed, and the reaction solution was concentrated under reduced pressure. The remaining solid was recrystallized from diethyl ether at -20°C. The product was obtained as a yellow solid.

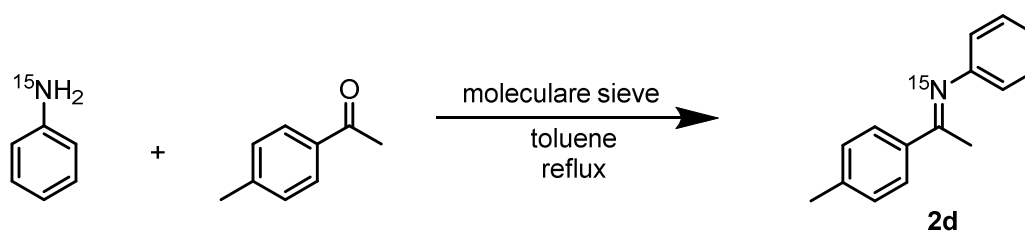
¹H-NMR (400.1 MHz, CD₂Cl₂): δ_H = 7.77 (m, 2H, Aryl-H), 7.50 (m, 1H, Aryl-H), 7.42 (m, 2H, Aryl-H), 7.33 - 7.26 (m, 3H, Aryl-H), 7.18 - 7.10 (m, 4H, Aryl-H), 6.95 (m, 1H, Aryl-H), 6.78 (m, 2H, Aryl-H)

¹³C-NMR {¹H} (100.6 MHz, CD₂Cl₂): δ_C [ppm] = 168.3, 151.9, 139.9, 136.7, 131.1, 129.7, 129.6, 128.8, 128.8, 128.5, 128.2, 122.2, 121.0

¹⁵N-NMR (60.8 MHz, CD₂Cl₂): δ_N [ppm] = 330.2

4 Disulfonimides Versus Phosphoric Acids

(E)-1-(4-methylphenyl)-N-phenylethan-1-imine (98% ^{15}N) **2d**



Molecular sieves 4 Å (9.8 g) were activated by 450°C under reduced pressure. Under argon atmosphere 4-methylacetophenone (2.27 mL, 2.28 g, 17.0 mmol, 1.6 eq) and aniline (98% ^{15}N , 1 ml, 1.02 g, 11.0 mmol) were added to the Schlenk flask and dissolved in 33 ml toluene. The solution was heated to reflux overnight with a drying tube filled with CaCl_2 . The molecular sieves were removed, and the reaction solution was concentrated under reduced pressure. The remaining solid was recrystallized from petroleum ether at -20°C. The product was obtained as yellow needles.

$^1\text{H-NMR}$ (400.1 MHz, CD_2Cl_2) δ_{H} [ppm] = 7.86 (m, 2H, Aryl-H), 7.34 (m, 2H, Aryl-H), 7.25 (m, 2H, Aryl-H), 7.06 (m, 1H, Aryl), 6.76 (m, 2H), 2.40 (s, 3H, - CH_3) 2.18 (d, $^3J_{\text{HN}} = 1.76$ Hz, 3H, - CH_3)

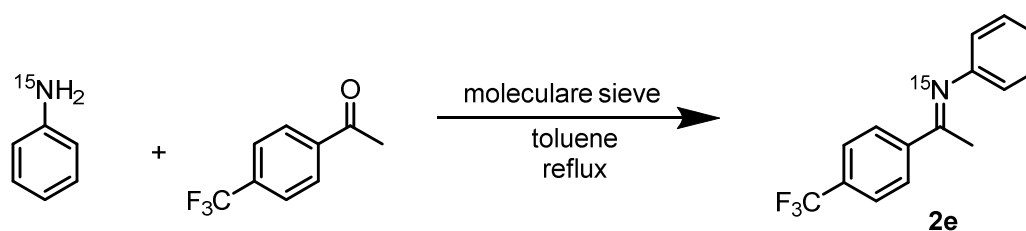
$^{13}\text{C-NMR}$ [^1H] (100.6 MHz, CD_2Cl_2): δ_{C} [ppm] = 165.3, 152.4, 141.2, 133.9, 129.5, 129.3, 127.5, 123.3, 119.7, 21.5, 17.4

$^{15}\text{N-NMR}$ (40.5 MHz, CD_2Cl_2): δ_{N} [ppm] = 328.9

^1H - and ^{13}C -spectra were in accordance with the literature.^[41]

4 Disulfonimides Versus Phosphoric Acids

(E)-1-(4-trifluoromethylphenyl)-N-phenylethan-1-imine (98% ¹⁵N) **2e**



Molecular sieves 4 Å (5 g) were activated by 350°C under reduced pressure. Under argon atmosphere 4-trifluoromethylacetophenone (3.66 g, 19.5 mmol, 1.3 eq) and aniline (98% ¹⁵N, 1.40 ml, 1.40 g, 15.0 mmol) were added to the Schlenk flask and dissolved in 25 ml toluene. The solution was heated to reflux overnight with a drying tube filled with CaCl₂. The molecular sieves were removed, and the reaction solution was concentrated under reduced pressure. The remaining solid was recrystallized from methanol at -20°C. The product was obtained as yellow needles.

¹H-NMR (400.1 MHz, CD₂Cl₂) δ_H [ppm] = 8.11 (m, 2H, Aryl-H), 7.72 (m, 2H, Aryl-H), 7.37 (m, 2H, Aryl-H), 7.11 (m, 1H, Aryl), 6.79 (m, 2H), 2.25 (s, 3H, -CH₃)

¹³C-NMR {¹H} (100.6 MHz, CD₂Cl₂): δ_C [ppm] = 164.5, 151.7, 143.2, 132.1, 129.4, 128.0, 125.6, 124.6, 123.9, 119.5, 17.5

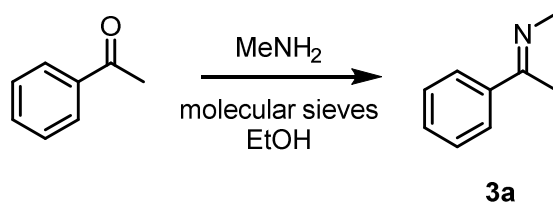
¹⁵N-NMR (40.5 MHz, CD₂Cl₂): δ_N [ppm] = 338.2

¹⁹F-NMR {¹H} (376 MHz, CD₂Cl₂): δ_F [ppm] = - 63.1

¹H- and ¹³C-spectra were in accordance with the literature.^[42]

4 Disulfonimides Versus Phosphoric Acids

(E)-N-methyl-1-phenylethan-1-imine **3a**



N-Methyl imine **3a** was synthesized following the literature procedure.^[9] A solution of methylamine (33 % in EtOH, 5 mL, 40 mmol, 4 eq.) was added to a flask containing molecular sieves 4 Å (2.5 g). The mixture was cooled to 0° C, and freshly distilled acetophenone (1.2 mL, 10 mmol) was added. The mixture was stirred at rt for 3 days, filtered, and the solid residue washed with DCM. The solvents were then evaporated under reduced pressure to give the product as a clear yellow oil (0.88 g, 66 % yield).

¹H-NMR (400.1 MHz, CDCl₃) δ_H [ppm] 7.82 – 7.75 (m, 2H), 7.42 – 7.33 (m, 3H), 3.33 (s, 3H), 2.23 (s, 3H).

¹³C-NMR {¹H} (100.6 MHz, CDCl₃) δ_C [ppm] 167.2, 141.2, 129.4, 128.0, 126.5, 39.5, 15.1.

¹H- and ¹³C-spectra were in accordance with the literature.^[9]

4 Disulfonimides Versus Phosphoric Acids

4.5.2. Sample preparation of binary complexes in CD_2Cl_2

The DSI-catalyst was weighted directly into a 5 mm NMR-tube and dried for 20 min at 120°C under reduced pressure. Under argon atmosphere the imine was added. CD_2Cl_2 (0.6 ml) and 1.0 ml of tetramethylsilane atmosphere were added to the tube. If not mentioned a 1:1 catalyst/imine-ratio was used. Despite careful sample preparation hydrolysis of the imine could not be completely prevented. Therefore, the catalyst/imine-ratios are slightly different than 1:1. A concentration 50 mmol/L was used for all samples, except the sample with the ^{15}N -labeled DSI (30 mM). Between the measurements the samples were stored at -80°C.

4.5.3. Spectrometer data

NMR experiments were performed on Bruker Avance III HD 400 MHz spectrometer, equipped with 5 mm BBO BB-1H/D probe head with Z-Gradients and a Bruker Avance III HD 600 MHz spectrometer, equipped with a 5 mm CPPBBO BB- $^1\text{H}/^{19}\text{F}$. Temperature was controlled in the VT-experiments by BVT 3000 and BVTE 3900. For NMR measurements employing standard NMR solvents 5 mm NMR tubes were used. All pulse programs used are standard Bruker NMR pulse programs. NMR Data were processed, evaluated and plotted with TopSpin 3.2. Further plotting of the spectra was performed with Corel Draw X7. ^1H and ^{13}C chemical shifts were referenced to TMS or the respective solvent signals. The heteronuclei ^{15}N and ^{19}F and were referenced, employing $\nu(\text{X}) = \nu(\text{TMS}) \times \Xi_{\text{reference}} / 100 \%$ according to Harris *et al.*^[43] The following frequency ratios and reference compounds were used: $\Xi(^{15}\text{N}) = 10.132912$ (lq. NH_3) and $\Xi(^{19}\text{F}) = 94.094011$ (CCl_3F). All pulse programs used are standard Bruker NMR pulse programs.

4 Disulfonimides Versus Phosphoric Acids

4.5.4. NMR Parameters and Spectra of the binary DSI/imine Complexes

Experimental ^1H and ^{15}N chemical shifts and $^1J_{\text{HN}}$ coupling constants

Table S 1: NMR parameters ($\delta(\text{NHN})$, $\delta(\text{NHN})$ and $^1J_{\text{HN}}$) of DSI/imine-complexes in CD_2Cl_2 at 180K. [a] value obtained from ^1H , ^{15}N -HMBC; [b] at 230 K; [c] at 170 K. (n.d. = not determined)

	$\delta(\text{NHN})$ [ppm]	$\delta(\text{NHN})$ [ppm]	$^1J_{\text{HN}}$ ^[b] [Hz]
$(\text{CF}_3)_2$ -DSI 1e/2aE	12.86	188.70	90.6 ^[b]
$(\text{CF}_3)_2$ -DSI 1e/2aZ	13.92	196.4	88.8 ^[b]
CF_3 -DSI 1f/2aE	13.06	190.20	n.d.
CF_3 -DSI 1f/2aZ	14.18	197.4	88.8 ^[c]
$(\text{CF}_3)_2$ -DSI 1e/2bE	14.24	n.d.	-
$(\text{CF}_3)_2$ -DSI 1e/2bZ	14.99	205.8 ^[a]	~80.6 ^[a]
CF_3 -DSI 1f/2bE	14.66	n.d.	-
CF_3 -DSI 1f/2bZ	15.16	n.d.	-
$(\text{CF}_3)_2$ -DSI 1e/3aE	11.81	182.8 ^[a]	91-92 ^[a]
$(\text{CF}_3)_2$ -DSI 1e/3aZ	12.56	190.5 ^[a]	-
TRIP 1a/3aE	14.74	195.4 ^[a]	84.6 ^[a]
TRIP 1a/3aZ	15.36	201.5 ^[a]	-
BINSA 1g/2eE	13.13	202.1	90.2

4 Disulfonimides Versus Phosphoric Acids

4.5.5. Complete set of spectra

$(CF_3)_2$ -DSI **1e/2a** (CD_2Cl_2 , 180K)

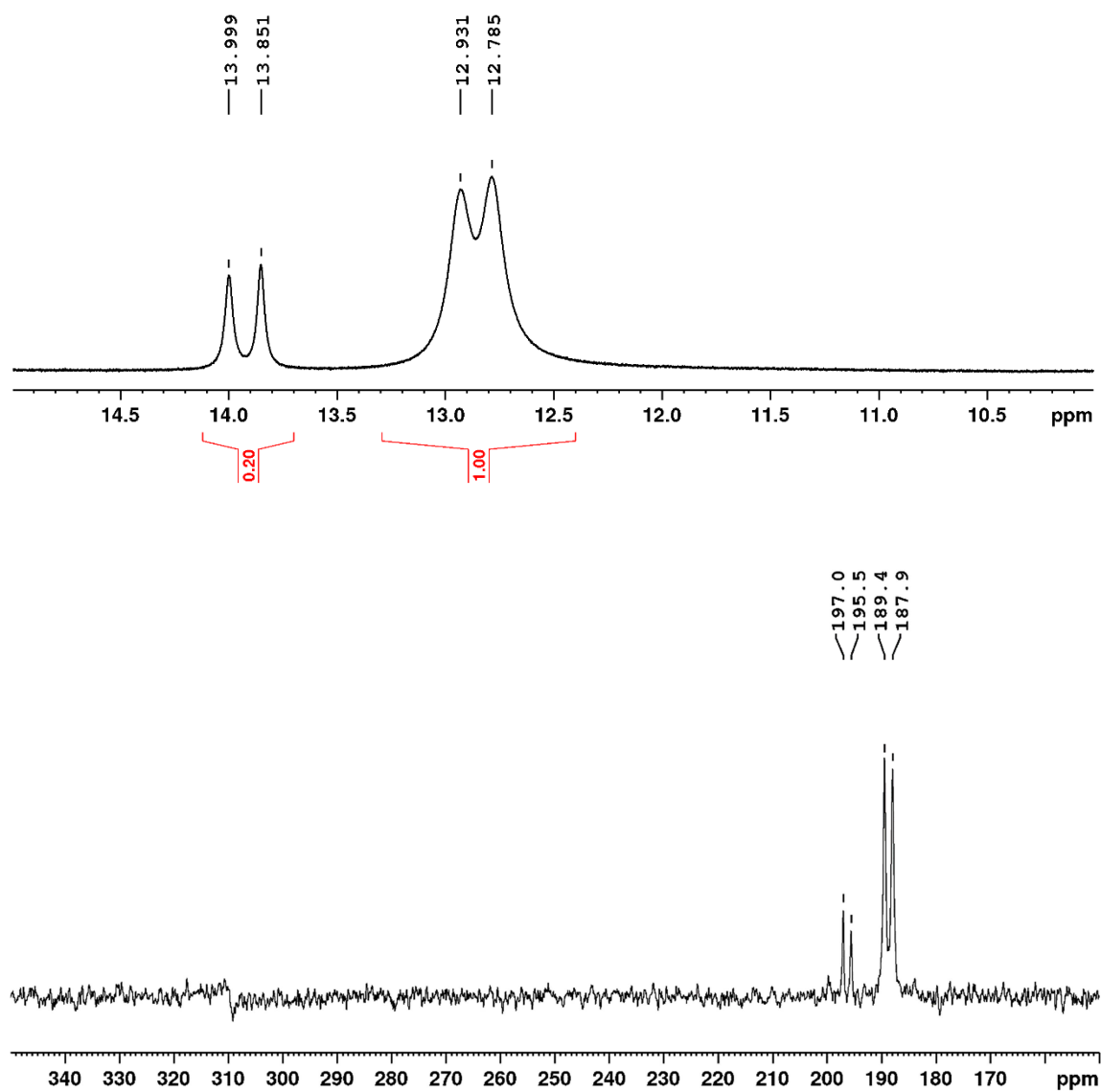


Figure S 1: Low field section of the 1H spectrum (BF1 = 600.0 MHz; *zg30*; NS = 32; DS = 0; TD = 65536; D1 = 1; SW = 26.04; O1P = 12) and the ^{15}N spectrum (BF1 = 60.8 MHz; *zg30*; NS = 1024; DS = 0; TD = 65536; SW = 507.5 ppm; O1P = 200) of the $(CF_3)_2$ -DSI **1e/2a**-complex in CD_2Cl_2 at 180K.

4 Disulfonimides Versus Phosphoric Acids

CF₃-DSI 1f/2a (CD₂Cl₂, 180K)

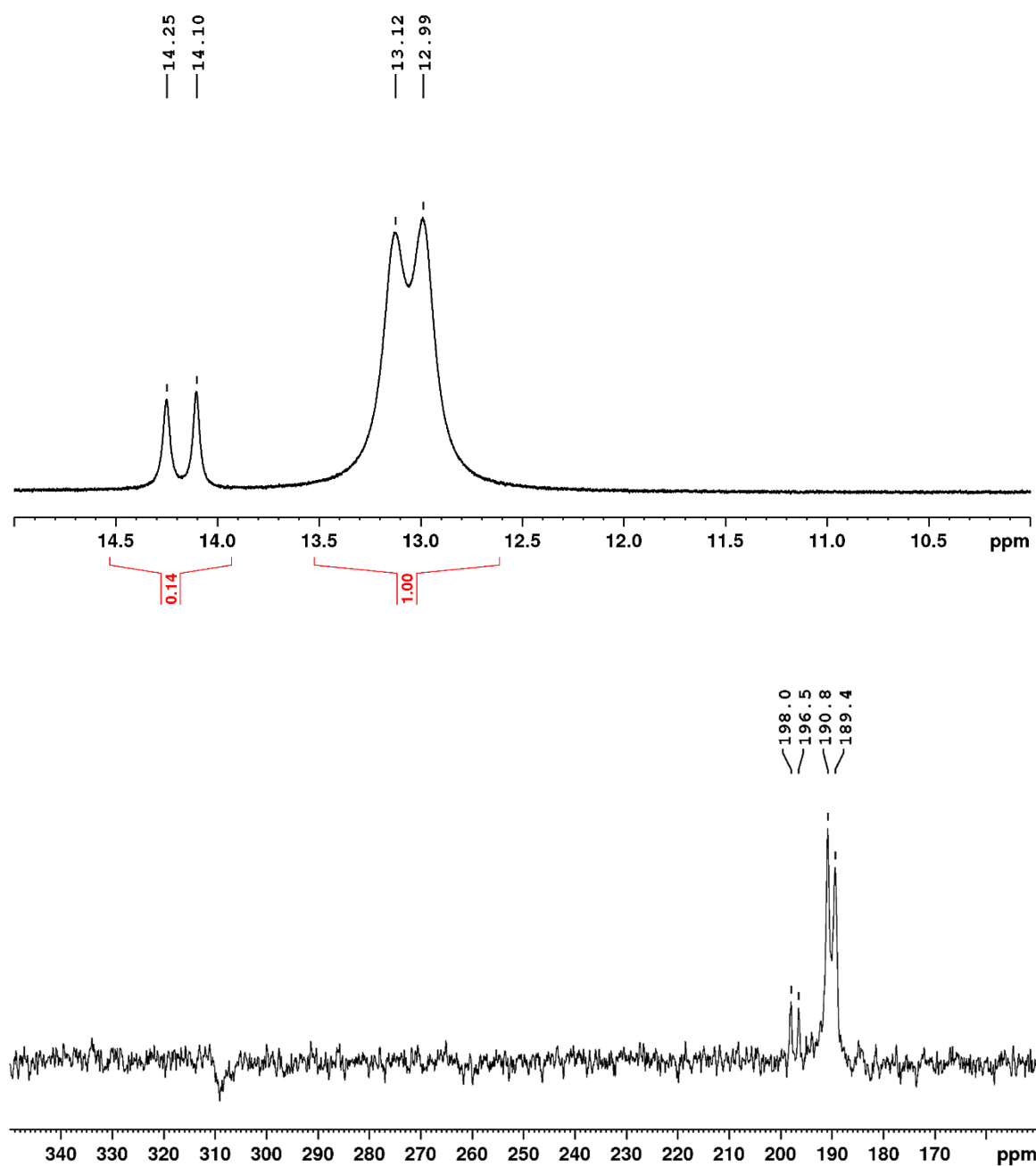


Figure S 2: Low field section of the ¹H spectrum (BF1 = 600.0 MHz; *zg30*; NS = 32; DS = 0; TD = 65536; D1 = 1; SW = 26.04; O1P = 12) and the ¹⁵N spectrum (BF1 = 60.8 MHz; *zg30*; NS = 1024; DS = 0; TD = 65536; SW = 507.5 ppm; O1P = 200) of the CF₃-DSI **1f/2a**-complex in CD₂Cl₂ at 180K.

4 Disulfonimides Versus Phosphoric Acids

(CF₃)₂-DSI **1e/2b** (CD₂Cl₂, 180K)

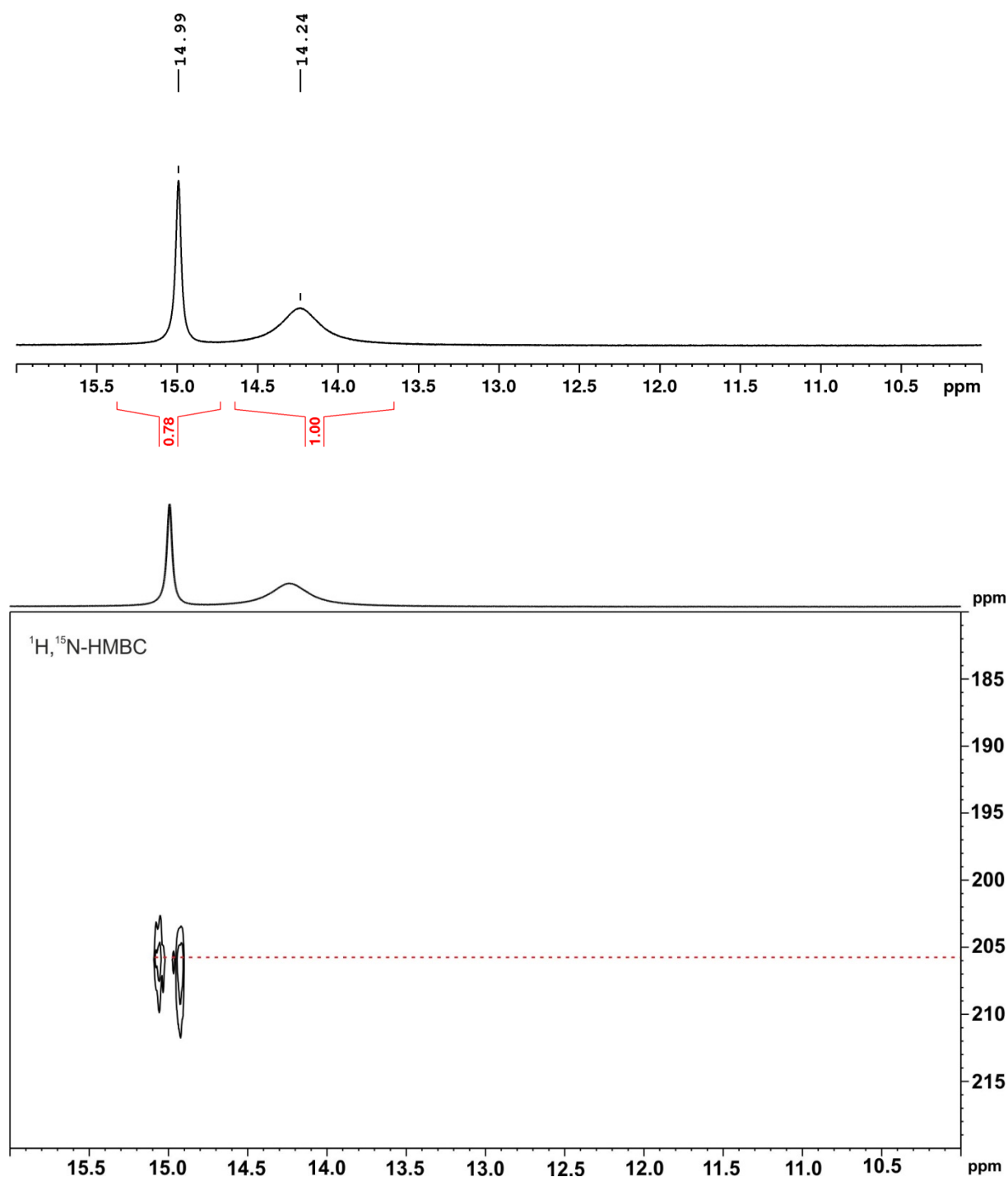


Figure S 3: Low field section of the ¹H spectrum (BF1 = 600.0 MHz; *zg30*; NS = 32; DS = 0; TD = 65536; D1 = 1; SW = 26.04; O1P = 12) and the ¹H, ¹⁵N-HMBC spectrum (BF1 = 600.0 MHz; BF2 = 60.8 MHz; *inv4gplrndqf_swfix*; NS = 32; DS = 16; TD-F2 = 4096; TD-F1 = 128; D1 = 4; SW-F2 = 22.04 ppm; SW-F1 = 499.9 ppm; O1P-F2 = 10; O1P-F1 = 200) of the (CF₃)₂-DSI **1e/2b**-complex in CD₂Cl₂ at 180K.

4 Disulfonimides Versus Phosphoric Acids

CF_3 -DSI **1f/2b** (CD_2Cl_2 , 180K)

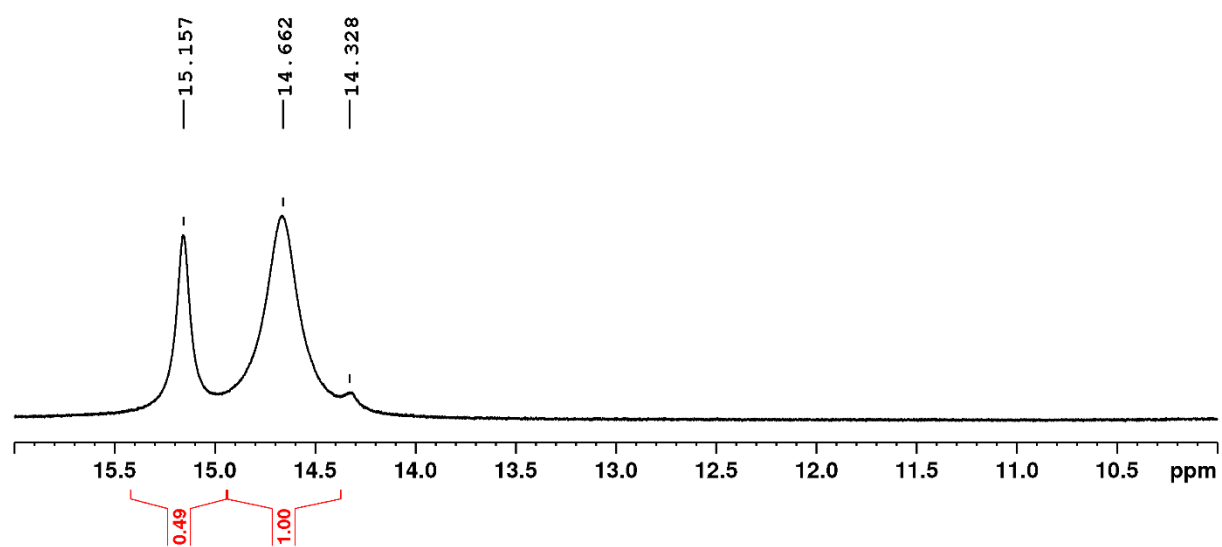


Figure S 4: Low field section of the 1H spectrum (BF1 = 600.0 MHz; zg30; NS = 32; DS = 0; TD = 65536; D1 = 1; SW = 26.04; O1P = 12) of the CF_3 -DSI **1f/2b**-complex in CD_2Cl_2 at 180K.

4 Disulfonimides Versus Phosphoric Acids

$(CF_3)_2$ -DSI **1e/3a** (CD_2Cl_2 , 180K)

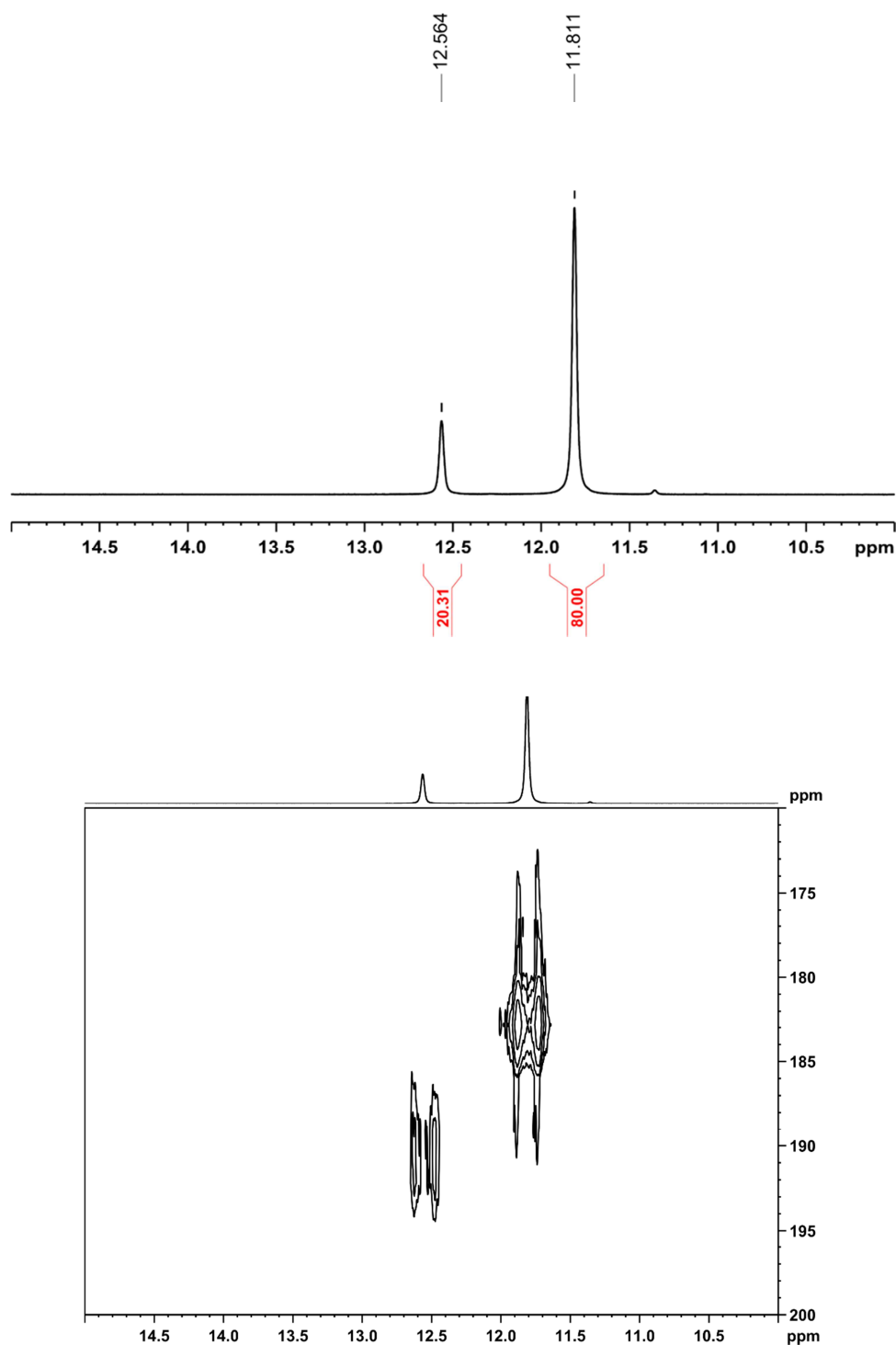


Figure S 5: Low field section of the 1H spectrum (BF1 = 600.0 MHz; *zg30*; NS = 64; DS = 0 TD = 32892; D1 = 2; SW = 24.03; O1P = 6) and the $^1H, ^{15}N$ -HMBC spectrum (BF1 = 600.0 MHz; BF2 = 60.8 MHz; *inv4gplrndqf_swfix*; NS = 64; DS = 16; TD-F2 = 4096; TD-F1 = 128; D1 = 6; SW-F2 = 14 ppm; SW-F1 = 400 ppm; O1P-F2 = 6.36; O1P-F1 = 200) of the $(CF_3)_2$ -DSI **1e/3a** (non- ^{15}N -labelled)-complex in CD_2Cl_2 at 180K.

4 Disulfonimides Versus Phosphoric Acids

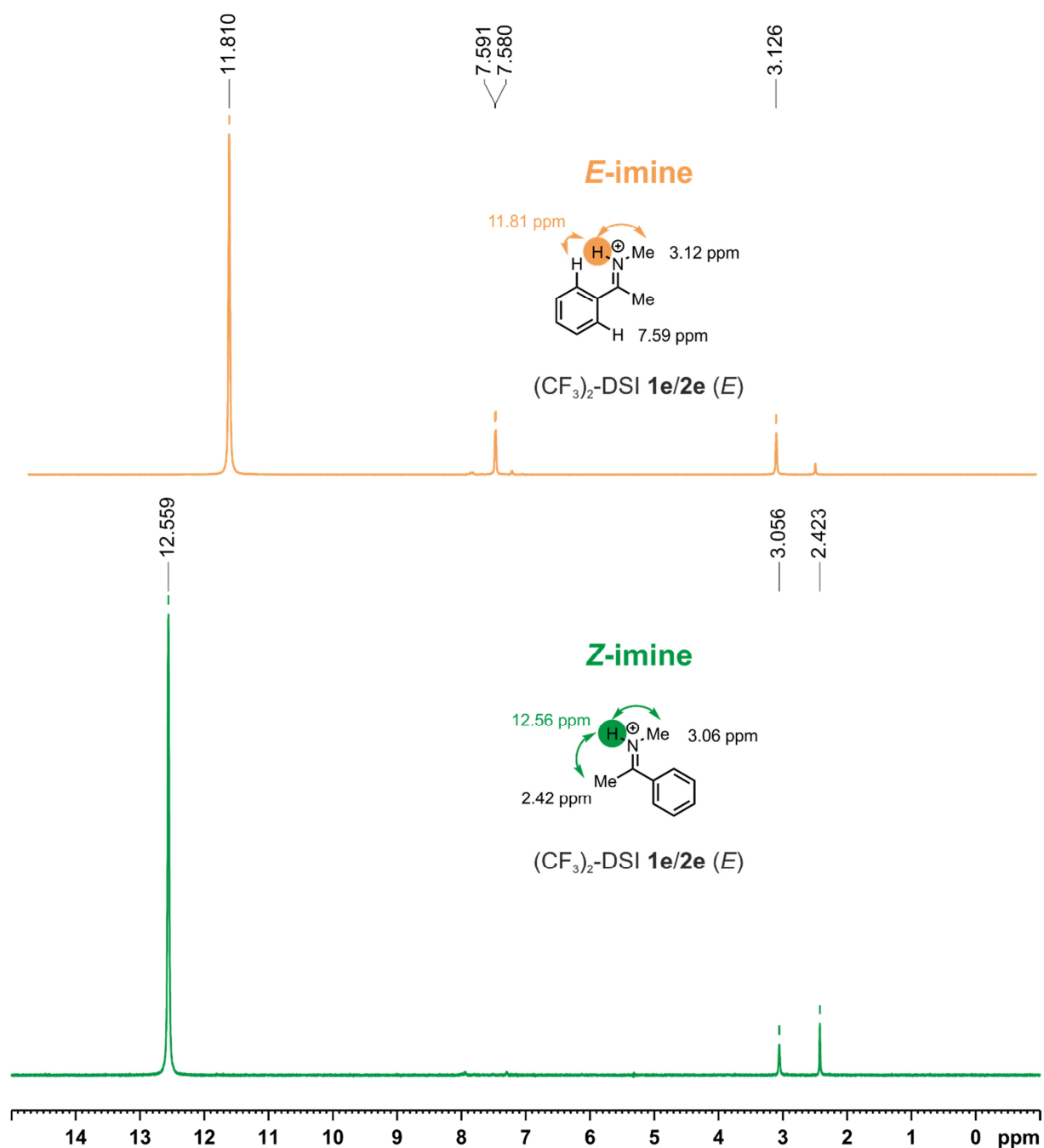


Figure S 6: 1D selective ^1H NOESY spectra (BF1 = 600.0 MHz; *selnogp*; NS = 128; DS = 2; TD = 65536; D1 = 2; SW = 24 ppm; O1P = 6, mixing time D8 = 150 ms) of the $(\text{CF}_3)_2\text{-DSI 1e/3a}$ (non- ^{15}N -labelled)-complex in CD_2Cl_2 at 180K irradiated at δ 11.81 ppm (top spectrum) and 12.56 ppm (bottom spectrum).

4 Disulfonimides Versus Phosphoric Acids

TRIP 1a/3a (CD₂Cl₂, 180K)

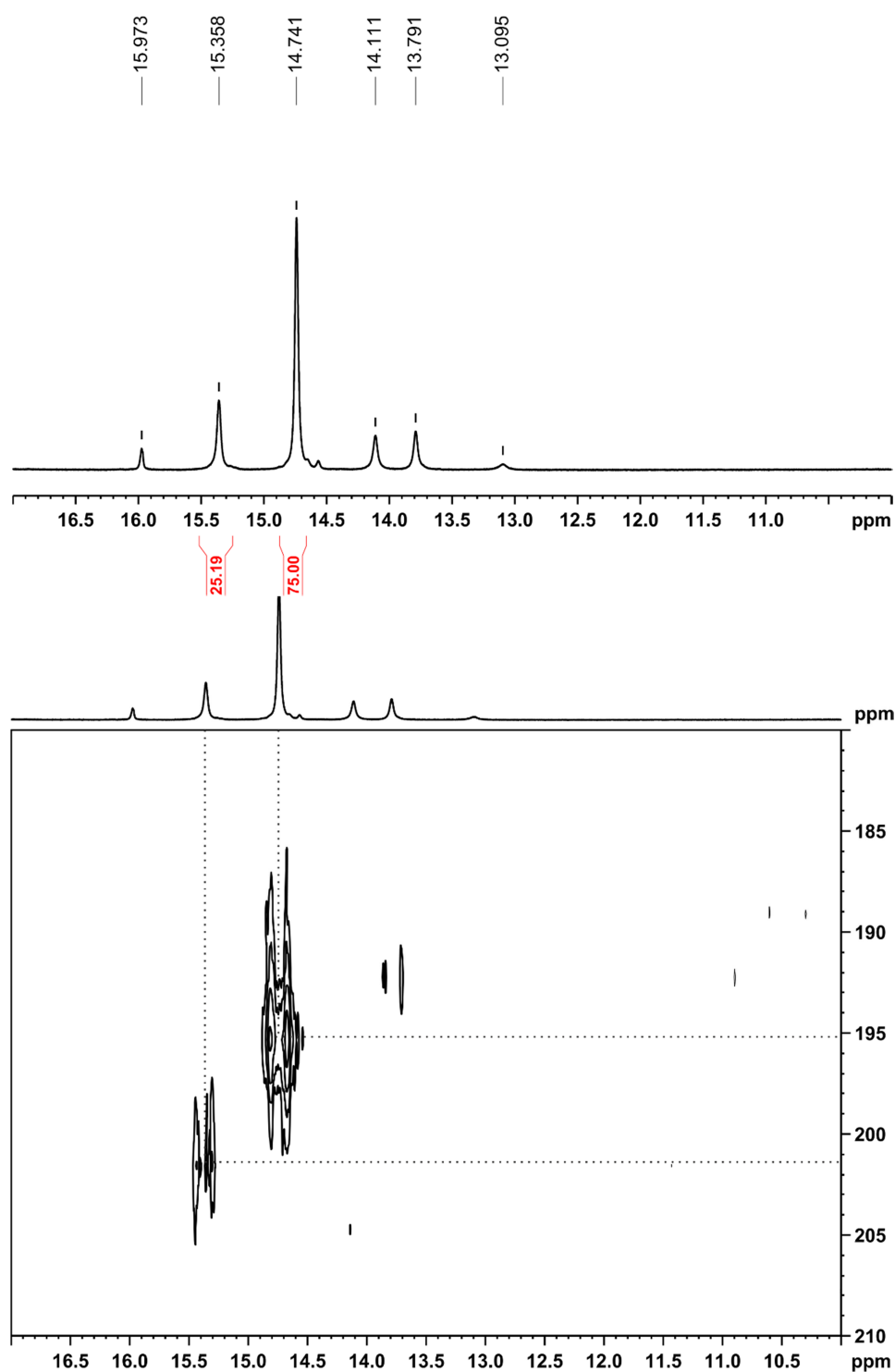


Figure S 7: Low field section of the ¹H spectrum (BF1 = 600.0 MHz; *zg30*; NS = 64; DS = 0 TD = 32892; D1 = 2; SW = 24.03; O1P = 6) and the ¹H,¹⁵N-HMBC spectrum (BF1 = 600.0 MHz; BF2 = 60.8 MHz; *inv4gplrndqf_swfix*; NS = 64; DS = 16; TD-F2 = 4096; TD-F1 = 128; D1 = 6; SW-F2 = 18 ppm; SW-F1 = 400 ppm; O1P-F2 = 7.98; O1P-F1 = 200) of the TRIP **1a/2e** (non-¹⁵N-labelled)-complex in CD₂Cl₂ at 180K.

4 Disulfonimides Versus Phosphoric Acids

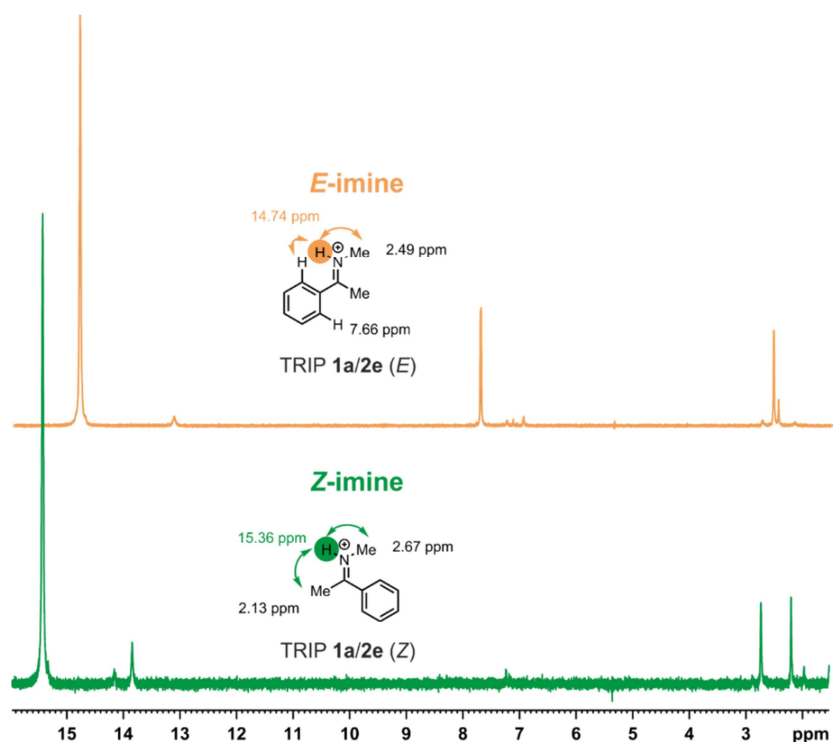


Figure S 8: ¹H 1D selective NOESY spectra (BF1 = 600.0 MHz; *selnogp*; NS = 128; DS = 2; TD = 65536; D1 = 2; SW = 24 ppm; O1P = 6, mixing time D8 = 150 ms) of the TRIP **1a/3a** (non-¹⁵N-labelled)-complex in CD₂Cl₂ at 180K irradiated at δ 14.74 ppm (top spectrum) and 15.36 ppm (bottom spectrum).

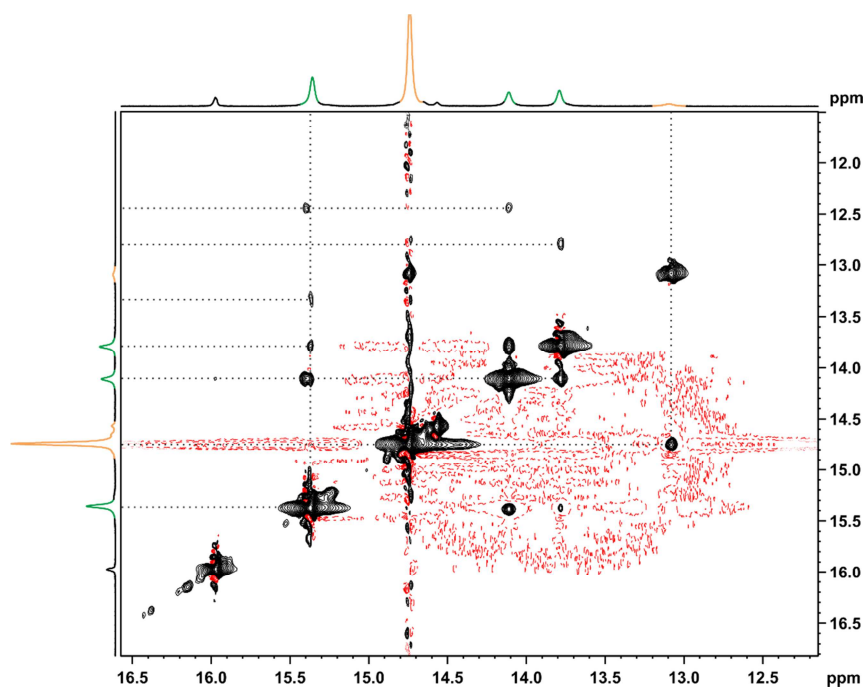


Figure S 9: Low field section of ¹H 2D NOESY spectrum (BF1 = 600.0 MHz; *noeygpph*; NS = 24; DS = 16; TD1 = 256; D1 = 4; SW = 18 ppm; O1P = 8, mixing time D8 = 100 ms) of the TRIP **1a/3a** (non-¹⁵N-labelled)-complex in CD₂Cl₂ at 180K, showing the presence of various *E*- and *Z*-complexes.

4 Disulfonimides Versus Phosphoric Acids

BINSA **1g/2e** (CD_2Cl_2 , 180K)

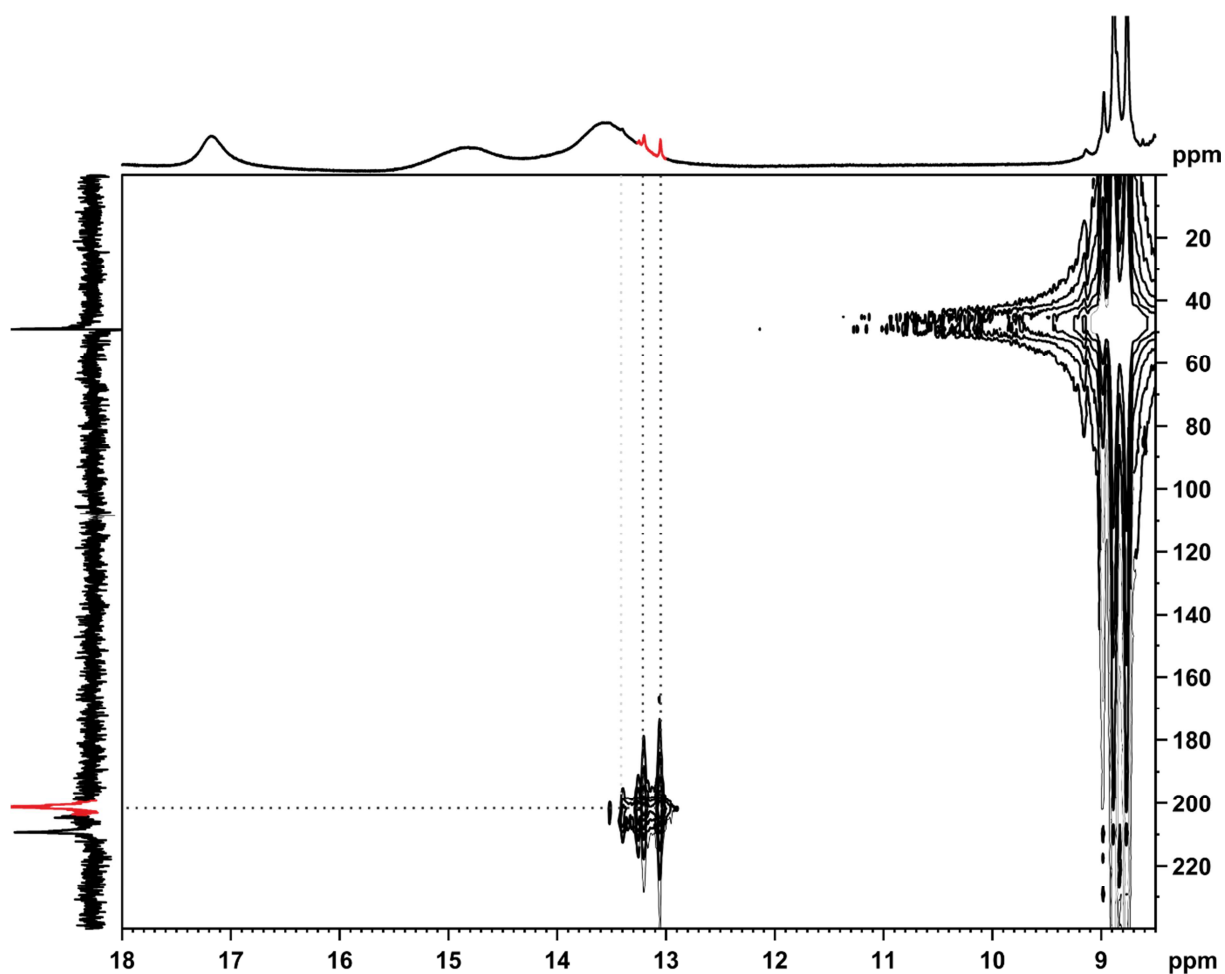


Figure S 10: Low field section of the 1H spectrum (BF1 = 600.0 MHz; *zg30*; NS = 64; DS = 0 TD = 32892; D1 = 2; SW = 22; O1P = 10), ^{15}N spectrum (BF1 = 60.8 MHz; *zg30*; NS = 2048; DS = 0; TD = 65536; SW = 507.5 ppm; O1P = 200) and the $^1H,^{15}N$ -HMBC spectrum (BF1 = 600.0 MHz; BF2 = 60.8 MHz; *inv4gplrndqf_swfix*; NS = 16; DS = 16; TD-F2 = 4096; TD-F1 = 128; D1 = 6; SW-F2 = 22 ppm; SW-F1 = 500 ppm; O1P-F2 = 10; O1P-F1 = 200) of the BINSA **1g/2e**-complex in CD_2Cl_2 at 180K.

4.5.6. Steiner-Limbach correlation

Theory

For the theory behind the hydrogen bond analysis of the chemical shifts using the Steiner-Limbach curve see the supporting material of the reference.^[5,44]

Used fit parameters for the Steiner-Limbach curve

Table S 2: Used NMR parameters ($\delta(\underline{\text{N}})^\circ$, $\delta(\underline{\text{HN}})^\circ$, $\delta(\underline{\text{OHN}})^*$, $\delta(\underline{\text{OH}})^\circ$, $\delta(\underline{\text{HN}})^\circ$, $\delta(\underline{\text{OHN}})^*$) as well as the correction factors (f, g, c^{H} , d^{H}) used for the fit of the Steiner-Limbach curve are shown. They were taken from reference^[5] and slightly modified to our initial study of TRIP/imine-complexes.^[44]

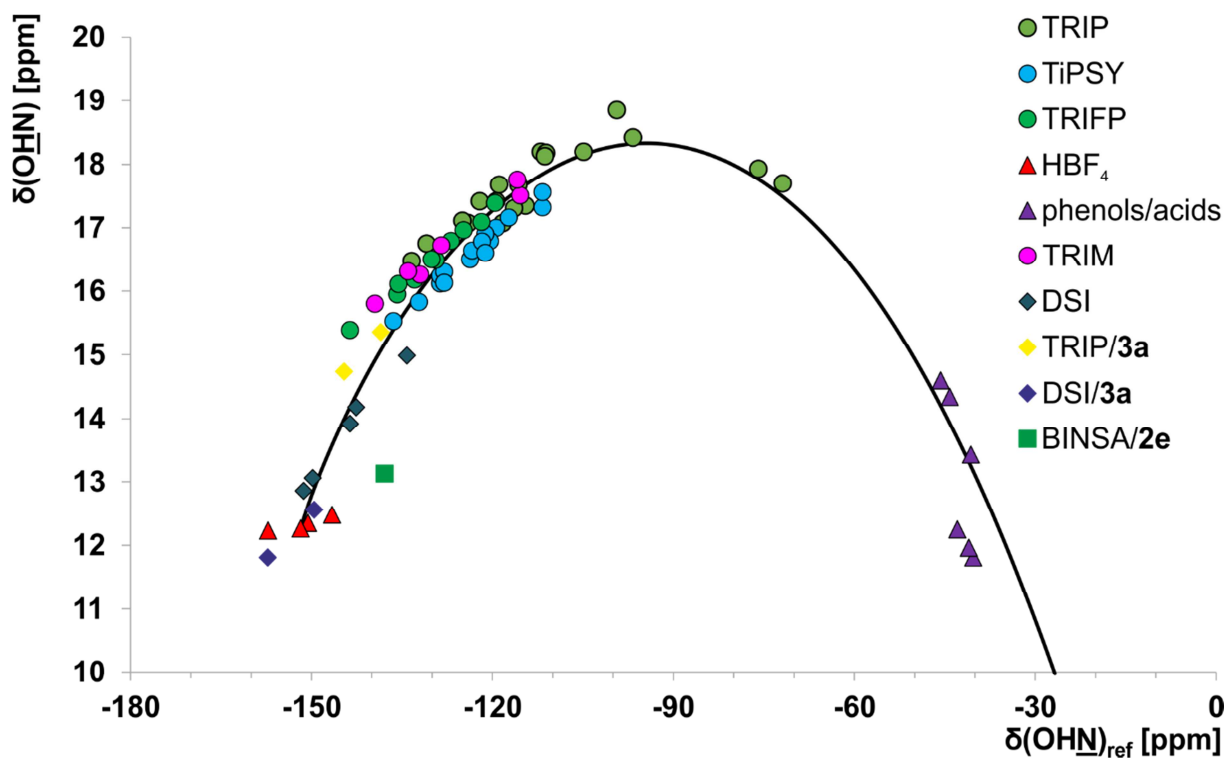
systems	$\delta(\underline{\text{N}})^\circ$ [ppm]	$\delta(\underline{\text{HN}})^\circ$ [ppm]	$\delta(\underline{\text{OHN}})^*$ [ppm]	$\delta(\underline{\text{OH}})^\circ$ [ppm]	$\delta(\underline{\text{HN}})^\circ$ [ppm]	$\delta(\underline{\text{OHN}})^*$ [ppm]	f	g	c^{H}	d^{H}
imine/TRIP ^[44]	0	-170	-6	2	6	16	8	2	360	0.3
imine/TiPSY	0	-151.6	-4.89	1.04	12.33	14.2	7.3	1.36	349.9	0.33
imine/TRIFP										
imine/TRIM ^[5]										
imine /DSI	0	-151.6	-4.89	1.04	12.33	14.2	7.3	1.36	349.9	0.33

Referencing of the ¹⁵N chemical shift

As proposed in literature the ¹⁵N chemical shifts were referenced to the chemical shift of the non-hydrogen bonded imine ¹⁵N-labeled (E)-1-(4-bromophenyl)-N-phenylethan-1-imine ($\delta^{15}\text{N} = 340.8 \text{ ppm}^{[44]}$, 300 K, CD_2Cl_2).^[35] Thus, the ¹⁵N chemical shifts reflect the deviation of the complexed imines from their neutral form ($\delta^{15}\text{N} = \sim 330 \text{ ppm}$) and range from -90 to -150 ppm. Because of this correction $\delta(\underline{\text{N}})^\circ$ can be set to 0.

4 Disulfonimides Versus Phosphoric Acids

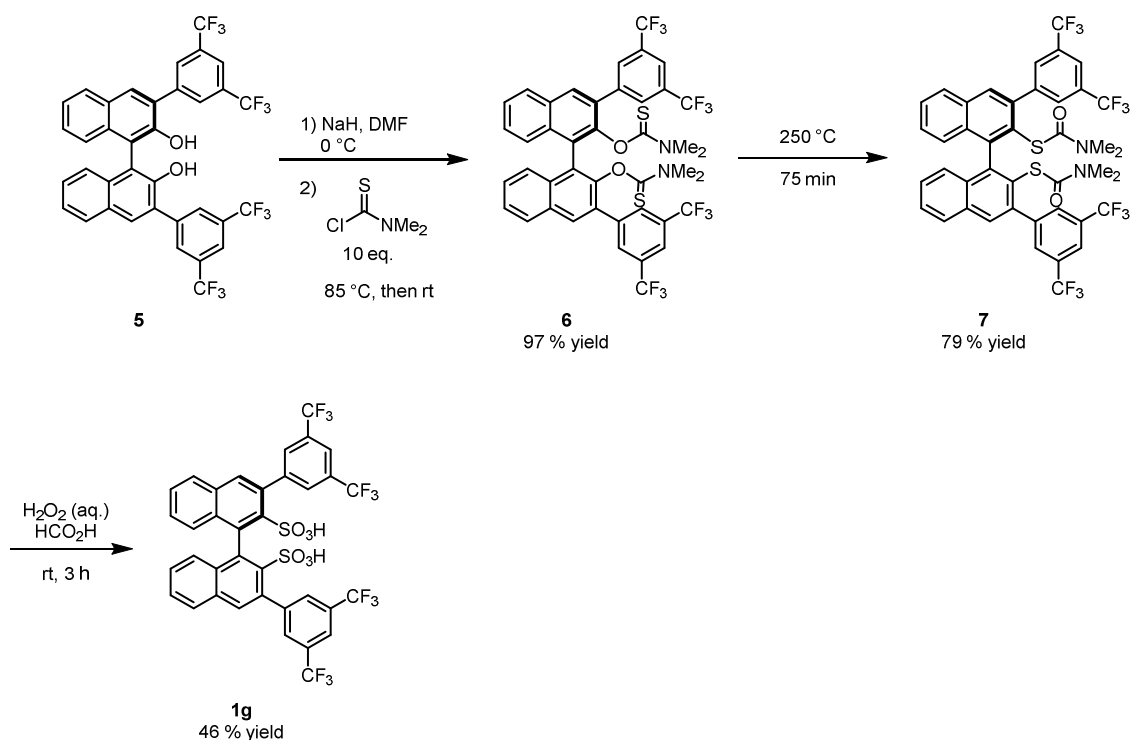
Steiner-Limbach curve with TRIP/3a-, (CF₃)₂-DSI/3a- and BINSAs/2e-complexes



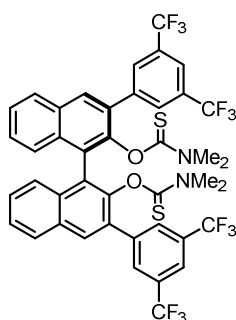
4.5.7. ¹⁵N-labeling of the DSI 1e

Synthesis of the DSI-precursor BINSAs

The disulfonic acid BINSAs (**1g**) was synthesized according to the literature.^[13]



(R)-3,3'-Bis[3,5-bis(trifluoromethyl)phenyl]-1,1'-binaphthyl-2,2'-diyl-O,O'-bis(N,N-dimethylthiocarbamate) (6)



To a suspension of NaH (60 % suspension in mineral oil, 72 mg, 1.75 mmol, 5 eq.) in anhydrous DMF (2 mL) was added solid diol (*R*)-**5** (250 mg, 0.35 mmol). After the mixture turned red, *N,N*-dimethylthiocarbamoylchloride (189 mg, 1.53 mmol, 4.4 eq) was added and the mixture was stirred at 85 °C overnight. The mixture was cooled down, another portion of

4 Disulfonimides Versus Phosphoric Acids

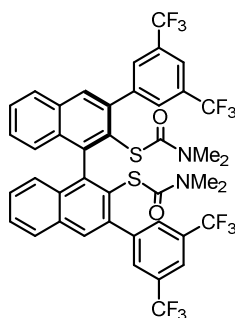
NaH (5 eq.) and *N,N*-dimethylthiocarbamoylchloride (5 eq.) was then added and the mixture was stirred at rt for 5 days. The reaction was quenched by the addition of 2 % aq. KOH (20 mL) and the precipitate was filtered. The solid residue was then dissolved in DCM (20 mL) and washed with sat. aq. NaCl (20 mL). The layers were separated, and the aqueous layer extracted with DCM (20 mL). The combined organic layers were dried over MgSO₄, filtered and the solvent evaporated under reduced pressure. The residue was purified by silica gel column chromatography (eluent hexanes/EtOAc 98:2 – 90:10) to give *O,O'*-thiocarbamate **6** (300 mg, 97 % yield) as a white solid.

¹H-NMR (400.3 MHz, CDCl₃) δ_H [ppm] 8.17 – 7.70 (m, 10 H), 7.60 – 7.27 (m, 6H), 2.04 – 3.12 (m, 12H).

¹⁹F-NMR {¹H} (376.5 MHz, CDCl₃) δ_F [ppm] -63.21, -63.23, -63.3.

¹H- and ¹⁹F-spectra were in accordance with the literature.^[13] Compound exists as a mixture of rotamers.

(*R*)-3,3'-Bis[3,5-bis(trifluoromethyl)phenyl]-1,1'-binaphthyl-2,2'-diyl-*S,S'*-bis(*N,N*-dimethylthiocarbamate) (7)



Solid **6** (300 mg, 0.34 mmol) was stirred at 250 °C for 75 min. The flask was then cooled down and the residue was purified by silica gel column chromatography (eluent hexanes/EtOAc 95:5) to give *S,S'*-thiocarbamate **7** (237 mg, 79 % yield) as a white solid.

¹H-NMR (400.3 MHz, CDCl₃) δ_H [ppm] 8.08 (br s, 4H), 7.98 (br s, 2H), 7.95 – 7.90 (m, 2H), 7.86 (br s, 2H), 7.54 – 7.48 (m, 2H), 7.34 – 7.28 (m, 2H), 7.28 – 7.22 (m, 2H), 2.47 (br s, 12H).

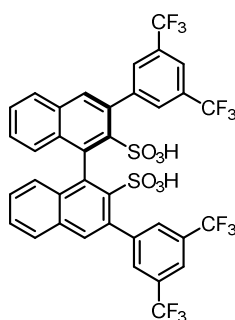
4 Disulfonimides Versus Phosphoric Acids

¹⁹F-NMR {¹H} (376.5 MHz, CDCl₃) δ_F [ppm] -62.6.

¹³C-NMR {¹H} (100.6 MHz, CDCl₃) δ_C [ppm] 165.1, 144.5, 143.4, 141.1, 133.4, 132.9, 130.6 (m), 130.5 (q, *J*_{CF} = 32.8 Hz), 129.8, 127.9, 127.8, 127.6, 127.3, 127.2, 123.5 (q, *J*_{CF} = 272.6 Hz), 120.3 (m), 36.9 – 36.0 (m).

¹H- and ¹³C-spectra were in accordance with the literature.^[13]

(*R*)-3,3'-Bis[3,5-bis(trifluoromethyl)phenyl]-1,1'-binaphthyl-2,2'-disulfonic acid (1g**)**



Hydrogen peroxide (30 % aq., 1 mL) was added to HCO₂H (8 mL) and the mixture was stirred at rt for 1 h. A solution of **7** (227 mg, 0.257 mmol) in DCM (4 mL) was then added and the mixture was stirred at rt for 2 h. The mixture was then filtered through a pad of silica gel, washed with DCM, and the solvents were evaporated under reduced pressure. The residue was purified by silica gel column chromatography (eluent DCM/MeOH 20:1 – 10:1) to give **1g** (probably as a sodium salt, 100 mg, 46 % yield) as a white solid. The solid was dissolved in DCM (20 mL), washed with 6 M aq. HCl (12 mL), and the aqueous layer was extracted with DCM (2 x 15 mL). The organic layers were combined, the solvent evaporated under reduced pressure and the remaining water was removed by azeotropic distillation with toluene (3 x 20 mL) to give **1g** (BINSAs, 76 mg, 34 %) as a brown solid.

¹H-NMR (400.3 MHz, CD₃OD) δ_H [ppm] 8.23 (s, 4H), 7.94 (d, *J* = 8.2 Hz, 2H), 7.91 (s, 2H), 7.82 (s, 2H), 7.52 (t, *J* = 7.6 Hz, 2H), 7.32 (t, *J* = 7.8 Hz, 2H), 7.09 (d, *J* = 8.6 Hz, 2H).

¹⁹F-NMR {¹H} (376.5 MHz, CD₃OD) δ_F [ppm] -63.9.

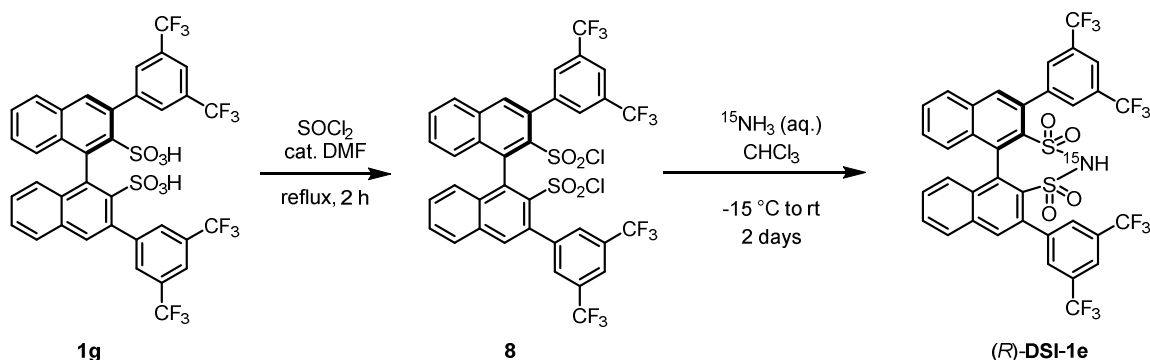
¹³C-NMR {¹H} (100.6 MHz, CD₃OD) δ_C [ppm] 147.0, 139.6, 137.8, 136.7, 134.6, 134.2, 132.6, 132.1, 131.0 (q, *J*_{CF} = 33.0 Hz), 129.0, 128.8, 128.7, 128.3, 125.3 (q, *J*_{CF} = 271.8 Hz), 121.3 (m).

4 Disulfonimides Versus Phosphoric Acids

^1H - and ^{13}C -spectra were in accordance with the literature.^[13]

Synthesis of the ^{15}N -labeled DSI **1e**

The ^{15}N -DSI **1e** was synthesized from its precursor BINSAs using $^{15}\text{NH}_3$ (aq.) (instead of 2 M NH_3 in MeOH) by following the literature procedure.^[13]



BINSAs **1g** (90 mg, 0.110 mmol) was dissolved in thionylchloride (2.5 mL), anhydrous DMF (10 μL) was added and the mixture was refluxed for 2 h. The solvent was then evaporated under reduced pressure. The remaining solid was triturated with anhydrous Et_2O (2 x 1 mL) to give **8** as a white solid, which was used further without any purification.

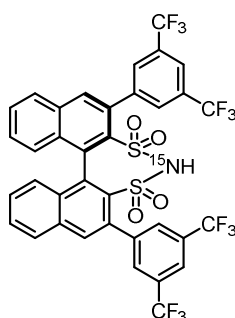
$^1\text{H-NMR}$ (400.3 MHz, $\text{THF-}d_8$) δ_{H} [ppm] 8.33 (s, 2H), 8.31 – 8.21 (m, 4H), 8.19 – 8.13 (m, 4H), 7.86 – 7.80 (m, 2H), 7.59 – 7.54 (m, 2H), 7.34 (d, $J = 8.8$ Hz, 2H).

$^{19}\text{F-NMR}$ { ^1H } (376.5 MHz, $\text{THF-}d_8$) δ_{F} [ppm] -62.5.

^1H - and ^{19}F -spectra were in accordance with the literature.^[13]

4 Disulfonimides Versus Phosphoric Acids

(R)-¹⁵N-DSI **1e**



As no product was detected during a reaction of **8** with aq. ¹⁵NH₃ using THF as the solvent, biphasic conditions were applied:

Crude sulfonic acid dichloride **8** was dissolved in CHCl₃ (35 mL), cooled to -15 °C and 7 M aq. ¹⁵NH₃ (4 mL) was added over 5 h. The mixture was stirred at -15 °C for 24 h and then at rt for 2 days. Then 14 M aq. ¹⁵NH₃ (2 mL) was added and the reaction stirred overnight. The reaction was quenched by the addition of 5 % aq. KHSO₄ (15 mL) and extracted with CHCl₃ (3 x 25 mL). The combined organic layers were dried over MgSO₄, filtered and the solvent evaporated under reduced pressure. The residue was purified by silica gel column chromatography (eluent DCM/MeOH 40:1). The purified product was dissolved in DCM (5 mL) and washed with 6 M aq. HCl (5 mL), and the aqueous layer was extracted with DCM (5 mL). The organic layers were combined and washed again with 6 M aq. HCl (10 mL). The aqueous layer was extracted with DCM (10 mL). The organic layers were combined, the solvent evaporated under reduced pressure and the remaining water was removed by azeotropic distillation with toluene (6 x 20 mL) to give DSI-**1e** (16 mg) as a brown solid.

¹H-NMR (600.0 MHz, CD₂Cl₂) δ_H [ppm] = 8.18 – 8.11 (m, 4H), 8.07 (br s, 2H), 8.04 – 7.97 (m, 4H), 7.83 (t, *J* = 7.8 Hz, 2H), 7.56 (t, *J* = 7.8 Hz, 2H), 7.27 (d, *J* = 8.7 Hz, 2H), 4.30 – 5.60 (br s).

¹³C-NMR {¹H} (100.6 MHz, CD₂Cl₂): δ_C [ppm] = 141.2, 138.6, 134.3, 134.2, 133.6, 132.2, 130.9 (m), 130.5, 129.2, 129.0 (m), 128.7, 128.1, 123.3 (q, *J*_{CF} = 273.0 Hz), 122.4, 121.7 (m).

¹⁹F-NMR {¹H} (376 MHz, CD₂Cl₂): δ_F [ppm] = -62.9, -63.0.

¹⁵N-NMR {inverse-gated ¹H} (40.5 MHz, CDCl₃): δ_N [ppm] = 200.6.

The spectral data of the purified product **1e** match the published data.^[13]

4 Disulfonimides Versus Phosphoric Acids

4.5.8. Comparison of the spectra of ^{15}N -labelled and not labeled $(\text{CF}_3)_2\text{-DSI } 1\text{e}/2\text{a}$ (CD_2Cl_2 , 180K)

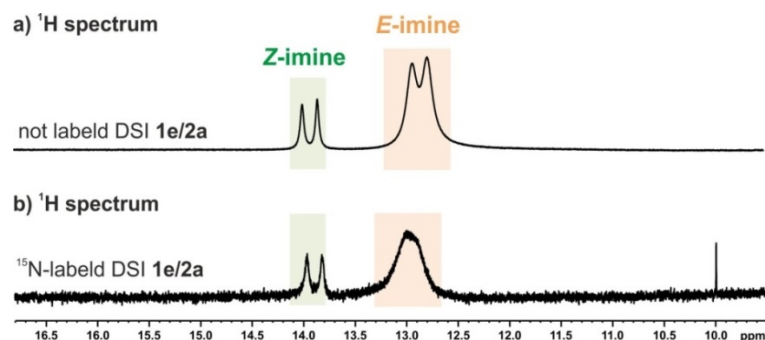


Figure S 11: a) Low field section of the ^1H spectrum of DSI **1e** and ^{15}N -labelled imine **2a** (1:1, 50 mM) in CD_2Cl_2 at 180K. b) The region of the hydrogen bonds within the ^1H spectra of ^{15}N -labelled $(\text{CF}_3)_2\text{-DSI } 1\text{e}$ and ^{15}N -labelled imine **2a** (1:1, 32 mM) in CD_2Cl_2 at 180K. The signal of the hydrogen bonded proton in the binary *E*-complex is significantly broadened.

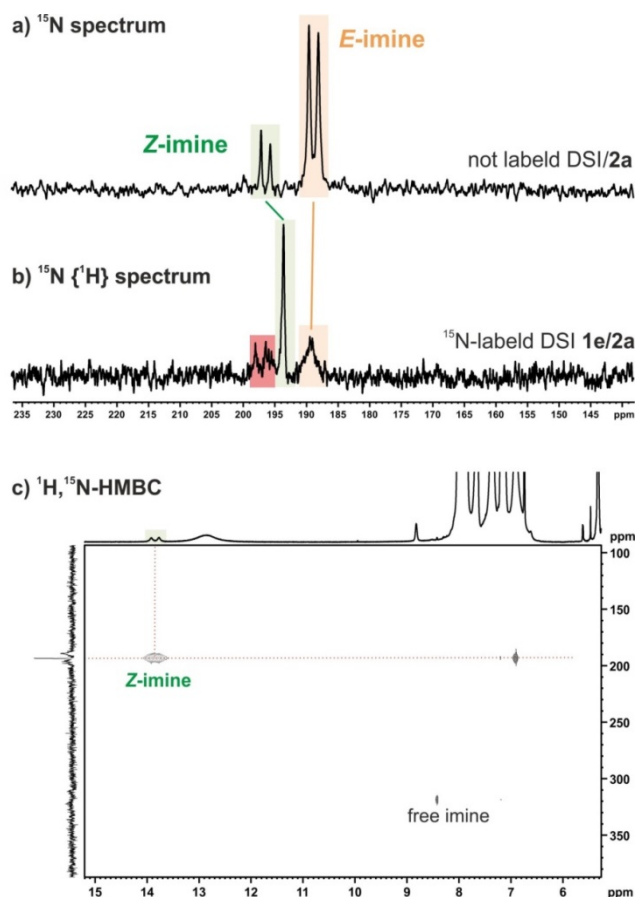
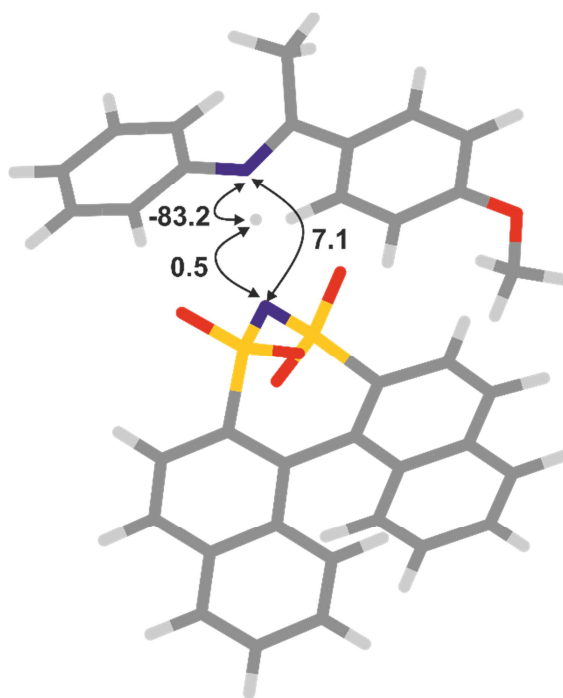


Figure S 12: a) ^{15}N spectrum of DSI **1e** and ^{15}N -labelled imine **2a** (1:1, 50 mM) in CD_2Cl_2 at 180K. b) To increase the sensitivity of the ^{15}N spectra an inverse gated decoupled ^{15}N spectra was recorded of the ^{15}N -labelled DSI **1e** and imine **2a** (1:1, 32 mM) in CD_2Cl_2 at 180 K. The red signals may be from the ^{15}N of the catalyst within the binary *E*- and *Z*-complex. c) To identify the observed signals a ^1H , ^{15}N -HMBC at 180K was measured.

4 Disulfonimides Versus Phosphoric Acids

4.5.9. Calculated ${}^2\text{h}J_{\text{NN}}$, ${}^1J_{\text{NH}}$ and ${}^1\text{h}J_{\text{NH}}$ coupling constants

For the coupling constant calculations of *Type E_N*, reduced model (truncated 3,3'-substituents) based on the groundstate were used. TPSS with IGLO-III basis set were used in the calculation.

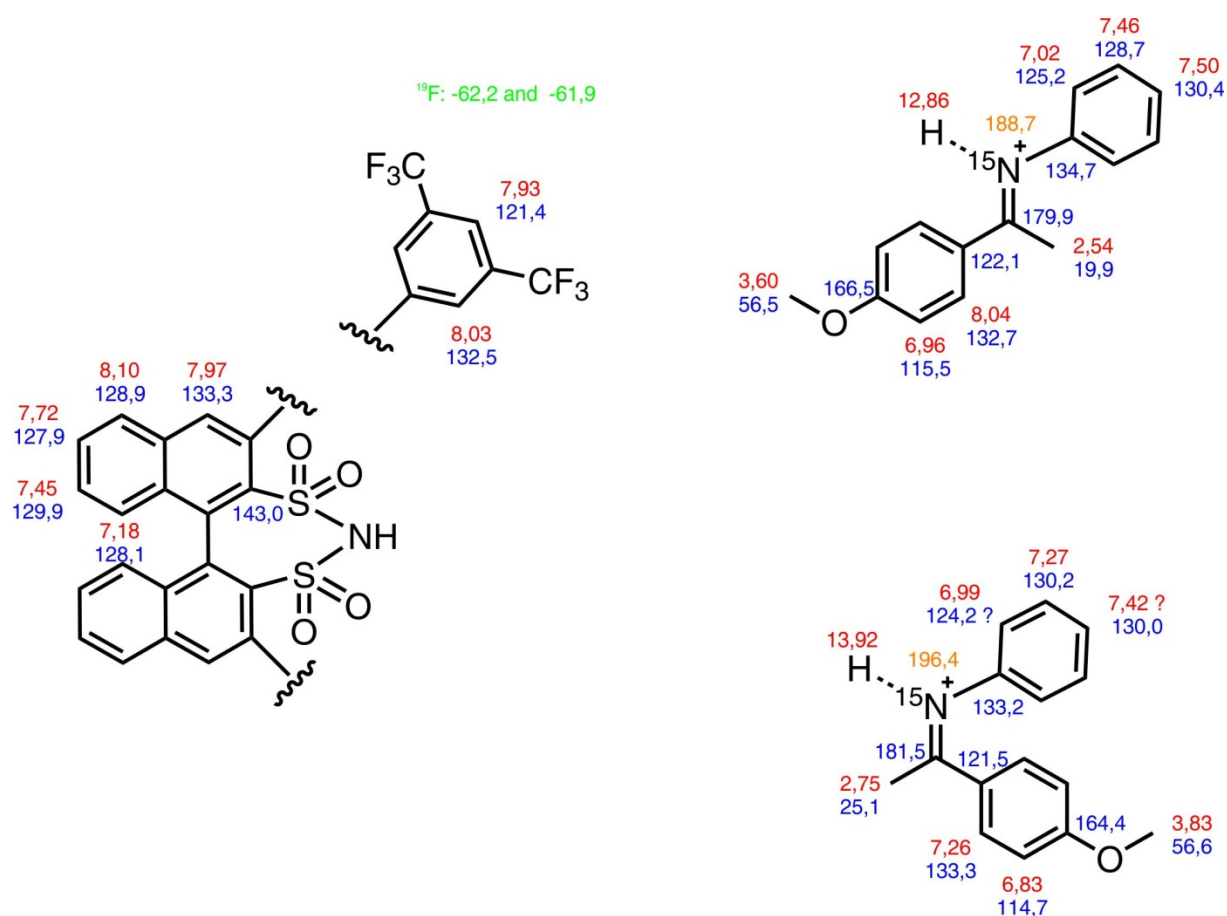


4 Disulfonimides Versus Phosphoric Acids

4.5.10. Assignments of the ^1H and ^{13}C chemical shifts

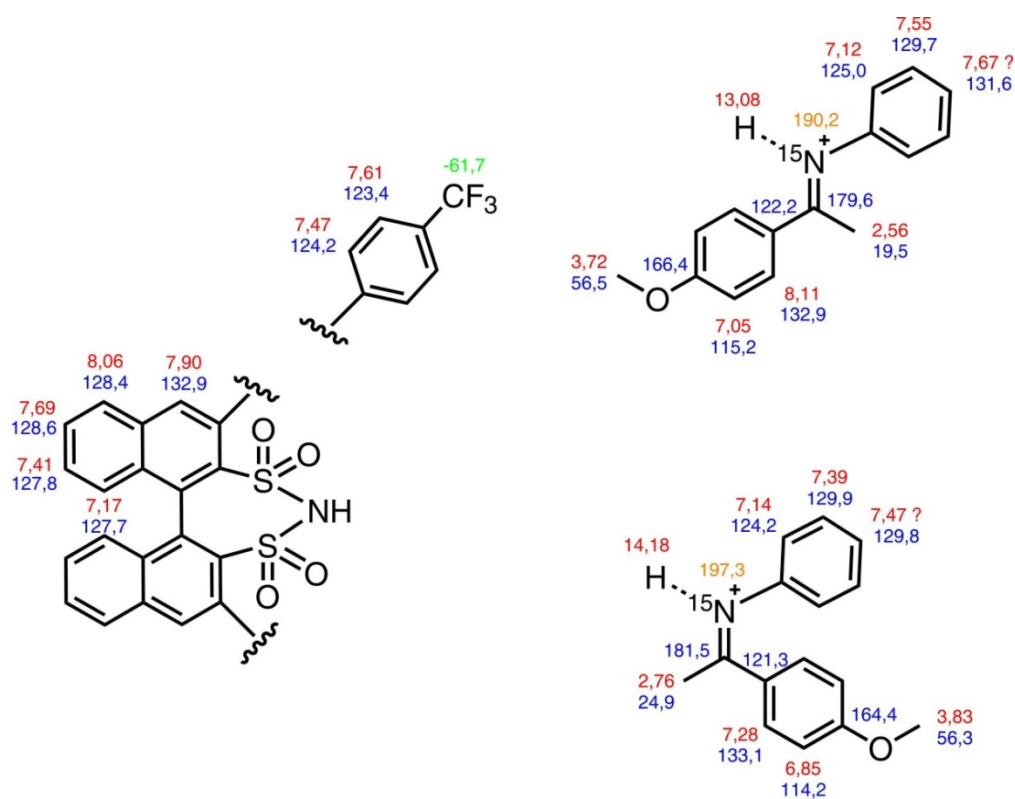
The ^1H (red) and ^{13}C (blue) chemical shifts of all investigated binary complexes were assigned with standard 2D NMR experiments ($^1\text{H},^1\text{H}$ -COSY, $^1\text{H},^1\text{H}$ -TOCSY, $^1\text{H},^1\text{H}$ -NOESY, $^1\text{H},^{13}\text{C}$ -HSQC, $^1\text{H},^{13}\text{C}$ -HMBC) at 180 K. The ^{15}N (orange) and ^{19}F (green) chemical shifts were assigned with $^1\text{H},^{19}\text{F}$ -HMBC and $^1\text{H},^{15}\text{N}$ -HMBC spectra respectively.

$(\text{CF}_3)_2\text{-DSI } 1\text{e}/2\text{a}$ (CD_2Cl_2 , 180K)

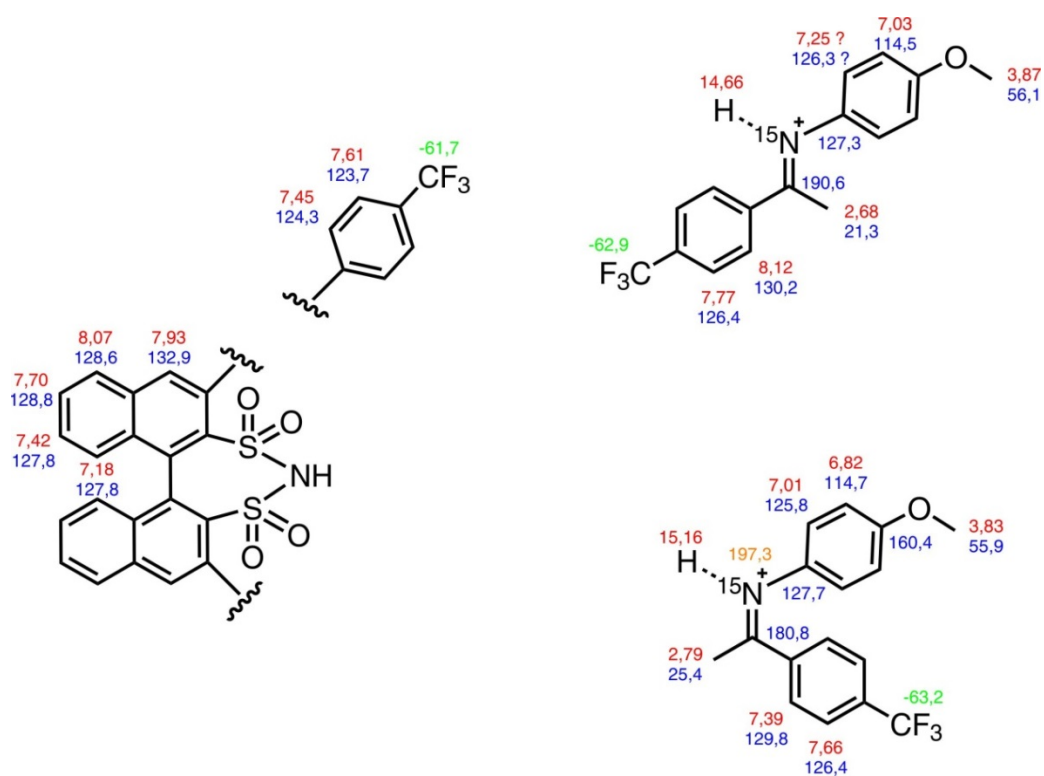


4 Disulfonimides Versus Phosphoric Acids

CF₃-DSI 1f/2a (*CD₂Cl₂*, 180K)



CF₃-DSI 1f/2b (*CD₂Cl₂*, 180K)



4 Disulfonimides Versus Phosphoric Acids

4.5.11. Predicted structures of the DSI-complexes by calculations

E-complexes

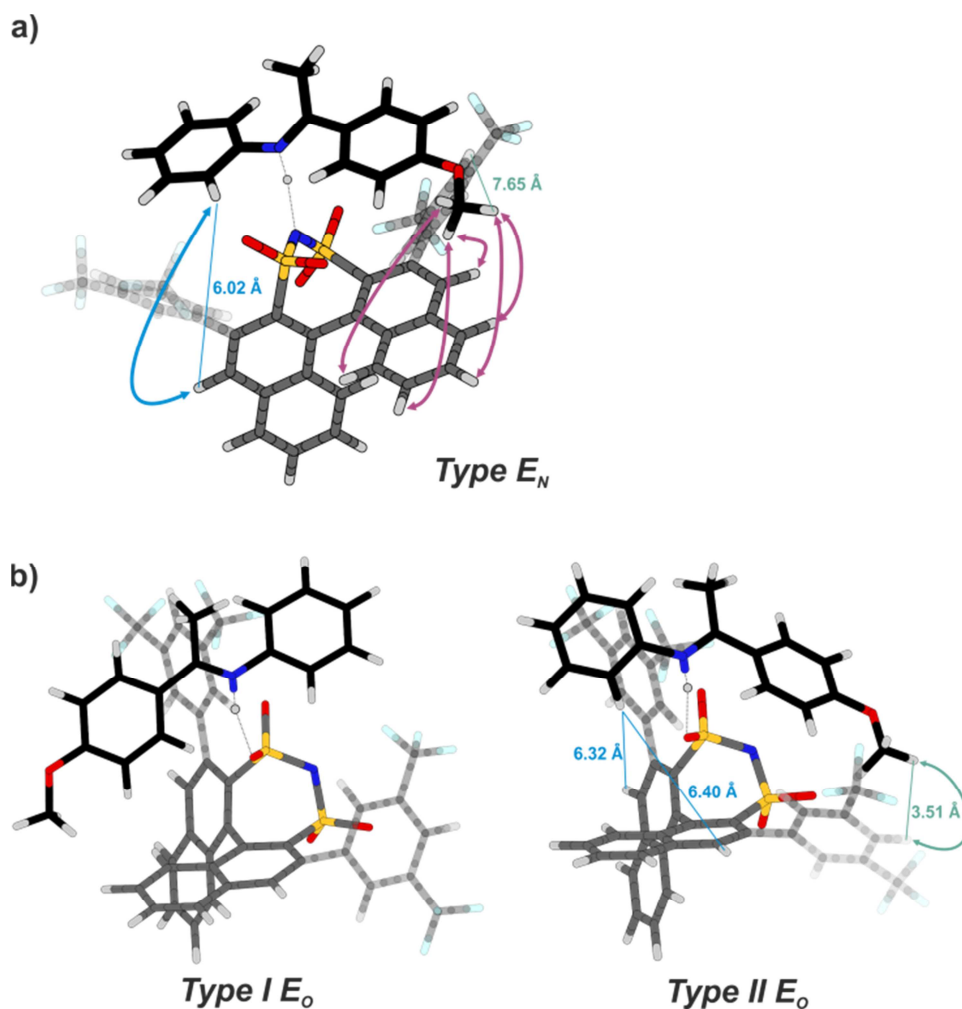


Figure S 13: Calculations predict for the DSI/imine **2a**-complexes the existence of a) one stable structure, where a hydrogen bond to the nitrogen of the DSI-catalyst (*type E_N*), is formed and b) several orientations with a hydrogen bond to one of the oxygens. The two most stable structures are shown. While the purple and blue NOEs are not unambiguous for one structure, *type II E_o* of both DSI/**2a**-complexes could be identified by the observation of the green NOE. All distances given in this figure were obtained from calculations.

For computational data see appendix (DVD).

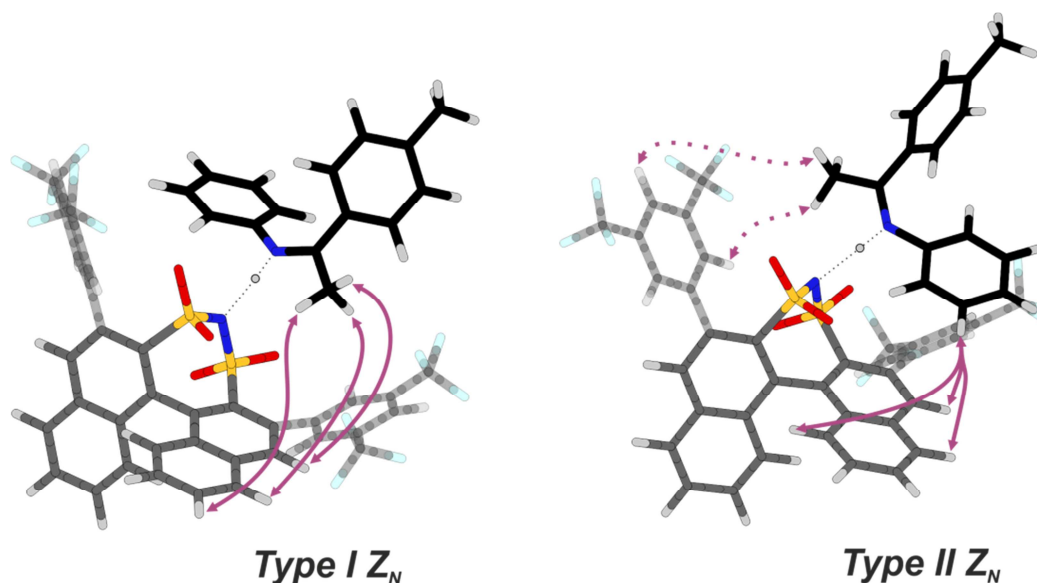
Z-complexes

Figure S 14: Calculations predict two stable structures for the DSI/**Z-2a**-complex, where the hydrogen bond to the nitrogen is formed. Within the CF_3 -DSI/**Z-2b**-complex some characteristic NOEs (shown in purple) indicate the existence of both structures (see below). However, for the other complexes it was not possible to identify the different structures. This may be due to the fast exchange of several hydrogen bonded species.

For computational data see appendix (DVD).

4.5.12. Structure identification of all binary complexes

The structural investigations of the binary DSI-complexes were done in analogous to our previous investigations.^[4,20]

Selective ^1H NOESY, 2D $^1\text{H}, ^1\text{H}$ -NOESY and $^1\text{H}, ^{19}\text{F}$ -HOESY spectra were used to identify the structures of complexes **E-2a-b/1e-f** in solution. All spectra were measured in CD_2Cl_2 at 180 K. One orientation (**TYPE E_N**) was identified by the NOE pattern between the varying *p*-methoxy-groups of the imines **2a** and parts of the BINOL backbone of **1e** and **1f**. In the complexes **E-2a/1e-f**, the *p*-methoxy-groups were excited in selective ^1H NOESY spectra. In the **E-2b/1f**-complex no characteristic NOEs were found to proof the existence of **TYPE E_N**. But its existence was assumed due to the computationally calculated preference for this structure. Nevertheless, one of the other orientations (**TYPE II E_O**) was identified by 2D $^1\text{H}, ^1\text{H}$ -NOESY spectra with a mixing time of 300 ms in all investigated complexes. Here the characteristic NOE between aniline moiety and the backbone was found. Nevertheless, in

4 Disulfonimides Versus Phosphoric Acids

the *E*-**2a/1f**-complex the NOE between aniline moiety and the backbone can be assumed. In contrast to the TRIP **1a/2b**-complexes, it was not possible to excite selectively the methoxy-group of the anisidine moiety of the imine **2b** due to overlap. But in 2D $^1\text{H},^1\text{H}$ -NOESY the characteristic NOEs between the methoxy group and the BINOL backbone were found.

Selective ^1H NOESY and 2D $^1\text{H},^1\text{H}$ -NOESY spectra were used to identify the structures of complexes **Z-2a-b/1e-f** in solution. All spectra were measured in CD_2Cl_2 at 180 K. The selective excitation of the α -methyl-group of both *Z*-imines **2a-2b** in selective ^1H NOESYs show NOE transfer to the whole catalyst-backbone as well as to the protons on the 3,3'-substituents. Also with a mixing time of 25 ms this NOE pattern was observed. Therefore, it is impossible to identify **TYPE IZ_N** and **TYPE IIZ_N** unambiguous. But for the **1d/2b**-complex in the 2D $^1\text{H},^1\text{H}$ -NOESY some characteristic NOEs indicates the existence of **TYPE IZ_N** and **TYPE IIZ_N**.

NOE build-up curve

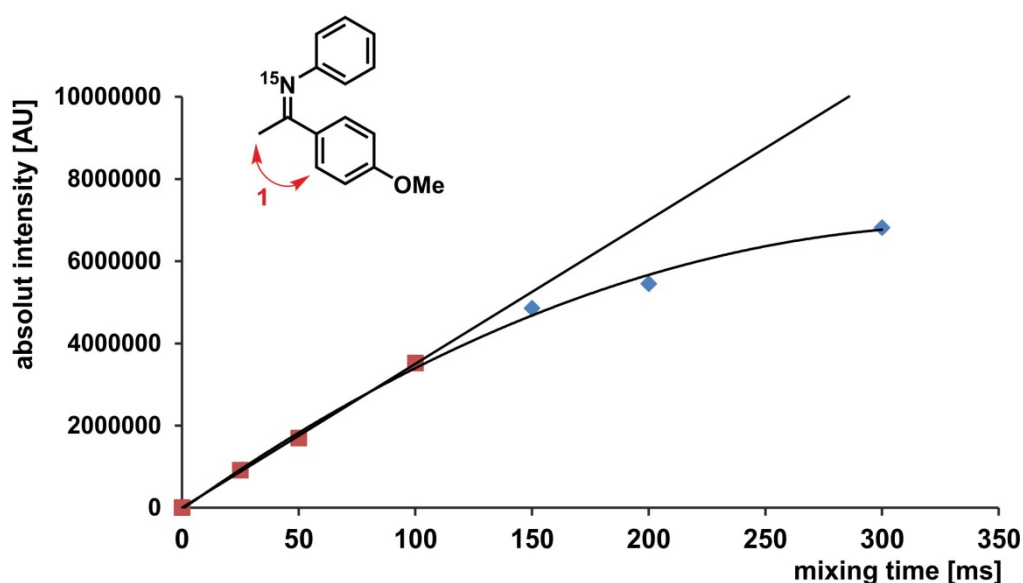


Figure S 15: Selective 1D ^1H -NOESYs of the **1e/2a**-complex in CD_2Cl_2 at 180 K with different mixing times were measured. The α -methyl group of the imine was excited. The resulting build-up of the intensity of intramolecular NOE 1 (red arrow) is shown. Due to spin diffusion effects, even with 100 ms mixing time a deviation from a linear build was observed.

4 Disulfonimides Versus Phosphoric Acids

$(CF_3)_2$ -DSI **1e/2a** (CD_2Cl_2 , 180K)

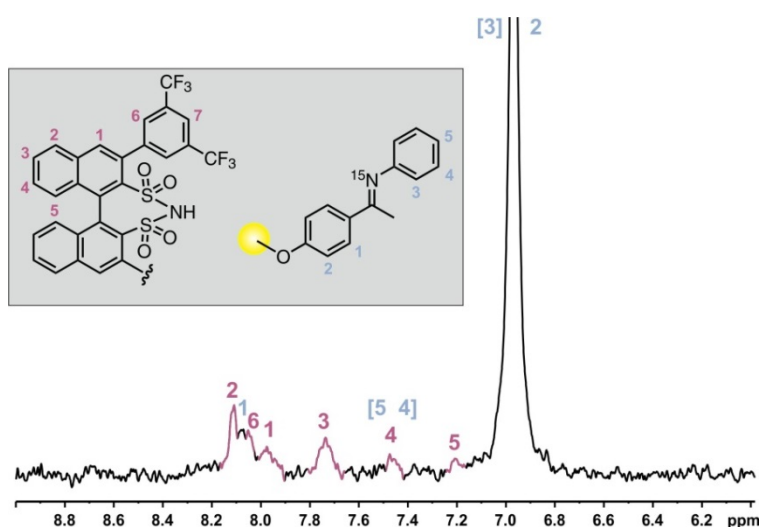


Figure S 16: A section of a selective 1D 1H -NOESY ($\tau_{mix} = 100$ ms, RE-Burp pulse) excited on the *p*-methoxy group of **E-2a** (yellow circle) at 180 K in CD_2Cl_2 is shown. NOEs are visible to the complete catalyst backbone, indicating the existence of *type E_N*. However, also for some of the less populated *type E_O*-orientations (e.g. *type IE_O*) NOEs between the *p*-methoxy group of **E-2a** (yellow circle) and the BINOL backbone were expected. But due to the fact, that the NOE to proton 2 (purple) of the BINOL backbone is the strongest in combination with the comparison of the calculated distances these groups (*type E_N* = 3.18 Å and *type IE_O* = 5.12 Å) it can be assumed, that *type E_N* exists in solution. The signals of the protons in brackets are overlapping.

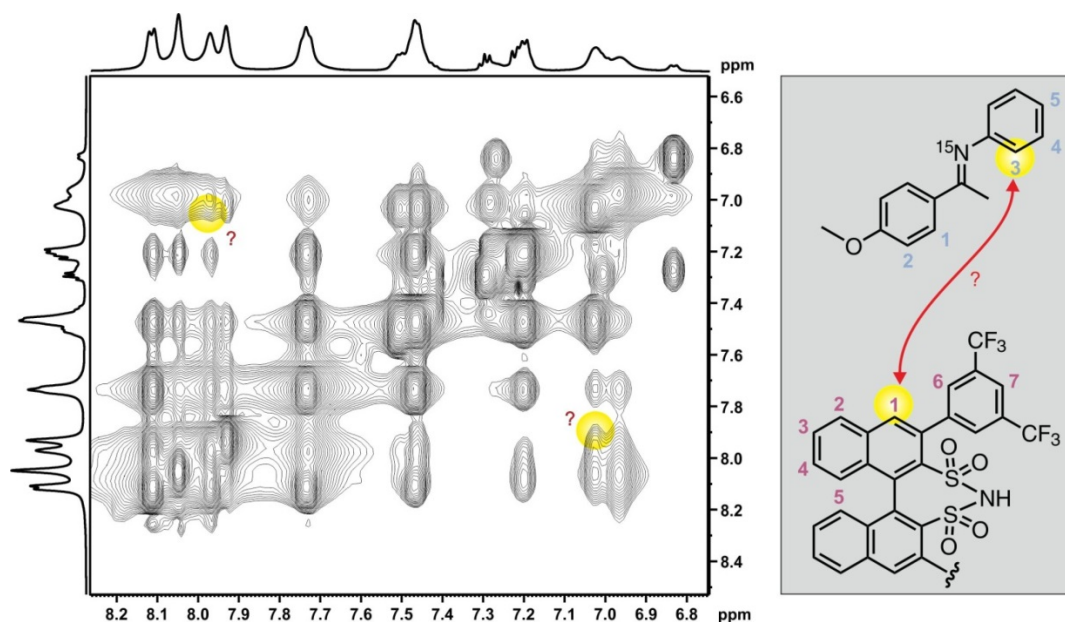


Figure S 17: A 2D $^1H, ^1H$ NOESY spectrum ($\tau_{mix} = 300$ ms) of complex **1e/2a** at 180 K in CD_2Cl_2 . In contrast to the CPA-complexes the NOE (labeled in yellow) between proton 1 of the DSI (purple) and proton 3 of the imine (blue) does not identify *type IIE_O* unambiguously, because these calculated distances for *type E_N* (6.02 Å) and *type IIE_O* (6.32 Å and 6.40 Å) are similar. See figure S13.

4 Disulfonimides Versus Phosphoric Acids

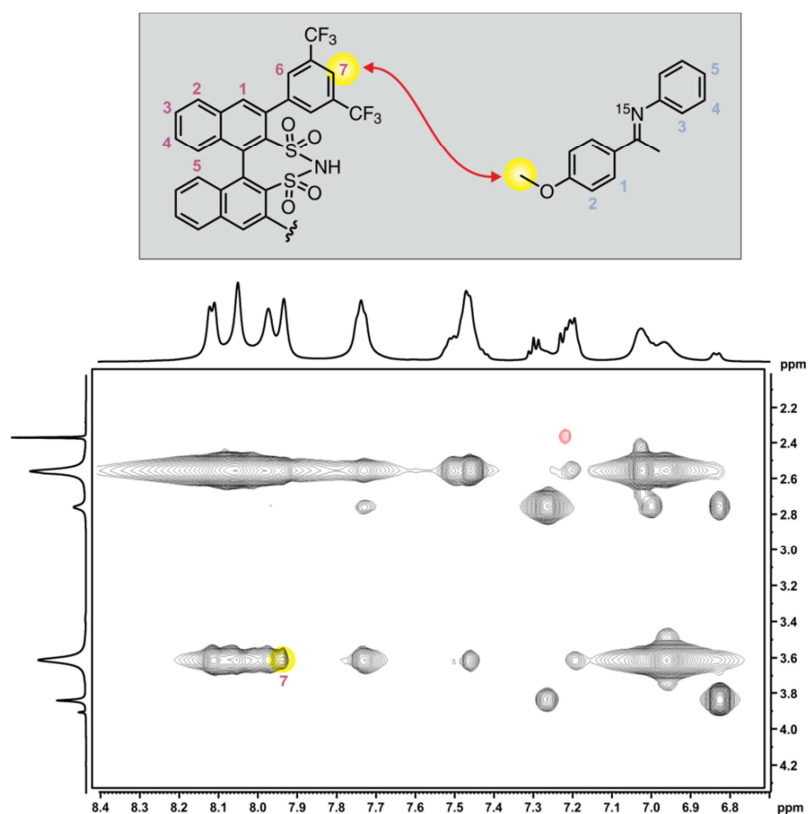


Figure S 18: A 2D $^1\text{H},^1\text{H}$ NOESY spectrum ($\tau_{\text{mix}} = 300$ ms) of complex **1e/2a** at 180 K in CD_2Cl_2 . The NOE (labeled in yellow) between proton 7 of the DSI (purple) and the p-methoxy-group of the imine suggest the existence of *type IIE_O*. The calculated distances between these groups are in *type E_N* (7.65 Å) are significantly bigger than in *type IIE_O* (3.51 Å). In [figure S11](#) this NOE is shown in green.

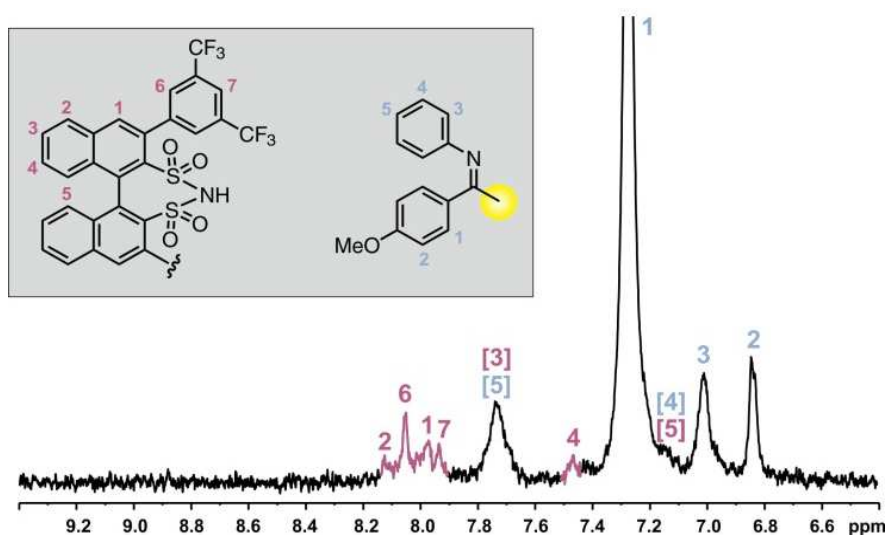


Figure S 19: A section of a selective 1D $^1\text{H},^1\text{H}$ -NOESY ($\tau_{\text{mix}} = 100$ ms, Gauss180 pulse) excited on the α -methyl group of **Z-2a** (yellow circle) at 180 K in CD_2Cl_2 is shown. NOEs are visible to the complete catalyst backbone. Due to the extreme motion of the imine inside the binary complex no experimental determination of the existing structures of the Z-complexes was possible. The signals of the protons in brackets are overlapping.

4 Disulfonimides Versus Phosphoric Acids

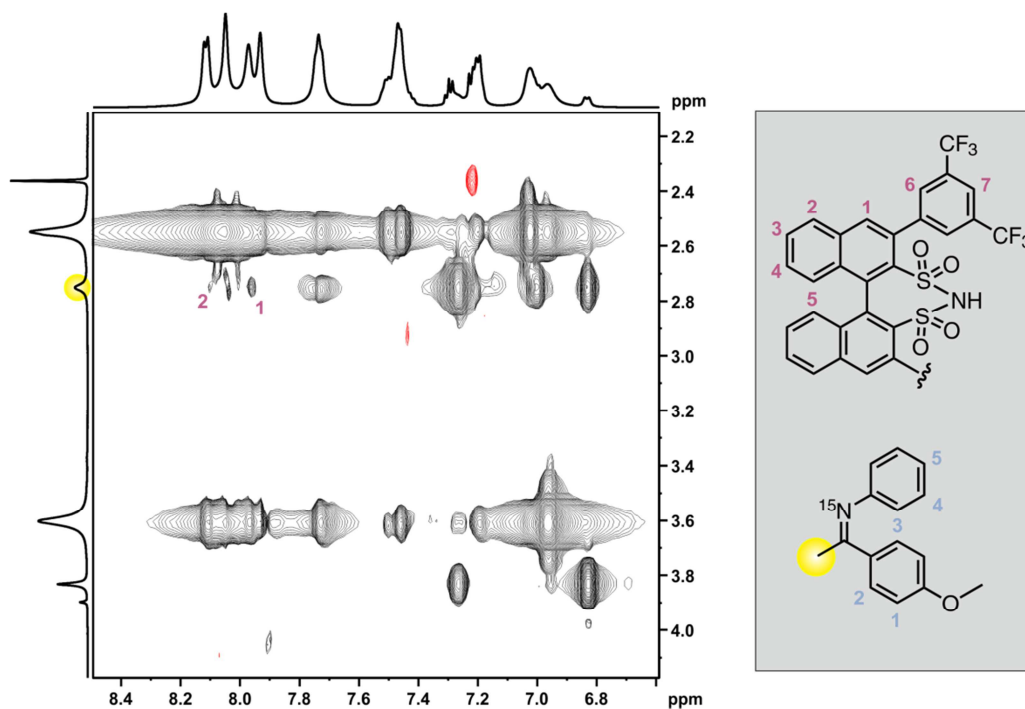


Figure S 20: 2D $^1\text{H}, ^1\text{H}$ NOESY spectrum ($\tau_{\text{mix}} = 300$ ms) of complex **1e/2a** at 180 K in CD_2Cl_2 . The slight NOEs between the α -methyl-group of the imine (labeled in yellow) and some protons of the backbone of the catalyst (purple 1 and 2) give a hint for the existence of *type IZ_N*. On the other hand the experimental proof of *type IIZ_N* was not possible.

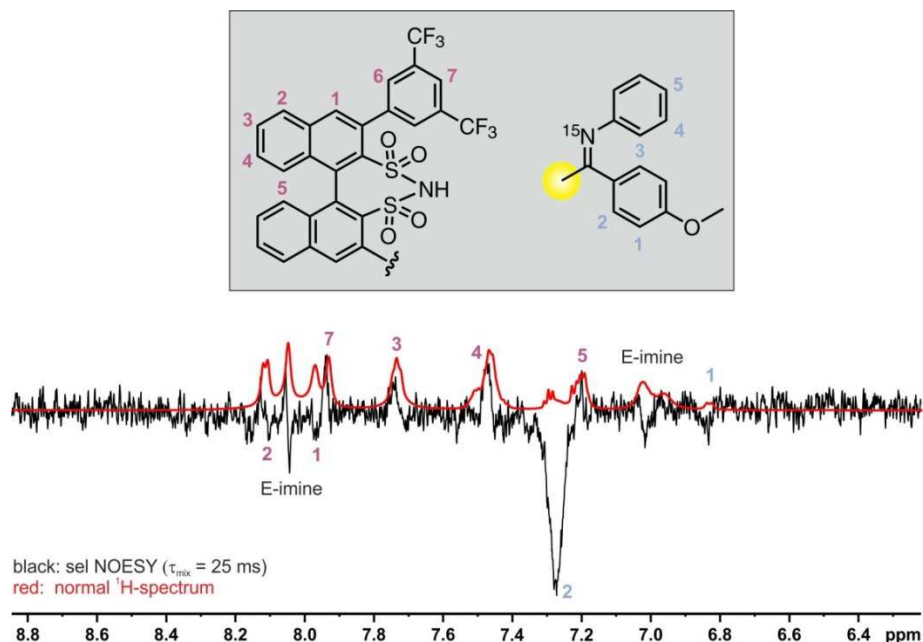


Figure S 21: A section of a selective 1D $^1\text{H}, ^1\text{H}$ -NOESY ($\tau_{\text{mix}} = 25$ ms, Gauss180 pulse) excited on the α -methyl group of **Z-2a** (yellow circle) at 180 K in CD_2Cl_2 is shown. NOEs to the most protons of the catalyst backbone can be obtained. Due to the high excess of the binary *E*-complex it was not possible to excite exclusively the α -methyl group of *Z*-imine. Potentially also small parts of the α -methyl group of *E*-imine were excited. Therefore also the NOEs to the aromatic protons of the *E*-imine are visible.

4 Disulfonimides Versus Phosphoric Acids

CF₃-DSI 1f/2a (CD₂Cl₂, 180K)

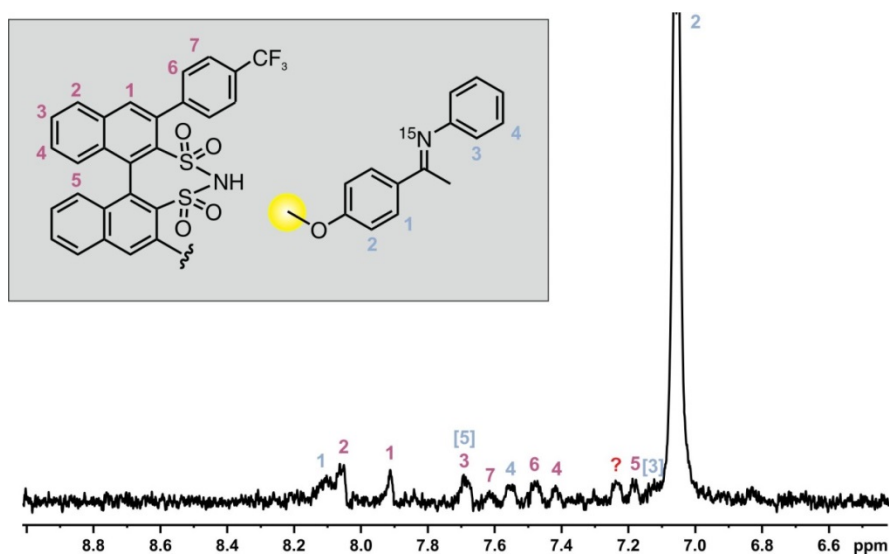


Figure S 22: A section of a selective 1D ¹H-NOESY ($\tau_{\text{mix}} = 100$ ms, RE-Burp pulse) excited on the *p*-methoxy group of *E*-2a (yellow circle) at 180 K in CD₂Cl₂ is shown. NOEs are visible to the complete catalyst backbone, indicating the existence of *type E_N*. However, also for some of the less populated *type E_O*-orientations (e.g. *type IE_O*) NOEs between the *p*-methoxy group of *E*-2a (yellow circle) and the BINOL backbone were expected. But in analogy the Figure S 19 the strong NOEs to the protons 1 and 2 of the backbone (purple) indicate the existence auf *type E_N*. Nevertheless the sterically less demanding 3,3'-substituents of the catalyst seems to enable a higher mobility of the imine in the complex. Therefore the intensity to the NOE to the proton 2 of the backbone (purple) is increased compared to the (CF₃)₂-DSI 1e/2a-complex. The signals of the protons in brackets are overlapping. The signal marked with a red ? might be from toluene (*E*-complex : *Z*-complex : toluene = 7.6:1:1 in the investigated sample).

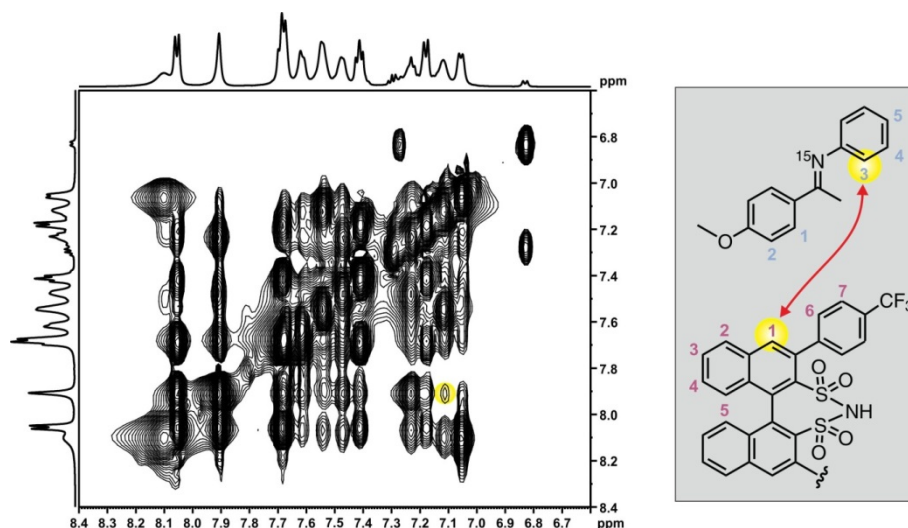


Figure S 23: 2D ¹H,¹H NOESY spectrum ($\tau_{\text{mix}} = 300$ ms) of complex 1f/2a at 180 K in CD₂Cl₂. In contrast to the CPA-complexes the NOE between proton 1 of the DSI (purple) and proton 3 of the imine (blue) does not identify *type IE_O* (labeled in yellow) unambiguously.

4 Disulfonimides Versus Phosphoric Acids

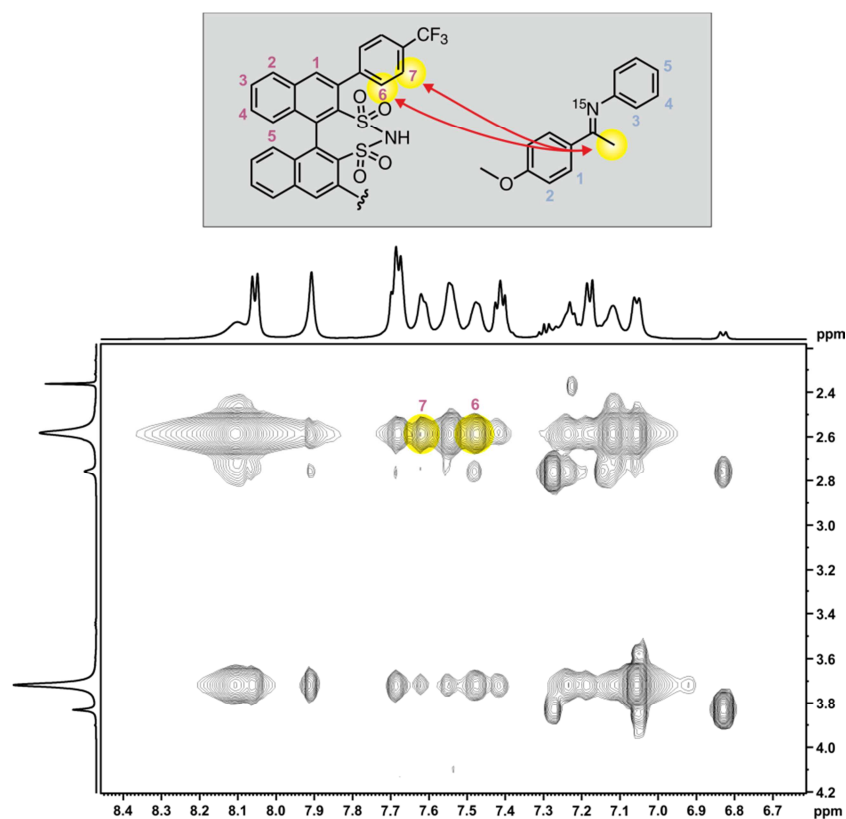


Figure S 24: A 2D $^1\text{H},^1\text{H}$ NOESY spectrum ($\tau_{\text{mix}} = 300$ ms) of complex **1f/2a** at 180 K in CD_2Cl_2 . The NOE (labeled in yellow) between the 3,3'-substituents of the DSI (purple 6 and 7) and the p-methoxy-group of the imine suggest the existence of *type II* E_O . These assumption is based on the calculated distances between these groups are for the **1e/2a**-complex (see green NOE in figure S 13).

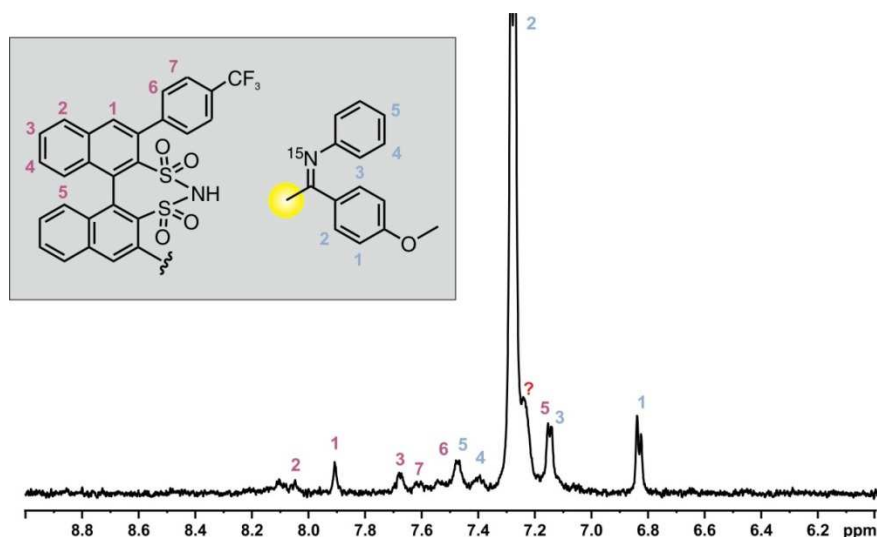


Figure S 25: A section of a selective 1D $^1\text{H},^1\text{H}$ -NOESY ($\tau_{\text{mix}} = 100$ ms, Gauss180 pulse) excited on the α -methyl group of **Z-2a** (yellow circle) at 180 K in CD_2Cl_2 is shown. NOEs are visible to the complete catalyst backbone. Due to the extreme motion of the imine inside the binary complex no experimental determination of the existing structures of the *Z*-complexes was possible. The signal marked with a red ? might be from toluene. Therefore, that the excited α -methyl group of **Z-2a** is close to the methyl-group of toluene it might also be excited (*E*-complex : *Z*-complex : toluene = 7.6:1:1 in the investigated sample).

4 Disulfonimides Versus Phosphoric Acids

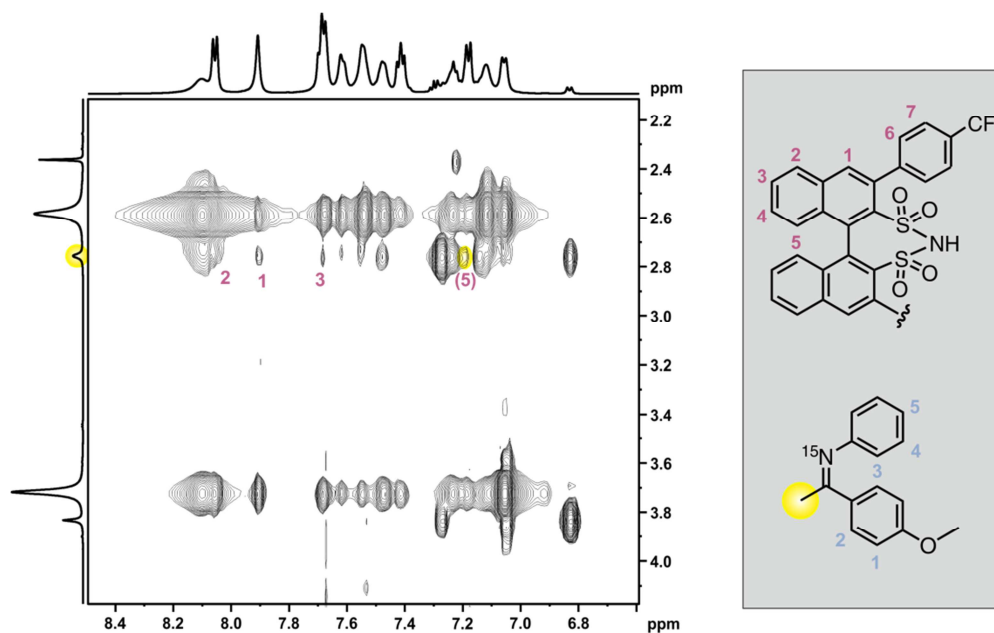


Figure S 26: 2D $^1\text{H}, ^1\text{H}$ NOESY spectrum ($\tau_{\text{mix}} = 300$ ms) of complex **1f/2a** at 180 K in CD_2Cl_2 . The slight NOEs between the α -methyl-group of the imine (labeled in yellow) and some protons of the backbone of the catalyst (purple 1, 2, 3 and 5) give a hint for the existence of *type IZ_N*. On the other hand the experimental proof of *type IIZ_N* was not possible.

CF₃-DSI **1f/2b** (CD_2Cl_2 , 180K)

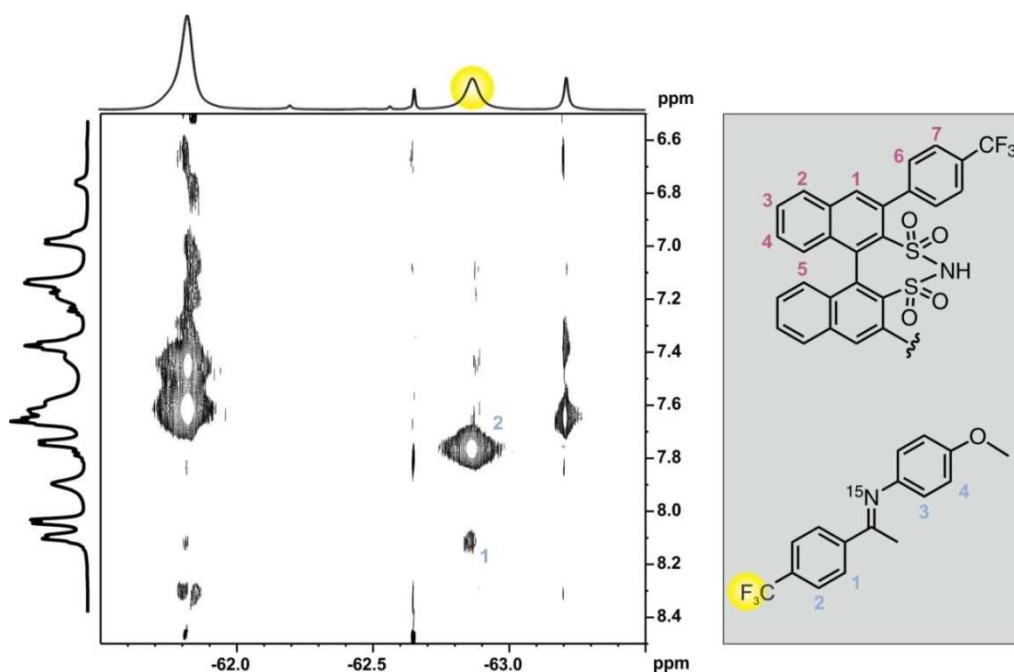


Figure S 27: The $^1\text{H}, ^{19}\text{F}$ -HOESY spectra of complex **1f/2b** at 180 K in CD_2Cl_2 . The trifluoromethyl group of **E-2b** (labeled in yellow) shows none of the expected signals (purple 1 and 2) to the backbone of the catalyst. Therefore this spectrum could not be used to identify *type E_N*.

4 Disulfonimides Versus Phosphoric Acids

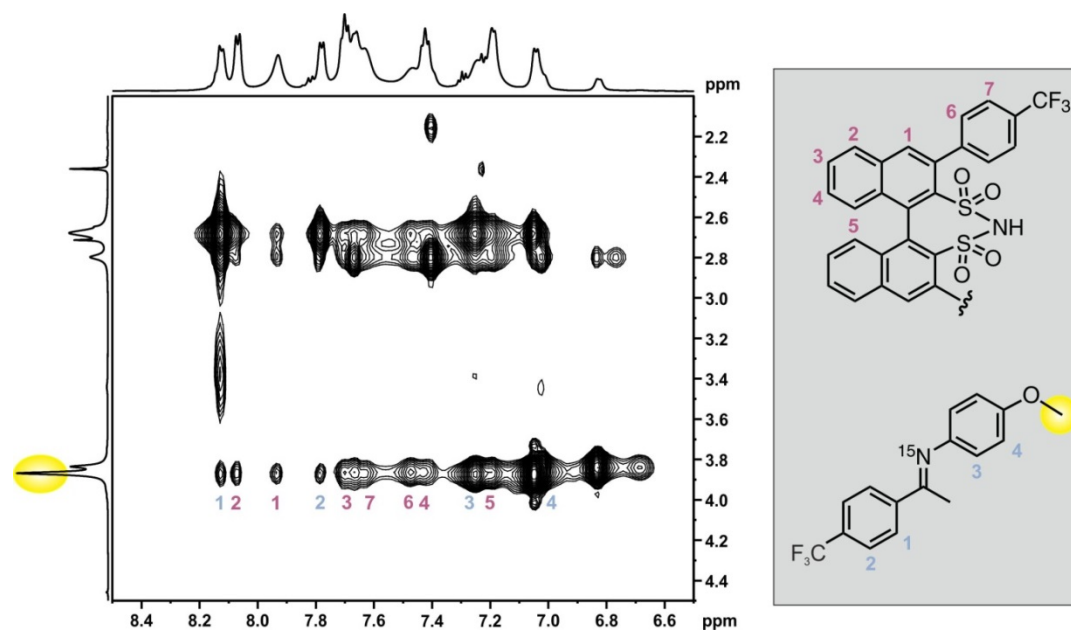


Figure S 28: 2D $^1\text{H}, ^1\text{H}$ NOESY spectrum ($\tau_{\text{mix}} = 300$ ms) of complex **1f/2b** at 180 K in CD_2Cl_2 . The existence of *type II* E_O is assumed because of the strongest NOEs between the methoxy-group of the imine (labeled in yellow) and the catalyst-backbone (purple 3, 4 and 5). Whereas, the NOEs between the methoxy-group of the imine (labeled in yellow) and the 3,3'-substituents of the catalyst (purple 6 and 7) can be obtained from all three orientations (*type E_N*, *type I* E_O and *type II* E_O). The measurement of a selective 1D $^1\text{H}, ^1\text{H}$ -NOESY, where the α -methyl group of *E-2b* is excited, is not possible due to signal-overlap. Thus, no unambiguous experimental proof for the *type E_N* was found, but due to the situation in the other complexes and the computationally predicted preference for this orientation, nevertheless the existence of *type E_N* was assumed.

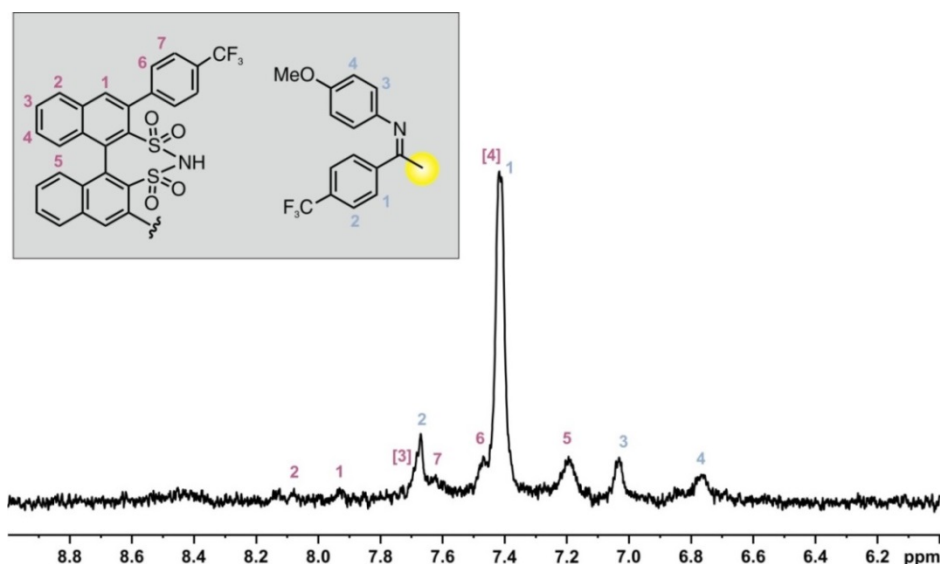


Figure S 29: A section of a selective 1D $^1\text{H}, ^1\text{H}$ -NOESY ($\tau_{\text{mix}} = 100$ ms, Gauss180 pulse) excited on the α -methyl group of *Z-2b* (yellow circle) at 180 K in CD_2Cl_2 is shown. Due to the extreme motion of the imine inside the binary complex no experimental determination of the existing structures of the *Z*-complexes was possible. NOEs are visible to the complete catalyst backbone. The signals of the protons in brackets are overlapping.

4 Disulfonimides Versus Phosphoric Acids

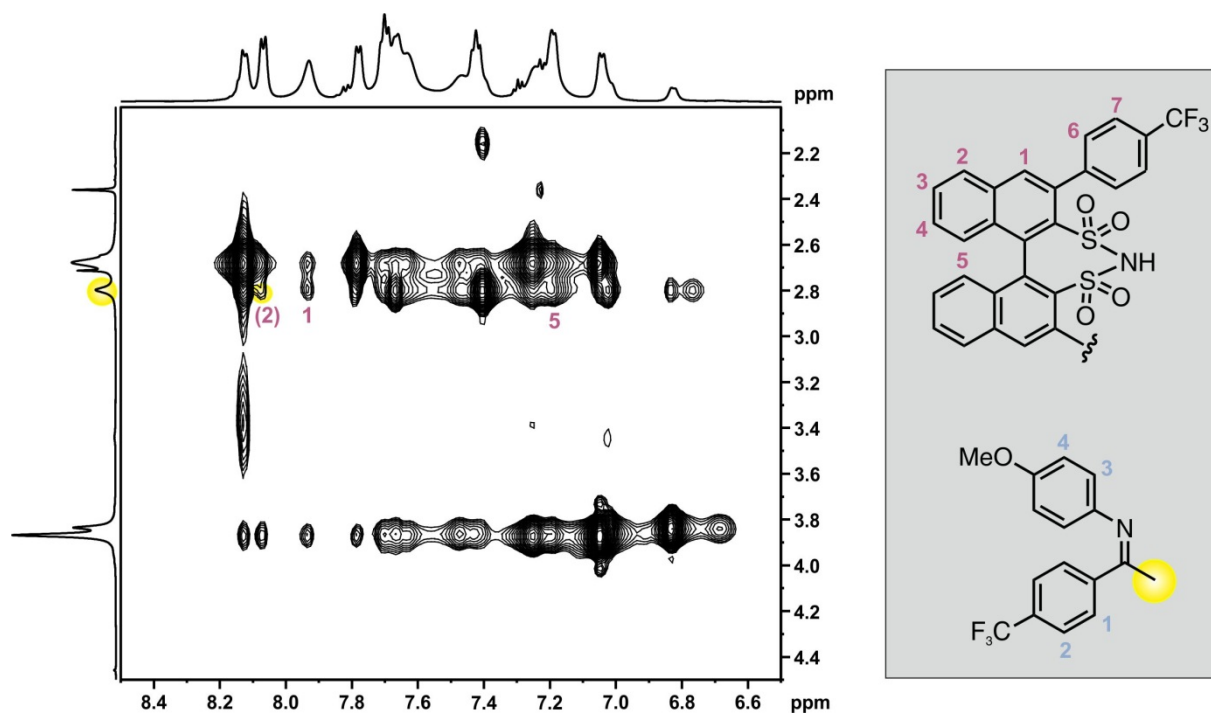


Figure S 30: 2D $^1\text{H}, ^1\text{H}$ NOESY spectrum ($\tau_{\text{mix}} = 300$ ms) of complex **1f/2b** at 180 K in CD_2Cl_2 . The slight NOEs between the α -methyl-group of the imine (labeled in yellow) and some protons of the backbone of the catalyst (purple 1, 2 and 5) give a hint for the existence of *type IZ_N*.

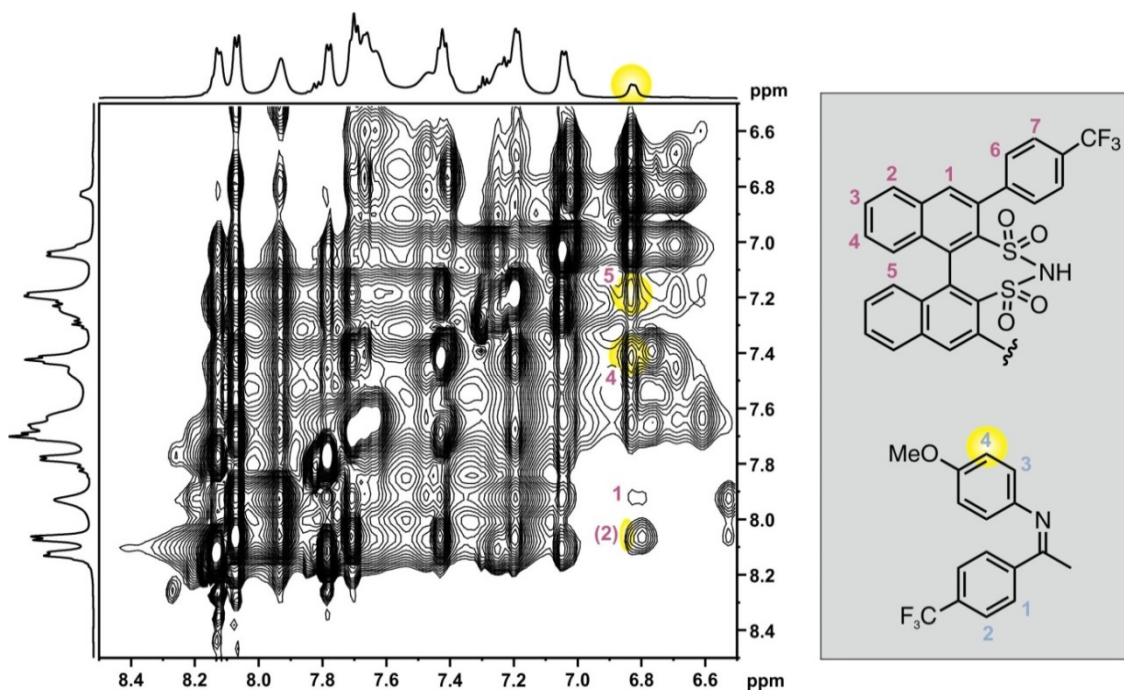


Figure S 31: 2D $^1\text{H}, ^1\text{H}$ NOESY spectrum ($\tau_{\text{mix}} = 300$ ms) of complex **1f/2b** at 180 K in CD_2Cl_2 . The existence of *type II Z_N* could be assumed because of the slight NOEs between the aniline moiety of the imine (blue 4) and the backbone of the catalyst (purple 1, 2, 4 and 5).

4.5.13. In-situ NMR-kinetics of the transfer hydrogenation

Imine **2a** (11.95 mg for **1e**-sample or rather 11.87 mg for **1f**-sample, 0.05 mmol, 1.0 eq) and diethyl 1,4-dihydro-2,6-dimethyl-3,5-pyridinedicarboxylate (16.8 mg for **1e**-sample or rather 18.7 mg for **1f**-sample, 0.07 mmol, 1.4 eq) were weighted directly into a NMR tube and solved in 0.3 ml dry, deuterated dichloromethane. Under argon atmosphere 0.2 ml of a catalyst stock solution (0.01 eq, 3.01 mg **1e** in 1.5 mL dry CD₂Cl₂ respectively 3.83 mg **1f** in 2 mL dry CD₂Cl₂). Immediately after addition of the catalyst a ¹H-in-situ-NMR kinetic was measured at 313.15 K. The imine **2a** was prepared as described in the experimental section 1.2. Both catalysts as well as Hantzsch ester were purchased from Sigma Aldrich.

For reasons of comparison, the intensity of the α -methyl group of the imine in the first spectrum was calibrated to 1. Since for structure determination and hydrogen bond analysis dichloromethane was used, the reaction kinetics were also performed in deuterated dichloromethane. A further advantage of using dichloromethane is the better separated signals, which enable therefore a more exact integration.

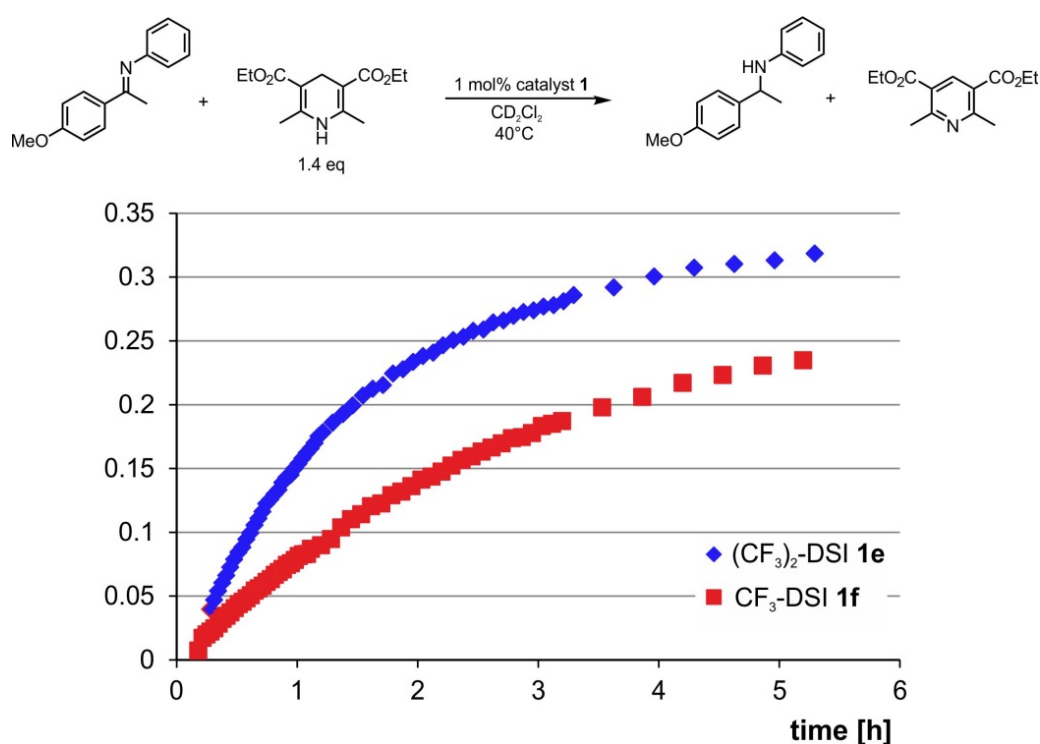


Figure S 32: The reaction profiles for the symmetric transfer hydrogenation of imine **2a** are shown. The kinetics were done in-situ in the NMR spectrometer with 1.4 equivalents of Hantzsch ester and 1 mol% catalyst ((CF₃)₂-DSI **1e** and CF₃-DSI **1f**) at 40°C in CD₂Cl₂

4 Disulfonimides Versus Phosphoric Acids

4.5.14. Reaction kinetics of the transfer hydrogenation

Representative procedure for the ex-situ kinetics with imine 2a

A Schlenk tube with an additional attached septum was dried at 300 °C for 15 min under reduced pressure. The flask was left to cool down and was flushed with argon. Imine **2a** (73.7 mg, 327 μmol, 1.0 eq.) and Hantzsch Ester (116.0 mg, 457.8 μmol, 1.4 eq.) were weighed into the tube. The tube was evacuated and flushed with argon three times. A standard stock solution of 1,3,5-trimethoxybenzene (54 mM) in anhydrous toluene was prepared and 3 mL of the standard stock solution were added to the tube under argon flow. The setup was put into a metal-heating block and preheated to 35 °C. A catalyst stock solution was prepared by dissolving the catalyst (2.9 mM) in anhydrous toluene. To start the reaction, the catalyst stock solution (1.0 mL, 0.009 eq., 0.9 mol % catalyst) was added to the reaction solution. After 1, 5, 10, 15, 20, 25, 30, 45 and 60 min, samples of the reaction mixture (≈ 0.1 mL) were taken via a septum and quenched by adding to a solution of *n*-hexane (2.0 mL) and NEt₃ (10 μL, 7.3 μg, 0.072 mmol, 100 eq. based on the catalyst). The mixture was filtered through a PTFE syringe filter and analyzed by chiral HPLC. Previously, it was shown that the addition of NEt₃ quenches the reaction and that the standard does not interfere with the reaction.

The kinetics with the imines **2c** and **2d** were performed at the same scale.

4.5.15. HPLC conditions

(E)-1-(4-methoxyphenyl)-N-phenylethan-1-imine 2a

CSP-HPLC, CHIRALPAK IC column (4.6mm x 250 mm, particle size: 5 μm), eluent *n*-hexane/*i*-propanol 99/1, flowrate 0.9 mL/min, column compartment temperature 20°C, λ = 220 nm.

Retention times: toluene/NEt₃: τ₁ = 3.7 min; major (*R*)-amine: τ₂ = 10.8 min; minor (*S*)-amine: τ₃ = 11.8 min; 1,3,5-trimethoxybenzene: τ₄ = 16.0 min; imine **2a**: τ₅ = 25.7 min; HE-pyridine: τ₆ = 42.9 min.

4 Disulfonimides Versus Phosphoric Acids

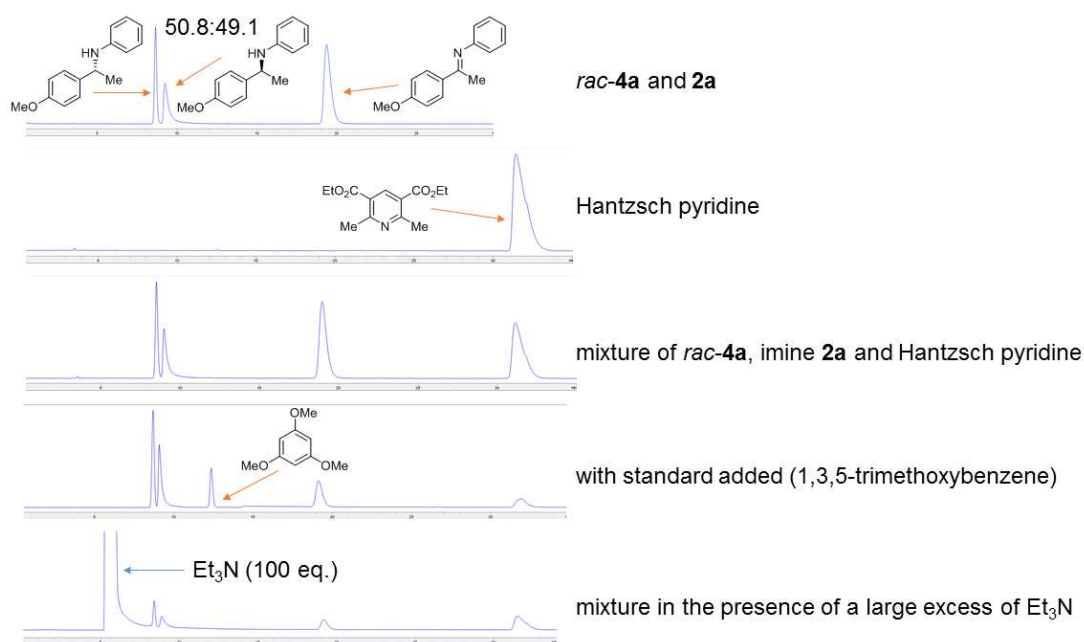


Figure S 33: CSP-HPLC chromatograms of the reaction components in the transfer hydrogenation of **2a**.

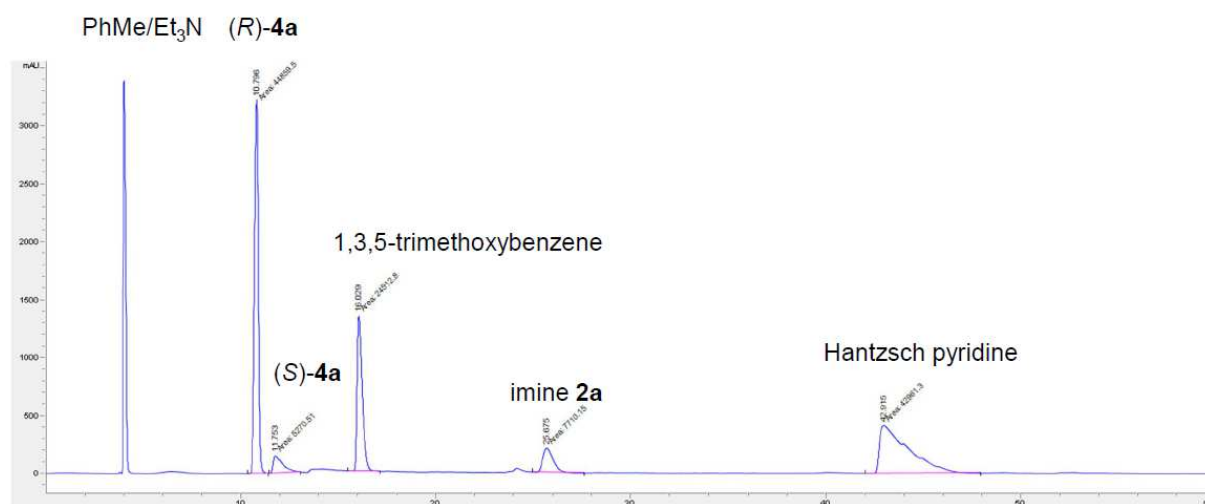


Figure S 34: Representative CSP-HPLC chromatogram of a sample taken during the transfer hydrogenation of imine **2a**. HPLC conditions: Chiralpak IC, *n*-hexane/*i*-propanol 99:1, 0.9 mL·min⁻¹, 20 °C, 220 nm detection.

4 Disulfonimides Versus Phosphoric Acids

N,1,1-triphenylmethanimine **2c**

CSP-HPLC, CHIRALPAK IC column (4.6mm x 250 mm, particle size: 5 μ m), eluent *n*-hexane/*i*-propanol 99/1, flowrate 0.9 mL/min, column compartment temperature 20°C, λ = 220 nm.

Retention times: toluene/ NEt_3 : τ_1 = 3.7 min; product **4c**: τ_2 = 5.1 min; imine **2c**: τ_3 = 8.6 min; 1,3,5-trimethoxybenzene: τ_4 = 16.0 min; HE-pyridine: τ_5 = 43.0 min.

An aliquot from the quenched samples was diluted 4x with *n*-hexane before syringe filtering and HPLC analysis because of the high absorption of the product at higher conversion.

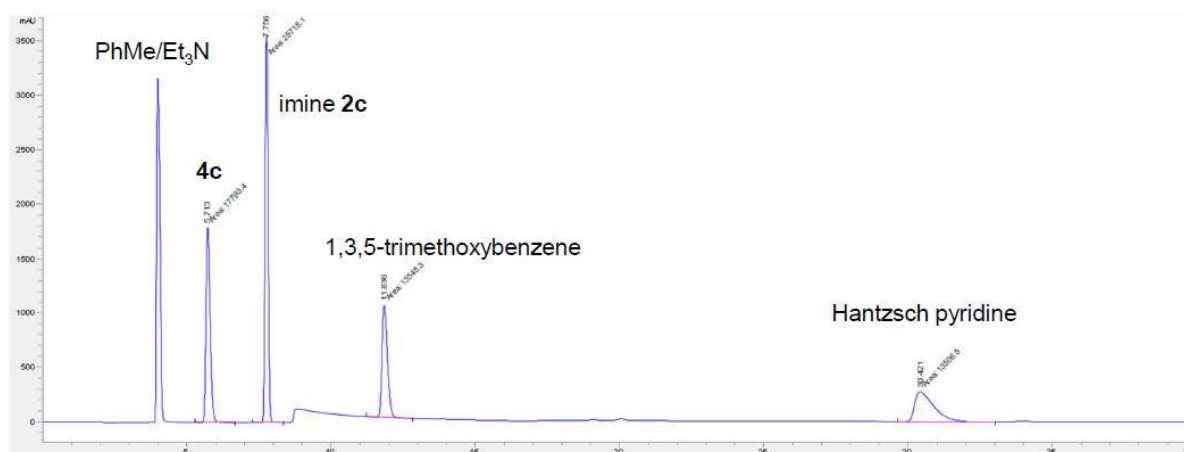


Figure S 35: Representative CSP-HPLC chromatogram of a sample taken during the transfer hydrogenation of imine **2c**. HPLC conditions: Chiralpak IC, *n*-hexane/*i*-propanol 99:1, 0.9 mL.min⁻¹, 20 °C, 220 nm detection.

(E)-1-(4-methylphenyl)-*N*-phenylethan-1-imine (98% ¹⁵N) **2d**

CSP-HPLC, CHIRALCEL OD-H column (4.6mm x 250 mm, particle size: 5 μ m), eluent *n*-hexane/*i*-propanol 98/2, flowrate 0.9 mL/min, column compartment temperature 20°C, λ = 220 nm.

Retention times: toluene/ NEt_3 : τ_1 = 4.0 min; HE-pyridine: τ_2 = 6.3 min; minor (*S*)-amine **4d**: τ_3 = 9.2 min; 1,3,5-trimethoxybenzene: τ_4 = 9.4 min; major (*R*)-amine **4d**: τ_5 = 10.2 min; imine **2d**: τ_6 = 11.7 min.

4 Disulfonimides Versus Phosphoric Acids

Because of the partially overlapping peaks of the minor enantiomer of the product and the standard, the enantiomeric ratio of the product was determined at 254 nm, where the standard absorbs minimally. The integral of the minor enantiomer at 220 nm was calculated from the *er* and the major enantiomer peak, and the integral of the standard was calculated by subtraction from the overlapping peak.

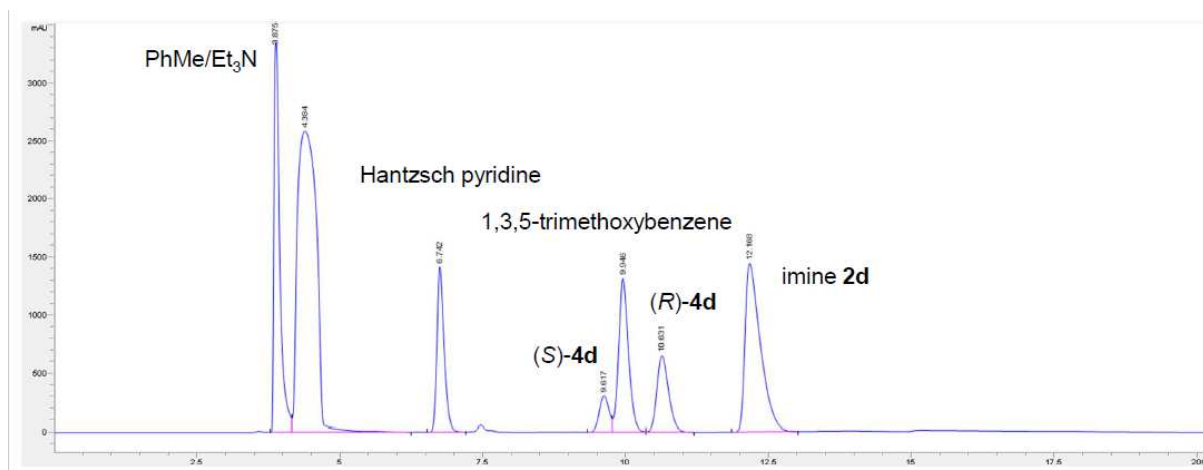


Figure S 36: Representative CSP-HPLC chromatogram of a sample taken during the transfer hydrogenation of imine **2d**. HPLC conditions: Chiralcel OD-H, *n*-hexane/*i*-propanol 98:2, 0.9 mL.min⁻¹, 20 °C, 220 nm detection.

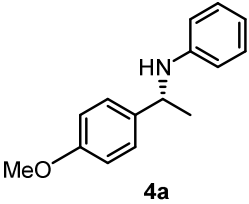
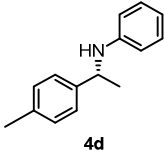
4.5.16. Enantiomeric excess by using different catalysts

The enantiomeric ratios of the chiral amines were determined from crude reaction mixtures by CSP-HPLC after substantial conversion to the products (usually after 2 h). We observed that *ee* is constant during the reaction.

The orientation of components in the ternary complex is decisive for the stereoselectivity. Due to observed enantioselectivities in a similar range (68 – 78 % *ee*, corresponding to energy difference approx. 1 kJ.mol⁻¹) in the transfer hydrogenation of *N*-aryl imines with catalysts TRIFP **1b**, (CF₃)₂-DSI **1e** and BINSAs, which have identical chirality, BINOL backbone and 3,3'-substituents, there must be similar non-covalent interactions in the active transition state. Hence, the acidic motif of the catalyst does not seem to influence the selectivity, provided there is a hydrogen bond anchor. On the other hand, this motif is a crucial factor for the reactivity.

4 Disulfonimides Versus Phosphoric Acids

Table S 3: The obtained *ee*-values for the asymmetric transfer hydrogenation in toluene at 35°C by using different (*R*)-catalysts are shown. The *ee*-values were determined from the crude reaction mixture after 120 min by chiral HPLC. [a] After isolation. See reference.^[39]

chiral amine	catalyst	<i>ee</i> [%]
 4a	(<i>R</i>)-TRIP 1a	85 ^[a]
	(<i>R</i>)-TRIFP 1b	74 ^[a]
	(<i>R</i>)-TRIM 1d	84
	(<i>R</i>)-(CF ₃) ₂ -DSI 1e	78
	(<i>R</i>)-CF ₃ -DSI 1f	70
	(<i>R</i>)-BINSA 1g	68
 4d	(<i>R</i>)-TRIP 1a	78
	(<i>R</i>)-(CF ₃) ₂ -DSI 1e	40
	(<i>R</i>)-CF ₃ -DSI 1f	32

The orientation of components in the ternary complex is decisive for the stereoselectivity. Due to observed enantioselectivities in a similar range (68 – 78 % *ee*, corresponding to energy difference approx. 1 kJ.mol⁻¹) in the transfer hydrogenation of *N*-aryl imines with catalysts TRIFP **1b**, (CF₃)₂-DSI **1e** and BINSA, which have identical chirality, BINOL backbone and 3,3'-substituents, there must be similar non-covalent interactions in the active transition state. Hence, the acidic motif of the catalyst does not seem to influence the selectivity, provided there is a hydrogen bond anchor. On the other hand, this motif is a crucial factor for the reactivity.

4.5.17. Reactivity analysis

1-(4-methoxyphenyl)-*N*-phenylethan-1-amine **4a**

From the position of the data points of the DSI-complexes on the Steiner-Limbach curve (Figure 3b) it is obvious, that both DSI/**2a**-complexes form weaker hydrogen bonds than the CPA-complexes. On the left side of the curve, a weaker hydrogen bond denotes a more acidic proton donor, i.e. a more complete proton transfer.^[5] By comparison of the exact ¹⁵N chemical shifts in the DSI/**2a**-complexes (for values see SI), it is apparent that the (CF₃)₂-DSI **1e** is just slightly more acidic than the CF₃-DSI **1f** (Figure 3b). Previously, we have shown that for the CPA-catalyzed transfer hydrogenation, the least acidic TRIP (i.e. forming the

4 Disulfonimides Versus Phosphoric Acids

strongest hydrogen bond) shows the fastest overall reaction rate.^[5] Based on this observation, we expected the reactions with the DSIs **1e** and **1f** to be the slowest. However, the transfer hydrogenation of imine **2a** and (CF₃)₂-DSI **1e** (calculated pK_a 0.05 in DMSO)^[45] is the fastest, whereas with CF₃-DSI **1f** and TRIP **1a** (calc. pK_a 3 – 4 in DMSO) the overall reaction rate is similar (Figure 8). Nevertheless, the small differences in the internal acidity of the two DSIs should not reflect this huge reactivity differences. This unexpected discrepancy seems to be due to the reduced influence of the hydrogen bond as a structural anchor by using more acidic DSI-catalysts. On the other hand, the considerable difference in acidity between CPAs and DSIs should not result in similar reactivity of TRIP **1a** and CF₃-DSI **1f**, if also in the extended pK_a range a direct correlation between the acidity and reactivity exists. The even slower reaction rate of TRIM (**1d**), which has smaller substituents (large steric parameter AREA θ 61),^[27] showing the importance of the bulky 3,3'-substituents and dispersion effects for the reaction rate (cf. **1a** AREA θ 51). Additionally, the transfer hydrogenation was carried out with an extremely acidic, but structural similar BINOL-derived sulfonic acid BINSAs **1g** (calc. pK_a -9 in DMSO). Surprisingly the reaction was extremely slow, and the overall reaction rate was similar to TRIFP (Figure 8). This observation might be explained by the low tendency of BINSAs **1g** to form the ternary complex due to the internal stabilization by a hydrogen bond, resulting in the lack of a proper bifunctional moiety. Reaction with TiPSY (**1c**) is extremely slow and only traces of the product were detected after several hours, probably because of very bulky 3,3'-substituents (small AREA θ 29).

Thus, no correlation between reactivity and acidity of catalysts with different acidic functional groups was found. In conclusion, these results suggest that the previously established acidity/reactivity-relationship^[5] is only applicable if the crucial catalytic sites of the catalyst are not changed.

4 Disulfonimides Versus Phosphoric Acids

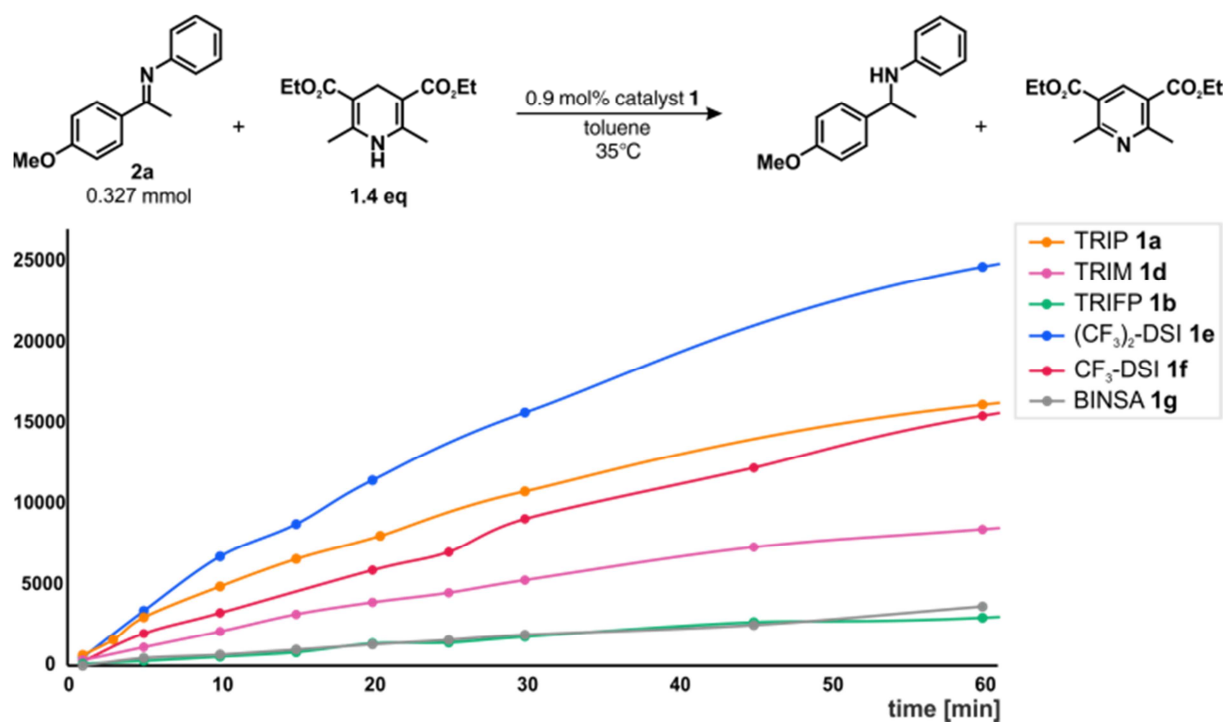


Figure S 37. The reactivities of the asymmetric transfer hydrogenation of imine **2a** are shown. The reaction profiles of three CPAs **1a**, **1b** and **1d**^[5] are compared with the more acidic DSIs **1e** and **1f**. Additionally, the even more acidic BINSA **1g** was used as a catalyst. The kinetics were done ex-situ and the samples analyzed by CSP-HPLC. All reactions were done in a 0.327 mmol scale with 1.4 equivalents of Hantzsch ester and 0.9 mol% catalyst at 35°C in toluene.

For imine **2d**, the same order of reactivity was found for the three investigated catalysts (TRIP **1a** and both DSIs **1e** and **1f**, see chapter 0). However, for imine **2c**, the fastest reaction was observed with CF₃-DSI **1f**, suggesting that the steric requirements of the bulkier imine **2c** can change the reactivity order (see chapter 0). Thus, not only the structure of the catalyst (size of the binding pocket^[5] and acidic motif) is crucial for the reactivity, but also the properties of substrate should not be neglected.

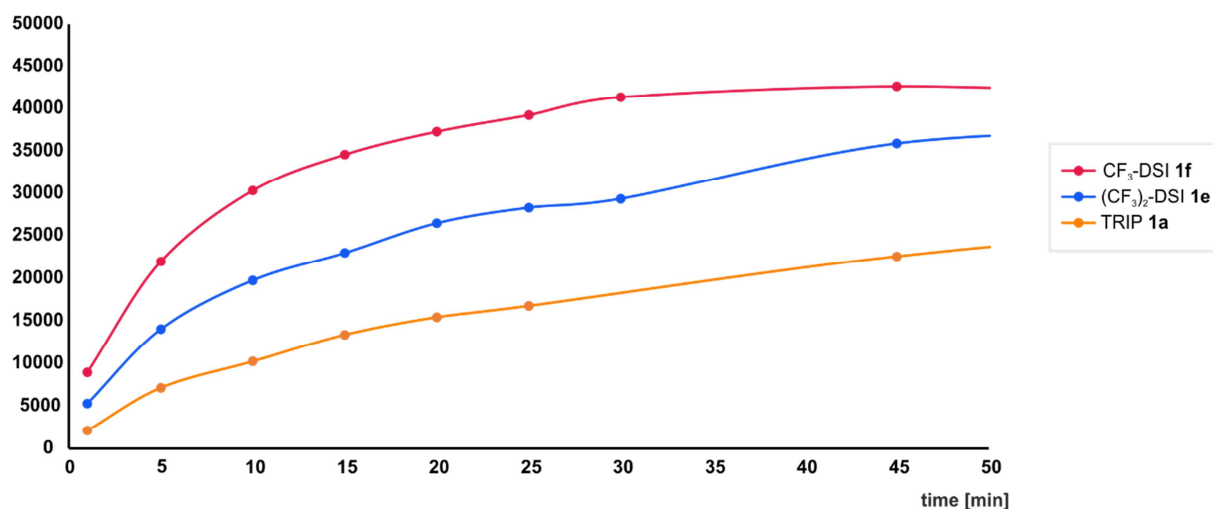
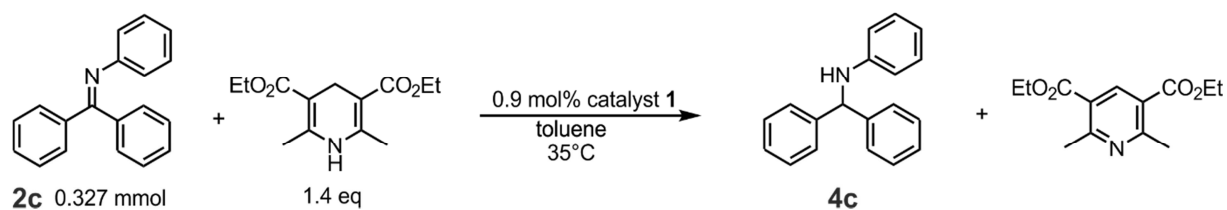
N-benzhydryl aniline 4c

Figure S 38: The formation of **4c** in the asymmetric transfer hydrogenation of imine **2c** is shown. The kinetics were done ex-situ and the samples analyzed by CSP-HPLC. The reaction was conducted with 1.4 equivalents of Hantzsch ester and 0.9 mol% catalyst with 0.5 eq. 1,3,5-trimethoxybenzene as the standard at 35°C in PhMe.

Sulfonylimide catalyst (CF₃)₂-DSI (**1e**) gives faster reaction than phosphoric acid TRIP (**1a**). However, in this case the reaction is even faster with CF₃-DSI (**1f**), most probably due to steric reasons. Catalyst **1f** is endowed with smaller 3,3'-substituents than both **1a** and **1e**, which probably is the decisive factor with bulky substrates such as **2c**.

4 Disulfonimides Versus Phosphoric Acids

1-(4-methylphenyl)-N-phenylethan-1-amine (98% ¹⁵N) **4d**

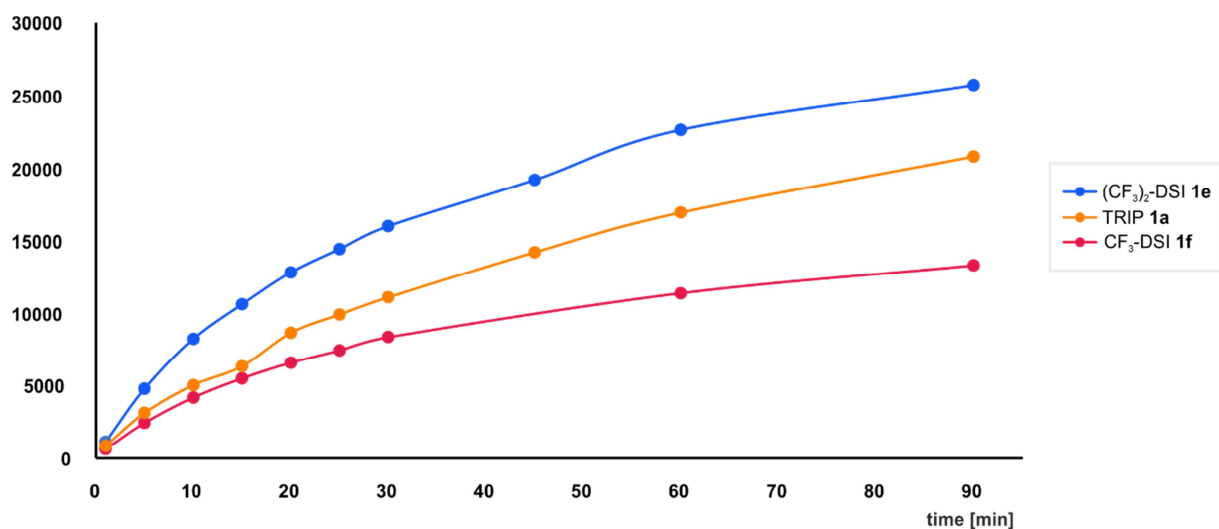
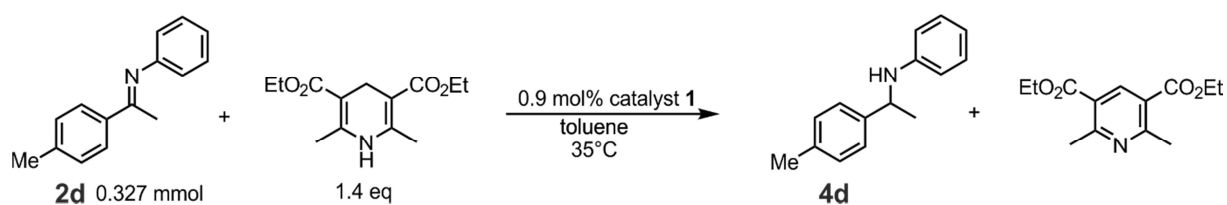


Figure S 39: The formation of **4d** in the asymmetric transfer hydrogenation of imine **2d** is shown. The kinetics were done ex-situ and the samples analyzed by CSP-HPLC. The reaction was conducted with 1.4 equivalents of Hantzsch ester and 0.9 mol% catalyst with 0.5 eq. 1,3,5-trimethoxybenzene as the standard at 35°C in PhMe.

In the transfer hydrogenation of **2d**, the reactivity order with three different catalysts corresponds to the order observed in the transfer hydrogenation of **2a**.

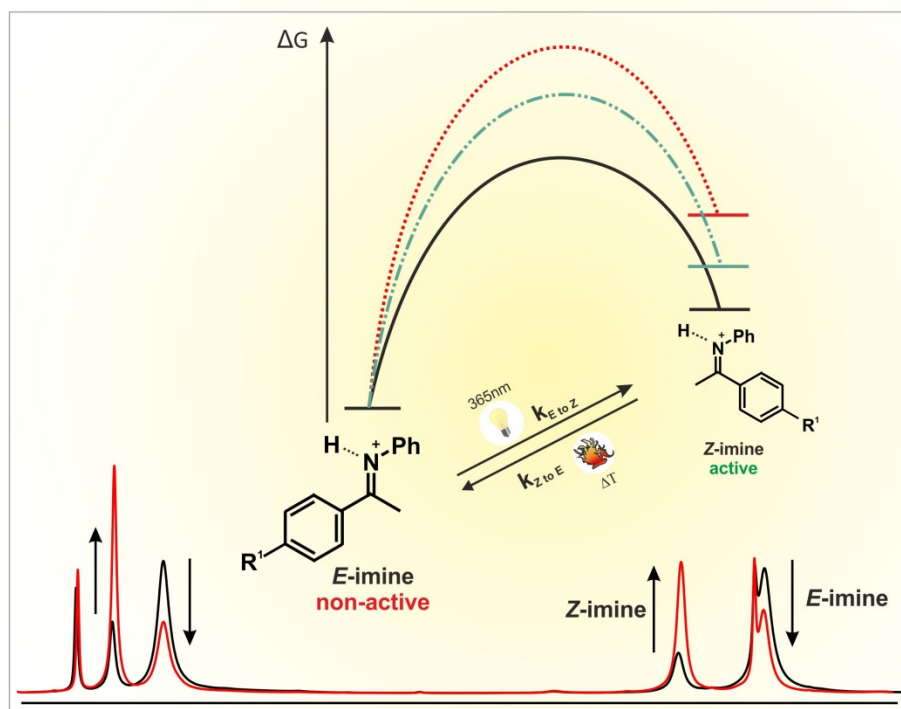
4.6. References

- [1] D. Parmar, E. Sugiono, S. Raja, M. Rueping, *Chem. Rev.* **2014**, *114*, 9047–9153.
- [2] M. Terada, *Synthesis (Stuttg.)* **2010**, 1929–1982.
- [3] N. Sorgenfrei, J. Hioe, J. Greindl, K. Rothermel, F. Morana, N. Lokesh, R. M. Gschwind, *J. Am. Chem. Soc.* **2016**, *138*, 16345–16354.
- [4] J. Greindl, J. Hioe, N. Sorgenfrei, F. Morana, R. M. Gschwind, *J. Am. Chem. Soc.* **2016**, *138*, 15965–15971.
- [5] K. Rothermel, M. Melikian, J. Hioe, J. Greindl, J. Gramüller, M. Zabka, N. Sorgenfrei, T. Hausler, F. Morana, R. M. Gschwind, *Chem. Sci.* **2019**, *accepted*. DOI:10.1039/C9SC02342A
- [6] R. R. Knowles, E. N. Jacobsen, *Proc. Natl. Acad. Sci.* **2010**, *107*, 20678–20685.
- [7] R. Maji, S. C. Mallojjala, S. E. Wheeler, *Chem. Soc. Rev.* **2018**, *47*, 1142–1158.
- [8] T. Akiyama, K. Mori, *Chem. Rev.* **2015**, *115*, 9277–9306.
- [9] V. N. Wakchaure, P. S. J. Kaib, M. Leutzsch, B. List, *Angew. Chemie - Int. Ed.* **2015**, *54*, 11852–11856.
- [10] D. Nakashima, H. Yamamoto, *J. Am. Chem. Soc.* **2006**, *128*, 9626–9627.
- [11] M. Rueping, B. J. Nachtsheim, W. Ieawsuwan, I. Atodiresei, *Angew. Chemie - Int. Ed.* **2011**, *50*, 6707–6720.
- [12] M. Rueping, A. Kuenkel, I. Atodiresei, *Chem. Soc. Rev.* **2011**, *40*, 4539–49.
- [13] P. García-García, F. Lay, P. García-García, C. Rabalakos, B. List, *Angew. Chemie Int. Ed.* **2009**, *48*, 4363–4366.
- [14] M. Treskow, J. Neudörfel, R. Giernoth, *European J. Org. Chem.* **2009**, 3693–3697.
- [15] H. He, L. Y. Chen, W. Y. Wong, W. H. Chan, A. W. M. Lee, *European J. Org. Chem.* **2010**, 4181–4184.
- [16] T. James, M. Van Gemmeren, B. List, *Chem. Rev.* **2015**, *115*, 9388–9409.
- [17] I. Čorić, B. List, *Nature* **2012**, *483*, 315–319.
- [18] L. Liu, P. S. J. Kaib, A. Tap, B. List, *J. Am. Chem. Soc.* **2016**, *138*, 10822–10825.
- [19] S. Prévost, N. Dupré, M. Leutzsch, Q. Wang, V. Wakchaure, B. List, *Angew. Chemie - Int. Ed.* **2014**, *53*, 8770–8773.
- [20] M. Melikian, J. Gramüller, J. Hioe, J. Greindl, R. M. Gschwind, *Chem. Sci.* **2019**, *10*, 5226–5234.
- [21] M. Rueping, E. Sugiono, C. Azap, T. Theissmann, *Org. Lett.* **2005**, *7*, 3781–3783.
- [22] K. Kaupmees, N. Tolstoluzhsky, S. Raja, M. Rueping, I. Leito, *Angew. Chemie Int. Ed.* **2013**, *52*, 11569–72.
- [23] W. Tang, S. Johnston, J. A. Iggo, N. G. Berry, M. Phelan, L. Lian, J. Bacsá, J. Xiao, *Angew. Chemie - Int. Ed.* **2013**, *52*, 1668–1672.
- [24] H. Kim, G. Gerosa, J. Aronow, P. Kasaplar, J. Ouyang, J. B. Lingnau, P. Guerry, C. Farès, B. List, *Nat. Commun.* **2019**, *10*, 1–6.
- [25] R. Maji, S. C. Mallojjala, S. E. Wheeler, *Chem. Soc. Rev.* **2018**, *47*, 1142–1158.
- [26] L. Simón, J. M. Goodman, *J. Org. Chem.* **2011**, *76*, 1775–1788.
- [27] J. P. Reid, J. M. Goodman, *J. Am. Chem. Soc.* **2016**, *138*, 7910–7917.
- [28] M. Orlandi, F. D. Toste, M. S. Sigman, *Angew. Chemie - Int. Ed.* **2017**, *56*, 14080–14084.
- [29] M. Orlandi, J. A. S. Coelho, M. J. Hilton, F. D. Toste, M. S. Sigman, *J. Am. Chem. Soc.*

4 Disulfonimides Versus Phosphoric Acids

- 2017, 139, 6803–6806.
- [30] F. Duarte, R. S. Paton, *J. Am. Chem. Soc.* **2017**, 139, 8886–8896.
- [31] R. Maji, P. A. Champagne, K. N. Houk, S. E. Wheeler, *ACS Catal.* **2017**, 7, 7332–7339.
- [32] S. E. Wheeler, T. J. Seguin, Y. Guan, A. C. Doney, *Acc. Chem. Res.* **2016**, 49, 1061–1069.
- [33] T. J. Seguin, S. E. Wheeler, *ACS Catal.* **2016**, 6, 7222–7228.
- [34] H. Benedict, I. G. Shenderovich, O. L. Malkina, V. G. Malkin, G. S. Denisov, N. S. Golubev, H. H. Limbach, *J. Am. Chem. Soc.* **2000**, 122, 1979–1988.
- [35] S. Sharif, G. S. Denisov, M. D. Toney, H. Limbach, *J. Am. Chem. Soc.* **2007**, 129, 6313–6327.
- [36] A. J. Dingley, S. Grzesiek, *J. Am. Chem. Soc.* **1998**, 120, 8293–8297.
- [37] F. Cordier, S. Grzesiek, *J. Am. Chem. Soc.* **1999**, 121, 1601–1602.
- [38] J. M. Crawford, M. S. Sigman, *Synth.* **2019**, 51, 1021–1036.
- [39] P. Renzi, J. Hioe, R. M. Gschwind, *J. Am. Chem. Soc.* **2017**, 139, 6752–6760.
- [40] J. S. M. Samec, J. E. Bäckvall, *Chem. - A Eur. J.* **2002**, 8, 2955–2961.
- [41] Y. Schramm, F. Barrios-Landeros, A. Pfaltz, *Chem. Sci.* **2013**, 4, 2760–2766.
- [42] A. V. Malkov, A. Mariani, K. N. Macdougall, P. Kočovský, **2004**, 6, 2253–2256.
- [43] R. K. Harris, E. D. Becker, S. M. Cabral De Menezes, R. Goodfellow, P. Granger, *Concepts Magn. Reson. Part A Bridg. Educ. Res.* **2002**, 14, 326–346.
- [44] N. Sorgenfrei, J. Hioe, J. Greindl, K. Rothermel, F. Morana, N. Lokesh, R. M. Gschwind, *J. Am. Chem. Soc.* **2016**, 138, 16345–16354.
- [45] C. Yang, X. S. Xue, X. Li, J. P. Cheng, *J. Org. Chem.* **2014**, 79, 4340–4351.

5 A Quantitative Analysis of the *E,Z*-Isomerization of Hydrogen Bonded *N*-Aryl-Imines



Kerstin Rothermel, Johnny Hioe and Ruth M. Gschwind

All NMR measurements as well as the complete analysis of the obtained data were performed by **Kerstin Rothermel**. Dr. Johnny Hioe contributed with theoretical calculations.

5 A Quantitative Analysis of the *E,Z*-Isomerization

5.1. Abstract

Recently, our group developed method to decrypt the transition states of the asymmetric transfer hydrogenation of imines by light (DTS-hv method). However, for the successful use of this technique it is required that the isomerization is the rate-determining step. Up to now, there are only indirect hints for a slow isomerization, but the experimental quantification of the isomerization rates is still missing. Therefore, no direct comparison between the isomerization rate and other possible rate-determining was possible. Thus, by means of in-situ NMR photoisomerization a detailed quantification of the imine-isomerization was conducted. Due to the different reactivities of the previously investigated Brønsted acid catalysts with varying acidities, the influence of the degree of imine-protonation on the isomerization rate was of particular interest. This analysis showed a rough dependency between the degree of imine-protonation and the *Z*-to-*E*-isomerization rate. However, the observed *Z*-to-*E*-isomerisation for the imine in the binary complex with the sterical most demanding catalyst was slower than expected. Thus, apart from the imine protonation also the sterical properties of the catalyst seem to affect the isomerization rate. On the other hand, the *E*-to-*Z*-isomerisation rates were less affected by the bulk of the catalyst, indicating the consideration of the sterical contribution in the stabilisation of the *Z*-imine. Furthermore, the analysis of the thermal isomerization barriers at low temperatures confirms the interplay of the sterical environment of the imine and the degree of protonation being responsible for the isomerization rates. At higher temperatures a decreasing contribution of the imine-protonation was observed, while the sterical factor increases.

5.2. Introduction

In the field of pharmacology the control over conformation and activity of molecules is of great interest.^[1] Particularly suitable molecules are photoswitches, which can be converted between two thermodynamically stable forms through an external stimulus (i.e. irradiation). Thus, a light-sensitive functionality can be introduced, either by incorporation into large biomolecules or the use as enzyme ligands. By irradiation with an appropriate wavelength the pharmacologic active substance is formed and reacts locally with a high efficiency.^[2,3] In this way the irradiation with a defined wavelength can be used to control the activity of different drugs from the outside.^[2] Several organic compounds have been reported with the necessary properties of a photoswitch,^[1] but one of the most popular and well-studied example is still azobenzene (Figure 1).^[1,4-6] The trans-azobenzene can be switched to the cis-form by irradiation with UV light (300 -

5 A Quantitative Analysis of the E,Z-Isomerization

400 nm). Thus, the geometry and also the chemical behavior (i.e. polarity) changes.^[5-7] The cis-azobenzene can be back-isomerized to the trans-form either by irradiation with blue light (> 400nm) or by thermal relaxation.^[1,2,5,6] For the well-known azobenzene and its derivatives the switching takes place *via* a cis-trans-isomerization. Although, other mechanisms, like reversible ring closure and ring opening electrocyclization, are known.^[4-6,8]

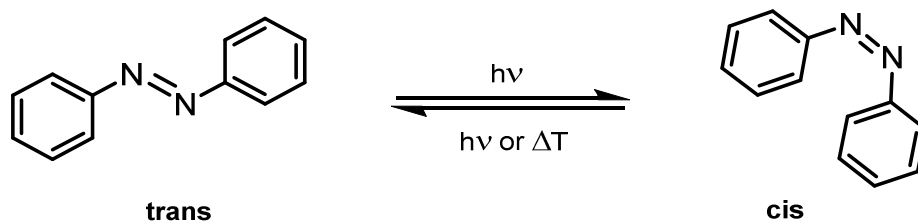


Figure 1: The trans-azobenzene can be isomerized to the cis-form by irradiation with UV light (300 - 400 nm).^[5,6] The back-isomerization takes place by irradiation with blue light (> 400nm) or by thermal relaxation.^[5,6]

Also, in chemical reactions isomerization often plays an important role. Amongst others, the Keto-enol tautomerism is a special form of isomerism and is one step in several reaction mechanisms, like α -functionalization of carbonyls, carboxyls and ketones (i.e. Mannich reaction) or condensation reactions (i.e aldol condensation, claisen condensation, and more).^[9] Another type of isomerism is the rearrangement of individual atoms or small groups. An example of the [1,2]-rearrangements in carbocation's is the Wagner-Meerwein rearrangement, which is exemplarily a step in the mechanism of Friedel-Crafts alkylation or selected olefin-isomerizations.^[9] Furthermore, in intramolecular cyclizations the isomerization of the substrate to the reactive conformation is often essential.^[10-12] Also for the Brønsted acid catalyzed reduction of imines the isomerization of the thermodynamic more stable *E*-imine to the active *Z*-imine is a key step.^[13]

In 2005, Rüping *et al.* proposed a mechanism for this asymmetric imine reduction (Figure 2), in which the imine **2** is protonated by the phosphoric acid catalyst **1** and therefore a hydrogen-bond assisted ion pair, the so-called binary complex, is formed.^[14] Subsequently, the hydride is transferred from the Hantzsch ester **3** and the chiral amine **4** is formed.^[14] Our previous studies about the active transition state in this asymmetric transfer hydrogenation showed that the reaction takes place *via* the transition states of the less populated *Z*-imine, while the *E*-imine is the thermodynamically more stable

5 A Quantitative Analysis of the *E,Z*-Isomerization

isomer. Hence, it became obvious that the isomerization of the imine has to play a crucial role within the reaction mechanism.^[13]

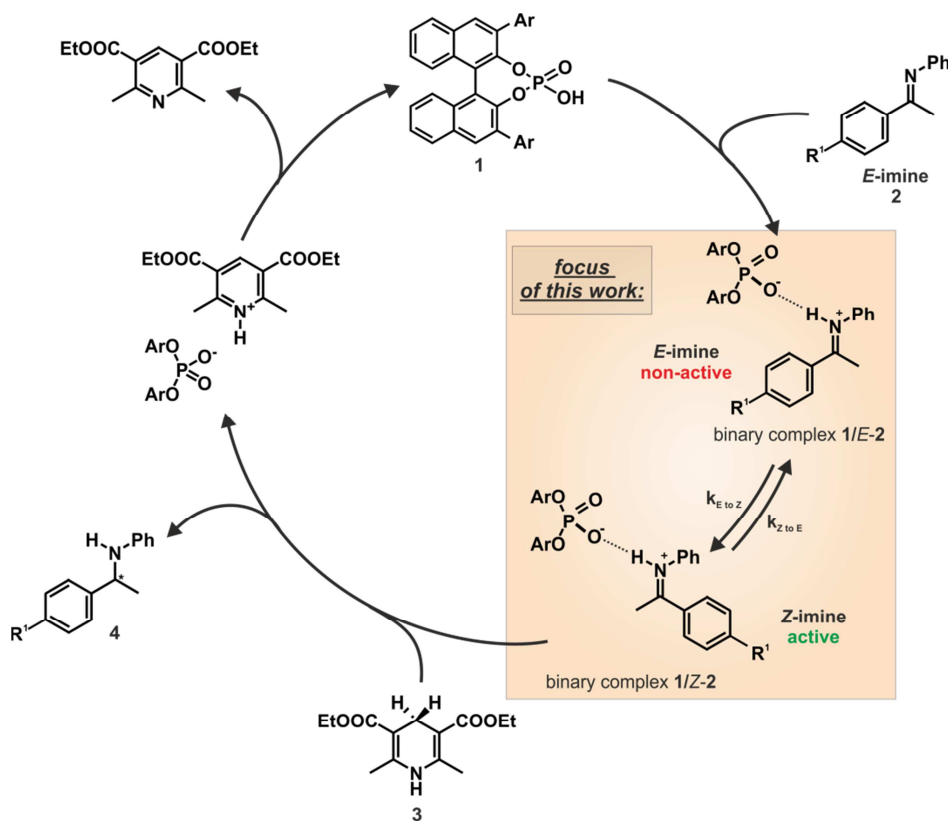


Figure 2: Proposed catalytic cycle of Brønsted acid catalyzed transfer hydrogenation of imines.^[14] Focus of this work was the detailed investigation of the isomerization of the imine.

Since, the transition state of the *Z*-imine seems to give the major product,^[13] a *via* isomerization increased amount of the *Z*-imine means a faster reaction under the assumption that the isomerization is the rate-determining step. One common method for the isomerization of imines is the irradiation with light,^[13,15–17] and indeed we could show that the investigated *N*-aryl-imines can be isomerized to their *Z*-forms by irradiating with 365 nm.^[13] However, due to the small thermal barrier between both isomers, a fast thermal back-isomerization of the *Z*-imines was observed at room temperature.^[15] In our previous work we assume a slow isomerization on the NMR timescale because of the separated signals for both isomers in ¹H-spectra of the binary complex (Figure 3).^[13] However, this assumption contradicts some theoretical calculations, which predict a fast equilibrium between *E*- and *Z*-imine in the presence of an acidic catalyst.^[18–21] Nevertheless, an experimentally determination of the isomerization rates is still missing.

5 A Quantitative Analysis of the *E,Z*-Isomerization

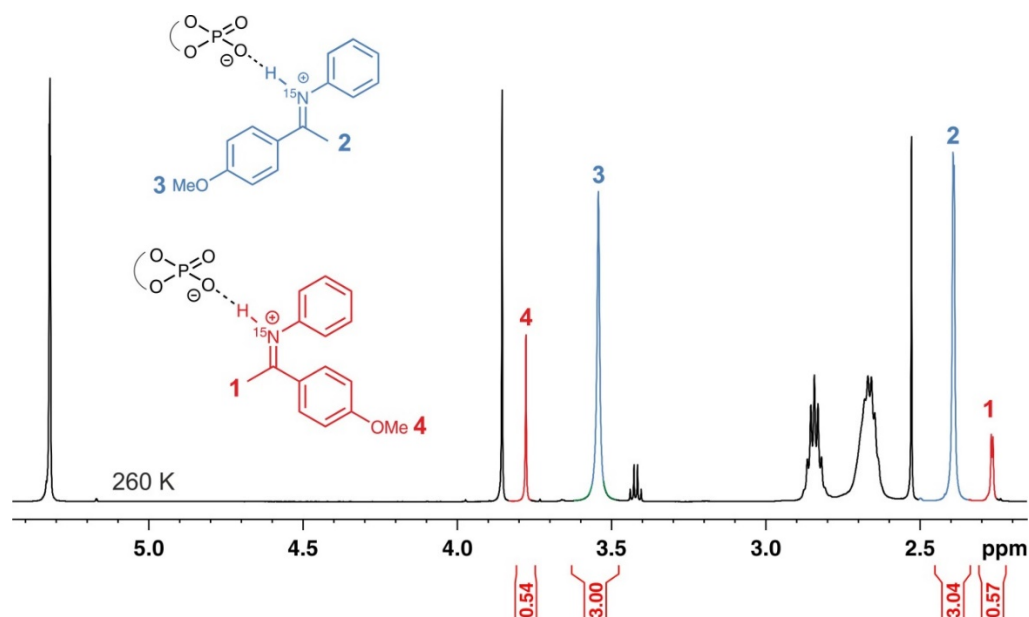


Figure 3: The ^1H spectra of a 1:1-sample containing the depicted imine and phosphoric acid catalyst in CD_2Cl_2 at 260 K show separated signals for the *E* and the *Z*-imine in the binary complex. This is a hint for a slow isomerization, at least on the NMR-timescale.

In general, different theories are known to describe a reaction (and also the isomerization) on a molecular level. One well-known example is the Eyring-theory, developed by Henry Eyring in 1935, which is based on transition state theory.^[22] For visualization of the reaction mechanism the Gibbs energy ΔG can be plotted vs. the reaction coordinate (in case of an isomerization see Figure 4b). At the maximum of the energy profile the transition state is located. By taking a closer look to the reaction profile of the isomerization it becomes visible that during the *E*-to-*Z*-isomerization the *E*-imine has to overcome the energy barrier of the transition state. The necessary energy can be supplied exemplarily by irradiation or heating. Afterward the product (in our case the *Z*-imine) is formed without additional energy consumption. However, the formation of a pre-equilibrium between the reactants and the transition states, which is described by the equilibrium constant K^\ddagger , is assumed (Figure 4a). This means that after reaching the transition state once again both isomers can be formed. However, in the following only the productive pathway to the *Z*-isomer is considered.

Finally, the Gibbs energy of activation $\Delta G_{\text{total}} = \Delta G_1 + \Delta G_2$ for the formation of the transition state from the starting materials is directly correlated with the rate constant k . This mathematical correlation is called Eyring equation (1):^[22]

5 A Quantitative Analysis of the E,Z-Isomerization

$$k = \frac{k_B T}{h} * e^{-\frac{\Delta G_{total}}{RT}} \quad (1)$$

Consequently, the higher the energy barrier (the bigger ΔG) the slower is the reaction (the smaller is k). The energy profile for the investigated isomerization of imines is shown in Figure 4b.

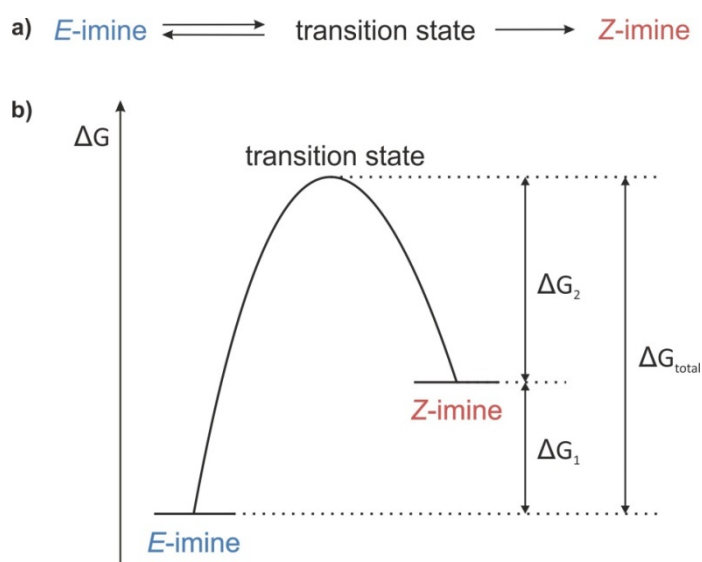


Figure 4: a) The Eyring-theory assumes a pre-equilibrium between starting materials (here: E -imine) and the transition state. This equilibrium is described by the equilibrium constant K^\ddagger . After the formation of the transition states the product (here: Z -imine) or the starting material (here: E -imine) can be formed without additional energy consumption. b) The energy profile for the isomerization of imines is shown. In general, the E -imine is energetically more favored than the Z -imine. For the both isomerization processes (E -to- Z and Z -to- E) the energy barrier of the transition state has to be overcome.

Since, by definition $\Delta G = \Delta H - T \Delta S$, an alternative form of the Eyring equation (2) can be obtained:

$$k = \frac{k_B T}{h} * e^{\frac{\Delta S}{R}} * e^{-\frac{\Delta H}{RT}} \quad (2)$$

Thus, also the thermodynamic variables enthalpy ΔH and entropy ΔS can be mathematically derived from a theoretical model. For the sake of completeness, it must be pointed out that ΔH and ΔS as well as the rate constant k are highly temperature dependent. The empirical correlation between temperature and rate constant was found by Arrhenius in the 19th century and is known as the Arrhenius equation (3):^[23]

5 A Quantitative Analysis of the *E,Z*-Isomerization

$$k = A * e^{\frac{-E_a}{RT}} \quad (3)$$

Where, A is the pre-exponential factor and depends on the order of the investigated reaction. E_a is the temperature independent activation energy for the reaction.

The isomerization around C-N-double bonds can take place over two different mechanisms: either rotation or inversion (Figure 5).^[24,25] In case of a rotation the Ph-substituent rotates around the C-N-single bond of the zwitterionic resonance structure. During this process both sp^2 -hybridisation and the resulting bond angle (C-N-Ph) remains (Figure 5a).^[24] In contrast, the inversion takes place by flipping the Ph-substituent within one plane from the trans- to the cis-position (or *vice versa*). Thus, during the inversion the bond angle (C-N-Ph) increases meanwhile to 180° , while the C-N-bond remains mainly unaffected (Figure 5b).^[24] For guanidinium salts, which do not possess a free electron pair, an inversion could be excluded.^[26] Similarly, a more acidic CPA-catalyst increases the degree of imine-protonation within the investigated binary complexes and thus the free electron pair of the nitrogen may be progressively blocked. As a result, the inversion should be more hindered in the case of a high degree of imine-protonation.

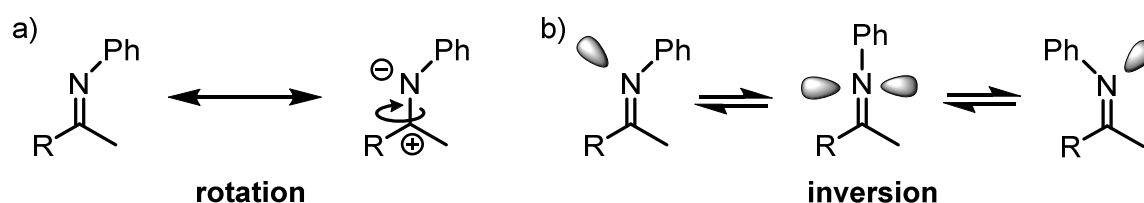


Figure 5: The *E/Z*-isomerization of imines is possible via a) rotation and b) inversion.^[24]

In general, these isomerization mechanisms (rotation and inversion) can be distinguished by an analysis of the thermodynamic variables ΔH and ΔS . Our group also investigated the mechanism of the aggregation of phosphoramidite ligands.^[27] There, we assumed large negative ΔS values (-90 to -160 J/Kmol) in combination with small ΔH values (0 to 20 kJ/mol) for crowded transition states, which are typical for inversions around a nitrogen atom.^[27-29] Whereas, for the rotation around the C-N-bond higher ΔS (0 to 70 J/Kmol) values as well as higher ΔH values (40 to 60 kJ/mol) were proposed.^[27] It has to be emphasized, that in literature many different contradictory interpretations of the isomerization mechanisms on the basis of ΔG , ΔH and ΔS were proposed.^[24,27-34] For this reason and the high temperature dependency of ΔS and ΔH this analysis has to be considered with extreme caution.

5.3. Results and Discussion

5.3.1. Model system

The rate constants of the isomerization were investigated for three free imines **2a**, **2b** and **2c**, which exhibit different electronic properties, as well as for several binary complexes (Figure 6). Since, the influence of the imine-protonation on the isomerization rate was of great interest, four different catalysts with varying acidities were chosen (for the acidities of the CPAs see chapter 3). The acidity of the three chiral phosphoric acid (CPA) catalysts **1a-1c** is within an order of magnitude, while the disulfonimide catalyst **1d** is by far more acidic. Therefore, the DSI catalyst **1d** was selected as a model system for an almost completely protonated imine (see chapter 4 and reference^[35]). Especially, for the binary complexes the overlapping signals of *E*- and *Z*-imine were very challenging. Thus, no separated signals could be observed for **1c/2b**, **1c/2c** and **1c/2d**. It was also tried to analyze the ¹⁹F-spectra of the **1c/2b**-complex, but the assignment of the signals was ambiguous. Nevertheless, the *p*-methoxy-groups of the imine **2a** are often well separated and thus the access to the isomerization rates for the binary complexes with the CPAs **1a – 1d** and imine **2a** between 220 and 250 K was possible. For all NMR-spectroscopic investigations CD₂Cl₂ was used, since this solvent provided the smallest linewidths.

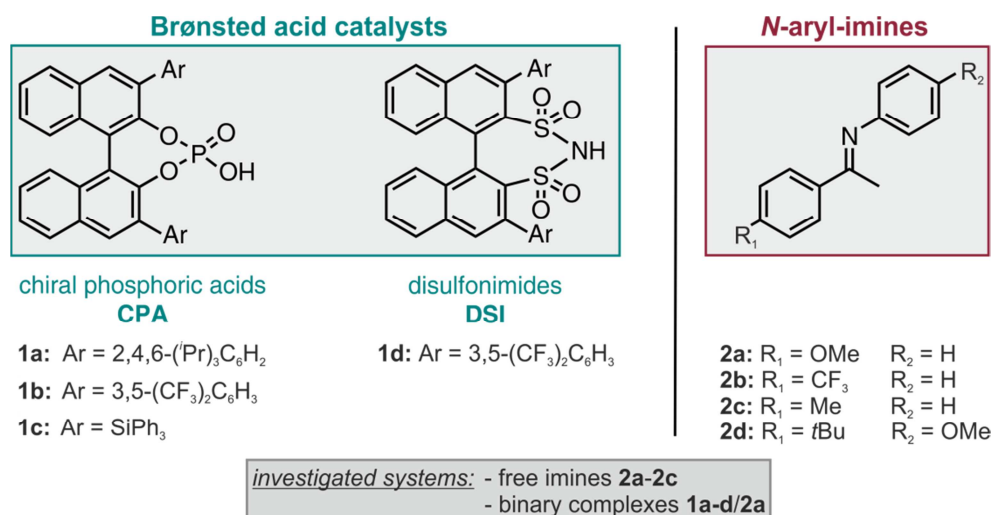


Figure 6: The isomerization rates of the free imines **2a–2c** were determined. Additionally, the influence of the degree of imine-protonation on the isomerization rate was investigated within the binary complexes consisting of imine **2a** and the CPAs **1a-1c** between 220 and 240K in CD₂Cl₂. For the complexes with imine **2a** and DSI **1d** the isomerization rates between 230 and 250 K in CD₂Cl₂ were determined. Investigations with **1c/2d** were not possible because of signal overlap. For the investigation of the binary CPA-complexes at 230 K see also reference.^[36]

5 A Quantitative Analysis of the *E,Z*-Isomerization

5.3.2. *Z*-to-*E*-isomerization

For the measurements of the thermal *Z*-to-*E*-isomerization rates first the thermodynamically more stable *E*-imine was photoisomerized inside the spectrometer to its *Z*-form using a 365 nm LED (for the in-situ NMR illumination set-up see reference^[37]). The advantage of the in-situ NMR illumination is that the progress of the isomerization can be easily monitored *via* signal integration. To prevent the thermal back isomerization to the *E*-imine, low temperature was applied and the photoisomerization was executed at 190 K. During the irradiation at 365 nm the amount of *Z*-imine increased until the photostationary state was reached after 3 to 6 hours (Figure 7, step I). For example, the photostationary state of the free imine **2a** at 190 K in CD₂Cl₂ was reached after 3 hours (constant *E/Z*-ratio of 1/1.7; for the other systems see chapter 5.5.1). In a next step, the spectrometer was warmed up to the different temperatures between 200 and 250K and the decay curves of the *Z*-imine were detected similar to Haag and Saalfrank.^[38] This temperature range was chosen, since only above 200 K the *Z*-isomer is decomposed in a reasonable amount of time and at temperatures higher than 250 K the thermal back-isomerization is so fast, that it was not possible to record the decay curves of the *Z*-imine by NMR-spectroscopy. During the warming up the sample was still illuminated but due to the faster thermal back isomerization (*Z*-to-*E*) at elevated temperatures the amount of *Z*-imine was slightly decreased (Figure 7, step II). Finally, the decay curves of the *Z*-imine were measured until the initial *E/Z*-ratio was reached (Figure 7, step III). For these decay curves a row of ¹H-spectra were recorded and the well separated signals of the *p*-OMe-group of imine **2a** were integrated (for imine **2b** and **2c**: α -methyl-group). In all cases the signal of the *E*-imine in the first spectrum was referenced to 1.

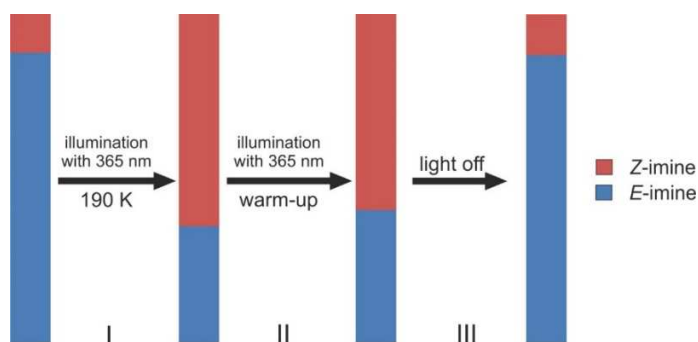


Figure 7: The experimental procedure for the determination of the isomerization rates is shown. After sample preparation the *Z*-imine is significantly less populated compared to the *E*-imine. By irradiation at 365 nm at low temperatures (190 K) the amount of *Z*-imine can be increased (step I). Even though continuous irradiation during the warming-up (to temperatures between 220 and 250 K) of the spectrometer small amounts of the *Z*-imine isomerizes thermally back to the *E*-imine (step II). Finally, the decay curves of the *Z*-imine at different temperatures in the dark were recorded (step III).

5 A Quantitative Analysis of the E,Z-Isomerization

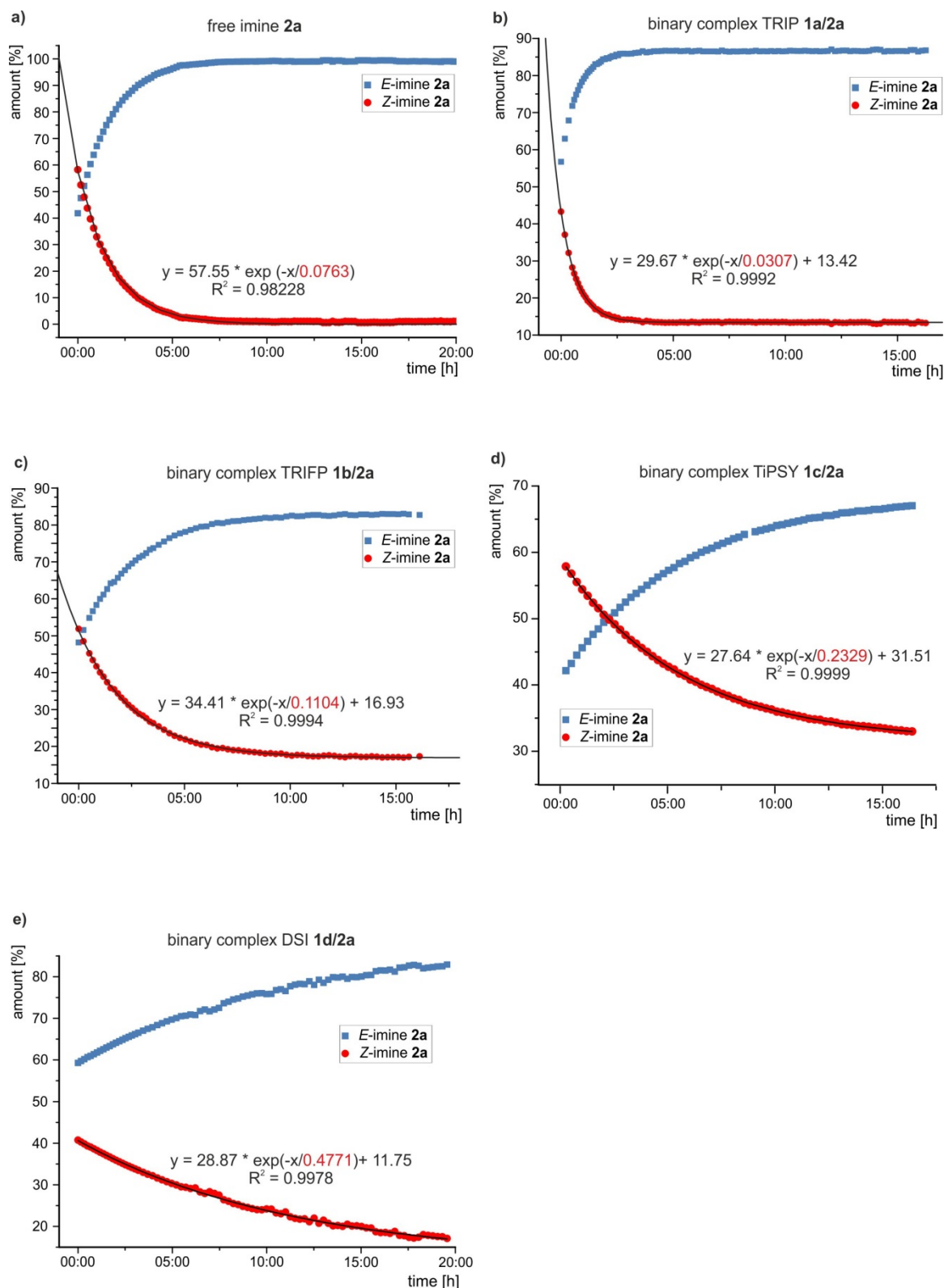


Figure 8: After irradiation at 365 nm the amount of Z-imine could be increased significantly. Afterwards the decay curves of the Z-imine were recorded at 230 K for different binary complexes **1a-d/2a** and the free imine **2a** in CD_2Cl_2 . All decay curves are fitted mathematically and therefore the isomerization rates $k_{Z \rightarrow E}$ ($= 1/\text{red value}$) can be determined. For decay curves of the binary CPA-complexes see also reference.^[36]

5 A Quantitative Analysis of the E,Z-Isomerization

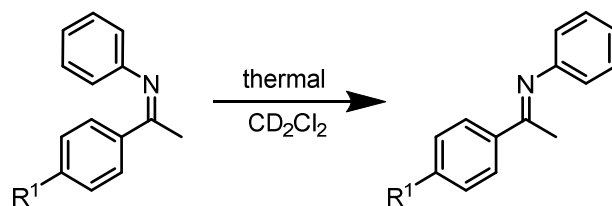
The observed decay curves can be fitted mathematically. Since, the Z-to-E-isomerization is a first order reaction the isomerization constant $k_{Z \rightarrow E}$ can be obtained from equation (4). Selected decay curves with imine **2a** and all catalysts **1a-1d** at 230 K are shown in Figure 8 (for the other decay curves see chapter 5.5.3.).

$$y = A_1 * e^{-k_{Z \rightarrow E} x} + y_0 \quad (4)$$

All observed Z-to-E-isomerization rates $k_{Z \rightarrow E}$ are summarized in Table 1. Finally, the free Gibbs energy ΔG_2 can be calculated out of the Eyring equation (5). The values are also given in Table 1.

$$k_{Z \rightarrow E} = \frac{(k_B * T)}{h} * e^{-\frac{\Delta G_2}{RT}} \quad (5)$$

Table 1: The isomerization rates $k_{Z \rightarrow E}$ of different binary imine/catalyst complexes and three free imines were determined in CD_2Cl_2 at different temperatures. Furthermore, the related ΔG_2 values were calculated out of the Eyring equation (5).



entry	catalyst	R ¹	T [K]	$k_{Z \rightarrow E}$ [$\cdot 10^{-3}$ 1/s]	ΔG_2 [kJmol ⁻¹]
1	TRIP 1a	OMe	220	3.36	63.74
2	TRIP 1a	OMe	230	9.04 ^[a]	64.83 ^[a]
3	TRIP 1a	OMe	240	23.03	65.87

4	TRIFP 1b	OMe	220	1.27	65.53
5	TRIFP 1b	OMe	230	2.52 ^[a]	67.28 ^[a]
6	TRIFP 1b	OMe	240	7.22	68.19

7	TiPSY 1c	OMe	220	0.31	68.10
8	TiPSY 1c	OMe	230	1.19 ^[a]	68.71 ^[a]

5 A Quantitative Analysis of the E,Z-Isomerization

9	TiPSY 1c	OMe	240	5.88	68.60

10	DSI 1d	OMe	230	0.58	70.08
11	DSI 1d	OMe	235	1.91	69.32
12	DSI 1d	OMe	240	1.03	72.08
13	DSI 1d	OMe	250	4.97	71.89

14	-	OMe	200	0.02	66.24
15	-	OMe	210	0.08	67.37
16	-	OMe	220	0.76	66.47
17	-	OMe	230	3.64	66.57
18	-	OMe	240	18.8	66.27
19	-	OMe	250	70.7	66.37

20	-	CF ₃	210	0.12	66.57

21	-	Me	210	0.12	66.63

[a] see reference.^[36]

Since, the isomerization barriers ΔG_2 are directly correlated with the isomerization rates via the Eyring equation (5) the observed trends are only described on the isomerization rates $k_{Z \rightarrow E}$. Furthermore, the sterical environment of the imine is expected to influence the isomerization rate or rather the isomerization mechanism significantly, thus the free imines and the imines in the binary complexes were analyzed separately.

Initially, the isomerization rates at 210 K of three free imines with different electronic properties were compared. Independent on the substituent, for all free imines **2a-2c** the observed isomerization rates are in the same order of magnitude ($0.08 \cdot 10^{-3} - 0.12 \cdot 10^{-3} \text{ s}^{-1}$). Hence, the substitution pattern of the free imines does not influence the isomerization rate significantly. However, the analysis of the Hammett parameters ($\sigma(p\text{-OMe}) = -0.27$, $\sigma(p\text{-Me}) = -0.16$, $\sigma(p\text{-CF}_3) = +0.54$) shows that the *p*-methoxy-substituent

5 A Quantitative Analysis of the *E,Z*-Isomerization

is the most electron donating group and thus suggest the highest single bond character of the CN-bond for the imine **2a**. Consequently, for the imine **2a** the fastest isomerization rate was expected, if the isomerization takes place *via* rotation (see chapter 5.2). Since, this is not the case and the isomerization of imine **2b** and **2c** is even slightly faster than the isomerization of imine **2a**, the observed isomerization rates hint at an inversion-mechanism - at least for the free imines (for a detailed discussion of the isomerization mechanism see chapter 5.3.6.).

Subsequently, the isomerization rates of all investigated binary complexes (**1a-d/2a**) were compared at 230 K. All of them showed faster *Z*-to-*E*-isomerization rates ($0.58 \cdot 10^{-3} - 9.04 \cdot 10^{-3} \text{ s}^{-1}$) than the free imines ($0.08 \cdot 10^{-3} - 0.12 \cdot 10^{-3} \text{ s}^{-1}$). Furthermore, the following order was observed: $k_{Z \text{ to } E}(\text{DSI}) < k_{Z \text{ to } E}(\text{TiPSY}) < k_{Z \text{ to } E}(\text{TRIFP}) < k_{Z \text{ to } E}(\text{TRIP})$. This sequence of the isomerization rates is not directly reflected in the degree of imine-protonation caused by the acidity of the catalyst ($\text{pK}_{\text{aDSI}} < \text{pK}_{\text{aTRIFP}} < \text{pK}_{\text{aTiPSY}} < \text{pK}_{\text{aTRIP}}$, see chapter 3 and 4 as well as reference^[35,36]), indicating that also other factors, such as the steric demand of the 3,3'-substituents, contribute to the isomerization rate. To compare the sterical demand of the CPA-catalyst the usage of the AREA (θ) values, which describe the cone angle of the substrate binding pocket, is well suited.^[39] The AREA (θ) values for TRIP and TRIFP (TRIP: 51, TRIFP: 62) are similar, while the small AREA (θ) value of TiPSY (29) reflects the sterical very demanding SiPh₃-substituents.^[39] However, for catalysts with a similar steric demand (TRIP, TRIFP and DSI) the increasing protonation of the imine seem to slow down the isomerisation. Thus, for the imine in the binary complex with the highly acidic DSI a considerable decrease of the isomerisation rate was observed, even though the size of the binding pocket of the DSI and TRIP are similar (see chapter 4 and reference^[35]). Whereas, the catalyst with the sterically most demanding 3,3'-substituents (TiPSY, AREA (θ): 29) deviates from the observed trend. Potentially, the reduced isomerization rate of TiPSY can be traced back to the small binding pocket, which hinders the isomerization process. Overall, these results suggest that the isomerization rate is dependent on the protonation of the imine, but also the steric of the catalyst seems to have an impact on the isomerization rate.

5.3.3. *E*-to-*Z*-Isomerization

Since, it was shown previously, that the asymmetric transfer hydrogenation takes place *via* the transition states of the less populated *Z*-imine, while the *E*-imine is the thermodynamically more stable isomer,^[13] the investigation of the isomerization rates for the *E*-to-*Z*-isomerisation is of particular interest. As depicted in Figure 4, the

5 A Quantitative Analysis of the E,Z-Isomerization

isomerization barrier of the *E*-to-*Z*-isomerization (ΔG_{total}) is the sum of the isomerization barrier of the *Z*-to-*E*-isomerization (ΔG_2) and the energetic difference between *E*- and *Z*-imine (ΔG_1). Since, the ΔG_2 was already determined (see chapter 5.3.2), now the *E*-to-*Z*-isomerization is investigated. Initially, the energetic difference between *E*- and *Z*-imine (ΔG_1) was determined by means of the Boltzmann distribution (equation (6)) in the thermodynamic equilibrium of the binary complex. Whereby, N_0 is the integral of the thermodynamic more stable *E*-imine and N_i the amount of the *Z*-imine.

$$\frac{N_i}{N_0} = e^{\frac{-\Delta G_1}{k_B T}} \quad (6)$$

After a mathematical transformation the Gibbs free energy ΔG_1 per mole can be obtained from equation (7), where R is the gas constant ($= 8.314 \text{ JK}^{-1}\text{mol}^{-1}$) and T the temperature in Kelvin.

$$\Delta G_1 = -RT * \ln\left(\frac{N_i}{N_0}\right) \quad (7)$$

Due to an *E/Z*-ratio between 1/0.2 and 1/0.5 in the binary complexes, the populations of the *E*- and *Z*-imine were easily determined *via* integration of the ^1H -spectra. Therefore, the Gibbs free energy ΔG_1 of the binary complexes could be derived exclusively from experimental data (equation (7)). In contrast, the free imine exists mainly as *E*-isomer (> 99%) and thus, the integration of the free *Z*-imine signals was not possible in an appropriate error range. To substitute the experimentally not accessible ΔG_1 values of the free imines, theoretical calculations were conducted. Since, the Gibbs free energy ΔG is widely temperature-independent the calculated ΔG_1 values for the free imine **2a** at 295.15K were assumed for the whole temperature range between 200-250 K (entry 14-19 in Table 2). The ΔG_1 values of the imines **2b** and **2c** were not calculated.

Next, the isomerization barrier of the *E*-to-*Z*-isomerization (ΔG_{total}), which is composed of the previously obtained ΔG_2 (from the *Z*-to-*E*-isomerization rate $k_{Z \text{ to } E}$) and the ΔG_1 (derived from the Boltzmann distribution), has to be calculated (equation (8)). Finally, with these ΔG_{total} values the *E*-to-*Z*-isomerization rate $k_{E \text{ to } Z}$ can be determined out of the Eyring equation (9).

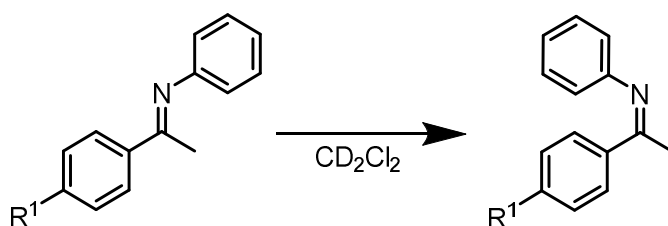
$$\Delta G_{\text{total}} = \Delta G_2 + \Delta G_1 \quad (8)$$

5 A Quantitative Analysis of the E,Z-Isomerization

$$k_{E \text{ to } Z} = \frac{k_B T}{h} * e^{\frac{-(\Delta G_1 + \Delta G_2)}{RT}} \quad (9)$$

The resulting ΔG_1 as well as the $k_{E \text{ to } Z}$ are presented in Table 2.

Table 2: The experimentally obtained ΔG_1 values as well as the isomerization rates $k_{E \text{ to } Z}$ at different temperatures in CD_2Cl_2 are shown.



entry	catalyst	R ¹	T [K]	ΔG_1 [kJmol ⁻¹]	$k_{E \text{ to } Z}$ [*10 ⁻³ 1/s]
1	TRIP 1a	OMe	220	3.53	0.49
2	TRIP 1a	OMe	230	3.63 ^[a]	1.36 ^[a]
3	TRIP 1a	OMe	240	3.71	3.60

4	TRIFP 1b	OMe	220	2.77	0.28
5	TRIFP 1b	OMe	230	3.31 ^[a]	0.45 ^[a]
6	TRIFP 1b	OMe	240	3.41	1.31

7	TiPSY 1c	OMe	220	1.43	0.14
8	TiPSY 1c	OMe	230	1.41 ^[a]	0.57 ^[a]
9	TiPSY 1c	OMe	240	1.09	3.40

10	DSI 1d	OMe	230	3.25	0.11
11	DSI 1d	OMe	235	3.38	0.34
12	DSI 1d	OMe	240	3.37	0.19
13	DSI 1d	OMe	250	3.46	0.94

5 A Quantitative Analysis of the *E,Z*-Isomerization

14	-	OMe	200	6.90 ^[b]	0.0004
15	-	OMe	210	6.90 ^[b]	0.002
16	-	OMe	220	6.90 ^[b]	0.02
17	-	OMe	230	6.90 ^[b]	0.10
18	-	OMe	240	6.90 ^[b]	0.59
19	-	OMe	250	6.90 ^[b]	2.56

[a] see reference.^[36] [b] calculated. Due to the widely temperature independence of the Gibbs energy ΔG the calculated values at 298K free imine **2a** were used over the whole temperature range between 210 and 250 K.

In general, the *E*-to-*Z*-isomerization is by far slower than the *Z*-to-*E*-isomerization. This was already expected because the *E*-imine is the thermodynamically more stable isomer. In the following, only the isomerization rates for the binary complexes at 230 K were compared because the *E*-to-*Z*-isomerization rates of the free imines are experimentally not accessible. In contrast to the *Z*-to-*E*-isomerization the observed isomerization rates follow the degree of protonation: $k_{E \text{ to } Z}(\text{DSI}) < k_{E \text{ to } Z}(\text{TRIFP}) < k_{E \text{ to } Z}(\text{TiPSY}) < k_{E \text{ to } Z}(\text{TRIP})$. That means that for the almost completely protonated imine in the DSI/**2a**-complex (for details see chapter 4 and reference^[35]) the isomerization rate is the smallest ($0.11 \cdot 10^{-3} \text{ s}^{-1}$). The isomerization of the imine in the binary complex with the most acidic^[36] phosphoric acid TRIFP is faster ($0.45 \cdot 10^{-3} \text{ s}^{-1}$), followed by TiPSY ($0.57 \cdot 10^{-3} \text{ s}^{-1}$) and for the least acidic^[36] TRIP the isomerization is the fastest ($1.36 \cdot 10^{-3} \text{ s}^{-1}$). Nevertheless, these differences in the isomerization rates do not reflect the differences in the internal acidity exactly (see chapter 3 and 4 as well as reference^[35,36]). Thus, similar to the *Z*-to-*E*-isomerisation also the *E*-to-*Z*-isomerization rate seems to be not only dependent on the acidity, but also other factors such as the sterics of the catalyst may contribute. Whereby, this additional contribution has to be less pronounced than for the *Z*-to-*E*-isomerization. However, according to the principle of the microscopic reversibility it is not possible that the sterical demand of the catalyst affect both isomerization processes (*Z*-to-*E* and *E*-to-*Z*) differently. Since the *E*-to-*Z*-isomerization rates were derived from ΔG_1 and ΔG_2 , whereby for ΔG_2 previously a dependency on the sterics was found (chapter 5.3.2), the ΔG_1 has to compensate the sterical factor anyhow. Consequently, the stabilisation of the *Z*-imine seems to be dependent on the sterics of

5 A Quantitative Analysis of the *E,Z*-Isomerization

the catalyst. To compare the observed *E/Z*-ratio in the binary complexes at 230 K with the sterical demand of the catalyst, the AREA (θ) values were used. These sterical descriptors for CPAs were introduced by Goodman *et. al.* and describe the cone angle of the substrate binding pocket.^[39] This comparison clearly shows, that for the catalyst with the smallest AREA (θ) value (29, TiPSY) the by far highest population of *Z*-imine (32% *Z*-imine) was observed. In contrast for TRIP and TRIFP similar AREA (θ) values (TRIP: 51, TRIFP: 62) as well as similar *E/Z*-ratios (TRIP: 13% *Z*-imine, TRIFP: 15 % *Z*-imine) were found. This observation is in accordance with the assumption of Goodman *et. al.*, that for catalysts with small binding pockets (i.e. small AREA (θ) values) the interactions between imine and the 3,3'-substituents are energetically more costly than the internal steric repulsion of the substituents within the *Z*-imine.^[39] Consequently, the population of the *Z*-imine in the binary complexes is increased. Thus, the stabilisation of the *Z*-imine seems to reflect the sterics of the catalyst to some extent and due to that the *E*-to-*Z*-isomerization rates are less affected by the sterical demand of the 3,3'-substituents than *Z*-to-*E*-isomerization rates.

Overall, it was shown that the *E*-to-*Z*-isomerization rates are reduced with a higher degree of imine-protonation. Furthermore, the *E*-to-*Z*-isomerization rates are less affected by the sterics of the catalyst than the *Z*-to-*E*-isomerization rates, but rather the sterics seems to be reflected in the stabilisation of the *Z*-imine.

5.3.4. Thermal Isomerization Barriers of the Imines at low temperature

Since, the rate of the *Z*-imine-formation as well as the rate of *Z*-imine-degradation influence the overall amount of the active *Z*-imine, it is necessary to consider both, *E*-to-*Z*- and *Z*-to-*E*-isomerization, for investigations regarding the impact of the isomerization on the overall reaction rate. The analysis of the isomerization barriers, which are given by the Gibbs free energy ΔG , offers a good opportunity to consider both processes. For reasons of clarity, all values for ΔG_1 , ΔG_2 and ΔG_{total} obtained from the experimental isomerization rates are summarized once again in Table 3.

5 A Quantitative Analysis of the *E,Z*-Isomerization

Table 3: The ΔG_1 values for the binary complexes could be determined from the Boltzman distribution (6) at different temperatures in CD_2Cl_2 . In contrast, the related ΔG_2 values were calculated with the Eyring equation (5) after determination of the experimental *Z*-to-*E*-isomerization rate ($k_{Z \rightarrow E}$). ΔG_{total} is the sum of ΔG_1 and ΔG_2 .

entry	catalyst	imine	T [K]	ΔG_1 [kJmol ⁻¹]	ΔG_2 [kJmol ⁻¹]	ΔG_{total} [kJmol ⁻¹]
1	TRIP 1a	2a	220	3.53	63.74	67.28
2	TRIP 1a	2a	230	3.63 ^[a]	64.83 ^[a]	68.46 ^[a]
3	TRIP 1a	2a	240	3.71	65.87	69.58
4	TRIFP 1b	2a	220	2.77	65.53	68.30
5	TRIFP 1b	2a	230	3.31 ^[a]	67.28 ^[a]	70.59 ^[a]
6	TRIFP 1b	2a	240	3.41	68.19	71.60
7	TiPSY 1c	2a	220	1.43	68.10	69.53
8	TiPSY 1c	2a	230	1.41 ^[a]	68.71 ^[a]	70.11 ^[a]
9	TiPSY 1c	2a	240	1.09	68.60	69.69
10	DSI 1d	2a	230	3.25	70.08	73.32
11	DSI 1d	2a	235	3.38	69.32	72.69
12	DSI 1d	2a	240	3.37	72.08	75.45
13	DSI 1d	2a	250	3.46	71.89	75.34
14	-	2a	200	6.90 ^[b]	66.24	73.14
15	-	2a	210	6.90 ^[b]	67.37	74.27
16	-	2a	220	6.90 ^[b]	66.47	73.37
17	-	2a	230	6.90 ^[b]	66.57	73.47
18	-	2a	240	6.90 ^[b]	66.27	73.17

5 A Quantitative Analysis of the *E,Z*-Isomerization

19	-	2a	250	6.90 ^[b]	66.37	73.27
20	-	2b	210	-	66.57	-
21	-	2c	210	-	66.63	-

[a] see reference.^[36] [b] calculated. Due to the widely temperature independence of the Gibbs energy ΔG the calculated values at 298K free imine **2a** were used over the whole temperature range between 210 and 250 K.

The experimentally derived ΔG_1 and ΔG_2 values of the binary complexes are slightly dependent on the temperature (see Table 3). Nevertheless, the experimentally observed ΔG_2 values of the free imine **2a** are almost stable between 200 K and 250 K. Thus, the assumption of the calculated ΔG_1 (298.5 K) value of the free imine **2a** for the whole temperature range between 200 K and 250 K seems not to be a problem. In contrast, for the binary complexes the differences in temperature have an impact on the ΔG_1 values. This is most probably due to the different conformational stabilizations of the 3,3'-substituents of the catalysts at different temperatures, influencing the stabilization of the *Z*-imine. The energetic difference between *E*- and *Z*-imine (ΔG_1) is for TRIP **1a**, TRIFP **1b** and DSI **1d** in the same order of magnitude (between 2.7 and 3.7 kJmol⁻¹). However, the ΔG_1 values of TiPSY **1c** are even smaller (between 1.1 and 1.4 kJmol⁻¹). This means, the population of the *Z*-imine in the TiPSY-complex is significantly increased compared to the other catalysts. This is most probably, due to the sterically very demanding 3,3'-substituents, which reduce the size of the binding pocket significantly and thus the internal repulsion of the imine-substituents is energetically more favored than the interactions between the imine and the 3,3'-substituents.^[39] Furthermore, the isomerization barriers (ΔG_{total}) of all investigated binary complexes with the exception of TiPSY **1c** increase at higher temperatures (Figure 9). Thus, the sterically very demanding 3,3'-substituents of TiPSY seems to control the isomerization barriers in some way. Interestingly, the ΔG_2 -values of the TiPSY-complex are similar at all investigated temperatures ($\Delta \Delta G_2 \approx 0.6$ kJmol⁻¹), whereas the ΔG_2 of the complexes with the other catalysts differs between 2 and 3 kJmol⁻¹. Due to the small contribution of the ΔG_1 on the *E*-to-*Z*-isomerization barriers (ΔG_{total}), the ΔG_2 -values seem to be responsible for the various temperature dependences of the different catalysts. This was verified by the observation, that the *E*-to-*Z*-isomerization barriers (ΔG_{total}) as well as the *Z*-to-*E*-isomerization barriers (ΔG_2) of TiPSY **1c** are similar between 220 and 240 K, whereas a temperature dependence for the ΔG_1 -values of TiPSY **1c** was found. Thus, the sterical influence of the different catalysts on the *Z*-to-*E*-isomerization of the imine

5 A Quantitative Analysis of the *E,Z*-Isomerization

has to be so pronounced that it is also reflected in the *E*-to-*Z*-isomerization barriers. Finally, this shows once again that the interplay of the sterical environment of the imine and the degree of protonation are responsible for the isomerization rates.

When comparing the *E*-to-*Z*-isomerization barriers (ΔG_{total}) at 230 K, it became apparent that the almost complete protonation of the imine **2a** through the DSI **1d** (for details see chapter 4 and reference^[35]) seems to enlarge the barrier (around 73 kJmol⁻¹, for exact values see table 3) compared to the hydrogen bonded binary CPA-complexes (**1a/2a**, **1b/2a** and **1c/2a**, around 70 kJmol⁻¹). This is in accordance with the previously obtained dependency between isomerization rate and degree of protonation (see chapter 5.3.2. and 5.3.3.). Hence, with the most acidic DSI **1d** the imine is almost completely protonated and thus the isomerization is mostly hindered, implying a higher *E*-to-*Z*-isomerization barrier (ΔG_{total}).

Overall, a higher *E*-to-*Z*-isomerization barrier (ΔG_{total}) was found for a more protonated imine. Nevertheless, the temperature dependence of the *E*-to-*Z*-isomerization barrier of the binary complexes with TRIP, TRIFP and DSI, which is in contrast to the almost constant ΔG_{total} -values of the TiPSY-complex, confirms once again that apart the degree of protonation also the sterical environment of the imine influences the isomerization.

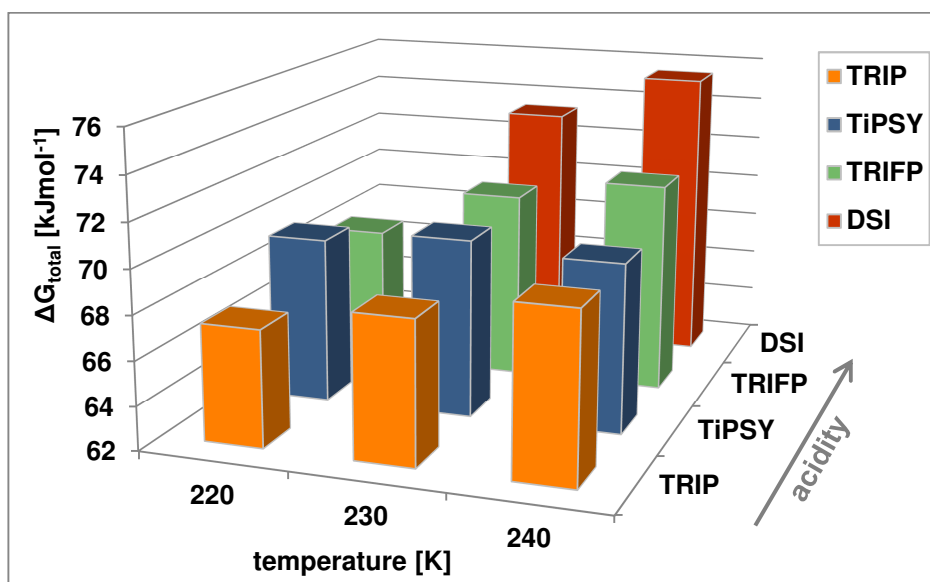


Figure 9: The experimentally derived *E*-to-*Z*-isomerization barriers (ΔG_{total}) of the binary imine-complexes with TRIP, TiPSY, TRIFP and DSI are shown at 220 K, 230 K and 240 K.

5 A Quantitative Analysis of the E,Z-Isomerization

5.3.5. Extrapolation of the Thermal Isomerization Barriers to 298 K

Because of the fast thermal back isomerization of the Z-imine at room temperature the experimental determination of the isomerization rates could only be conducted at temperatures between 200 and 250 K (see above). In contrast, the asymmetric transfer hydrogenation is usually carried out between 25°C and 60°C.^[14,40,41] Therefore, by using the so-called Eyring-Polanyi plot, which correlates $\ln(k/T)$ versus $1/T$, also the isomerization barriers at 25°C (= 298.15 K) were determined (for the E-to-Z-isomerization see Figure 10 and for the Z-to-E-isomerization see chapter 5.5.5.). The observed linear fit equations enable the access to some thermodynamic variables. On the one hand the Gibbs energy ΔG at 298.15 K for the E-to-Z- and Z-to-E-isomerization processes can be determined by extrapolating and analyzing the curves. However, this is only valid under the assumption that the isomerization mechanism does not change at different temperatures. On the other hand, the enthalpy ΔH and the entropy ΔS can be calculated out of the linear equation (see chapter 5.3.6. and 5.5.5).

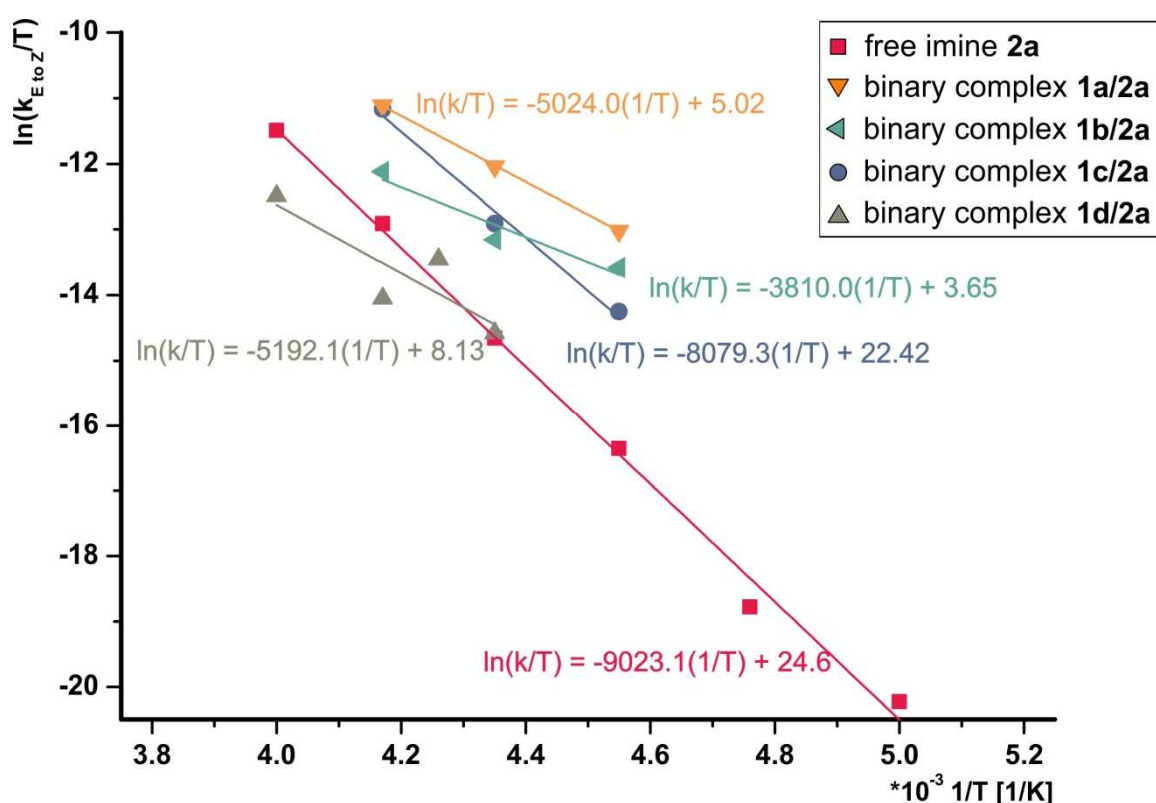


Figure 10: The Eyring-Polanyi plot for the E-to-Z-isomerization of the free imine **2a** and the imine in different binary complex (**1a/2a**, **1b/2a**, **1c/2a** and **1d/2a**) is shown. The $\ln(k/T)$ is plotted versus $1/T$. From the linear fit the thermodynamic variables $\Delta G^{298.15K}$, ΔS and ΔH are accessible.

5 A Quantitative Analysis of the *E,Z*-Isomerization

By analyzing and extrapolating the Eyring-Polanyi plot (Figure 10), for the free imine **2a** an *E*-to-*Z* activation free energy $\Delta G_{\text{total}}^{298.15\text{K}}$ of +72.9 kJmol⁻¹ was obtained at 298.15 K. Theoretical calculations proposed an free energy barrier of ($\Delta G_{\text{calc}}^{\ddagger 298.15\text{K}} = +80.1$ kJmol⁻¹), which is significantly higher than the experimentally derived value, most probably due to the inaccuracy in the entropy calculation.^[42] Considering the importance of the isomerization within the binary complex for the outcome of the reaction, we also investigated the effect of protonation by the catalyst on the isomerization barrier at 298.15 K. Therefore, also the Eyring-Polanyi plots for the binary complexes with catalysts **1a-1c** and the more acidic **1d** were analyzed. All obtained values for the *E*-to-*Z*-isomerization are shown in Table 4 and the isomerization barriers are additionally visualized in Figure 11.

Table 4: The isomerization rate at 298K $k_{\text{Z-to-E}}^{298.15\text{K}}$, and the Gibbs energy at 298K $\Delta G_{\text{total}}^{298.15\text{K}}$, for free imine **2a** and different binary complexes (**1a/2a**, **1b/2a**, **1c/2a** and **1d/2a**) were obtained from the Eyring-Polanyi plot. All values shown in this table are related to the *E*-to-*Z*-isomerization.

entry	catalyst	imine	$k_{\text{E-to-Z}}^{298\text{K}}$ [1/s]	$\Delta G_{\text{total}}^{298\text{K}}$ [kJmol ⁻¹]
1	TRIP 1a	2a	0.002	88.2
2	TRIFP 1b	2a	0.03	81.5
3	TiPSY 1c	2a	2.77	70.5
4	DSI 1d	2a	0.03	81.9
5	-	2a	1.05	72.9

The *E*-to-*Z*-isomerization barrier at 298.15 K of the TiPSY/**2a**-complex is a little bit smaller ($\Delta G_{\text{total}}^{298.15\text{K}} = +70.5$ kJmol⁻¹) than for the free imine **2a** ($\Delta G_{\text{total}}^{298.15\text{K}} = +72.9$ kJmol⁻¹). Whereas the *E*-to-*Z*-isomerization barrier of TRIFP/**2a** and DSI/**2a** are very similar ($\Delta G_{\text{total}}^{298.15\text{K}} \approx 82$ kJmol⁻¹, for exact values see Table 4). The *E*-to-*Z*-isomerization barrier for TRIP/**2a** is by far the highest ($\Delta G_{\text{total}}^{\ddagger 298.15\text{K}} = +88.2$ kJmol⁻¹). Especially the isomerization barrier of the completely protonated imine (**1d/2a**) differs not significantly compared to the CPA/imine complexes, indicating that the protonation of the imine seems not to influence the *E*-to-*Z*-isomerization process at 298.15 K. This observation contradicts the previously obtained correlation between acidity of the catalysts with

5 A Quantitative Analysis of the *E,Z*-Isomerization

similar sterical demand and the isomerization rates at 230 K (see chapter 5.3.4). It is notable, that for both catalysts with equal 3,3'-substituents (TRIFP and DSI) *E*-to-*Z*-isomerization barriers are very similar (around 82 kJmol⁻¹), while the *E*-to-*Z*-isomerization barriers of TiPSY (70.5 kJmol⁻¹) and TRIP (88.2 kJmol⁻¹) deviate. In general, the *E*-to-*Z*-isomerization barriers of TiPSY at 298 K are still in the same order of magnitude than at lower temperatures ($\Delta\Delta G_{\text{total}} = 1$ kJmol⁻¹). In contrast for the other catalysts huge differences were obtained ($\Delta\Delta G_{\text{total}}$ between 8 and 21 kJmol⁻¹). These observations indicate that the contribution of the imine-protonation on the isomerization rates decreases at higher temperatures, while the sterical factor increases. Thus, at higher temperatures the influence of the entropic factor ΔS^\ddagger on the Gibbs free energy ΔG^\ddagger seems to be increased (see equation (10)) compared to the situation at lower temperatures (see chapter 5.3.4.). The huge influence of the entropy ΔS^\ddagger on the isomerization is also reflected in the high deviation of the activation energy E_a from the isomerization barrier ΔG_{total} (for values and discussion see chapter 5.5.4.).

$$\Delta G^\ddagger_{\text{total}} = \Delta H^\ddagger - T\Delta S^\ddagger \quad (10)$$

Overall, these results imply that above 298 K the catalyst is able to activate the substrate and induce stereoselectivity, but the degree of protonation does not influence the isomerization significantly. However, the estimated isomerization barriers at 298 K for the free imine **2a** and all investigated binary complexes (**1a/2a**, **1b/2a**, **1c/2a** and **1d/2a**) are significantly higher compared to the hydride transfer via *type IZ* and *type IIZ* (calculated: 45-54 kJmol⁻¹),^[13] indicating a potential rate-determining step in the transfer hydrogenation of imines (for discussion about the rate determining step see chapter 3 and reference^[36]).

5 A Quantitative Analysis of the E,Z-Isomerization

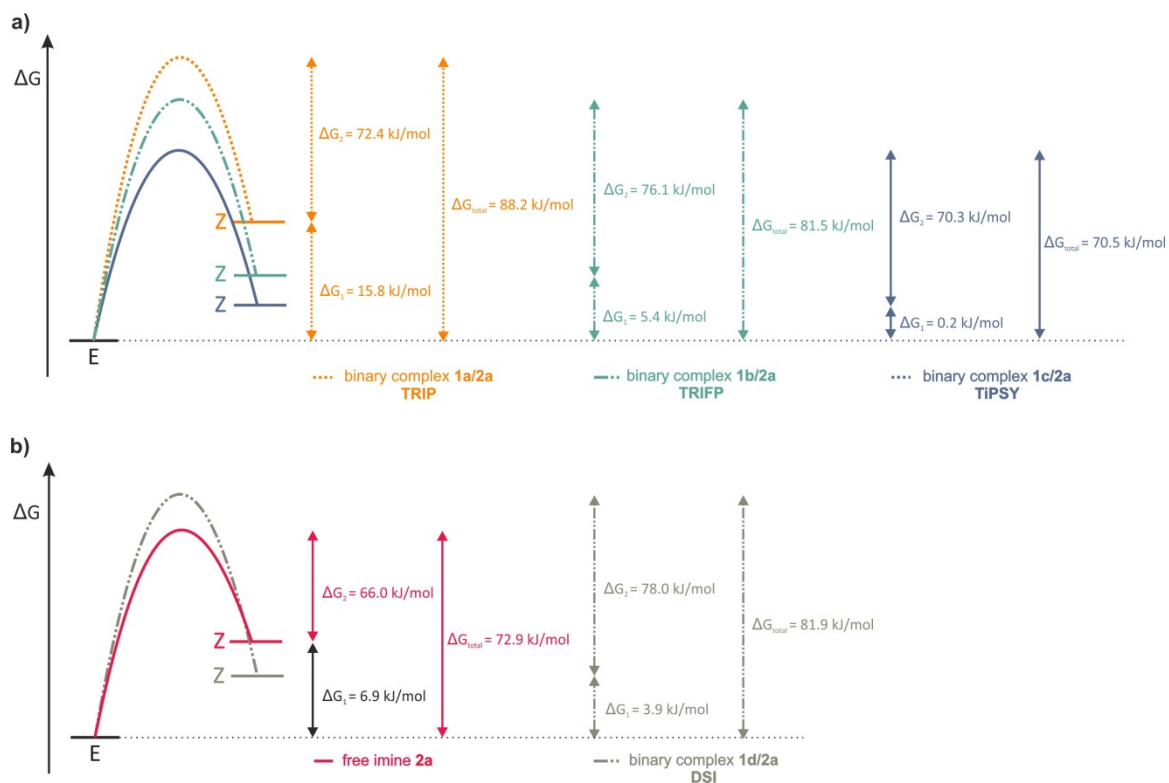


Figure 11: The energy profiles for the isomerization at 298 K of the imine **2a** in a) CPA-complexes as well as in b) its free and completely protonated forms in CD_2Cl_2 are shown. The values for ΔG_{total} and ΔG_2 were obtained from the extrapolation of the Eyring-Polanyi plot (for ΔG_{total} see Figure 10 and for ΔG_2 see chapter 5.3.2). ΔG_1 is calculated out of the difference between ΔG_2 and ΔG_{total} . For the free imine ΔG_1 is obtained from calculations.

5 A Quantitative Analysis of the E,Z-Isomerization

5.3.6. Isomerization mechanism

As already mentioned in chapter 5.3.2., a comparison of the isomerization rates of the free imines **2a-c** with the Hammett parameters of their varying substituents suggests that the isomerization takes place *via* inversion. The Hammett parameters ($\sigma(p\text{-OMe}) = -0.27$, $\sigma(p\text{-Me}) = -0.16$, $\sigma(p\text{-CF}_3) = +0.54$) show that the *p*-methoxy-substituent is the most electron donating group and thus indicate the highest single bond character of the CN-bond for the imine **2a**. In principle, it is assumed that in case of a rotation-mechanism the Ph-substituent of the imine rotates around the CN-single bond within the zwitterionic resonance structure. Consequently, for the imine with the highest single bond character (here: imine **2a**) the fastest isomerization should be observed, if the isomerization takes place *via* rotation. However, this is not the case and the isomerization of imine **2b** and **2c** is even slightly faster than the isomerization of imine **2a**. These observations suggest at least for the free imines an isomerization *via* inversion. Furthermore, it was shown previously that the isomerization of guanidinium salts, without a free electron pair, no inversion-mechanism is possible.^[26] Hence, the at least rough dependency of the isomerization rate on the degree of imine-protonation (see chapter 5.3.2 and 5.3.3.) enhances the assumption of an inversion.

In addition, the thermodynamic variables enthalpy ΔH and entropy ΔS can provide information about the isomerization mechanism. Both, enthalpy and entropy are accessible from the Eyring-Polanyi plot (for the *E*-to-*Z*-isomerization see Figure 10 and for the *Z*-to-*E*-isomerization see chapter 5.5.5.). Thus, the slope is $-\Delta H/R$ and the intercept is put together of $\ln(k_B/h) + \Delta S/R$ (for linear equations see for the *E*-to-*Z*-isomerization Figure 10 and for the *Z*-to-*E*-isomerization see chapter 5.5.5.). Where R is the gas constant ($= 8.314 \text{ JK}^{-1}\text{mol}^{-1}$), k_B the Boltzman constant ($= 1.38 \cdot 10^{-23} \text{ JK}^{-1}$) and h the Planck's constant ($= 6.62 \cdot 10^{-34} \text{ Js}^{-1}$). The obtained values for the enthalpy ΔH are all in the same order of magnitude ($31.7 - 75 \text{ kJmol}^{-1}$, for exact values see Table 5). Indeed the entropy for the free imine **2a** is slightly higher than for the binary complexes. The experimental values for the entropy ΔS of the binary complexes are between -11.1 and $-167.2 \text{ JK}^{-1}\text{mol}^{-1}$. Whereas, the entropy ΔS for the free imine **2a** is positive ($7.1 \text{ JK}^{-1}\text{mol}^{-1}$). In analogy to our previous study of phosphoramidites the large negative values for the entropy ΔS are typical for crowded transition states, indicating an inversion process.^[27,28,32] However, it has to be mentioned explicitly, that this analysis has to be considered with extreme caution. This is due to the reason, that in literature many different interpretations, which often contradict each other, regarding the isomerization mechanisms on the basis of ΔG , ΔH and ΔS were found.^[24,27-34] Additionally, ΔS and ΔH

5 A Quantitative Analysis of the E,Z-Isomerization

are highly temperature-dependent. Therefore the obtained values have a big error range.

Overall, the experimental data obtained from the isomerization rates of the free imine and the binary complexes as well as the analysis of enthalpy and entropy indicate that the isomerization mainly takes place *via* inversion. Furthermore, the structural and vibrational analysis of the transition states confirm the assumption of an inversion.^[42]

Table 5: The enthalpy ΔH and entropy ΔS for free imine **2a** and different binary complexes (**1a/2a**, **1b/2a**, **1c/2a** and **1d/2a**) were obtained from the Eyring-Polanyi plot. All values shown in this table are related to the *E*-to-*Z*-isomerization.

entry	catalyst	imine	ΔH [kJmol ⁻¹]	ΔS [JK ⁻¹ mol ⁻¹]
1	TRIP 1a	2a	41.8	-155.8
2	TRIFP 1b	2a	31.7	-167.2
3	TIPSY 1c	2a	67.2	-11.1
4	DSI 1d	2a	43.2	-130.0
5	-	2a	75.0	7.1

5.3.7. Photosensitized isomerization of imine **2a** at 455 nm

Since the absorption of the imine **2a** is between 250 and 400 nm, it is not possible to isomerize **2a** directly to its *Z*-form by irradiation with a 455 nm LED (Figure 12b). However, in literature several examples of photosensitized isomerizations are known. Thus, stilbenes, β -alkylstyrene, olefins and alkenes can be photoisomerized by using a photosensitizer.^[43-46] For example Gilmour *et al.* could show that the *E*-to-*Z*-isomerization of olefins and alkenes with riboflavin as photosensitizer is a highly effective method.^[45,46] Furthermore, there are also some examples for the photosensitized isomerization of C-N-double bonds,^[15] but the photoisomerization of oximes has been by far more investigated, due to their higher conformational stability at room temperatures.^[15] Common photosensitizers for the oxime-isomerization are acetophenone and benzophenone derivatives as well as 2-acetonaphthone.^[47,48] Further known photosensitizers, which exhibit a sufficient extinctions coefficient at 455 nm, are

5 A Quantitative Analysis of the E,Z-Isomerization

RFTA, TCBQ and DDQ.^[49] For this reason, we also tried to isomerize the imine **2a** by irradiation at 455 nm LED in the presence of three different photosensitizers (RFTA, TCBQ and DDQ, for structure and UV-absorption-spectra see Figure 12a und c).

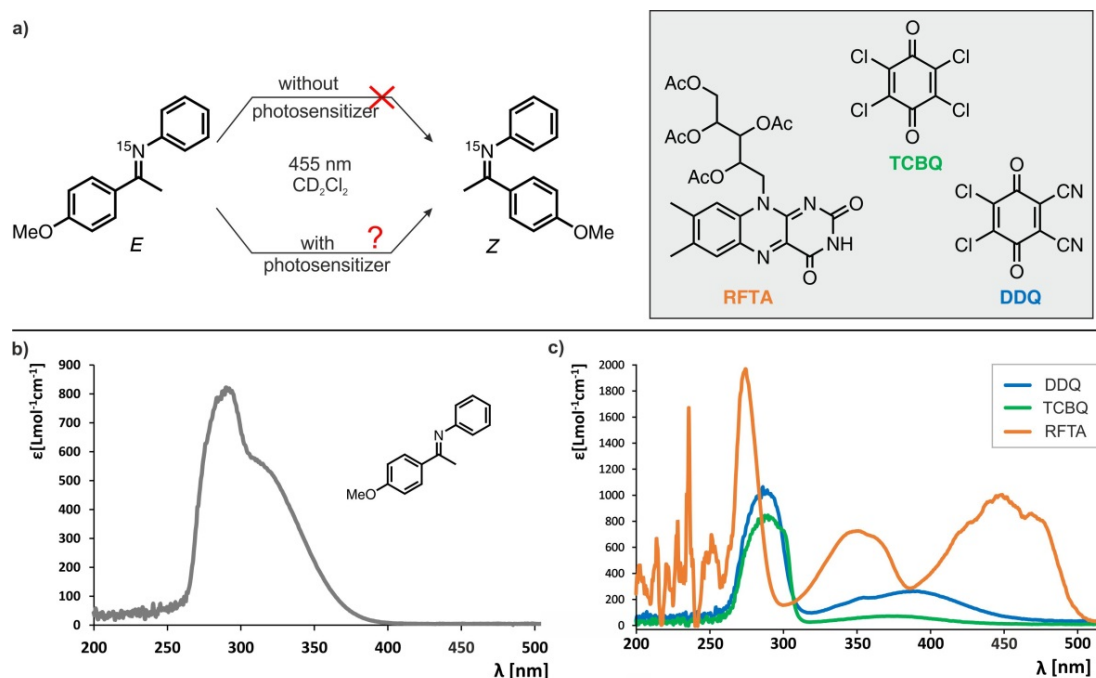


Figure 12: a) The isomerization of imine **2a** with 455 nm irradiation is not possible. Here we tried to isomerize **2a** in the presence of a photosensitizer. Therefore, three photosensitizers were tested. b) The absorption spectra of imine **2a** in dichloromethane is shown. The imine does not absorb at 455 nm. c) The absorption spectra of all three photosensitizers are shown. At 455 nm RFTA has by far the biggest extinction coefficients ($948.9 \text{ Lcm}^{-1}\text{mol}^{-1}$) followed by DDQ ($61.8 \text{ Lcm}^{-1}\text{mol}^{-1}$) and TCBQ ($12.8 \text{ Lcm}^{-1}\text{mol}^{-1}$).

By the photoisomerization with RFTA and 455 nm LED after one hour approximately 9 % Z-imine could be observed (Figure 13). Whereby the photostationary state (around 11% Z-imine) was reached after 2.5 hours. Even by using 10 mol% RFTA instead of 5 mol% or using dry and degassed CD_2Cl_2 the amount of Z-imine could not be increased significantly. Also, with TCBQ it was possible to isomerize the imine, but after three hours just around 5% Z-imine could be observed. Although if the extinction coefficient of DDQ ($\epsilon = 61.8 \text{ Lcm}^{-1}\text{mol}^{-1}$) is higher than for TCBQ ($\epsilon = 12.8 \text{ Lcm}^{-1}\text{mol}^{-1}$) no isomerization in the presence of DDQ was possible (Figure 13). Indeed, the isomerization at 455 nm and all photosensitizer is by far not so effective than by irradiation at 365 nm (around 60% Z-imine after 3h). In contrast to the isomerization with 365nm^[13], it was not possible to speed the asymmetric transfer hydrogenation up by irradiation at 455 nm in the presence of RFTA. Even though the increased amount of the

5 A Quantitative Analysis of the *E,Z*-Isomerization

reactive *Z*-imine^[13], for both reactions (dark and irradiated), the same isolated yield (42%) after 5 hours were observed. On the contrary the *ee*-values decreased in the presence of RFTA (455 nm: 73%, dark: 85%).

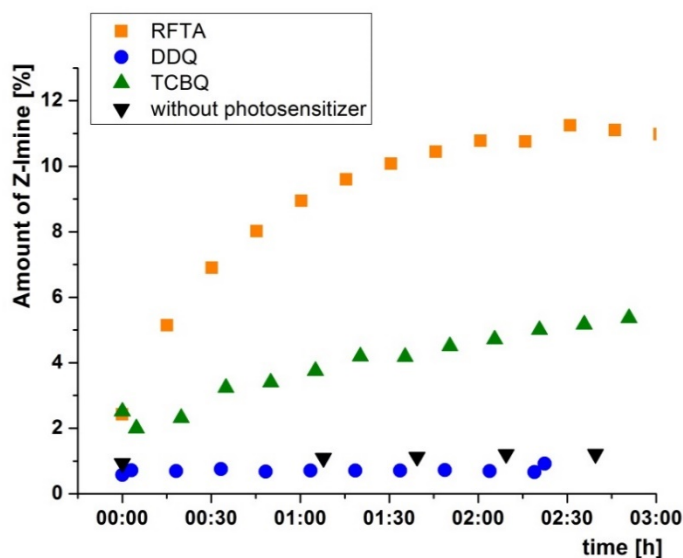


Figure 13: By irradiation at 455 nm LED the imine **2a** could be isomerized in the presence of RFTA (orange curve) and TCBQ (green curve). In contrast, it was no *Z*-imine could be detected with DDQ (blue curve) or without a photosensitizer (black curve). All of these curves were measured directly inside the NMR-spectrometer in CD_2Cl_2 at 190K. For the set-up of the illumination unit see reference.^[37]

Gilmour et al. proposed a triplet energy transfer from the photosensitizer to the substrate.^[45] In case of the investigated isomerization that would mean that the triplet state energy of the photosensitizer has to be higher than that one of the excited state of the imine. Calculations predict a triplet state energy $E^{\text{T}1}$ for the *E*-imine **2a** of 310kJ/mol and for RFTA of 230kJ/mol.^[42] The triplet state energies of TCBQ ($E^{\text{T}1}(\text{TCBQ}) = 237.4\text{kJ/mol}$)^[49] and DDQ ($E^{\text{T}1}(\text{DDQ}) = 257.6\text{kJ/mol}$)^[49] are just slightly higher than for RFTA, but still considerable smaller than the triplet state energy of the excited state of the imine. Nevertheless, the photosensitized *E*-to-*Z*-isomerization with 455 nm is possible (at least with RFTA and TCBQ). Thus, it is most likely that no triplet energy transfer occurs. In contrast, a single-electron transfer from the imine to the photosensitizer is more probable (Figure 14). At least in theory, the reduction potential of the excited RFTA ($E^0(^1\text{RFTA}/^2\text{RFTA}^-) = 1.67\text{ V vs. SCE}$)^[50] allows the oxidation of the imine **2a** to the radical-cation ($E^0(\mathbf{2a}/\mathbf{2a}^+) = 1.25\text{ V vs. SCE}$ in acetonitrile, CV spectra see in chapter 5.5.6.). Another hind for the assumed photoinduced single electron transfer it that a fluorescence emission quenching of RFTA in the presence of a high

5 A Quantitative Analysis of the *E,Z*-Isomerization

excess of imine **2a** was observed (see chapter 5.5.7.). Thus, the inefficient isomerization with 455 nm compared to 365 nm can be potentially explained by the short lifetime of the radical cation. In the time frame of this work, the reaction pathways from the radical cation to the *E*-imine (dotted arrow in Figure 14) were not investigated.

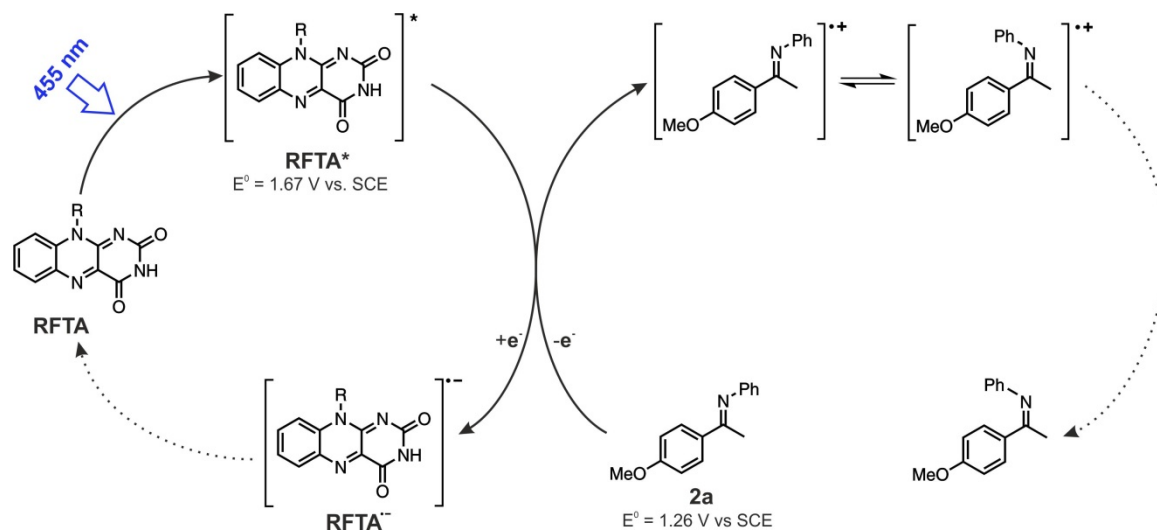


Figure 14: Proposed photosensitized electron transfer from the excited RFTA to the *E*-imine **2a**. At least, the redox potentials of the excited RFTA^[50] and imine **2a** in acetonitrile would allow this electron transfer. However, the dotted reaction pathways were not investigated within this work. Nevertheless, the increased amount of *E*-imines was unambiguously verified by ¹H-NMR-spectra.

5.4. Conclusion

By means of NMR-spectroscopy, a detailed quantification of the *E*-to-*Z*- and *Z*-to-*E*-isomerization of three free imines and four binary Brønsted acid/imine-complexes was performed. The varying acidities of the catalysts allowed the investigation of the isomerization rates dependent on the degree of imine-protonation. This analysis revealed that the increasing protonation of the imine hinders the isomerization of the imine. Thus, the smallest isomerization rates were observed for the almost completely protonated imine with the highly acidic DSI-catalyst. At least for the *Z*-to-*E*-isomerisation rate, the catalyst with the sterically most demanding 3,3'-substituents (TiPSY), does not follow this trend. This observation demonstrates that apart from the imine protonation also the steric bulk of the catalyst contributes to the isomerization rate. Since, the *E*-to-*Z*-isomerisation rates are less affected by the steric demand of the 3,3'-substituents it can be assumed that in this case the steric contribution is already considered in the stabilisation of the *Z*-imine. The observed isomerization rates are directly correlated with isomerization barriers *via* the Eyring equation. Thus, the analysis of the thermal

5 A Quantitative Analysis of the *E,Z*-Isomerization

isomerization barriers at low temperatures confirms that the interplay of the sterical environment of the imine and the degree of protonation are responsible for the isomerization rates. In general, for catalysts with similar sterical demanding 3,3'-substituents a higher *E*-to-*Z*-isomerization barrier was found for a more protonated imine. Furthermore, the extrapolation of the Eyring-Polanyi plot enables the access to the isomerization barriers at room temperature, which cannot be measured directly due to the fast thermal back reaction of the *Z*-imine at 298 K, under the assumption that the isomerization mechanism is not changing at different temperatures. Interestingly, no correlation between isomerization barriers at room temperature and degree of protonation was found. This observation is in contrast to the results from the low temperature analysis, where at least a rough dependency of the isomerization rate on the degree of imine-protonation was found. When comparing the isomerization barriers at room temperature with the sterical properties of the catalysts, it became obvious that the contribution of the imine-protonation on the isomerization rates decreases at higher temperatures, while the sterical factor increases.

Additionally, some initial studies regarding the isomerisation mechanism were performed. In general, it is imaginable that the isomerization takes place *via* inversion or rotation. Up to now, the experimental data obtained from the isomerization rates of the free imine and the binary complexes as well as the analysis of enthalpy and entropy suggests that the isomerization mainly takes place *via* inversion. Similarly, the calculations predict also an inversion-mechanism.

Furthermore, the principle of photosensitized isomerisation, which is known from literature, was also applied. Thus, the investigated imines could be photoisomerized with 455 nm LED in the presence of a suitable photosensitizer, even if the imine is not absorbing 455 nm. Nevertheless, the direct photoisomerization with 365 nm was by far more efficient.

5 A Quantitative Analysis of the *E,Z*-Isomerization

5.5. Supporting information

5.5.1. *E/Z*-ratios after reaching the photostationary state

Table 6: The following *E/Z*-ratios were obtained in the photostationary state after the irradiation with 365 nm at 190 K in CD₂Cl₂. The values were determined by integration of α -CH₃-groups of the free imines respectively the hydrogen bond signals of the binary complexes in the ¹H-NMR spectra.

entry	system	irradiation time [h]	<i>E</i> -imine [%]	<i>Z</i> -imine [%]
1	free imine 2a	3	37	63
2	free imine 2b	6	38	62
3	free imine 2a	4.5	36	64
4	TRIP 1a/2a	4,5	55	45
5	TRIFP 1b/2a	6	49	51
6	TIPSY 1c/2a	7	36	64
7	DSI 1d/2a	4	60	40

5.5.2. Temperature calibration

Since, the previously determined ΔS - and ΔH -values (chapter 5.3.6.) are highly temperature-dependent, special attention was given to the temperature stabilization inside the spectrometer. During the experimental procedure for the determination of the *Z*-to-*E*-isomerization rates, which are the basis for the ΔS - and ΔH -determination, the recording of the decay curves of the *Z*-imine starts directly after warming-up the spectrometer. Because of the partially fast decay of the *Z*-imine, especially at higher temperatures, it was not possible to wait a sufficient amount of time until a stable temperature was reached for certain. Therefore, it was tested how long it takes until a reasonable temperature-stabilization was reached in the spectrometer needs. Thus, the proton chemical shift of the hydrogen bonded proton was used to calibrate the temperature. By plotting the ¹H chemical shift versus the temperature a linear curve was observed (Figure 15).

5 A Quantitative Analysis of the *E,Z*-Isomerization

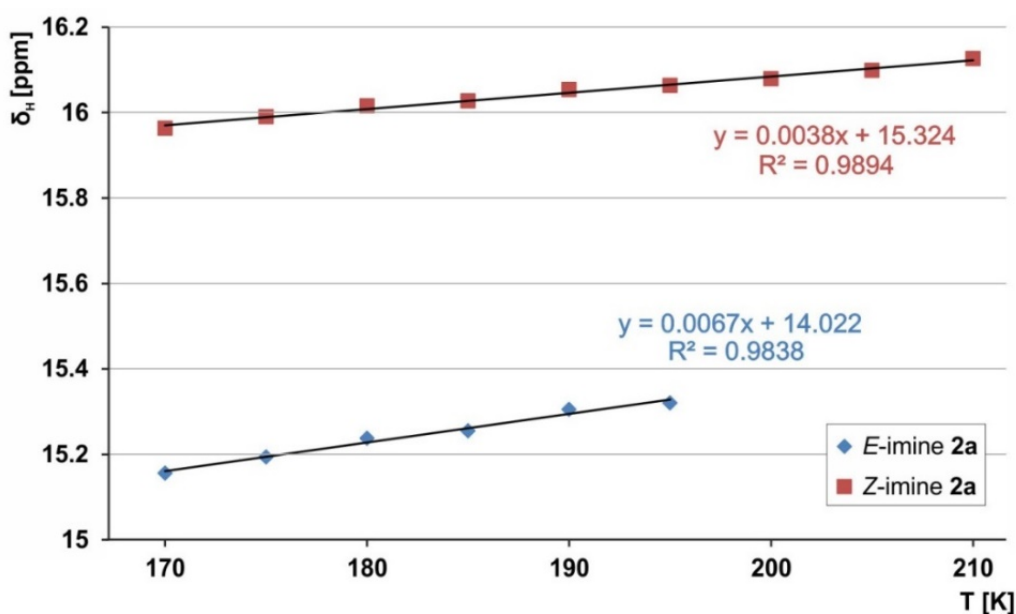


Figure 15: The ^1H chemical shift of the hydrogen bonded protons of *E*- and *Z*-complex (TRIFP **1b/2a**) were determined at different temperatures in CD_2Cl_2 and plotted versus each other. Therefore two linear curves were obtained. These can be used to calculate the real temperature in the NMR-tube.

The stability of the temperature was tested exemplary on the binary complex of TRIFP **1b** and imine **2a** at 210 K. By means of the linear equations and the observed chemical shifts of the hydrogen bonded protons the real temperature was calculated after different time steps. Hence, it was visible that the temperature is shifted only around one degree after 22 hours (Table 7).

Table 7: The chemical shifts of the hydrogen bonded protons of a 1:1 sample of TRIFP **1b** and imine **2a** in CD_2Cl_2 were used to calculate the real temperature inside the NMR-tube. The adjusted temperature was 210 K. Only a small shift of around one degree was observed after 22 hours. The used fit equations were taken from Figure 15.

entry	δ_E [ppm]	δ_Z [ppm]	t [min]	t [h]	T_{calc} (<i>E</i> -Fit) [K]	T_{calc} (<i>Z</i> -Fit) [K]
1	15.4216	16.1276	4.12	-	208.9	211.5
2	15.4177	16.1229	412.63	6.88	208.3	210.2
3	15.4157	16.1242	822.63	13.71	208.0	210.6
4	15.4154	16.1227	1332.63	22.21	208.0	210.2

5 A Quantitative Analysis of the E,Z-Isomerization

5.5.3. Additional decay curves

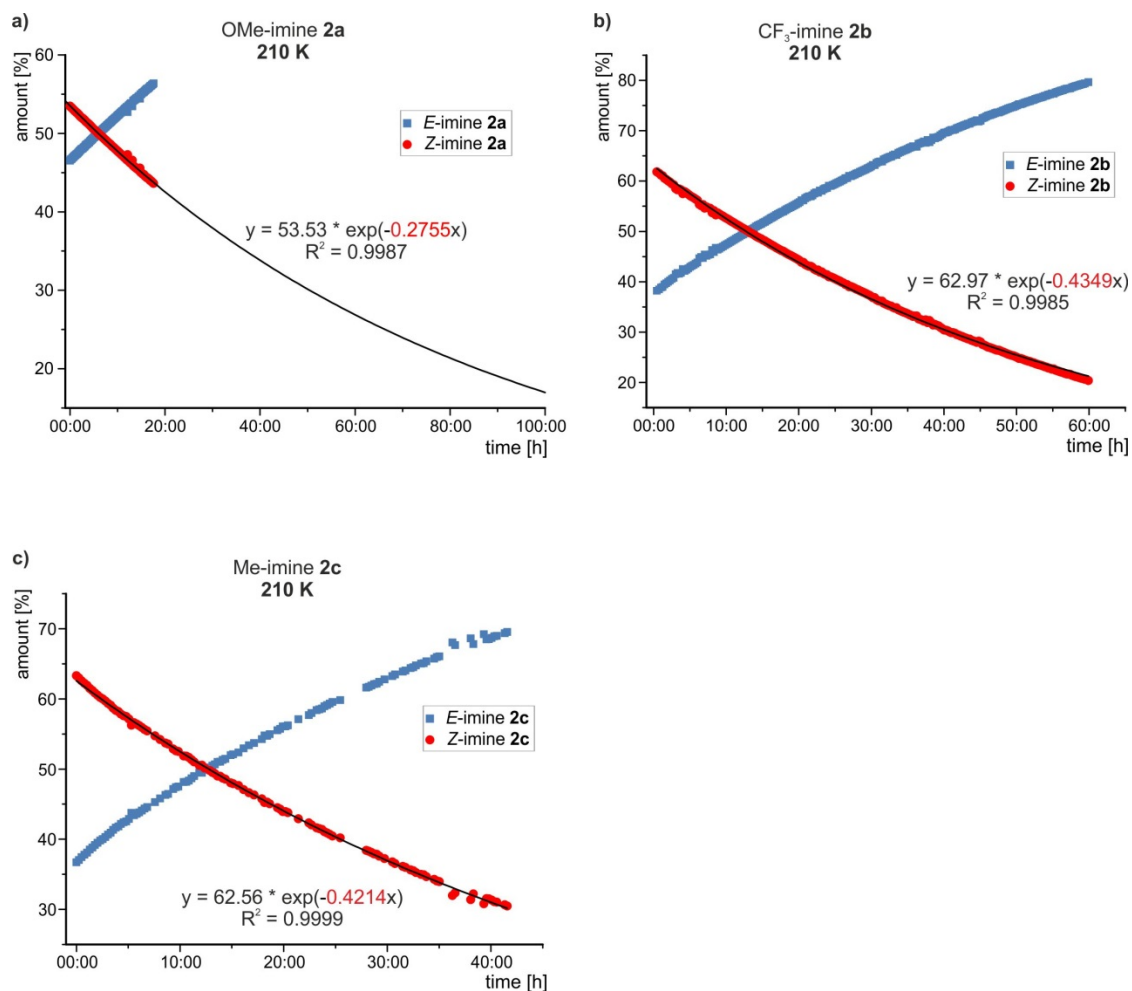


Figure 16: After irradiation at 365 nm the amount of Z-imine could be increased significantly. Afterwards the decay curves of the Z-imine of different free imines **2a-c** in CD₂Cl₂ were recorded at 210 K. All decay curves are fitted mathematically. Since, for the free imines in the thermodynamic equilibrium no Z-imine exists, the isomerization rates k_{Z-to-E} can be obtained directly from the fit equation (red value). The obtained values of k_{Z-to-E} are given in Table 1.

5 A Quantitative Analysis of the E,Z-Isomerization

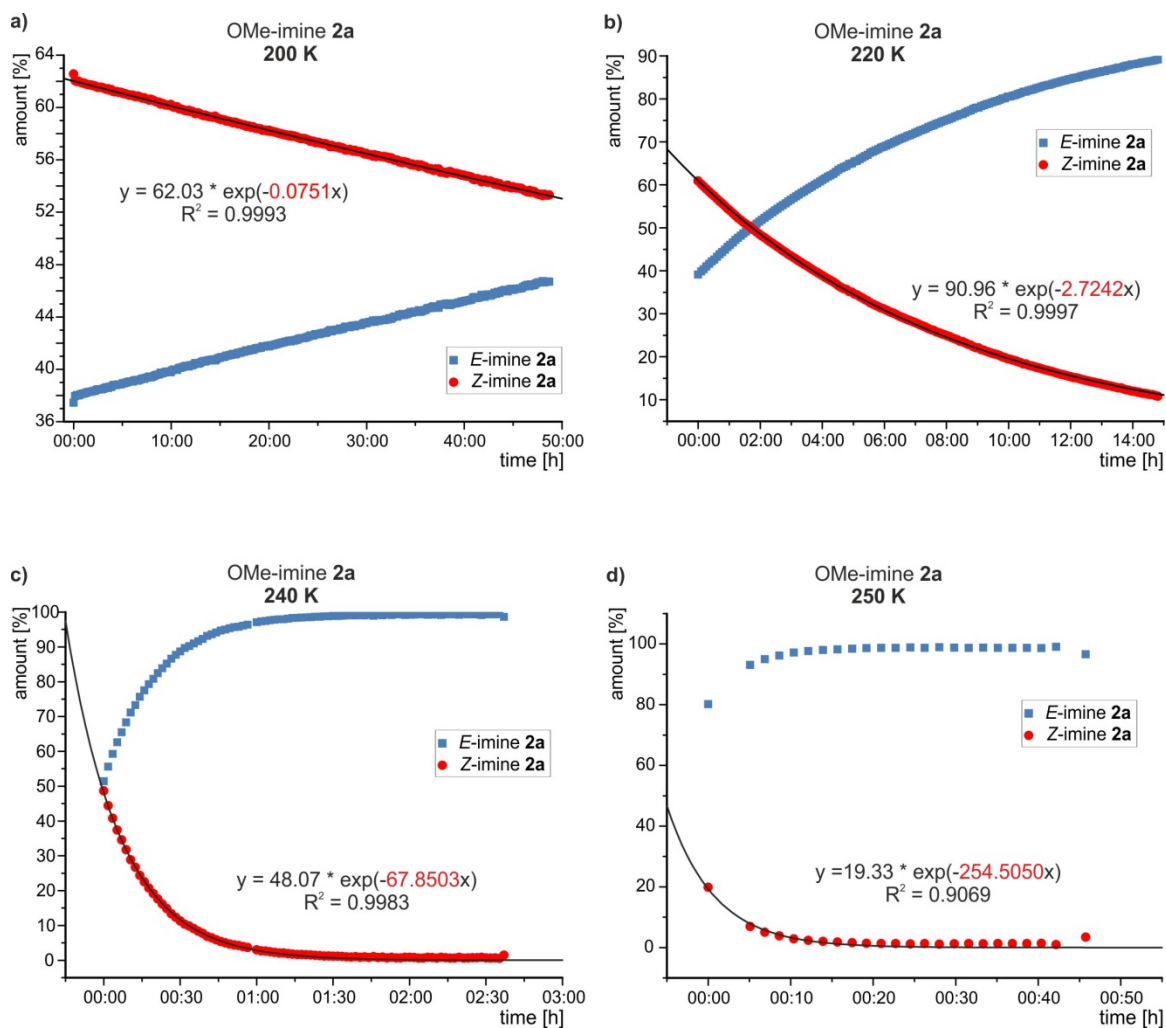


Figure 17: After irradiation at 365 nm the amount of Z-imine could be increased significantly. Afterwards the decay curves of the Z-imine **2a** in CD_2Cl_2 were recorded at different temperatures (200 K, 220 K, 240 K and 250 K). All decay curves are fitted mathematically. Since, for the free imines in the thermodynamic equilibrium no Z-imine exists, the isomerization rates $k_{Z\text{-to-E}}$ can be obtained directly from the fit equation (red value). The obtained values of $k_{Z\text{-to-E}}$ are given in Table 1.

5 A Quantitative Analysis of the E,Z-Isomerization

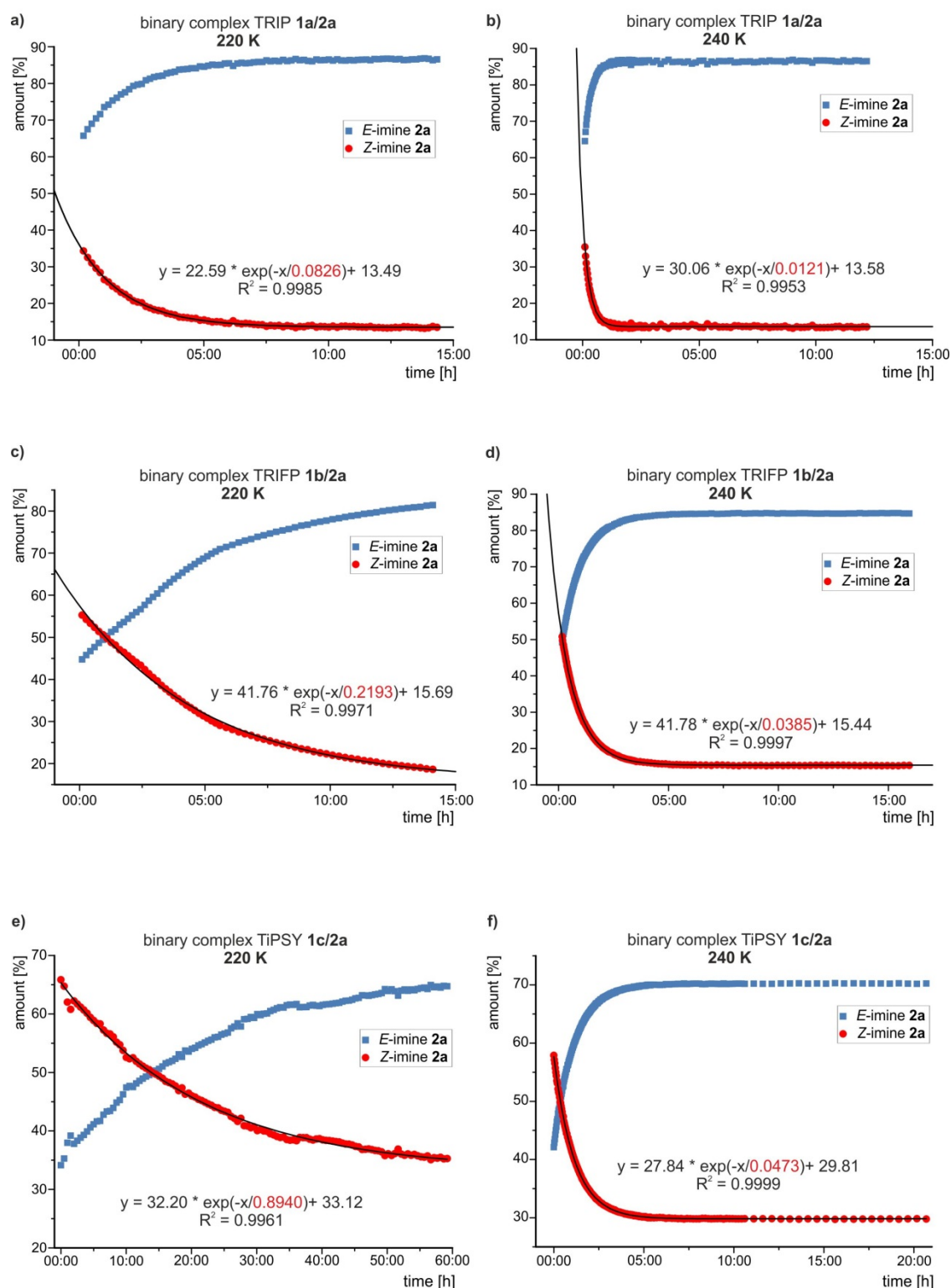


Figure 18: After irradiation at 365 nm the amount of Z-imine could be increased significantly. Afterwards the decay curves of the Z-imine were recorded at 220 K and 240K for different binary complexes **1a-c/2a** in CD_2Cl_2 . All decay curves are fitted mathematically and therefore the isomerization rates k_{Z-to-E} ($= 1/\text{red value}$) can be determined. The obtained values of k_{Z-to-E} are given in Table 1.

5 A Quantitative Analysis of the E,Z-Isomerization

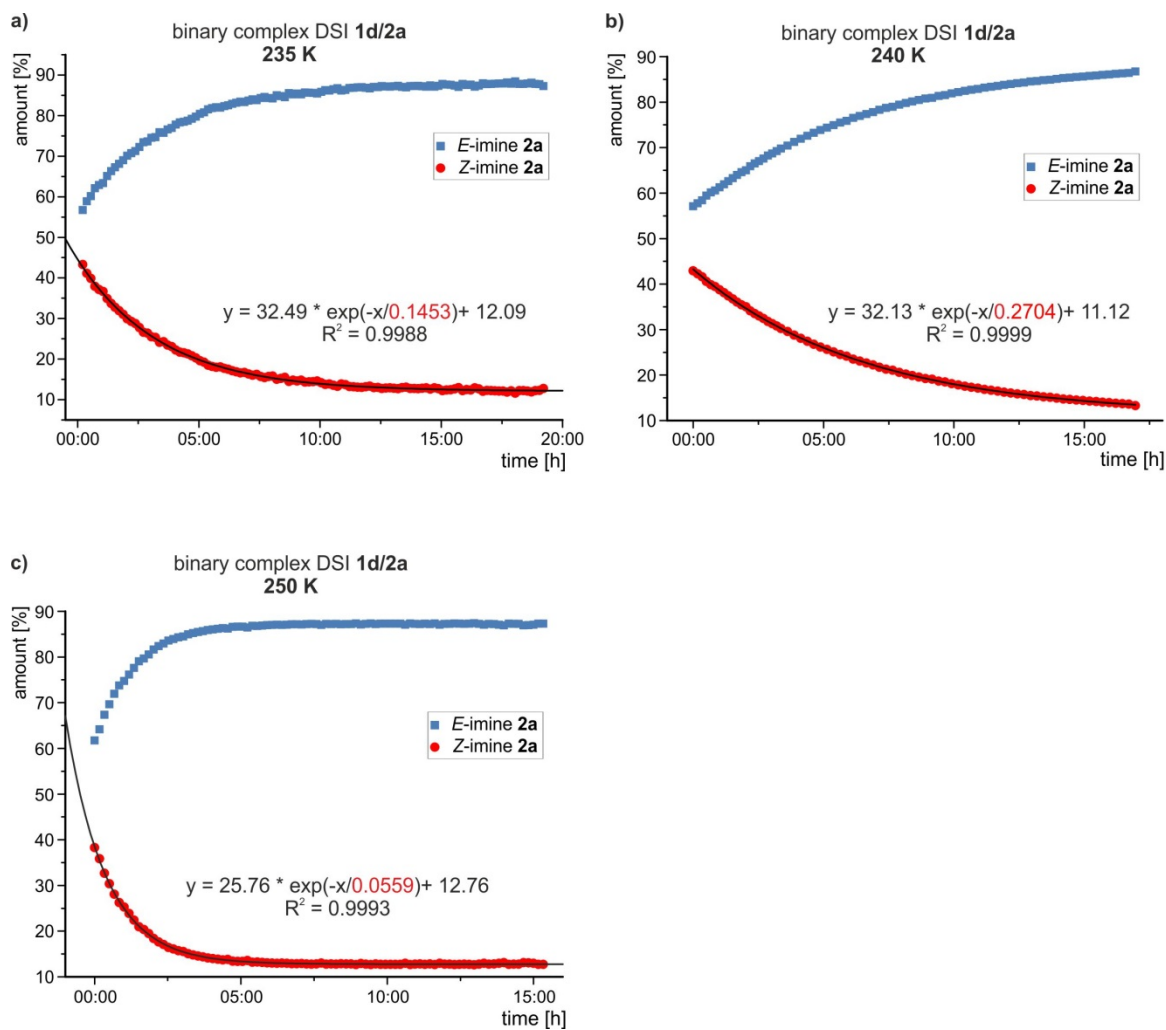


Figure 19: After irradiation at 365 nm the amount of Z-imine could be increased significantly. Afterwards the decay curves of the Z-imine were recorded at 235 K, 240K and 250K for different binary complexes **1d/2a** in CD_2Cl_2 . All decay curves are fitted mathematically and therefore the isomerization rates k_{Z-to-E} (= 1/"red value") can be determined. The obtained values of k_{Z-to-E} are given in Table 1.

5 A Quantitative Analysis of the E,Z-Isomerization

5.5.4. Determination of the activation energy E_a

The experimental activation energy E_a can be determined from the Arrhenius equation (11) after little mathematical transformations (12). After plotting the $\ln(k)$ vs. $1/T$ the slope is E_a/R .

$$k = A * e^{\frac{-E_a}{RT}} \quad (11)$$

$$\ln(k) = \frac{-E_a}{R} * \frac{1}{T} + \ln A \quad (12)$$

Where, R is the gas constant ($= 8.314 \text{ JK}^{-1} \text{ mol}^{-1}$) and A a pre-exponential factor, which is dependent on the order of the investigated reaction. The graphs for both isomerization processes are shown in Figure 20 and 21.

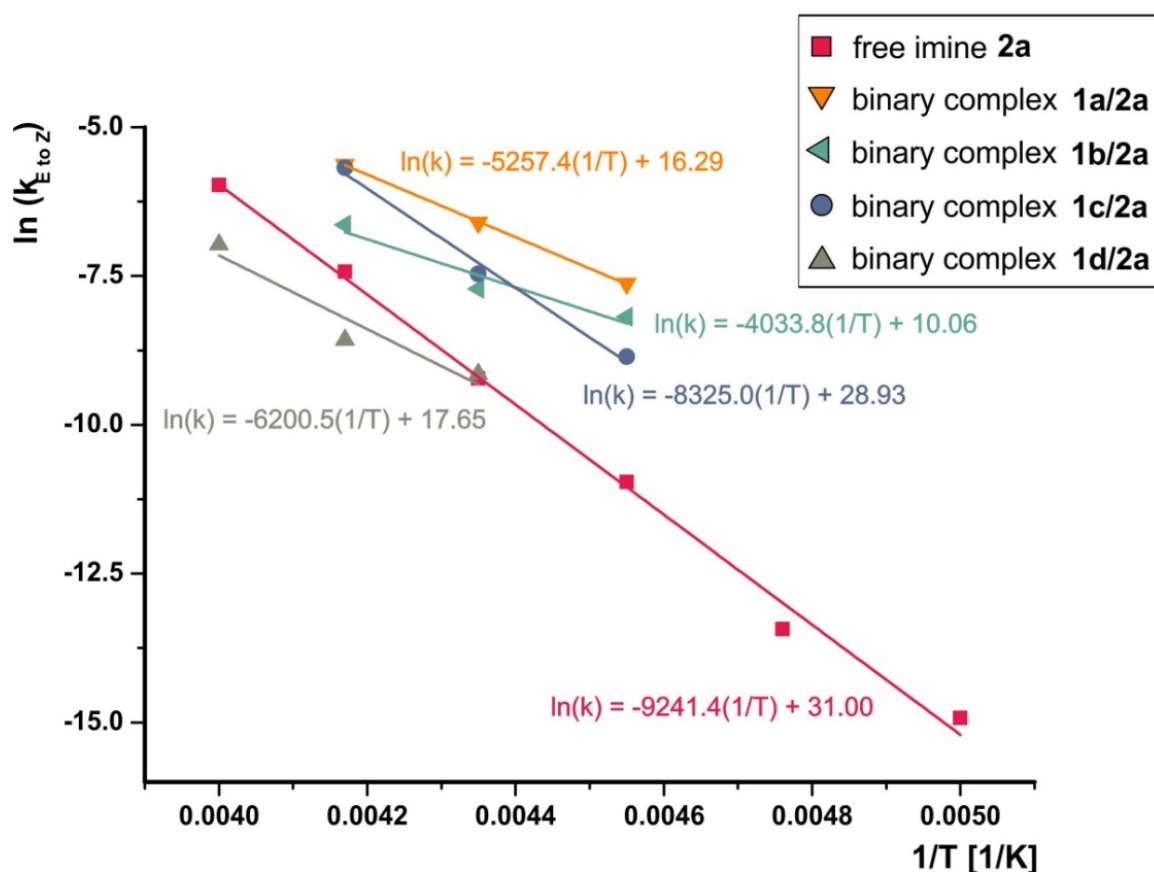


Figure 20: From the plot of $\ln(k)$ versus $1/T$, for the E -to- Z -isomerization of the free imine **2a** and the imine in different binary complex (**1a/2a**, **1b/2a**, **1c/2a** and **1d/2a**) the activation energies E_a can be determined.

5 A Quantitative Analysis of the E,Z-Isomerization

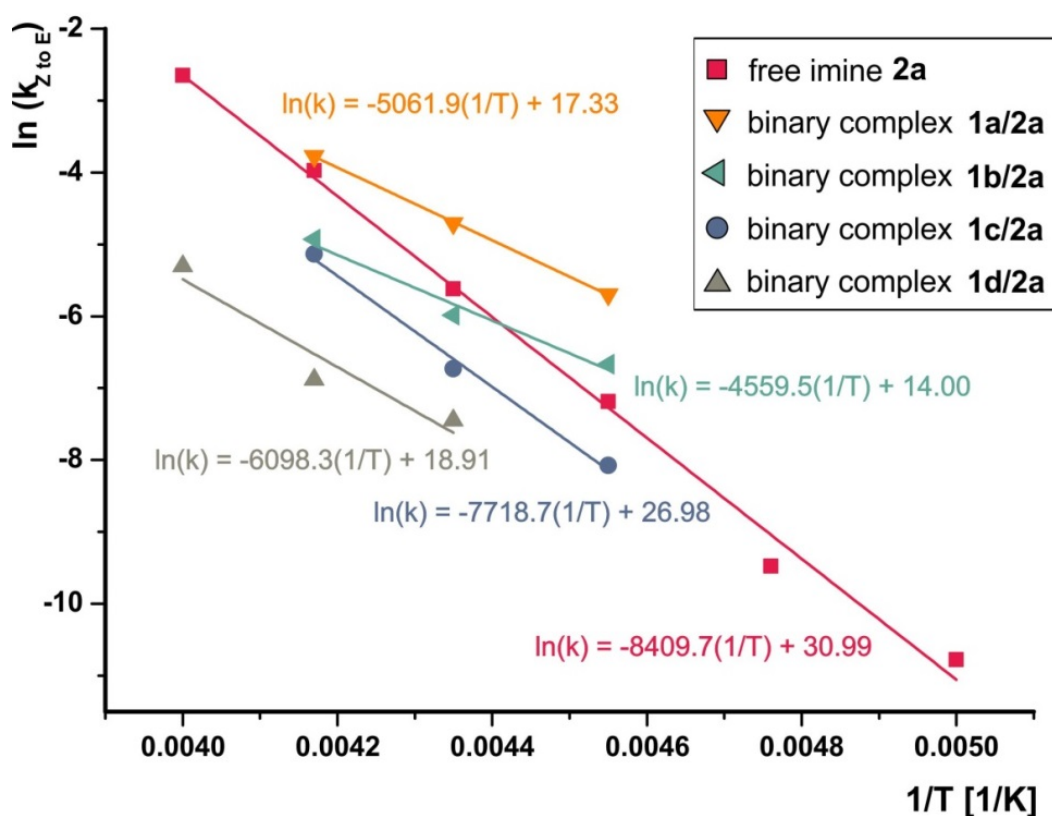


Figure 21: From the plot of $\ln(k)$ versus $1/T$, for the Z-to-E-isomerization of the free imine **2a** and the imine in different binary complex (**1a/2a**, **1b/2a**, **1c/2a** and **1d/2a**) the activation energies E_a can be determined.

For better comparison, the obtained activation energies E_a as well as the previously determined $\Delta G_{\text{total}}^{298\text{K}}$ values are summarized in Table 8. These parameters are based on different theoretical models (ΔG : Eyring theory, E_a : Arrhenius), however, both describe the energy, which is necessary to overcome the transition state. Surprisingly, the obtained E_a -respectively ΔG - values are deviating drastically. Only, the values for the free imine **2a** and the binary TiPSY/**2a**-complex are matching reasonably. For the binary complexes with TRIP, TRIFP and DSI deviations between 27 kJmol^{-1} and 49 kJmol^{-1} were received. These observations can be explained with the mathematical definition of E_a and ΔG (equation (13) and (14)).

$$E_a = \Delta H + RT \quad (13)$$

$$\Delta G = \Delta H - T\Delta S \quad (14)$$

The comparison of both equations shows, that the entropy ΔS is not contained in the definition of the activation energy E_a . In contrast, the definition of the Gibbs energy ΔG

5 A Quantitative Analysis of the E,Z-Isomerization

includes ΔS . This means, the differences between E_a and ΔG has to be due to an extremely high contribution of the entropy ΔS for the isomerization of the binary complexes with TRIP, TRIFP and DSI. In contrast, the sterically very demanding 3,3'-substituents of TIPSy, hinder the movement of the imine and therefore the contribution of the entropy is significantly decreased.

Table 8: The experimental activation energies E_a for both isomerization processes of the free imine **2a** and different binary complexes (**1a/2a**, **1b/2a**, **1c/2a** and **1d/2a**) were determined.

entry	catalyst	imine	$\Delta G_{\text{total}} (E\text{-to-Z})$ [kJmol ⁻¹]	$\Delta G_{\text{total}} (Z\text{-to-E})$ [kJmol ⁻¹]	$E_a (E\text{-to-Z})$ [kJmol ⁻¹]	$E_a (Z\text{-to-E})$ [kJmol ⁻¹]
1	TRIP 1a	2a	88.2	72.1	43.7	42.1
2	TRIFP 1b	2a	81.5	76.1	33.5	37.9
3	TiPSy 1c	2a	70.5	70.3	69.2	64.2
4	DSI 1d	2a	81.9	78.0	51.6	50.7
5	-	2a	72.6	66.0	76.8	69.9

5 A Quantitative Analysis of the E,Z-Isomerization

5.5.5. Eyring Polanyi plot for Z-to-E-isomerization

By extrapolating the observed linear equations of the Eyring-Polanyi plot (for the E-to-Z-isomerization see Figure 10 and for the Z-to-E-isomerization see Figure 22) the isomerization rate at 298.15 K can be determined. Hence the Gibbs energy ΔG at 298 K can be calculated with the Eyring equation:

$$k = \frac{k_B T}{h} * e^{\frac{-\Delta G}{RT}} \quad (13)$$

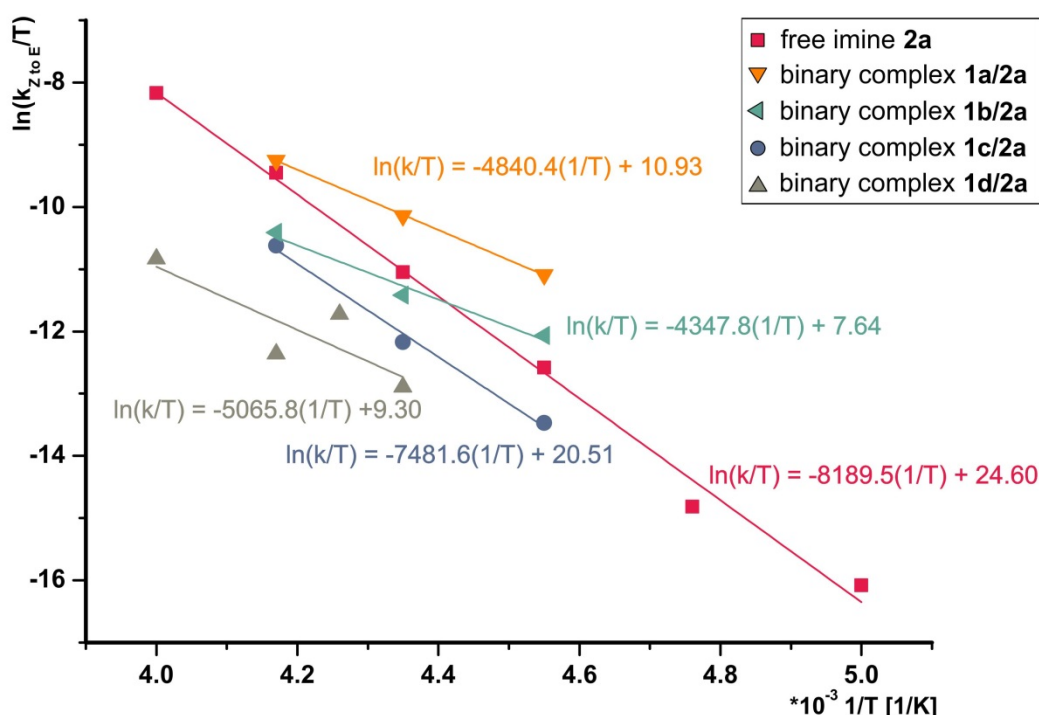


Figure 22: The Eyring-Polanyi plot for the Z-to-E-isomerization of the free imine **2a** and the imine in different binary complex (**1a/2a**, **1b/2a**, **1c/2a** and **1d/2a**) is shown. The $\ln(k/T)$ is plotted versus $1/T$. From the linear fit the thermodynamic variables $\Delta G^{298.15K}$, ΔS and ΔH are accessible.

As already mentioned, also the thermodynamic variables enthalpy ΔH and entropy ΔS are also accessible from the Eyring-Polanyi plot (Figure 10 and Figure 22) after a few mathematical transformations. Thus, the slope is $-\Delta H/R$ and the intercept is put together of $\ln(k_B/h) + \Delta S/R$. Where R is the gas constant ($= 8.314 \text{ JK}^{-1}\text{mol}^{-1}$), k_B the Boltzman constant ($= 1.38 \cdot 10^{-23} \text{ JK}^{-1}$) and h the Planck's constant ($= 6.62 \cdot 10^{-34} \text{ Js}^{-1}$).

$$k_{E \text{ to } Z} = \frac{k_B T}{h} * e^{\frac{-(\Delta G_{ges})}{RT}} = \frac{k_B T}{h} * e^{\frac{-(\Delta H - T\Delta S)}{RT}}$$

5 A Quantitative Analysis of the E,Z-Isomerization

$$\ln(k_{E \text{ to } Z}) = \ln\left(\frac{k_B T}{h}\right) + \frac{-\Delta H + T\Delta S}{RT} = \ln\left(\frac{k_B T}{h}\right) + \frac{-\Delta H}{RT} + \frac{\Delta S}{R}$$

$$\ln(k_{E \text{ to } Z}/T) = -\frac{\Delta H}{R} * \frac{1}{T} + \ln\left(\frac{k_B}{h}\right) + \frac{\Delta S}{R}$$

All obtained values for the Z-to-E-isomerization ($k_{Z\text{-to-E}}^{298\text{K}}$, $\Delta G_{\text{total}}^{298\text{K}}$, ΔH and ΔS) are summarized in Table 8. Similar to the situation for the E-to-Z-isomerization, also for the Z-to-E-isomerization the obtained values for the enthalpy ΔH are all in the same order of magnitude (36.1 – 68.1 kJmol⁻¹, for exact values see Table 9). Furthermore, the enthalpy ΔH values of both isomerization directions are very similar. The values for the entropy ΔS for the Z-to-E-isomerization in the binary complexes are between -27.0 and -134.0 JK⁻¹mol⁻¹. Thus they are slightly less negative, but the tendencies are still preserved. Whereas, the entropy ΔS for both isomerization processes of the free imine **2a** is almost the same and positive (E-to-Z-isomerization: 7.1 JK⁻¹mol⁻¹, Z-to-E-isomerization: 7.0 JK⁻¹mol⁻¹). Consequently, the large negative values for the entropy ΔS indicate an inversion process for the Z-to-E-isomerization of the binary complexes.^[27,28,32] This tendency is in accordance with the previously investigated E-to-Z-isomerization mechanism (chapter 5.3.6.).

Table 9: The isomerization rate at 298K $k_{Z\text{-to-E}}^{298\text{K}}$, Gibbs energy at 298K $\Delta G_{\text{total}}^{298\text{K}}$, enthalpy ΔH and entropy ΔS for free imine **2a** and different binary complexes (**1a/2a**, **1b/2a**, **1c/2a** and **1d/2a**) were obtained from the Eyring-Polanyi plot. All values shown in this table are related to the Z-to-E-isomerization

entry	catalyst	imine	$k_{Z\text{-to-E}}^{298\text{K}}$ [1/s]	$\Delta G_{\text{total}}^{298\text{K}}$ [kJmol ⁻¹]	ΔH [kJmol ⁻¹]	ΔS [JK ⁻¹ mol ⁻¹]
1	TRIP 1a	2a	1.48	72.1	40.2	-106.7
2	TRIFP 1b	2a	0.28	76.1	36.1	-134.0
3	TIPSY 1c	2a	3.05	70.3	62.2	-27.0
4	DSI 1d	2a	0.14	78.0	42.1	-120.2
5	-	2a	16.94	66.0	68.1	7.0

5 A Quantitative Analysis of the E,Z-Isomerization

5.5.6. Cyclic voltammetry of imine **2a**

The cyclic voltammetry (CV) measurements were performed in degassed acetonitrile containing 0.1 M tetra-*n*-butylammonium hexafluorophosphate as a conducting salt and using ferrocene/ferrocenium (Fc/Fc⁺) as an internal standard under argon atmosphere at room temperature. The measurements are carried out with an Autolab PGSTAT302N Metrohm. A glassy carbon electrode (working electrode), platinum wire counter electrode and Ag wire quasi-reference electrode were employed. The cyclic voltammogram is shown in the Figure 23. The oxidation potential of **2a** is irreversible and was determined at the 5% offset of the peak ($E_{\text{ox}} = +1.52 \text{ V vs Ag/AgCl} = +1.26 \text{ V vs SCE}$).^[51]

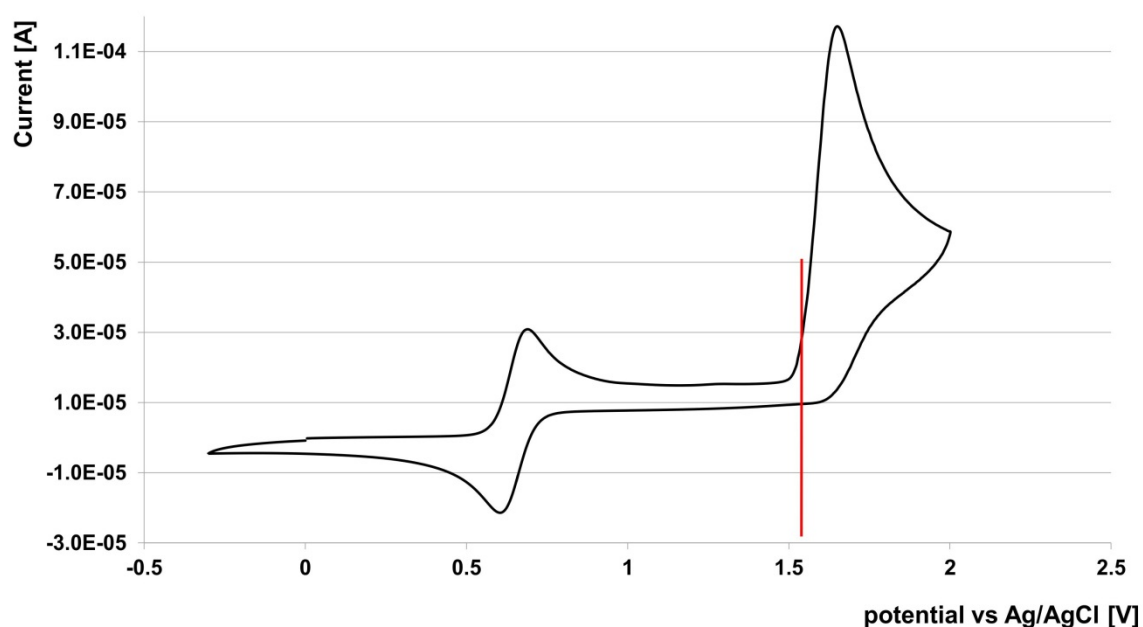


Figure 23: Cyclic voltammogram of imine **2a** in acetonitrile. The irreversible oxidation potential was determined at the 5% offset (indicated by the red line).

5 A Quantitative Analysis of the E,Z-Isomerization

5.5.7. Fluorescence emission quenching of RFTA

A fluorescence cuvette containing RFTA ($c_{\text{RFTA}} = 7.6 \cdot 10^{-6} \text{ molL}^{-1}$) in dichloromethane was placed in a fluorescence spectrometer (Fluoromax-4 Spectrofluorometer). The solution was irradiated at 430 nm and the fluorescence emission spectrum was measured (maximum intensity at 504 nm; black curve in Figure 24). After addition of 200 equivalents of the quencher (imine **2a**, red curve in Figure 24) the emission intensity at 504 nm was slightly decreased. To ensure that this decrease in intensity is because of fluorescence quenching an additional, undefined amount of imine was added. In this way a significant intensity decrease at 504 nm could be observed (blue curve in Figure 24). This indicates a weak electron transfer from RFTA to the imine **2a**.

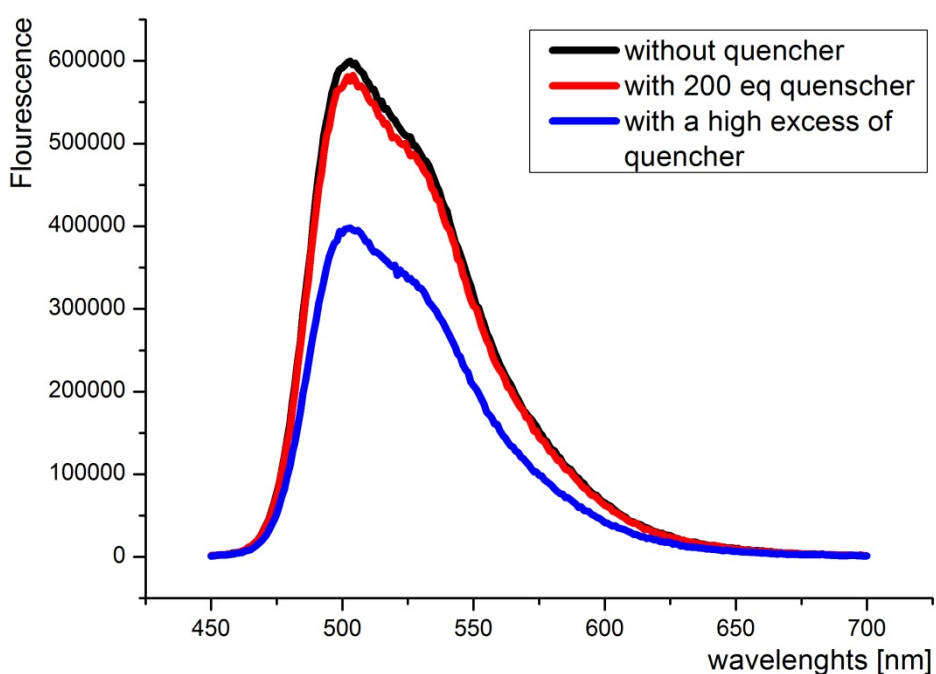


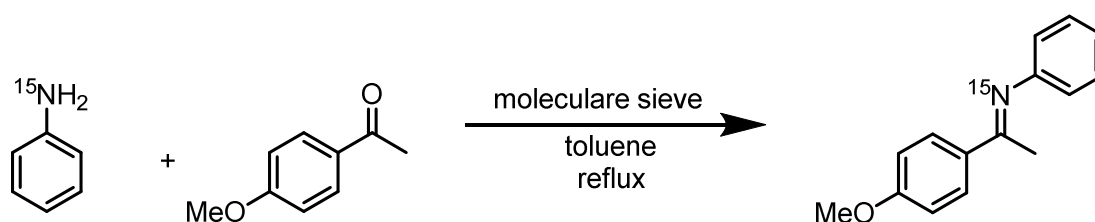
Figure 24: Emission spectra of RFTA (black curve) between 450 and 700 nm. After addition of the quencher (imine **2a**) the emission intensity is decreased (red and blue curve).

5 A Quantitative Analysis of the *E,Z*-Isomerization

5.5.8. Synthesis of the imines

The imines were prepared according to a modified literature procedure.^[52–57] The toluene was used either in p.A. quality or was dried by refluxing over sodium. The ¹⁵N-enriched aniline for the presented syntheses below was purchased from Euriso-top GmbH and Sigma Aldrich.

(E)-1-(4-methoxyphenyl)-*N*-phenylethan-1-imine (98% ¹⁵N) **2a**



After activation of the molecular sieves 4 Å (9.8 g) at 450°C under reduced pressure, 4-methoxyacetophenone (2.16 g, 14.3 mmol, 1.3 eq) and aniline (98% ¹⁵N, 1 ml, 1.02 g, 11.0 mmol) were added to the Schlenk flask under argon atmosphere. Then the reactants were dissolved in 33 ml dry toluene. The solution was refluxed overnight with a drying tube (filled with CaCl₂). The molecular sieves were removed, and the orange solution was concentrated under reduced pressure. The remaining solid was recrystallized from diethylether at -20°C. The product was obtained as yellow solid.

¹H-NMR (400.1 MHz, CD₂Cl₂): δ_H [ppm] = 7.95 (m, 2H, Aryl-H), 7.35 (m, 2H, Aryl-H), 7.07 (m, 1H, Aryl-H), 6.96 (m, 2H, Aryl-H), 6.77 (m, 2H, Aryl-H), 3.86 (s, 3H, -OCH₃), 2.18 (d, ³J_{HN} = 1.76 Hz, -CH₃)

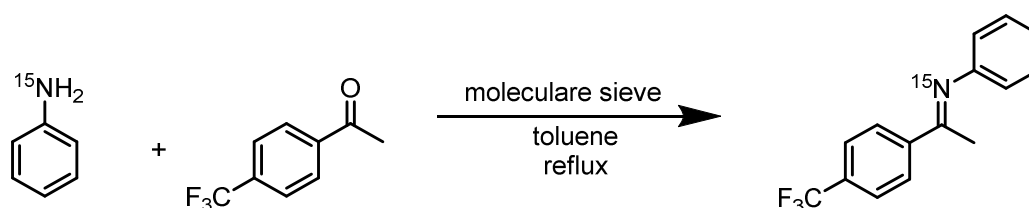
¹³C-NMR {¹H} (100.6 MHz, CD₂Cl₂): δ_C [ppm] = 164.5, 161.9, 152.5, 132.5, 129.3, 129.2, 123.2, 119.9, 113.9, 55.8, 17.2

¹⁵N-NMR (40.5 MHz, CD₂Cl₂): δ_N [ppm] = 325.5

¹H- and ¹³C-spectra were in accordance with the literature.^[58]

5 A Quantitative Analysis of the *E,Z*-Isomerization

(*E*)-1-(4-trifluoromethylphenyl)-*N*-phenylethan-1-imine (98% ¹⁵N) **2b**



After activation of the molecular sieves 4 Å (5 g) at 350°C under reduced pressure, 4-trifluoromethylacetophenone (3.66 g, 19.5 mmol, 1.3 eq) and aniline (98% ¹⁵N, 1.40 ml, 1.40 g, 15.0 mmol) were added to the Schlenk flask under argon. Then the reactants were dissolved in 25 ml dry toluene. The solution was heated to reflux overnight with a drying tube (filled with CaCl₂). The molecular sieves were removed, and the reaction solution was concentrated under reduced pressure. The remaining solid was recrystallized from methanol at -20°C. The product was obtained as yellow needles.

¹H-NMR (400.1 MHz, CD₂Cl₂): δ_H [ppm] = 8.11 (m, 2H, Aryl-H), 7.72 (m, 2H, Aryl-H), 7.37 (m, 2H, Aryl-H), 7.11 (m, 1H, Aryl), 6.79 (m, 2H), 2.25 (s, 3H, -CH₃)

¹³C-NMR {¹H} (100.6 MHz, CD₂Cl₂): δ_C [ppm] = 164.5, 151.7, 143.2, 132.1, 129.4, 128.0, 125.6, 124.6, 123.9, 119.5, 17.5

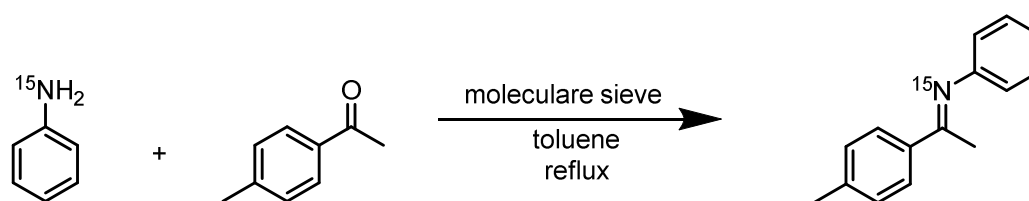
¹⁵N-NMR (40.5 MHz, CD₂Cl₂): δ_N [ppm] = 338.2

¹⁹F-NMR {¹H} (376 MHz, CD₂Cl₂): δ_F [ppm] = - 63.1

¹H- and ¹³C-spectra were in accordance with the literature.^[59]

5 A Quantitative Analysis of the *E,Z*-Isomerization

(*E*)-1-(4-methylphenyl)-*N*-phenylethan-1-imine (98% ¹⁵N) **2c**



After activation of the molecular sieves 4 Å (9.8 g) at 450°C under reduced pressure, 4-methylacetophenone (2.27 mL, 2.28 g, 17.0 mmol, 1.6 eq) and aniline (98% ¹⁵N, 1 ml, 1.02 g, 11.0 mmol) were added to the Schlenk flask under argon atmosphere. Then the reactants were dissolved in 33 ml dry toluene. The solution was heated to reflux overnight with a drying tube (filled with CaCl₂). The molecular sieves were removed, and the reaction solution was concentrated under reduced pressure. The remaining solid was recrystallized from petroleum ether at -20°C. The product was obtained as yellow needles.

¹H-NMR (400.1 MHz, CD₂Cl₂): δ_H [ppm] = 7.86 (m, 2H, Aryl-H), 7.34 (m, 2H, Aryl-H), 7.25 (m, 2H, Aryl-H), 7.06 (m, 1H, Aryl-H), 6.76 (m, 2H), 2.40 (s, 3H, -CH₃), 2.18 (d, ³J_{HN} = 1.76 Hz, 3H, -CH₃)

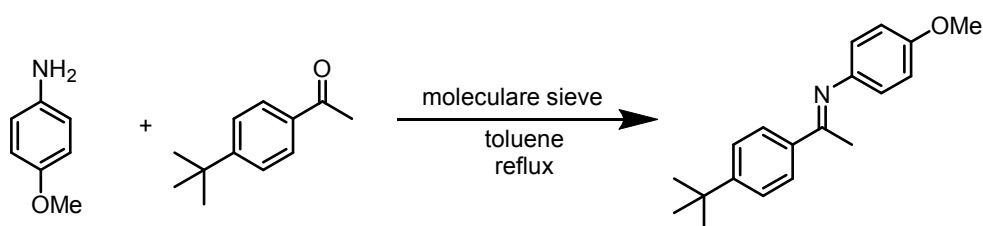
¹³C-NMR {¹H} (100.6 MHz, CD₂Cl₂): δ_C [ppm] = 165.3, 152.4, 141.2, 133.9, 129.5, 129.3, 127.5, 123.3, 119.7, 21.5, 17.4

¹⁵N-NMR (40.5 MHz, CD₂Cl₂): δ_N [ppm] = 328.9

¹H- and ¹³C-spectra were in accordance with the literature.^[55]

5 A Quantitative Analysis of the *E,Z*-Isomerization

(*E*)-1-(4-(*tert*-butyl)phenyl)-*N*-(4-methoxyphenyl)ethan-1-imine **2d**



After activation of the molecular sieves 4 Å (10 g) at 450°C under reduced pressure, 4-*tert*-butylacetophenone (1.93 mL, 1.86 g, 10.6 mmol, 1.3 eq) and anisidine (1 g, 8.13 mmol) were added to the Schlenk flask under argon atmosphere. Then the reactants were dissolved in 33 ml dry toluene. The solution was heated to reflux overnight with a drying tube (filled with CaCl₂). The molecular sieves were removed, and the reaction solution was concentrated under reduced pressure. The remaining solid was recrystallized from diethylether at -20°C. The product was obtained as yellow needles.

¹H-NMR (400.1 MHz, CD₂Cl₂): δ_H [ppm] = 7.93 (m, 2H, Aryl-H), 7.49 (m, 2H, Aryl-H), 6.92 (m, 2H, Aryl-H), 6.74 (m, 2H, Aryl-H), 3.82 (s, 3H, -OCH₃), 2.24 (s, 3H, -CH₃), 1.38 (s, 9H, *t*-Bu)

¹³C-NMR {¹H} (100.6 MHz, CD₂Cl₂): δ_C [ppm] = 165.1, 155.9, 153.7, 145.1, 137.1, 126.9, 125.2, 120.7, 114.2, 55.4, 34.7, 31.0, 16.9

¹H- and ¹³C-spectra were in accordance with the literature.^[60]

5 A Quantitative Analysis of the *E,Z*-Isomerization

5.5.9. Sample Preparation

The deuterated dichloromethane was purchased from Deutero or Sigma Aldrich and freshly distilled over CaH₂ to remove traces of water. All catalysts were purchased from Sigma Aldrich. All samples were stored in an -80°C freezer during the measurements. Even after careful sample preparation, partial hydrolysis of the imine could not be completely prevented. Therefore the imine/catalyst-ratios deviate slightly from 1:1.

Free imine 2a in CD₂Cl₂

5.11 mg (*E*)-1-(4-methoxyphenyl)-*N*-phenylethan-1-imine (98% ¹⁵N) **2a** (22.6 μmol) were weighted in a commercial available amber thin wall NMR-tube and dissolved in 0.5 mL dry CD₂Cl₂.

Free imine 2b in CD₂Cl₂

6.28 mg (*E*)-1-(4-trifluoromethylphenyl)-*N*-phenylethan-1-imine (98% ¹⁵N) **2b** (28.3 μmol) were weighted in a commercial available amber thin wall NMR-tube and dissolved in 0.5 mL dry CD₂Cl₂.

Free imine 2c in CD₂Cl₂

4.95 mg (*E*)-1-(4-methylphenyl)-*N*-phenylethan-1-imine (98% ¹⁵N) **2c** (23.5 μmol) were weighted in a commercial available amber thin wall NMR-tube and dissolved in 0.5 mL dry CD₂Cl₂.

Imine 2a and TRIP 1a in CD₂Cl₂

20.75 mg (*R*)-TRIP **1a** (29.9 μmol) are weighted in a commercial available amber thin wall NMR-tube and dried under reduced pressure at 120°C for 20 minutes. Then 6.68 mg (*E*)-1-(4-methoxyphenyl)-*N*-phenylethan-1-imine (98% ¹⁵N) **2a** (29.5 μmol) and 0.5 mL dry CD₂Cl₂ were added under argon atmosphere.

5 A Quantitative Analysis of the E,Z-Isomerization

Imine 2a and TRIFP 1b in CD₂Cl₂

20.79 mg (R)-TRIFP **1b** (22.4 μmol) are weighted in a commercial available amber thin wall NMR-tube and dried under reduced pressure at 120°C for 20 minutes. Then 5.57 mg (*E*)-1-(4-methoxyphenyl)-N-phenylethan-1-imine (98% ¹⁵N) **2a** (20.5 μmol) and 0.5 mL dry CD₂Cl₂ were added under argon atmosphere.

Imine 2a and TiPSY 1c in CD₂Cl₂

25.25 mg (R)-TiPSY **1c** (29.1 μmol) are weighted in a commercial available amber thin wall NMR-tube and dried under reduced pressure at 120°C for 20 minutes. Then 6.66 mg (*E*)-1-(4-methoxyphenyl)-N-phenylethan-1-imine (98% ¹⁵N) **2a** (29.4 μmol) and 0.5 mL dry CD₂Cl₂ were added under argon atmosphere.

Imine 2a and DSI 1d in CD₂Cl₂

21.03 mg (R)-DSI **1d** (25.7 μmol) are weighted in a commercial available amber thin wall NMR-tube and dried under reduced pressure at 120°C for 20 minutes. Then 5.63 mg (*E*)-1-(4-methoxyphenyl)-N-phenylethan-1-imine (98% ¹⁵N) **2a** (24.9 μmol) and 0.5 mL dry CD₂Cl₂ were added under argon atmosphere. Finally, TMS-atmosphere was added.

Imine 2b and TiPSY 1c in CD₂Cl₂

21.02 mg (R)-TiPSY **1c** (24.3 μmol) are weighted in a commercial available amber thin wall NMR-tube and dried under reduced pressure at 120°C for 20 minutes. Then 6.61 mg (*E*)-1-(4-trifluoromethylphenyl)-N-phenylethan-1-imine (98% ¹⁵N) **2b** (25.0 μmol) and 0.5 mL dry CD₂Cl₂ were added under argon atmosphere.

Imine 2c and TiPSY 1c in CD₂Cl₂

21.63 mg (R)-TiPSY **1c** (25.0 μmol) are weighted in a commercial available amber thin wall NMR-tube and dried under reduced pressure at 120°C for 20 minutes. Then 5.23 mg (*E*)-1-(4-methylphenyl)-N-phenylethan-1-imine (98% ¹⁵N) **2c** (24.9 μmol) and 0.5 mL dry CD₂Cl₂ were added under argon atmosphere.

5 A Quantitative Analysis of the *E,Z*-Isomerization

Imine 2a and RFTA in CD₂Cl₂

5.24 mg (*E*)-1-(4-methoxyphenyl)-*N*-phenylethan-1-imine (98% ¹⁵N) **2a** (23.2 μmol) were weighted in a commercial available amber thin wall NMR-tube and evacuated. Then 0.2 mL dry CD₂Cl₂ and 0.3 mL of a RFTA-stock solution (5 mol%, 2.20 mg RFTA in 1 mL dry CD₂Cl₂) were added under argon atmosphere.

Imine 2a and DDQ in CD₂Cl₂

5.17 mg (*E*)-1-(4-methoxyphenyl)-*N*-phenylethan-1-imine (98% ¹⁵N) **2a** (22.9 μmol) were weighted in a commercial available amber thin wall NMR-tube and evacuated. Then 0.2 mL dry CD₂Cl₂ and 0.3 mL of a DDQ-stock solution (5 mol%, 0.89 mg DDQ in 1 mL dry CD₂Cl₂) were added under argon atmosphere.

Imine 2a and TCBQ in CD₂Cl₂

5.27 mg (*E*)-1-(4-methoxyphenyl)-*N*-phenylethan-1-imine (98% ¹⁵N) **2a** (23.3 μmol) were weighted in a commercial available amber thin wall NMR-tube and evacuated. Then 0.2 mL dry CD₂Cl₂ and 0.3 mL of a TCBQ-stock solution (5 mol%, 0.87 mg DDQ in 1 mL dry CD₂Cl₂) were added under argon atmosphere. Finally, TMS-atmosphere was added.

5 A Quantitative Analysis of the E,Z-Isomerization

5.6. References

- [1] W. Szymanski, J. M. Beierle, H. A. V Kistemaker, W. A. Velema, B. L. Feringa, *Chem. Rev.* **2013**, *113*, 6114–6178.
- [2] W. A. Velema, W. Szymanski, B. L. Feringa, *J. Am. Chem. Soc.* **2014**, *136*, 2178–2191.
- [3] M. M. Lerch, M. J. Hansen, G. M. van Dam, W. Szymanski, B. L. Feringa, *Angew. Chemie - Int. Ed.* **2016**, *55*, 10978–10999.
- [4] K. Rustler, M. J. Mickert, J. Nazet, R. Merkl, H. H. Gorris, B. König, *Org. Biomol. Chem.* **2018**, *16*, 7430–7437.
- [5] F. Hamon, F. Djedaini-Pilard, F. Barbot, C. Len, *Tetrahedron* **2009**, *65*, 10105–10123.
- [6] F. Hamon, F. Djedaini-Pilard, F. Barbot, C. Len, *Tetrahedron* **2010**, *66*, 2538.
- [7] G. S. Hartley, *Nature* **1937**, *140*, 281.
- [8] N. A. Simeth, L. M. Altmann, N. Wössner, E. Bauer, M. Jung, B. König, *J. Org. Chem.* **2018**, *83*, 7919–7927.
- [9] R. Brückner, *Reaktionsmechanismen*, Springer-Verlag, Berlin Heidelberg, **2007**.
- [10] S. Müller, B. List, *Synthesis (Stuttg.)* **2010**, 2171–2178.
- [11] S. Müller, B. List, *Angew. Chemie - Int. Ed.* **2009**, *48*, 9975–9978.
- [12] B. Heggen, M. Patil, W. Thiel, *J. Comput. Chem.* **2016**, *37*, 280–285.
- [13] P. Renzi, J. Hioe, R. M. Gschwind, *J. Am. Chem. Soc.* **2017**, *139*, 6752–6760.
- [14] M. Rueping, E. Sugiono, C. Azap, T. Theissmann, M. Bolte, *Org. Lett.* **2005**, *7*, 3781–3783.
- [15] A. Padwa, *Chem. Rev.* **1977**, *77*, 37–68.
- [16] J. M. Lehn, *Chem. - A Eur. J.* **2006**, *12*, 5910–5915.
- [17] Y. Osamura, S. Yamabe, K. Nishimoto, *Int. J. Quantum Chem.* **1980**, *18*, 457–462.
- [18] J. P. Reid, L. Simón, J. M. Goodman, *Acc. Chem. Res.* **2016**, *49*, 1029–1041.
- [19] T. Marcelli, P. Hammar, F. Himo, *Chem. - A Eur. J.* **2008**, *14*, 8562–8571.
- [20] L. Simón, J. M. Goodman, *J. Am. Chem. Soc.* **2008**, *130*, 8741–8747.
- [21] L. Simón, J. M. Goodman, *J. Org. Chem.* **2011**, *76*, 1775–1788.
- [22] H. Eyring, *Chem. Rev.* **1935**, *17*, 65–77.
- [23] T. Engel, P. Reid, *Physikalische Chemie*, **2006**.
- [24] H. Kessler, *Angew. Chem* **1970**, *82*, 237.
- [25] J. E. Johnson, N. M. Morales, A. M. Gorczyca, D. D. Dolliver, M. A. McAllister, *J. Org. Chem.* **2001**, *66*, 7979–7985.
- [26] H. Kessler, D. Leibfritz, *Tetrahedron Lett.* **1969**, 427–430.
- [27] K. Schober, E. Hartmann, H. Zhang, R. M. Gschwind, *Angew. Chemie - Int. Ed.* **2010**, *49*, 2794–2797.
- [28] M. I. Rodríguez-Franco, I. Dorronsoro, A. Castro, A. Martínez, *Tetrahedron* **2000**, *56*, 1739–1743.
- [29] C. H. Bushweller, C. Y. Wang, J. Reny, M. Z. Lourandos, *J. Am. Chem. Soc.* **1977**, *99*, 3938–3941.
- [30] C. H. Bushweller, J. W. O'Neil, H. S. Bilofsky, *Tetrahedron* **1971**, *27*, 5761–5766.
- [31] C. H. Bushweller, J. W. O'Neil, H. S. Bilofsky, *J. Am. Chem. Soc.* **1970**, *92*, 6349–6350.

5 A Quantitative Analysis of the E,Z-Isomerization

- [32] V. S. Dimitrov, N. G. Vassilev, *Magn. Reson. Chem.* **1995**, *33*, 739–744.
- [33] Y. Nagawa, T. Yamagaki, H. Nakanishi, *Tetrahedron Lett.* **1998**, *39*, 1393–1396.
- [34] M. Dewar, B. Jennings, *Tetrahedron Lett.* **1970**, *11*, 339–342.
- [35] K. Rothermel, M. Zabka, J. Hioe, R. M. Gschwind, *J. Org. Chem.* **2019**, *accepted*, DOI:10.1021/acs.joc.9b01811.
- [36] K. Rothermel, M. Melikian, J. Hioe, J. Greindl, J. Gramüller, M. Zabka, N. Sorgenfrei, T. Hausler, F. Morana, R. M. Gschwind, *Chem. Sci.* **2019**, *accepted*, DOI:10.1039/C9SC02342A.
- [37] C. Feldmeier, H. Bartling, E. Riedle, R. M. Gschwind, *J. Magn. Reson.* **2013**, *232*, 39–44.
- [38] Y. Luo, M. Utecht, J. Dokić, S. Korchak, H. M. Vieth, R. Haag, P. Saalfrank, *ChemPhysChem* **2011**, *12*, 2311–2321.
- [39] J. P. Reid, J. M. Goodman, *J. Am. Chem. Soc.* **2016**, *138*, 7910–7917.
- [40] S. Hoffmann, A. M. Seayad, B. List, *Angew. Chemie - Int. Ed.* **2005**, *44*, 7424–7427.
- [41] R. I. Storer, D. E. Carrera, Y. Ni, D. W. C. Macmillan, *J. Am. Chem. Soc.* **2006**, *128*, 84–86.
- [42] unpublished results by Johnny Hioe, **n.d.**
- [43] G. S. Hammond, J. Saltiel, *J. Am. Chem. Soc.* **1962**, *84*, 4983–4984.
- [44] T. Arai, H. Sakuragi, K. Tokumaru, *Chem. Lett.* **1980**, 261–264.
- [45] J. B. Metternich, R. Gilmour, *J. Am. Chem. Soc.* **2015**, *137*, 11254–11257.
- [46] J. B. Metternich, D. G. Artiukhin, M. C. Holland, M. Von Bremen-Kuhne, J. Neugebauer, R. Gilmour, *J. Org. Chem.* **2017**, *82*, 9955–9977.
- [47] A. Padwa, F. Albrecht, *J. Am. Chem. Soc.* **1972**, *94*, 1000–1002.
- [48] A. Padwa, F. Albrecht, *J. Am. Chem. Soc.* **1974**, *96*, 4849–4857.
- [49] N. A. Romero, D. A. Nicewicz, *Chem. Rev.* **2016**, *116*, 10075–10166.
- [50] B. Mühldorf, R. Wolf, *Chem. Commun.* **2015**, *51*, 8425–8428.
- [51] V. V. P. A. W. Addison, V. Pavlishchuk, *Inorganica Chim. Acta* **2000**, *298*, 97–102.
- [52] N. Sorgenfrei, J. Hioe, J. Greindl, K. Rothermel, F. Morana, N. Lokesh, R. M. Gschwind, *J. Am. Chem. Soc.* **2016**, *138*, 16345–16354.
- [53] J. Greindl, J. Hioe, N. Sorgenfrei, F. D. Morana, R. M. Gschwind, *J. Am. Chem. Soc.* **2016**, *49*, 15965–15971.
- [54] F. Aznar, C. Valde, *J. Am. Chem. Soc.* **2009**, *131*, 4031–4041.
- [55] Y. Schramm, F. Barrios-Landeros, A. Pfaltz, *Chem. Sci.* **2013**, *4*, 2760–2766.
- [56] F. H. Westheimer, K. Taguchi, *J. Org. Chem.* **1971**, *36*, 1570–1572.
- [57] M. C. Hansen, S. L. Buchwald, *Org. Lett.* **2000**, *2*, 713–715.
- [58] J. S. M. Samec, J. E. Bäckvall, *Chem. - A Eur. J.* **2002**, *8*, 2955–2961.
- [59] A. V. Malkov, A. Mariani, K. N. Macdougall, P. Kočovský, *Org. Lett.* **2004**, *6*, 2253–2256.
- [60] B. J. Fallon, E. Derat, M. Amatore, C. Aubert, F. Chemla, F. Ferreira, A. Perez-Luna, M. Petit, *J. Am. Chem. Soc.* **2015**, *137*, 2448–2451.

6 Conclusion

In recent years, BINOL-derived Brønsted acids have emerged as a preferred class of catalysts in the field of enantioselective organocatalysis. Despite the enormous success of these catalysts regarding the obtained excellent enantioselectivities, the high yields as well as the versatile applicability, the intermediates and activation modes are up to now largely unexplored. Nevertheless, for the asymmetric transfer hydrogenation of imines the existence of a pre-catalytic species, where the BINOL-derived Brønsted acid catalyst and the substrate form a hydrogen bonded ion pair, is postulated. Most probably, the introduction of the enantioselectivity proceeds within this ion pair, consisting of a cationic substrate species and a chiral anion provided by the catalyst. Therefore, in this thesis several of these binary Brønsted acid/imine-complexes were investigated by means of NMR-spectroscopy. By that, the interactions between different catalysts and substrates should be better understood, which subsequently allows the aimed choice of an optimal catalyst for a selected reaction.

Therefore, the second chapter of this thesis focusses on NMR-spectroscopic investigations of the binary complex, which consists of the chiral phosphoric acid TRIP and several ^{15}N -labeled imines. Due to the use of imines with different electronic and steric properties, the basicity of the substrate was varied. The ^{15}N -labeling of the imine allows, apart the measurement of the ^1H proton chemical shift, also the experimental access to the ^{15}N chemical shift and the three coupling constants ($^1J_{\text{NH}}$, $^{2\text{h}}J_{\text{PH}}$ and $^{3\text{h}}J_{\text{PN}}$). These parameters enable the detailed analysis of the formed hydrogen bond. Both ^1H and ^{15}N chemical shift are dependent on the position of the proton within the hydrogen bond: the closer the proton is shifted to the nitrogen the more highfield shifted are ^1H and ^{15}N chemical shift. Thus, the Steiner-Limbach curve, which correlates the ^1H and ^{15}N chemical shifts empirically, shows that most of the TRIP/imine complexes form strong hydrogen bonds with an ionic character. Additionally, from the parabolic fit curve the individual atomic distances r_{OH} and r_{NH} were calculated. Theoretical calculations predicted an asymmetric single well potential surface, which was confirmed experimentally by measuring the deuterium isotope effect. Similar to the chemical shifts also the $^1J_{\text{NH}}$ coupling constant is dependent on the degree of imine-protonation: the closer the proton is shifted to the nitrogen the larger is the $^1J_{\text{NH}}$ coupling constant. Furthermore, the trans-hydrogen bond $^{2\text{h}}J_{\text{PH}}$ and $^{3\text{h}}J_{\text{PN}}$ scalar coupling constants were quantified. Both are very sensitive on changes of the hydrogen bond geometry. Independent on the imine substitution pattern, mainly linear hydrogen bonds were

6 Conclusion

observed. Only the position of the hydrogen bonded proton varies, due to the basicity of the imine. Thus, the hydrogen bond can be seen as a structural anchor between substrate and catalyst.

In the third chapter of the thesis, the influence of the 3,3'-substituents of BINOL-derived chiral phosphoric acids was investigated. Therefore, a detailed hydrogen bond analysis from three additional phosphoric acid catalysts (TRIFP, TRIM and TiPSY) with three selected imines was done and compared to the previously investigated TRIP-complexes. Independent on the 3,3'-substituents, almost all binary complexes form strong, charge-assisted hydrogen bonds. Nevertheless, the acidity of the catalysts differs and therefore the position of the proton in the hydrogen bond is affected. Thus, the difference of the ^{15}N chemical shift in the binary complex of one imine with all four catalysts (TRIP, TRIFP, TRIM and TiPSY) could be used as a descriptor for the catalyst-acidity. In this way the first internal acidity scale for chiral phosphoric acid/imine-complexes was implemented. The order of the catalyst-acidity is slightly different for *E*- and *Z*-complexes. However, both internal acidity scales obtained from chemical shifts could be confirmed by the measured $^1J_{\text{NH}}$ coupling constants. Nevertheless, the calculated external acidity scale is not in accordance with the experimental internal acidity scales. On the other hand, the calculations of the internal acidities, for example in the form of computed $^1J_{\text{NH}}$ coupling constants, reflect the experimental results. Thus, the significant influence of the intermolecular interactions on the acidic properties of these complexes becomes apparent. At least for three of the four investigated phosphoric acid catalysts an inverse correlation of the acidity with the reactivity was found. That means the more acidic the catalyst, the slower is the over-all reaction rate. However, since the catalyst with the sterically most demanding 3,3'-substituents does not follow this trend it becomes visible, that at least for the asymmetric transfer hydrogenation, also other factors than the internal acidity influence the reactivity. The analysis of isomerization rates as well as further investigations regarding populations and chemical shifts of both binary and ternary complexes showed that a delicate balance between isomerization and ternary complex formation seems to be significantly responsible for the reactivity of the chiral phosphoric acid catalyst in the transfer hydrogenation. Due to the formation of strong hydrogen bonds with all investigated catalysts, it is most probably that the break-down of reactivity for the sterically most demanding catalyst is caused by the blocking of the binding pocket through the imine. Thus, the binding of the second substrate is hindered. Nevertheless, after consideration of the size of the binding pocket the internal acidity can be correlated with the overall-reaction rate in the asymmetric transfer hydrogenation.

The fourth chapter of this thesis investigated the hydrogen bond and structural properties of the structural similar BINOL-derived disulfonimide catalysts in their binary imine-complexes. The acidity of this class of catalysts is significantly increased compared to the previously investigated phosphoric acids. However, the observed ^1H and ^{15}N chemical shifts in combination with the $^1J_{\text{NH}}$ coupling constants revealed that also for the stronger Bronsted acids charge-separated but still hydrogen-bonded binary complexes are formed. Nevertheless, the hydrogen bond is considerable weakened compared to the phosphoric acid catalysts. Therefore, the almost complete loss of the hydrogen bond as structural anchor in the binary complex in combination with the increased number of hydrogen bond acceptors leads to a high mobility of the imine in the binary complex. This is also reflected in the theoretical calculations, which predict for both imine-isomers several orientations. Nevertheless, it was possible to verify the existence of at least two of the computational predicted, most stable structures for the *E*-complexes experimentally by various NOESY measurements. In one of these structures the formation of a hydrogen bond to the nitrogen in the other one to the oxygen of the disulfonimide catalyst was assumed. These observations proofed that not only the strongest possible hydrogen acceptor (nitrogen) is occupied. On the other hand, for the more compact *Z*-imines no structural preference was found. Furthermore, the reactivity of the different classes of catalysts in the transfer hydrogenation of several *N*-alkyl-imines was compared to the observed hydrogen bond strengths. However, no acidity/reactivity-correlation between the catalysts with varying acidic motives was found. Due to the the extremely weakening of the hydrogen bond in the disulfonimide- and sulfonic acid-complexes, not only the impact of the hydrogen bond as structural anchor in the pre-catalytic species seems to be drastically decreased but also the influence of the hydrogen bond strengths on the reactivity is attenuated. Finally, the binary complexes of an *N*-alkyl imine were investigated, because for this substrate highly acidic disulfonimide catalysts provide high yields and good enantioselectivities in the transfer hydrogenation while the less acidic phosphoric acid catalyst exhibit poor conversions and low stereoselectivities. The hydrogen bond analysis of the *N*-alkyl imine/TRIP-complexes revealed several additional complex structures, which have not yet been observed in the previously investigated *N*-aryl-imine-complexes. These additional structures and their equilibria may contribute to the poor performance of TRIP. In contrast, for the corresponding *N*-alkyl imine/DSI-complexes only the typical binary *E*- and *Z*-complexes were observed.

6 Conclusion

The focus of the fifth chapter was the detailed investigation of the imine-isomerization. Initially, the isomerization rates for both *E*-to-*Z*- and *Z*-to-*E*-isomerization rates of free imines as well as for a partially protonated imine in four different binary complexes were quantified. Since the isomerization seems to play an important role for the overall reaction rate of the asymmetric transfer hydrogenation, the impact of the degree of protonation on the isomerization was of great interest. This analysis showed that the *Z*-to-*E*-isomerization rate of a more protonated imine is reduced. However, the observed *Z*-to-*E*-isomerisation for the imine in the binary complex with the sterical most demanding catalyst (TiPSY) was slower than expected due to the internal acidity scale of the catalysts. Thus, apart from the imine protonation also the sterical properties of the catalyst seem to affect the isomerization rate. However, the *E*-to-*Z*-isomerisation rates were less affected by the bulkiness of the catalyst. This observation indicates that the sterical contribution is already considered in the stabilisation of the *Z*-imine. Furthermore, the analysis of the thermal isomerization barriers at low temperatures confirms the interplay of the sterical environment of the imine and the degree of protonation being responsible for the isomerization rates. Furthermore, the extrapolation of the Eyring-Polanyi plot enables the determination of the isomerization barriers at room temperature. Interestingly, the analysis of the isomerization barriers at 298 K showed, that the contribution of the imine-protonation on the isomerization rate decreases at higher temperatures, while the sterical factor increases. In general, all observed isomerization barriers (73-88 kJmol⁻¹) at 298 K are significantly higher than the calculated barriers for the hydride transfer *via type IZ* and *type IIZ* (calculated: 45-54 kJmol⁻¹). Thus, the hydride transfer could be excluded to be the rate determining step, if the ternary complex is formed sufficiently. Finally, it was shown that it is also possible to photoisomerize the imines by using a photosensitizer. Indeed the direct photoisomerization is by far more effective, than using one of the investigated photosensitizers. Both investigations of the reduction/oxidation potentials as well as fluorescence quenching experiments suggest a single-electron transfer from the imine to the photosensitizer followed by the isomerization of the radical cation.

In conclusion, in this thesis the interactions between different Brønsted acid catalysts and imines were investigated by NMR spectroscopy. First, the strong hydrogen bond between TRIP and various imines was investigated. In all cases the hydrogen geometry was not significantly affected by the substitution pattern of the imine. Therefore, the hydrogen bond seems to be a structural anchor of the pre-catalytic species. Since, the acidity of the catalysts is modulated by the variation of the 3,3'-substituents an internal

acidity scale based on the ^{15}N chemical shifts of the imine could be implemented. In this way it could be shown that the reactivity of the transfer hydrogenation correlates inverse with the internal acidity. However, isomerization and ternary complex formation also play an important role. For example, a break down in reactivity was observed if the sterical bulk of the 3,3'-substituents hinders the binding of the second substrate and thus the ternary complex formation is hampered. Additionally, the investigations of the more acidic disulfonimide catalyst showed, that the previously observed acidity/reactivity-correlation is not applicable between different classes of catalysts. This is most probably due to the extremely weakening of the hydrogen bond caused by the higher acidity of the disulfonimide catalyst, leading to an attenuated influence of the hydrogen bond strengths on the reactivity. Furthermore, by means of a detailed quantification of isomerization rates and barriers, it could be shown that the experimentally determined isomerization barriers are significantly higher than the calculated barriers for the hydride transfer. For this reason, the hydride transfer could be neglected as rate-determining step of the transfer hydrogenation, if the ternary complex is formed sufficiently. However, also the ternary complex formation can be assumed to be slow because of the low solubility of the Hantzsch ester. Unfortunately, up to now the ternary complex itself was not accessible in detail and may be the focus of further investigations.

7 Abbreviation Register

1D	one dimensional
2D	two dimensional
3D	three dimensional
AcOH	acetic acid
Å	ångström
BINOL	1,1'-bi-2-naphthol
BF	basic transmitter frequency
Boc	<i>tert</i> -butyloxycarbonyl
OP	transmitter frequency offset
bs	broad signal
COSY	correlation spectroscopy
cm	centimeter
°C	degree celsius
CSA	chemical shift anisotropy
D	delay
δ	chemical shift
DCM	dichloromethane
DD	dipolar dipolar
DFT	density functional theory
DPP	diphenyl phosphate
DS	dummy scans
EI	electron impact
ESI	electron spray ionization
EV	electron volt
GC-MS	gas chromatography – mass spectrometry
g	gram
h	hour(s)
HMBC	heteronuclear multiple bond correlation
HMQC	heteronuclear multiple quantum correlation
HSQC	heteronuclear single quantum coherence
HR-MS	high resolution mass spectrometry
<i>i</i> Pr	isopropyl
K	kelvin

7 Abbreviation Register

mg	milligram
mL	milliliter
mmol	millimole
mM	millimolar
MS	molecular sieves
n.d.	not determined
NMR	nuclear magnetic resonance
NOE	nuclear overhauser effect
NOESY	nuclear overhauser enhancement spectroscopy
NS	number of scans
p.A.	per analysis
pm	picometer
ppm	part per million
r.t.	room temperature
RT	retention time
SW	spectral width
μL	microliter
μmol	micromole
FID	free induction decay
TD	size of FID
TMA	trimethyl acetic acid
TMS	tetramethylsilane
(<i>R</i>)- TIPSY	3,3'-Bis(triphenylsilyl)-1,1'-binaphthyl-2,2'-diylhydrogenphosphate
(<i>R</i>)- TRIM	3,3'-Bis(2,4,6-trimethylphenyl)-1,1'-binaphthyl-2,2'- diylhydrogenphosphate
(<i>R</i>)- TRIFP	3,3'-Bis(3,5-trifluoromethylphenyl)-1,1'-binaphthyl-2,2'- diylhydrogenphosphate
(<i>R</i>)- TRIP	3,3'-Bis(2,4,6-triisopropylphenyl)-1,1'-binaphthyl-2,2'- diylhydrogenphosphate

Eidesstattliche Erklärung

(1) Ich erkläre hiermit an Eides statt, dass ich die vorliegende Arbeit ohne unzulässige Hilfe Dritter und ohne Benutzung anderer als der angegebenen Hilfsmittel angefertigt habe; die aus anderen Quellen direkt oder indirekt übernommenen Daten und Konzepte sind unter Angabe des Literaturzitats gekennzeichnet

(2) Bei der Auswahl und Auswertung haben mir die zu Beginn des jeweiligen Kapitels aufgeführten Personen in der jeweils beschriebenen Weise unentgeltlich geholfen.

(3) Weitere Personen waren an der inhaltlich-materiellen Herstellung der vorliegenden Arbeit nicht beteiligt. Insbesondere habe ich hierfür nicht die entgeltliche Hilfe eines Promotionsberaters oder anderer Personen in Anspruch genommen. Niemand hat von mir weder unmittelbar noch mittelbar geldwerte Leistungen für Arbeiten erhalten, die im Zusammenhang mit dem Inhalt der vorgelegten Dissertation stehen.

(4) Die Arbeit wurde bisher weder im In- noch im Ausland in gleicher oder ähnlicher Form einer anderen Prüfungsbehörde vorgelegt.

Regensburg, den _____

Kerstin Rothermel